Growth of Doped Transparent Conducting Oxides by Oxygen Plasma Assisted Atomic Beam Epitaxy



A thesis submitted to the University of Oxford for

The Degree of Doctor of Philosophy

Dong Myung Shin

Physical & Theoretical Chemistry
Department of Chemistry
University of Oxford
&
St. Catherine's College

To my wife, Minyoung,
with love and appreciation

Growth of Doped Transparent Conducting Oxides by Oxygen Plasma Assisted Atomic Beam Epitaxy

Dong Myung Shin, St. Catherine's College, Oxford

Doctor of Philosophy, Michaelmas Terms 2014

Abstract

Interest exists in the development of transparent conducting oxide materials, which have diverse applications in areas such as transparent coatings for display technologies, solar cells, and optoelectronics. Since many of the applications require the use of thin film forms, the need is to establish useful experimental approaches to the fabrication of such structures. One relatively new method in this area is oxygen-plasma assisted atomic beam epitaxy (OPABE) in which oxide layers are grown under normal molecular beam epitaxy (MBE) conditions with the addition of an oxygen atom beam to ensure full oxidation of the depositing metallic species. Work in this area has to date mainly focussed on the growth of relatively stable oxides such as ZnO, MgO and In_2O_3 which are the strongly thermodynamically favoured reaction products, across a broad range of reaction conditions. In contrast, the present work is concerned with the growth of Cu_2O and a range of delafossite materials, namely $CuInO_2$, $CuCrO_2$ and $CuGaO_2$, which are expected to require much more sensitive control to achieve the desired reaction product.

Studies of the OPABE growth of Cu_2O on MgO (100) and MgO (110) substrates have been carried out, using a broad range of physical techniques to characterise the grown Cu_2O deposits. It is demonstrated that CuO is the favoured reaction product at low growth temperatures, although Cu_2O becomes increasingly favoured as the

Abstract

growth temperature increases. Alternatively, it is also shown that a novel bilayer growth method, whereby some pure Cu is deposited prior to oxide growth, can be used to form the desired Cu (I) phase. Varying crystal orientations are seen, depending on the exact growth conditions; core level and valence band X-ray photoelectron spectroscopy (XPS), optical band gap and atomic force microscopy (AFM) measurements are used to characterise the deposits.

Further growth investigations of the delafossite compounds $CuInO_2$, $CuCrO_2$ and $CuGaO_2$ using OPABE are also recorded, and for the case of $CuInO_2$, comparison is also made with the pulsed laser deposition approach. For all three materials systems, oriented crystal growth on basal planes sapphire substrates is seen, with either the (001) plane or the (015) plane orienting parallel to the substrate depending on the growth temperature, provided approximately correct metal fluxes are used as set by the Knudsen-cell temperatures. The typical valence band electronic structure of delafossite materials is observed in all three cases, and XPS peak shifts suggest that the layers can be electrically doped by adding appropriate metal fluxes during growth. AFM measurements show the grown films are relatively rough and it is suggested that the growth mode follows an island growth mechanism in which oriented three dimensional islands formed at the start of growth gradually enlarge and coalesce as the film thickens. Optical absorption measurements are consistent with the generally accepted optical band gaps of the materials concerned.

Acknowledgements

I am thankful to Professor John S. Foord, my supervisor, who supported this project and offered advice and encouragement, which I took so much to heart. I am also indebted to Professor Russell G. Egdell, Drs. Robert Palgrave, David Payne, Anne Boulrange and Jingping Hu for going over successful experiments of the project and for spending invaluable hours with me in discussing various aspects. Finally I am grateful to Dr. Jisu Kim for his precious guidance for going UK.

Publications

1. **D. Shin**, J. S. Foord, D. J. Payne, T. R. Arnold, D. Aston, R. G. Egdell, K. G. Godinho, D. O. Scanlon, B. J. Morgan, G. W. Watson, E. Mugnier, C. Yaicle, A. Rougier, L. Colakerol, P. A. Glans, L. F. J. Piper, and K. E. Smith
"Comparative study of bandwidths in copper delafossites from X-ray emission spectroscopy" Physical Review B 80, 233105 (2009).

2. **D. Shin**, J. S. Foord, R. G. Egdell and A. Walsh
"Electronic structure of $CuCrO_2$ thin films grown on Al_2O_3(001) by oxygen plasma assisted molecular beam epitaxy" Journal of Applied Physics 112, 113718 (2012).

3. **D. Shin**, A. Bourlange, R. G. Egdell, and J. S. Foord
"Epitaxial growth of Cu_2O thin films by oxygen plasma assisted atomic beam epitaxy", in preparation for publication.

4. **D. Shin**, J. S. Foord and R. G. Egdell
"Epitaxial growth of $CuGaO_2$ and related delafossite compounds by OPABE", in preparation for publication.

Glossary

A

ACCEPTOR : An impurity in a semiconductor that accepts electrons. Boron is the primary acceptor used to dope silicon in the ion implantationprocess.
AMORPHOUS SOLID : In condensed matter physics and materials science, an amorphous (from the Greek a, without, morphé, shape, form) or non-crystalline solid is a solid that lacks the long-range order characteristic of a crystal. In some older books, the term has been used synonymously with glass. Nowadays, "amorphous solid" is considered to be the overarching concept, and glass the more special case: A glass is an amorphous solid that exhibits a glass transition. Polymers are often amorphous. Other types of amorphous solids include gels, thin films, and nanostructured materials.
AFM : Atomic force microscopy is a very high-resolution type of scanning probe microscopy, with demonstrated resolution on the order of fractions of a nanometer, more than 1000 times better than the optical diffraction limit.

B

BAND GAP : In solid-state physics, a band gap, also called an energy gap or bandgap, is an energy range in a solid where no electron states can exist. In graphs of the electronic band structure of solids, the band gap generally refers to the energy difference (in electron volts) between the top of the valence band and the bottom of the conduction band in insulators and semiconductors. This is equivalent to the energy required to free an outer shell electron from its orbit about the nucleus to become a mobile charge carrier, able to move freely within the solid material, so the band gap is a major factor determining the electrical conductivity of a solid. Substances with large band gaps are generally insulators, those with smaller band gaps are semiconductors, while conductors either have very small band gaps or none, because the valence and conduction bands overlap.

C

CARRIER : An electron or hole that carries electric charge through a conducting or semiconducting material.
CARRIER MOBILITY : A measure, typically specified in $cm^2/V \cdot s$, of how rapidly a charge carrier (an electron or hole) can move through a semiconductor in response to an applied electric field. The conductivity of a material is proportional to mobility multiplied by the concentration of carriers. High mobility is highly desirable in semiconductor devices because it leads to higher device performance through faster transistor switching.
CMOS (COMPLIMENTARY METAL OXIDE SEMICONDUCTOR) : A MOS device consisting of paired p-channel and n-channel transistors. Also used to refer to the family of manufacturing processes used to construct integrated circuits that feature CMOS transistors.
COLOR FILTER : A layer of an LCD flat panel display that is divided into transparent areas of red, green and blue, each of which overlays a transistor which is switched on an off to the full range of colors.
CONDUCTOR : A material that contains mobile charge carriers, such as electrons or ions.
CRYSTALLINE : A material that has atoms arranged in an ordered periodic array.
CVD (CHEMICAL VAPOR DEPOSITION) : A process for depositing thin films by exposing the substrate to one or more volatile precursors, which react and/or decompose on the substrate surface.

D

DELAFOSSITE : Delafossite is a copper iron oxide mineral with formula $CuAlO_2$ or $Cu^{1+}Al^{3+}O_2$. It is member of the delafossite mineral group with a general formula ABO_2, a group characterised by a sheet of linearly coordinated A cations stacked between edge-shared octahedral layers (BO_6). Delafossite along with other minerals of the ABO_2 group has been recognized for its electrical properties from insulation to metallic conduction. DEPOSITION : A process used to deposit a thin layer of insulating or conductive material onto the substrate.
DIELECTRIC : An insulator. Also used more specifically to refer to an insulator that may be polarized by an applied electric field. Two dielectrics commonly used in semiconductor processing are silicon dioxide (SiO_2) and silicon nitride (Si_3N_4).
DOPANT : An impurity added in controlled amounts to a material in order to modify some intrinsic characteristic, such as resistivity or melting point. The addition of a dopant to a semiconductor creates a material with predominantly negative (n-type) or positive (p-type) charge carriers depending on the dopant species.
DOPING : The introduction of impurities, or dopants. into the crystal lattice of a material to modify its electrical properties. To create n-type regions, arsenic (As), arsine (AsH_3), phosphine (PH_3) and anti-

mony (Sb) are commonly used. For p-type regions, typical dopants are boron (B), Boron Difluoride (BF_2) and Boron Trifluoride (BF_3).

E

ELECTRON : A stable subatomic particle with a negative electric charge that acts as a carrier of electricity.
EPITAXY : A method of depositing, or growing, a monocrystalline film where the deposited film takes on a lattice structure and orientation identical to those of the substrate. This enables a high-purity starting point for building a semiconductor device.

F

FET (FIELD EFFECT TRANSISTOR) : A type of transistor that relies on an electric field to control the flow of charge carriers in a semiconductor material.
FLAT PANEL DISPLAY (FPD) : Any consumer display device, such as an LCD or AMOLED, with a planar surface, in contrast to the curved front of cathode ray tube displays.
FERMI LEVEL : The Fermi level is the total chemical potential for electrons (or electrochemical potential for electrons) and is usually denoted by μ or EF. The Fermi level of a body is a thermodynamic quantity, and its significance is the thermodynamic work required to add one electron to the body (not counting the work required to remove the electron from wherever it came from). A precise understanding of the Fermi level—how it relates to electronic band structure in determining electronic properties, how it relates to the voltage and flow of charge in an electronic circuit—is essential to an understanding of solid-state physics.

H

HOLE : In semiconductors, a hole is the absence of an electron where one could exist in an crystal lattice. It can be thought of as the opposite of an electron, with a positive charge of exactly the same magnitude as an electron. If, in an electric field, an electron moves into this vacant site, the hole has effectively moved in the opposite direction.

I

INSULATOR : Nonconductive materials used to isolate electrically active areas of the device or chip from one another. Some commonly used insulators are silicon dioxide, silicon nitride, BPSG, and PSG.
INTEGRATED CIRCUIT (IC) : An electronic device that consists of many elements fabricated together on a single silicon substrate.
ITO (INDIUM TIN OXIDE) : A common TCO material. In_2O_3:Sn

J

JUNCTION : The interface between two semiconductor regions of differing dopant types. Usually refers to a p-n junction, at which the conductivity type changes from p-type to n-type.

K

k-VALUE : Also known as dielectric constant, often denoted by the Greek letter kappa (κ). An expression of the extent to which a material concentrates electric flux. In electronics, it refers to the capacitance of a material relative to silicon dioxide. A high k-value allows a transistor gate to be made smaller without increasing undesirable leakage. A low k-value is desirable in an insulating material such as one used to separate interconnects because it reduces charge build-up which wastes energy as heat, reducing the overall power consumption of a device. In addition, a low k-value allows faster signal propagation and thus faster switching speeds.

L

LATTICE : The orderly arrangement of atoms in a crystalline solid.
LED (LIGHT-EMITTING DIODE) : A semiconductor device that emits light when an electric current flows through it. An LED consists of a p-n junction which is constructed in such a way that a photon of light is emitted when a pair of charge carriers recombine.
LIQUID CRYSTAL DISPLAY (LCD) : A type of flat panel display that uses an array of backlit thin film transistors called a backplane to control each pixel.

Glossary

M

Molecular beam epitaxy : MBE is one of several methods of depositing single crystals. It was invented in the late 1960s at Bell Telephone Laboratories by J. R. Arthur and Alfred Y. Cho.[1] MBE is widely used in the manufacture of semiconductor devices, including transistors for cellular phones and WiFi. Molecular beam epitaxy takes place in high vacuum or ultra-high vacuum (10^{-8} Pa). The most important aspect of MBE is the deposition rate (typically less than 3000 nm per hour) allows the films to grow epitaxially. These deposition rates require proportionally better vacuum to achieve the same impurity levels as other deposition techniques. The absence of carrier gases as well as the ultra high vacuum environment result in the highest achievable purity of the grown films.

MOCVD (METAL-ORGANIC CHEMICAL VAPOR DEPOSITION) : MOCVD is a type of epitaxy process used to deposit compound semiconductor films, especially those used in the manufacture of high-brightness LEDs and power electronics. In an MOCVD process, a chemical reaction takes place at the surface of a substrate between organic compounds that contain the required metals and other elements.

MOS (METAL OXIDE SEMICONDUCTOR) : a structure obtained by growing a layer of silicon dioxide (SiO_2) on top of a silicon substrate and then depositing a layer of metal or polycrystalline silicon (the latter is commonly used). Often used to describe a transistor fabricated in this way.

N

N-TYPE : Semiconductor material that has negatively charged conductivity (an excess of electrons).

NEUTRALS : Particles traveling within an ion beam which have the same energy but no longer have a charge. Neutrals cannot be manipulated by external fields and will continue at a fixed velocity until colliding with the vacuum chamber walls or other particles.

O

ORGANIC LIGHT EMITTING DIODE (OLED) : A light-emitting device where photons are emitted as a result of electron-hole interactions in a thin film organic semiconductor.

P

P-TYPE : Semiconductor material that has positively charged conductivity (a deficiency of electrons).

PECVD (PLASMA ENHANCED CHEMICAL VAPOR DEPOSITION) : A CVD process using plasma energy to drive the deposition. This technique allows lower deposition temperatures, increases film density and purity.

PHONON : In physics, a phonon is a collective excitation in a periodic, elastic arrangement of atoms or molecules in condensed matter, such as solids and some liquids. Often referred to as a quasiparticle, it represents an excited state in the quantum mechanical quantization of the modes of vibrations of elastic structures of interacting particles.

PHOTON : A photon is an elementary particle, the quantum of light and all other forms of electromagnetic radiation. It is the force carrier for the electromagnetic force, even when static via virtual photons. The effects of this force are easily observable at both the microscopic and macroscopic level, because the photon has zero rest mass; this allows long distance interactions. Like all elementary particles, photons are currently best explained by quantum mechanics and exhibit wave–particle duality, exhibiting properties of both waves and particles. For example, a single photon may be refracted by a lens or exhibit wave interference with itself, but also act as a particle giving a definite result when its position is measured.

PLASMA : A fourth state of matter - not a solid, liquid or gas. In a plasma, the electrons are pulled free from the atoms and can move independently. The individual atoms are charged, even though the total number of positive and negative charges is equal, maintaining an overall electrical neutrality.

PLASMON : In physics, a plasmon is a quantum of plasma oscillation. The plasmon can be considered a quasiparticle since it arises from the quantization of plasma oscillations, just like phonons are quantizations of mechanical vibrations. Thus, plasmons are collective oscillations of the free electron gas density, for example, at optical frequencies. Plasmons can couple with a photon to create another quasiparticle called a plasma polariton.

PVD (PHYSICAL VAPOR DEPOSITION) : A process technology in which atoms of conducting material (aluminum, titanium nitride, etc.) are sputtered from a target of pure material, then deposited on the substrate to create the conducting circuitry within an integrated circuit or FPD.

Glossary

R

RADIO FREQUENCY: Radio frequency (RF) is a rate of oscillation in the range of around 3 kHz to 300 GHz, which corresponds to the frequency of radio waves, and the alternating currents which carry radio signals. RF usually refers to electrical rather than mechanical oscillations; however, mechanical RF systems do exist.

S

SEMICONDUCTOR : A material whose electrical conductivity is intermediate between that of metals (conductors) and insulators (non-conductors) and can be modified physically or chemically to increase or decrease its conductivity by the addition of dopants.
SOLAR CELL : A device that converts the energy of sunlight directly into electricity by the photovoltaic effect. Multiple cells are wired together to form modules.

SOLID-STATE : relating to the properties, structure, or reactivity of solid material; *especially* **:** relating to the arrangement or behavior of ions, molecules, nucleons, electrons, and holes in the crystals of a substance (as a semiconductor) or to the effect of crystal imperfections on the properties of a solid substance
SPUTTERING : A method of depositing a film where atoms are ejected from a solid target material due to bombardment of the target by energetic particles.

T

TARGET : In PVD, the target is the source of the material to be deposited. Atoms are ejected from the target as a result of the bombardment of energetic particles.
TCO (TRANSPARENT CONDUCTIVE OXIDE) : Doped metal oxide films used in optoelectronic devices such as flat panel displays, touch panels and photovoltaics. In LCDs, TCO layers form the electrodes that generate the electric field to polarize the liquid crystal. In touch panels, TCO layers are used for the sensing electrodes. In PV, the TCO forms the top electrode of the cell.
TEM (TRANSMISSION ELECTRON MICROSCOPE) : A transmission electron microscope that transmits a beam of electrons through an ultra-thin specimen. It operates on the same basic principle as the optical microscope but with much higher resolution.
THIN FILM : A layer of material ranging from fractions of a nanometer to several micrometers thick.
THIN-FILM TRANSISTOR (TFT) : A MOSFET manufactured with thin film technology, used primarily in the manufacturing of active matrix LCDs.

V

VACUUM : A pressure below atmospheric ambient, often referred to by specific pressure ranges (Rough vacuum, from atmosphere to 1×10^{-3} Torr, High vacuum, from to 1×10^{-3} Torr to 1×10^{-9} Torr, Ultra-high vacuum (UHV) – below 1×10^{-9} Torr)
VAPORIZER : In ion implantation, a device used to convert solid state ion source material into a gaseous state for ion beam production.
VIAS : Vertical pathways through dielectric layers that make electrical connections between interconnect layers.

W

WORK FUNCTION: In solid-state physics, the work function (sometimes spelled workfunction) is the minimum thermodynamic work (i.e. energy) needed to remove an electron from a solid to a point in the vacuum immediately outside the solid surface. Here "immediately" means that the final electron position is far from the surface on the atomic scale, but still too close to the solid to be influenced by ambient electric fields in the vacuum. The work function is not a characteristic of a bulk material, but rather a property of the surface of the material (depending on crystal face and contamination).

X

XPS : X-ray photoelectron spectroscopy (XPS) is a surface-sensitive quantitative spectroscopic technique that measures the elemental composition at the parts per thousand range, empirical formula, chemical state and electronic state of the elements that exist within a material. XPS spectra are obtained by irradiating a material with a beam of X-rays while simultaneously measuring the kinetic energy and number of electrons that escape from the top 0 to 10 nm of the material being analyzed. XPS requires high vacuum ($P \sim 10^{-8}$ millibar) or ultra-high vacuum (UHV; $P < 10^{-9}$ millibar) conditions, although a current area of development is ambient-pressure XPS, in which samples are analyzed at

pressures of a few tens of millibar.
X-radiation : (composed of X-rays) is a form of electromagnetic radiation. Most X-rays have a wavelength ranging from 0.01 to 10 nanometers, corresponding to frequencies in the range 30 petahertz to 30 exahertz (3×10^{16} Hz to 3×10^{19} Hz) and energies in the range 100 eV to 100 keV. X-ray wavelengths are shorter than those of UV rays and typically longer than those of gamma rays.

Contents

Abstract i

Acknowledgements iii

Publications iv

Glossary v

Contents x

1. Introduction

1.1. Background to Transparent Conducting Oxides 1

1.2. Optoelectronic Devices 2

1.2.1. n-type TCOs in Optoelectronic Devices 2

1.2.2. TCO Materials for Thin Film Electrodes 4

1.2.3. Alternative TCO Films for The Future 6

1.3. Structure of Metal Oxides 6

1.4. Frontier TCOs for Invisible Circuits 10

1.5. Aims of Current Thesis 13

References 16

2. Experimental Theory and Techniques

2.1. General Considerations of Crystal Growth 19

2.2. Molecular Beam Epitaxy (MBE) 27

2.2.1. Introduction 27

2.2.2. Ultra-High Vacuum (UHV) 29

2.2.3. MBE Beam Sources 31

2.2.4. Oxygen Plasma Assisted Atomic Beam Epitaxy (OPABE) 33

2.2.5. The SVT UHV-OPABE System 34

2.3. X-ray Spectroscopies 37

2.3.1. Introduction to Spectroscopic Methods 37

2.3.2. X-ray Photoelectron Spectroscopy (XPS) 38

2.3.3. XPS Implementation 58

2.3.4. X-ray Emission Spectroscopy (XES) 61

2.3.5. X-ray Absorption Spectroscopy (XAS) 62

2.3.6. XES, XAS Implementation 64

2.4. X-ray Diffraction and Surface Morphology 66

2.4.1. X-ray Diffraction (XRD) 66

2.4.2. XRD Implementation 68

2.4.3. Scanning Probe Microscopies 68
2.4.4. Implementation 75
2.4.5. Optical band gap 76
References 79

3. Epitaxial Growth of p-Type TCO Cu_2O Thin Films by Oxygen Plasma Assisted Atomic Beam Epitaxy

3.1. Introduction 86
3.1.1. Background 86
3.1.2. Crystal Structure and Electronic Configuration of Cu_2O 87
3.1.3. Evolution of The Crystal Growth of Cu_2O and Aims of The Present Work 91
3.2. Experimental Details 93
3.3. Results 94
3.3.1. XRD Analysis 94
3.3.2. Survey XPS Scan of OPABE Films 104
3.3.3. High Resolution XPS Analysis of Grown Films 106
3.3.4. Valence Band Spectra 111
3.3.5. Optical Band Gap 115
3.3.6. Investigation of Surface Morphology by AFM 119
3.4. Summary 122
References 124

4. Epitaxial Growth of Transparent $CuInO_2$ Thin Films by Oxygen Plasma Assisted Atomic Beam Epitaxy

4.1. Introduction 129
4.1.1. Background 129
4.1.2. Band Gap Energy of Delafossite Compounds $CuMO_2$ 133
4.1.3. Crystal Structure of Delafossite $CuMO_2$ 134
4.2. Experimental Details 135
4.3. Results 137
4.3.1. Stoichiometric Proportions of $CuInO_2$ Films on Differing Fluxes 137
4.3.2. X-ray Photoemission Spectra of Core Level and Occupied Valence Band States 138
4.3.3. X-ray Photoemission Spectra and Valence Band Shift Concerning Bipolar Doping 143
4.3.4. X-ray Diffraction of OPABE $CuInO_2$ Films 145
4.3.5. Optical Band Gap of OPABE $CuInO_2$ Films 148

4.3.6. Surface Morphology Investigation by AFM 151
4.4. Summary 153
References 155

5. $CuInO_2$ Thin Films by Pulsed Laser Deposition

5.1. Introduction 159
5.1.1. Background 159
5.1.2. Typical Experimental Set-Up Used for PLD 160
5.2. Experimental Details 161
5.2.1. Synthesis of Target 161
5.2.2. Film Preparation and Characterization 162
5.3. Results 163
5.3.1. Stoichiometries of PLD $CuInO_2$; Effect of Oxygen Pressure 163
5.3.2. X-ray Photoemission Spectra and The Occupied Density of States 165
5.3.3. X-ray Emission Spectra with PDOS of Cu 3d and O 2p 169
5.3.4. X-ray Absorption Spectra and Resonant X-ray Emission Spectra 173
5.3.5. Bipolar Doping for PLD $CuInO_2$ Thin Films 177
5.3.6. X-ray Diffraction of PLD $CuInO_2$ Thin Films 180
5.4. Summary 185
References 187

6. Epitaxial Growth of $CuCrO_2$ and $CuGaO_2$ Thin Films by OPABE

6.1. Introduction 190
6.1.1. Background 190
6.1.2. Electronic Properties of $CuCrO_2$ and $CuGaO_2$ 191
6.2. Experimental Details 192
6.3. Results 193
6.3.1. XRD Analysis of $CuCrO_2$ and $CuGaO_2$ Thin Films 193
6.3.2. Stoichiometric Proportions of $CuCrO_2$ and $CuGaO_2$ Thin Films Differing Growth Conditions 200
6.3.3. X-ray Photoemission Data of $CuCrO_2$ and $CuGaO_2$ Thin Films and Comparative Study of Ceramic Sample 202
6.3.4. Valence and Core Level Photoemission Spectra Shift Concerning n-Type Doping 210
6.3.5. Optical Band Gap of $CuCrO_2$ and $CuGaO_2$ OPABE Thin Films 215
6.3.6. Surface Morphology of $CuCrO_2$ and $CuGaO_2$ Thin Films by AFM 219

6.4. Concluding Remarks 225
References 226

7. Concluding Remarks 230
References 239

1 Introduction

1.1 Background to Transparent Conducting Oxides

The metal oxides constitute a varied and exciting class of materials, spanning metallic, semiconducting and insulating forms, with a range of useful optical, magnetic and electrical properties [1]. This range of properties results in a significant important role for oxide materials in current and next generation technologies; it also raises fascinating fundamental science issues. These issues deal with such matters as the band gaps, the electronic properties which range from superconducting to metallic to semiconducting to insulating, magnetic ordering behaviour (ferromagnetic, ferrimagnetic, antiferromagnetic), dielectric and piezoelectric properties [2].

In recent years, considerable interest has arisen in the field of transparent conducting oxides films, because of their current and future applications in developing electronic and optoelectronic devices [3]. Transparent conducting oxides (TCOs) are of value in areas such as infrared reflective coatings and in optoelectronic applications for electrodes for flat panel displays, including liquid crystal display (LCD), organic light emitting diodes (OLEDs), solar cells and digital devices for social networking systems such as smart phones and tablet PCs, as seen in figure 1.1 [4, 5].

Even though tin-doped (n-type) indium oxide (commonly named indium-tin-oxide, or ITO) thin films, which can be deposited by D.C. magnetic sputtering, have been widely used for flat panel displays, there are many challenges in the areas of TCOs to achieve technical advantages such as low resistivity, bipolar doping for homo junctions and low cost, especially relating to the supply of indium, the principal material of ITO [6]. Furthermore, current developments in optoelectronic applications have repeatedly needed thin film electrodes with specific optical and electrical properties.



Figure 1.1. Optoelectronic applications of TCOs in solar cells, thin film transistor liquid crystal display (TFT-LCD), organic light emitting diodes (OLEDs) and social networking systems such as smart phone and digital tablets. (Figures used under permission of the GNU free documentation licence)

1.2 Optoelectronic Devices

1.2.1 n-type TCOs in Optoelectronic Devices

TCOs, particularly ITO, are mainly used in this area as high performance transparent conductive coatings in optical devices, for example nitride-based light emitters such as InGaN-based, blue LEDs [4, 7]. As seen in figure 1.2, the TFT-LCD is using ITO as electrodes for the colour filter and circuit array substrate. The same is true in organic light emitting diodes (OLEDs) as shown in figure 1.3. An OLED comprises an electroluminescent layer which can be made from films of organic materials which emit radiation in response to an electric current. The layered film of organic semiconductor material is situated between two electrodes, the cathode and anode, all deposited on some substrate. In general, at least one of these electrodes

must be transparent and as expected ITO is commonly used as the anode material in OLED devices.

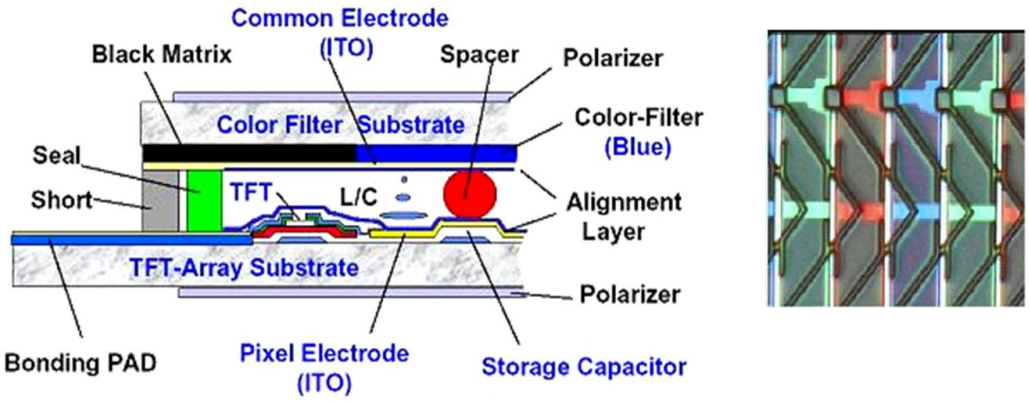


Figure 1.2. Systematic cross-section view of TFT-LCD (left) and top view of colour filter part in TFT-LCD. (Figures used under permission of the GNU free documentation licence)

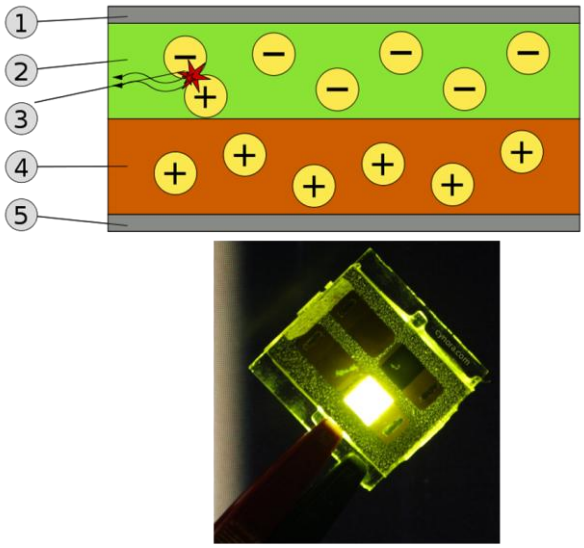


Figure 1.3. Upper image is schematic view of OLED: (1) cathode (-) layer (2) emissive layer (3) emission of radiation (4) conductive layer (5) anode (+) layer. Lower picture is green emitting OLED. (Figures used under permission of the GNU free documentation licence)

These are all passive applications. The primary reason behind this in the lack of good p-type TCO materials which would enable active oxide electronics based on p-n junctions to be developed.

1.2.2 TCO Materials for Thin Film Electrodes

TCO films which are in actual use as optically transparent electrodes are amorphous or polycrystalline structures since they are often prepared by techniques such as sputtering which result in these types of material, although single crystalline films can be grown by true epitaxy techniques [8]. TCO films such as ITO and Al-doped ZnO, exhibit a resistivity of the order of 10^{-3} Ω cm or less with an average optical transmittance around 80 % in the visible range [8] . With the aim of obtaining improved properties, lots of n-type TCO materials have been developed as seen in table 1.1. There are various components system such as single, binary and ternary compounds along with multicomponent oxides. The binary compounds such as ZnO-SnO_2 or In_2O_3-SnO_2, are favoured with regard to the relative ease of controlling the chemical composition in film depositions as compared with ternary and multicomponent oxides [6, 9]. However as can be seen in the table, quite complicated chemical formulations find potential application [10, 11].

Figure 1.4 shows the progressive change in minimum resistivity for representative doped binary compound TCO films based on ZnO, In_2O_3 and SnO_2. A resistivity of order of 10^{-5} Ω cm has been reported in recent work for ITO and ZnO:Al (AZO) [8]. Detailed electrical characterisation of materials such as AZO show Hall carrier concentrations of order of 10^{20}~10^{21} cm^{-3} with resistivities, in the range ρ of 5 x 10^{-4} ~ 8.5 x 10^{-5} Ω cm for films, which were prepared using pulsed laser deposition and RF magnetron sputtering [12, 13].

Table 1.1 n-type TCO semiconductors for thin film electrodes [8].

Material	Dopant or compound
SnO_2	Sb, F, As, Nb, Ta
In_2O_3	Sn, Ge, Mo, F, Ti, Zr, Hf, Nb, Ta, W, Te
ZnO	Al, Ga, B, In, Y, Sc, F, V, Si, Ge, Ti, Zr, Hf
CdO	In, Sn
$ZnO–SnO_2$	Zn_2SnO_4, $ZnSnO_3$
$ZnO–In_2O_3$	$Zn_2In_2O_5$, $Zn_3In_2O_6$
$In_2O_3–SnO_2$	$In_4Sn_3O_{12}$
$CdO–SnO_2$	Cd_2SnO_4, $CdSnO_3$
$CdO–In_2O_3$	$CdIn_2O_4$
$MgIn_2O_4$	
$GaInO_3$, $(Ga, In)_2O_3$	Sn, Ge
$CdSb_2O_6$	Y
$ZnO–In_2O_3–SnO_2$	$Zn_2In_2O_5–In_4Sn_3O_{12}$
$CdO–In_2O_3–SnO_2$	$CdIn_2O_4–Cd_2SnO_4$
$ZnO–CdO–In_2O_3–SnO_2$	

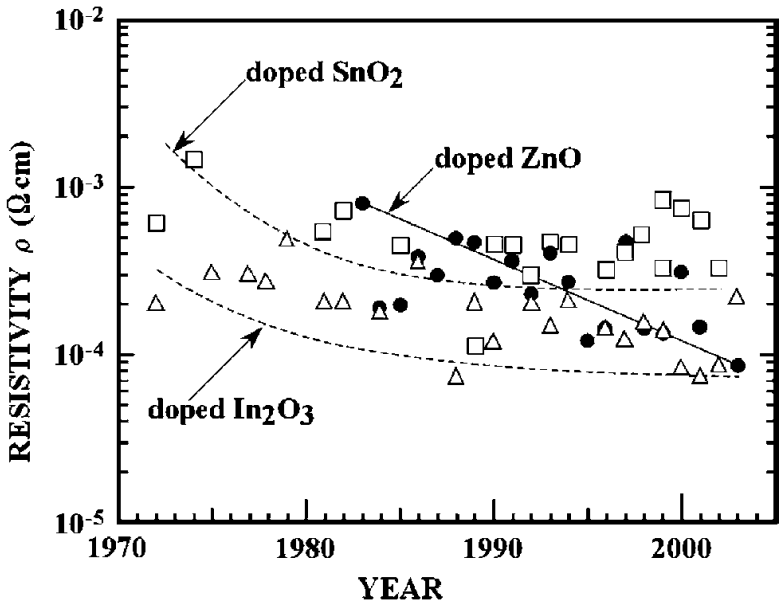


Figure 1.4. Reported resistivity of impurity-doped TCO films as binary compounds: doped SnO_2, doped In_2O_3 and doped ZnO along with years [8].

1.2.3 Alternative TCO Films for The Future

In recent years, the enormous demand for TCO materials as thin film transparent electrodes has rapidly increased in the area of not only flat panel displays such as TFT-LCD, plasma display Panel (PDP) and OLED, but also solar cells. The development of alternative TCO films is required to solve inevitable disadvantages of ITO such as significant price, and image sticking phenomena in displays [3, 14, 15]. Consequently there is interest in developing alternative TCO materials with differing properties, such as ZnO_2 with bipolar dopants of Zn or Al, and p-type TCOs like Cu delafossites, as seen in table 1.2 [16-21].

Table 1.2 p-type TCO semiconductors for thin film electrodes [16-21].

Material	p-type dopant
Cu_2O	N
$CuAlO_2$	Mg, Zn
$CuInO_2$	Ca
$CuCrO_2$	Mg, Zn
$CuGaO_2$	Ca, Cr
$SrCu_2O_2$	K
LaOCuS	Sr

1.3 Structure of Metal Oxides

The crystal structure of many metal oxides can be envisaged as an array of metal cations surrounded by doubly charged O^{2-} anions, packed commonly in cubic or hexagonal packing geometries. The metal sites are thus typically of an octahedral (6 coordinate) or a tetrahedral (4 coordinate) configuration. There are many crystallographic forms of simple binary oxides, including such coordination types as rocksalt-MO (*e.g.* MgO, CdO, CaO, NiO, CoO for 6:6 coordinate), corundum-M_2O_3

(*e.g*. Al_2O_3, V_2O_3, Cr_2O_3, Fe_2O_3, Ti_2O_3 for 6:4 coordinate), rutile-MO_2 (*e.g*. TiO_2, SnO_2, RuO_2 for 6:3 coordinate), wurtzite-MO (*e.g*. ZnO for 4:4 coordinate), and fluorite-MO_2 (*e.g*. CeO_2, UO_2 for 8:4 coordinate) [1]. For more complex materials, structures such as perovskite ABO_3 (*e.g*. $SrTiO_3$, $BaTiO_3$, $La_{1-x}Sr_xMnO_3$, Na_xWO_3) and spinel AB_2O_4 (*e.g*. $MgAl_2O_4$ and Fe_3O_4) need to be considered as common forms.

This thesis is concerned with conductive oxides so it is necessary to understand how the electronic properties arise. Whilst this is discussed in the relevant chapters, a simple overview is given here. The electronic structure of metal oxides is often discussed in terms of the theories of the *ionic model of bonding* and *band theory*. The ionic model of electronic structure suggests that the bonding is driven by electron transfer from the metal to the electronegative oxygen atoms, as seen in figure 1.5 [22, 23].

Figure 1.5(a) shows the 3*s* level of neutral Mg ($3s^2$) sits above the O 2*p* level of neutral O ($2p^4$), which is more electronegative than Mg. However these levels then are reversed for O^{2-} and Mg^{2+} ions free ion states, as seen in figure 1.5(b). The second electron affinity of an O atom is negative so the 2*p* level of O^{2-} is situated above the vacuum level. Figure 1.5(c) shows that the Madelung potential associated with the MgO lattice stabilizes the ionic configuration and causes a switchover in the energy levels for O^{2-} and Mg^{2+} ions [23]. However this leads to a band gap calculation for MgO which is much greater than the experimental value [24]. Two more effects have to be introduced which lead to a reduction in the calculated band gap. The first effect is electrostatic polarization, relating to the deformation of electron distribution in an electric field, as shown in figure 1.5(d). The other is the overlap and interaction of orbitals on the neighbouring ions which gives rise to appreciable Mg 3*s* conduction and O 2*p* valence bandwidth, as shown in figure 1.5(e).

The existence and treatment of delocalised energy bands in solids is described in *band theory*, which identifies that electrons moving in a periodic potential such as provided by a crystal lattice undergo strong perturbations from the free electron picture, resulting in the formation of energy bands and band gaps [1, 25].

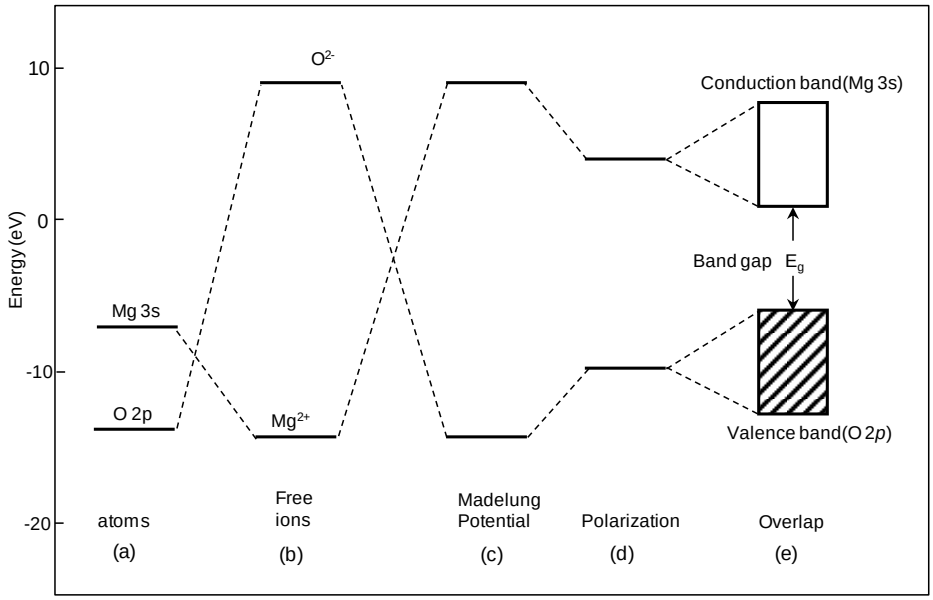


Figure 1.5. Ionic model of the band structure for MgO [23].

Bloch's theorem states that the eigenfunction for such a system may be written as the product of a plane wave envelope function and a periodic function (periodic Bloch function) $\upsilon_{nk}(r)$ that has the same periodicity as the potential [26]:

$$\Psi_{nk}(r) = e^{ikr}\, \upsilon_{nk}(r) \qquad (1.1)$$

The corresponding energy eigenvalues are $\varepsilon_n(k) = \varepsilon_n\ (k + K)$, periodic with periodicity K of a reciprocal lattice vector. The energies associated with the index *n* disperse continuously with wave vector k and form an energy band identified by band index *n*. The eigenvalues for given *n* are periodic in *k*; all distinct values of $\varepsilon_n(k)$ occur for *k*-values within the first Brillouin zone of the reciprocal lattice [26]. The form

of these wave functions in materials such as oxides can be envisaged from the so-called tight-binding model which ascribes the band states to the overlap of the valence atomic orbitals of the species present in the lattice.

A non-transition metal oxide with the metal in its maximum oxidation state would have an occupied (valence) band, arising from the overlap of the oxygen O 2*p* orbitals and an unoccupied (conduction) band composed of combinations of metal valence orbitals, for Mg the Mg 3*s* and 3*p* states. Pre-transition metal oxides such as alkaline-earth oxides (*e.g*. BaO, SrO, MgO) and Al_2O_3, follow this simple qualitative picture and are wide bandgap insulators (*e.g*. 9.5 ±0.5 eV, 14.0 ±0.5 eV, and 16.9 ±0.5 eV for BaO, SrO, and MgO, respectively), because of the large difference in electronegativity between the metal and oxygen [27]. Post-transition metal oxides such as ZnO, SnO_2 and In_2O_3, have a bandgap in the range of 3-4 eV and an *s*-like conduction band [28, 29]. These post-transition metal oxides have less ionic character than pre-transition metal oxides, since the O 2*p* orbitals are closer in energy to the metal ns/n*p* orbitals and therefore have much stronger hybridization [1, 25].

Transition metal oxides are more complicated because of the presence of partially filled *d* states in the valence shell which opens up the possibility of conductivity arising from partially filled electron bands. Again a good starting point is to consider a filled valence band derived from O 2*p* orbitals. However the lowest non-filled energy band is derived from overlap of the *d* orbitals rather than the higher metal *s*, *p* states. Thus for example TiO_2 is an insulator with a band gap of ~3 eV representing the energy gap between the filled O 2*p* band and the empty Ti *d* band (although mixing of these states certainly occurs). If *d* electrons are present then these partially filled *d* bands and can lead to metallic conductivity as seen in the d^1 compounds Ti_2O_3 and VO_2. The picture is more complicated however as seen in subsequent

chapters in this thesis since ligand field splitting needs to be taken into account in deciding if filled or empty bands are likely to be present. Finally it is worth noting that although band theory suggests many compounds of transition metals should be metallic, many are non-metallic in practice because electron repulsion produces electron localisation within the narrow *d* bands, expected because of poor orbital overlap, and a breakdown of band theory occurs [1].

1.4 Frontier TCOs for Invisible Circuits

For the advanced optoelectronic applications, it takes only a small thought to imagine the value of basic transparent electronic circuitry in both social networking devices and the national defence like military applications. Furthermore, much more sophisticated invisible circuits could be very useful, and scientists and engineers are vigorously pursuing new and highly innovative materials for such circuits, as well as understanding the properties of the materials concerned [30].

As understanding of a theoretical framework for the n-type transparent conducting oxide, the following diagram has suggested for the conditions by which the degenerate gas of electrons is formed upon doping, for example, In_2O_3 by SnO_2. Semiconducting In_2O_3 is best regarded as a host oxide lattice to which SnO_2 can be added as a substitutional dopant; thus the metal atom of higher valency (Sn^{4+}) forms a singly charged donor state (nominally Sn^{3+}; Figure 1.6) [31] by substituting for an In^{3+} atom of the host material. In_2O_3 itself has a particularly complex crystal structure (*ca*. 80 atoms per unit cell) but the one-electron electronic energy band model originally developed by Fan and Goodenough [32] still represents an excellent and transparent starting description for describing the electronic structure of both the pure and doped materials [31].

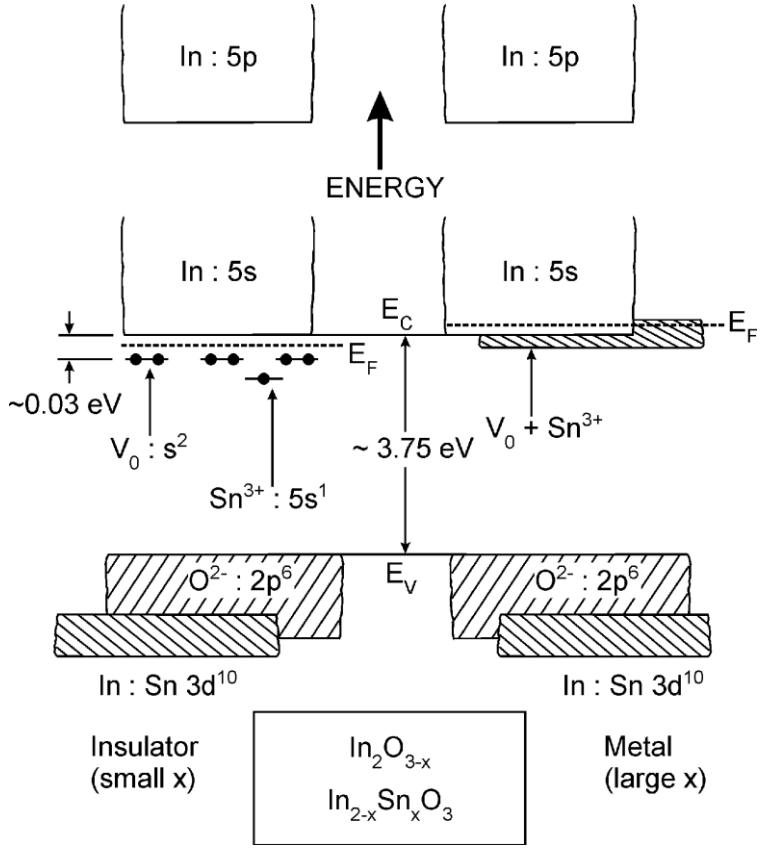


Figure 1.6. Schematic energy-band model for Sn-doped In_2O_3 for small x (insulating) and large x (metallic) modified from Fan and Goodenough [32]. The issue as to whether the 'impurity band' (for large x) is separate from, or placed inside the In 5s (host) conduction band is not resolved at this time. (adapted from ref. 31)

In_2O_3 has a filled valence band that is primarily oxygen 2p in character. The (filled) In $3d^{10}$ core levels also lie well below the valence band edge, as shown in Figure 1.6. The direct semiconductor band gap, denoted *E*g is 3.75 eV. It has been proposed that the conduction band is mainly derived from the indium 5s electrons and for the undoped material the Fermi energy is located half way between the valence and conduction bands. With the substitution of In^{3+} by Sn^{4+}, one electron donor or impurity states are formed below the (host) In 5s or 5sp conduction band [31].

One of new materials is copper delafossite compounds such as $CuAlO_2$ and $CuInO_2$, pioneered by Hiroshi Kawazoe and his colleague at Tokyo Institute of Technology [17, 18]. p-type transparent materials have crucially been needed, along with the n-type materials in which electrons are the carriers, to produce active materials in a micro-circuit such as diodes, and the delafossite material can display this electrical state.

For transparent circuits, the need is for electrical conducting semiconductor materials without the high density of electronic excitations which give rise to significant optical absorption as shown in a simple schematic below [30].

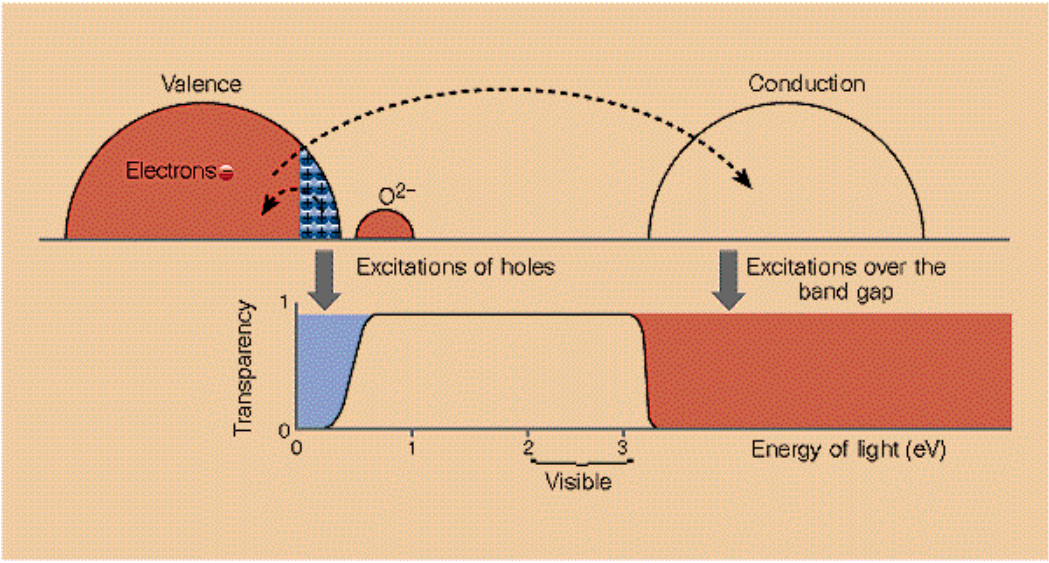


Figure 1.7. Schematic design of an electronic band gap for transparency [30].

Figure 1.7 shows that the energy gap between the filled valence band and empty conduction band, for a suitable p-type semiconductor, is higher than the energy of a visible photon. The material can be transparent, if the energy gap is bigger than around 3.1 eV, the energy of a blue photon situated with a wavelength of 400 nm, at

the short wavelength end of the visible spectrum. By contrast, photons in range of visible light (2.1~3.1 eV), do not have enough energy to excite an electron from the valence band to the conduction band but have too much energy to excite holes [30].

For these reasons as suggested in figure 1.7, the first challenge to make and understand materials with energy band gap above 3.1 eV, can be satisfied with delafossites such as $CuAlO_2$, which has been found to have a suitable band gap of 3.5 eV and is an insulator derived from Cu^+, Al^{3+}, and two O^{2-} [17]. The next problem is to convert this insulator into a transparent conductor, by introduction of low activation energy defect states or foreign dopant impurities. Thin film $CuAlO_2$ shows some conductivity which was explained by the fact that some extra oxygen was incorporated, possibly on interstitial sites, which trap electrons leaving behind empty states in the valence band which would act as positive charges (holes), as shown in figure 1.7 [17, 30]. The material's chemical formula would then be $CuAlO_{2+x}$ and the Hall effect measurements suggested hole carriers at a carrier concentration x of about 1/50000, in contrast to many other oxides which display n-type behaviour [33, 34]. Nevertheless, these Cu delafossite materials are still incompletely understood even though it has been known for two decades that thin films display a D.C. electrical conductivity nearly high enough for possible applications [35, 36].

1.5 Aims of Current Thesis

Oxide thin films can be made in various ways, such as sputtering, pulsed laser deposition and liquid/gas phase chemical vapour deposition. However these techniques offer comparably poor control of thin film properties.

Molecular beam epitaxy (MBE) is one of the most precise film growth techniques, which has been developed through academic studies of III-V semiconductors and practical applications [37].

This MBE approach can be adapted for oxide thin films, if an oxygen plasma assisted atomic beam is employed in addition to the normal metal evaporation *K*-cells used in MBE. This gives rise to so-called oxygen plasma assisted atomic beam epitaxy (OPABE) which can be expected to play a key role in research into oxide-on-oxide epitaxy [38, 39]. However the technique is still in its infancy compared to conventional MBE or many other oxide deposition techniques. The project in this thesis is concerned with developing OPABE and in using this technique to grow transparent conducting oxide thin films.

Specifically the main aim of the current project is to examine if films of Cu_2O and related copper delafossite compounds can be grown in a standard OPABE system, and to make some comparisons with materials grown with other methods. These materials present a particular challenge for OPABE, which has been used hitherto in applications where obtaining the "correct" metal valence state is easy, because of the corresponding chemical stability. A second challenge was to get the correct metal ratio (Cu : M) in the grown films in the standard MBE system which was available.

The first results chapter has focussed on the growth of cuprous oxide thin films by OPABE, a material which has various uses such as for catalysis, solar cells, photoelectron chromic devices, atomic scale quantum dots, and optical parametric oscillator. Cu_2O is a well known p-type semiconductor which can be further doped to modify electronic properties [40, 41]. It provides particular challenges in OPABE in view of the differing valences (+1, +2) which copper can adopt.

Subsequent projects have been involved the growth and characterisation of electronic, morphological and optical properties of grown films of various Cu delafossites such as $CuInO_2$, $CuCrO_2$ and $CuGaO_2$ with n-type and p-type doping, respectively and comparison is also made with films grown by pulsed laser deposition in the case of $CuInO_2$.

References

1. V. E. Henrich and P. A. Cox, *The surface science of metal oxides*. (Cambridge University Press, Cambridge ; New York, 1994).

2. S. A. Chambers, Advanced Materials **22** (2), 219-248 (2010).

3. W. A. Doolittle, A. G. Carver and W. Henderson, Journal of Vacuum Science & Technology B **23** (3), 1272-1276 (2005).

4. H. Hosono, H. Ohta, M. Orita, K. Ueda and M. Hirano, Vacuum **66** (3-4), 419-425 (2002).

5. J. Robertson, P. W. Peacock, M. D. Towler and R. Needs, Thin Solid Films **411** (1), 96-100 (2002).

6. T. Minami, MRS Bulletin **25** (8), 38-44 (2000).

7. J. Han and A. V. Nurmikko, IEEE Journal of Selected Topics in Quantum Electronics **8** (2), 289-297 (2002).

8. T. Minami, Semicond. Semiconductor Science and Technology **20** (4), S35-S44 (2005).

9. T. Minami, Journal of Vacuum Science & Technology a-Vacuum Surfaces and Films A **17** (4), 1765-1772 (1999).

10. A. L. Dawar and J. C. Joshi, Journal of Vacuum Science & Technology a-Vacuum Surfaces and Films **19** (1), 1-23 (1984).

11. K. L. Chopra, S. Major and D. K. Pandya, Thin Solid Films **102** (1), 1-46 (1983).

12. T. Minami, H. Nanto and S. Takata, Japanese Journal of Applied Physics Part 2-Letters 2, **23** (5), L280-L282 (1984).

13. T. Minami, K. Oohashi, S. Takata, T. Mouri and N. Ogawa, Thin Solid Films **193** (1-2), 721-729 (1990).

14. K. Suzuki, N. Hashimoto, T. Oyama, J. Shimizu, Y. Akao and H. Kojima, Thin Solid Films **226** (1), 104-109 (1993).

15. A. Kloppel, B. Meyer and J. Trube, Thin Solid Films **392** (2), 311-314 (2001).

16. H. Hiramatsu, K. Ueda, H. Ohta, M. Orita, M. Hirano and H. Hosono, Applied Physics Letters **81** (4), 598-600 (2002).

17. H. Kawazoe, M. Yasukawa, H. Hyodo, M. Kurita, H. Yanagi and H. Hosono, Nature **389** (6654), 939-942 (1997).

18. H. Yanagi, T. Hase, S. Ibuki, K. Ueda and H. Hosono, Applied Physics Letters **78** (11), 1583-1585 (2001).

19. K. Ueda, T. Hase, H. Yanagi, H. Kawazoe, H. Hosono, H. Ohta, M. Orita and M. Hirano, Journal of Applied Physics **89** (3), 1790-1793 (2001).

20. A. Kudo, H. Yanagi, H. Hosono and H. Kawazoe, Applied Physics Letters **73** (2), 220-222 (1998).

21. R. Nagarajan, A. D. Draeseke, A. W. Sleight and J. Tate, Journal of Applied Physics **89** (12), 8022-8025 (2001).

22. M. J. Sanders, M. Leslie and C. R. A. Catlow, Journal of the Chemical Society-Chemical Communications (19), 1271-1273 (1984).

23. G. V. Lewis and C. R. A. Catlow, Journal of Physics C-Solid State Physics **18** (6), 1149-1161 (1985).

24. D. M. Roessler and W. C. Walker, Physical Review **159** (3), 733-738 (1967).

25. P. A. Cox, NATO Advanced Study Institute Series **354**, 255-270 (1996).

26. C. Kittel, *Introduction to solid state physics*, 7th ed. (Wiley, New York, 1996).

27. P. Wargo and W. G. Shepherd, Physical Review **106** (4), 694-703 (1957).

28. O. Dulub, U. Diebold and G. Kresse, Physical Review Letters **90** (1) (2003).

29. M. Batzill and U. Diebold, Progress in Surface Science **79** (2-4), 47-154 (2005).

30. G. Thomas, Nature **389** (6654), 907-908 (1997).

31. P. P. Edwards, A. Porch, M. O. Jones, D. V. Morgan and R. M. Perks, Dalton Trans., 2995-3002 (2004).

32. J. C. C. Fan and J. B. Goodenough, Journal of Applied Physics **48** (8), 3524-3531 (1977).

33. G. Haacke, Annual Review of Materials Science **7**, 73-93 (1977).

34. J. M. Phillips, R. J. Cava, G. A. Thomas, S. A. Carter, J. Kwo, T. Siegrist, J. J. Krajewski, J. H. Marshall, W. F. Peck and D. H. Rapkine, Applied Physics Letters **67** (15), 2246-2248 (1995).

35. H. Hahn and C. Delorent, Zeitschrift Fur Anorganische Und Allgemeine Chemie **279** (5-6), 281-288 (1955).

36. F. A. Benko and F. P. Koffyberg, Journal of Physics and Chemistry of Solids **45** (1), 57-59 (1984).

37. B. A. Joyce and C. T. Foxon, Philips Technical Review **43** (5-6), 143-153 (1987).

38. A. Bourlange, D. J. Payne, R. G. Egdell, J. S. Foord, P. P. Edwards, M. O. Jones, A. Schertel, P. J. Dobson and J. L. Hutchison, Applied Physics Letters **92** (9) (2008).

39. R. G. Egdell, A. Bourlange, D. J. Payne, R. G. Palgrave, J. S. Foord, R. M. J. Jacobs, A. Schertel, J. L. Hutchison and P. J. Dobson, Thin Solid Films **517** (15), 4286-4294 (2009).

40. K. Maki and T. Itoh, Vacuum **81** (9), 1068-1076 (2007).

41. K. Maki and T. Itoh, Vacuum **81** (7), 904-910 (2007).

2 Experimental Theory and Techniques

2.1 General Considerations of Crystal Growth

In crystal growth technologies, the results observed commonly arise from a combination of thermodynamic and kinetic effects, so both areas should be considered. Thermodynamic reasoning for interfaces was pioneered by the theoretical physicist J. W. Gibbs in the late nineteenth century. Gibbs's core idea concerned the 'dividing surface' that is employed in describing the concentration profile change of molecular species between one level c_1 and another c_2 as shown in figure 2.1 across an interface [1, 2]. The interface between two phases can be quite vague chemically and thus difficult to define. However, Gibbs suggested that an artificial dividing layer of zero thickness could be used. Furthermore this can be positioned in such a way that the total number of moles of some reference species (for example the solvent is commonly used at liquid-air interfaces) is equal to the sum of the bulk volume-concentration of the two separate interfaces, as shown in the figure. This enables "excess" concentrations of other species in the system as a result of the presence of the interface to be accurately defined. In terms of energy, Gibbs's idea focussed on extensive thermodynamic potentials such as the bulk Helmholtz free energy F_b given by [1]:

$$dF_b = -SdT - pdV + \mu dN = 0 \qquad (2.1)$$

for a temperature T, volume V, particle number N, entropy S, pressure p and chemical potential μ. This equation can be expanded to the include systems depending on a surface area A. The total free energy in the surface now depends on A ($F_t = F(N_1, N_2, A)$) and

$$dF_t = dF_b\,(N_1, N_2) + f_s dA \qquad (2.2)$$

where f_s is the extra Helmholtz free energy per unit area due to the presence of the surface [1, 2].

By way of these concepts, we can describe surface tension. The surface tension, γ can be expressed as the reversible work completed in creating a unit area of new surface [1, 2],

$$\gamma = \lim (dA \rightarrow 0)\; dW/dA = (dF_t/dA)_{T,V} \qquad (2.3)$$

At equilibrium, a small crystal that forms in the presence of its vapour has a specific shape at temperature T. Because $dF = 0$ at constant T and volume V if the dividing surface is chosen appropriately, it follows that [1, 2]

$$\gamma dA = 0 \text{ or } \int \gamma dA \text{ is a minimum} \qquad (2.4)$$

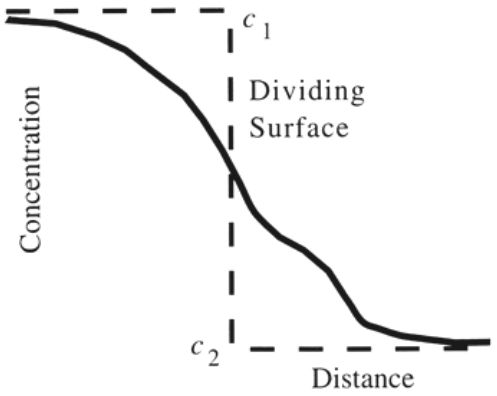


Figure 2.1. Schematic illustration of the 'dividing surface' in terms of macroscopic concentrations. (adapted from ref. 2)

The surface energy $\gamma(h\ k\ l)$ of course depends on the particular surface orientation $h\ k\ l$ so this equation presents an elegant route for discussing how the equilibrium shape of a crystal depends on the stabilities of the differing surfaces if the crystal orientation dependence of the surface energy can be understood [3]. The dependence of the surface energy on surface structure is often illustrated in terms of a terrace-ledge-kink model for a simple cubic system. This schematic model considers the bond strength φ of bulk atoms to their 6 bonding neighbours and the sublimation energy L, per unit volume of crystal. The surface atoms can be classified into the several kinds of species such as terrace, ledge, kink, adatom and vacancy in the schematic simple cubic crystal as shown in figure 2.2 [4, 5] and will be less stable because of the lower coordination number. For example, the three atom types terrace, ledge and kink, have a respective extra (positive) energy e_t with respect to bulk atoms, e_l with respect to terrace sites and e_k with respect to ledge sites. From the simple bond model [2, 4]

$$e_t = (6\text{-}5)\ \varphi/2a^2 = \varphi/2a^2 = La/6 \text{ per unit area,} \qquad (2.5)$$

$$e_l = (5\text{-}4)\ \varphi/2a = La^2/6 \text{ per unit length,} \qquad (2.6)$$

$$e_k = (4\text{-}3)\ \varphi/2 = La^3/6 \text{ per atom,} \qquad (2.7)$$

where the lattice parameter is a and 1 bond involves 2 atoms. In this model, bulk atoms have six bonds and a sublimation energy of $(6\varphi/2)\cdot(1/a^3)$. This model is often referred to as a Kossel crystal.

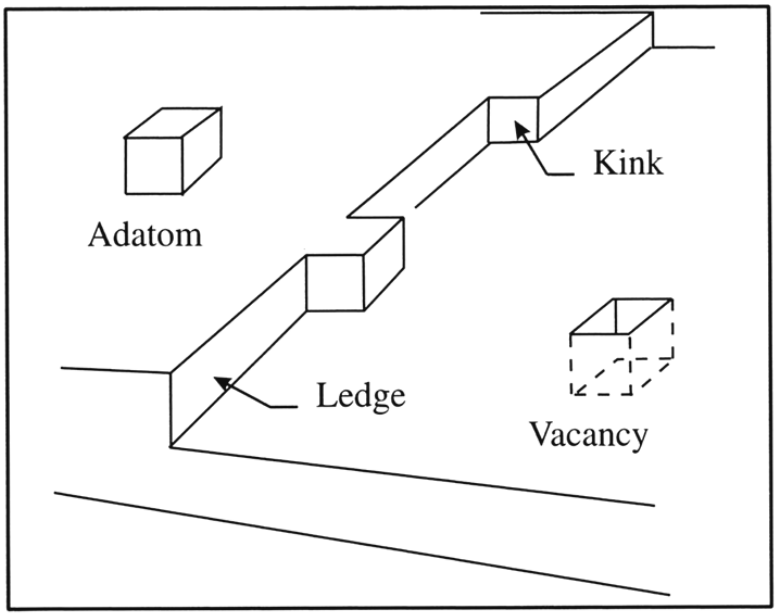


Figure 2.2. Drawing of a Kossel crystal shows the several kinds of atoms, adatoms, vacancies, terraces, ledges (steps) and kinks. (adapted from ref. 4 and 5)

The above picture applies to equilibrium, but deviations arise in the real situation because of kinetic effects. The Monte Carlo simulation of a Kossel crystal discussed above shows the surface in equilibrium with both the crystal and vapour as in figure 2.3 at differing temperatures [6]. The terraces are very smooth, and few adatoms or vacancies exist at low temperature. The surface become rougher as the temperature is raised as noted above due to the higher energy species. These ideas were developed for the non-equilibrium case in a classic paper published by Burton, Cabrera & Frank (1951), known as the BCF paper [7]. The BCF paper and developments are quite mathematical but it is useful to look at some simple cases. There are three categories of additional concepts for the non-equlibrium case used in the approach.

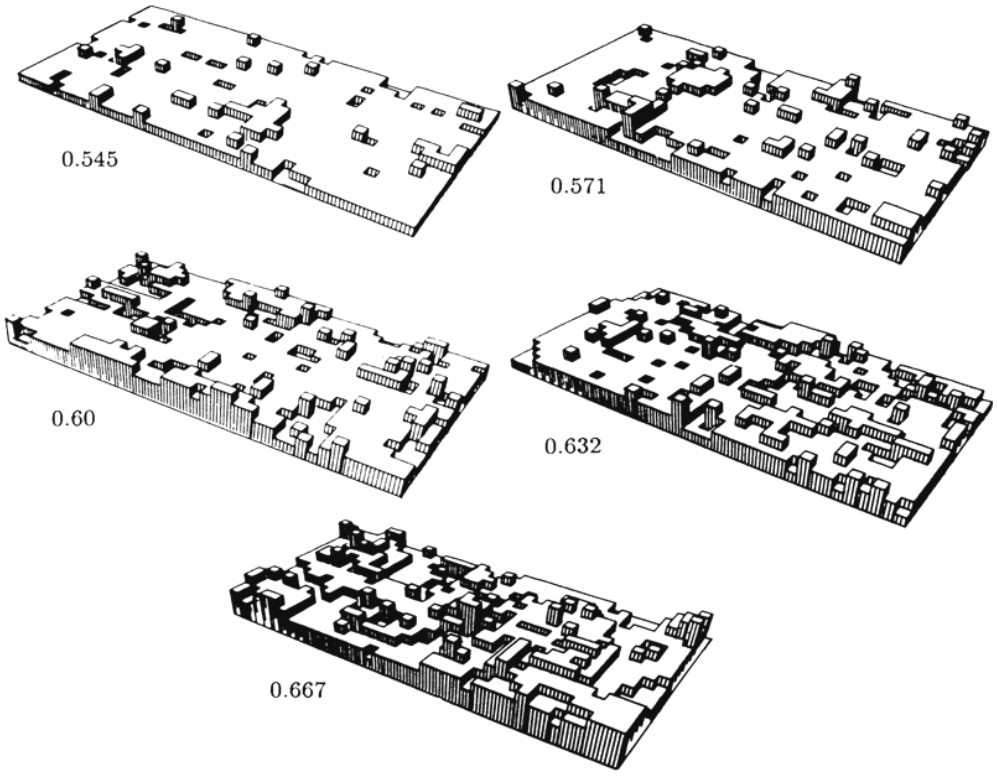


Figure 2.3. Evolution of the Kossel crystal by Monte Carlo simulation within the solid on solid model at five different temperatures (kT/φ) (adapted from ref. 6)

Firstly, the concept of supersaturation $S = (p/p_e)$ and $\Delta\mu = kT \ln S$, is used as a driving force for growth, where p is the actual gas pressure of the growth species and p_e the equilibrium pressure. $\Delta\mu$ is therefore zero in equilibrium, is positive for condensation, and negative for sublimation or evaporation. In terms of growth and evaporation, the deposition rate (R) or flux (F) can be expressed as R or $F = p/(2\pi mkT)^{1/2}$ from gas kinetic theory. Secondly, for loss of species from the surface, it is supposed an adatom has a positive desorption energy E_a. Therefore the rate of desorption is given by $v \cdot \exp(-E_a/kT)$ where v is a pre-exponential "attempt" frequency. Thirdly, the

adatom is able to diffuse on the surface, with a diffusion activation energy E_d. It would be expected that $E_d < E_a$.

From models based on these considerations, it provides the following points.

- Crystal growth is not easy on a perfect terrace, and substantial supersaturation is required.
- In general, crystals can be grown at rough surfaces faster than on smooth surfaces, such that the final "growth form" consists entirely of smooth slow growing surfaces.
- The existence of a screw dislocation in the crystal gives rise to steps such as ledges or kinks as illustrated by Monte Carlo calculations in figure 2.4, providing a mechanism for continuing growth at modest supersaturation [2, 6].

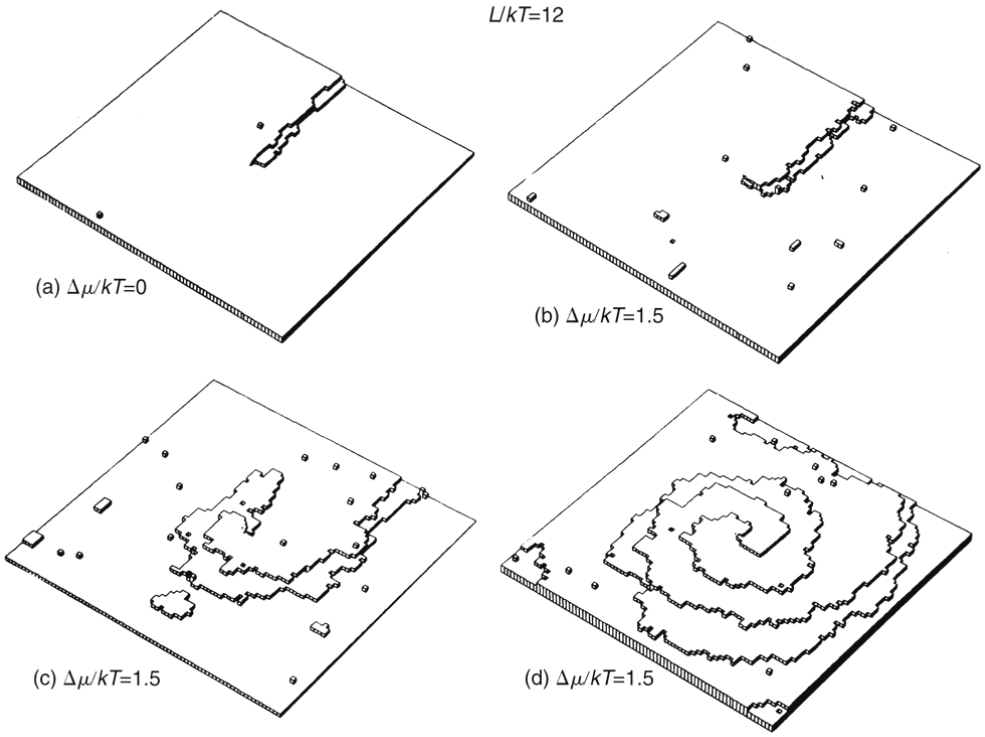


Figure 2.4. Monte Carlo simulation of a screw dislocation during deposition. (a) a double step in equilibrium, (b)-(d) as a function of time under supersaturation (1/kT)·Δμ=1.5 (adapted from ref. 6)

As an alternative to the atomistic approach, a microscopic point of view can provide a phenomenological description of thin film growth [8]. In general, three markedly different growth modes can be distinguished, depending on the surface and interfacial energies as well as lattice mismatch between the deposited materials and substrate. Figure 2.5 illustrates the three growth modes [9]. When the lattice mismatch is small and the interface binding is strong, the film grows in a layer-by-layer (Frank-Van der Merwe) mode. If the interface bonding is weak, the deposited material grows in 3D islanding (Volmer-Weber) mode. If the interface binding is strong but the lattice mismatch is relatively large, the film will grow in the layer-by-layer mode initially, followed by 3D-islanding. This process is known as the Stranski-Krastanov (S-K)

mode [2]. The initial wetting layer grows pseudomorphically with the same lattice constant of substrate, with a misfit strain which can be accommodated elastically below a critical thickness. The strain energy increases with film thickness. At certain point, it becomes energetically favourable to generate misfits and threading dislocations to relieve the build-up strain within the film. The growth temperature on the other hand provides thermal energy for atom diffusion and defect formation [2, 9].

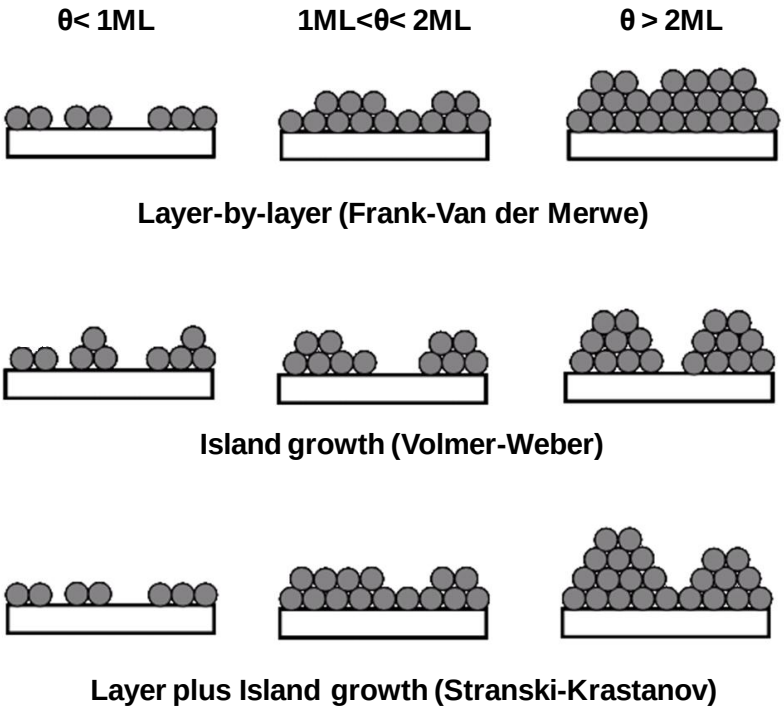


Figure 2.5. Schematics of of three growth modes of a film for different coverage (θ) regimes. (adapted from ref. 9)

In dynamic material growth processes, the thin-film is not in general under thermodynamic equilibrium [10, 11]. Thus, one needs to consider the kinetics of processes occurring on the surface, including the adsorption, diffusion, desorption, coarsening and nucleation of atoms, as well as the inter-layer migration of the atoms, as discussed above. The former factors can affect the lateral uniformity of the film,

while the latter factor can lead to a 2-D layer-by-layer or a 3-D growth mode. If the material favours a 2-D growth mode, sufficient inter-layer atomic transport is necessary. An important quantity this process is the Ehrlich-Schwoebel barrier (ES), which is the additional barrier for an adatom to jump down (or up) a step edge. If the ES barrier is large, it is hard for atoms to transport between layers. This will result to the 3-D growth. On the other hand, if the ES barrier is small, it is easy for atoms to undergo atomic inter-layer-transport. This will result in 2-D growth. Thus three kinetically controlled growth modes are step-flow growth, layer-by-layer growth, and multilayer growth [2, 10].

2.2 Molecular Beam Epitaxy (MBE)

2.2.1 Introduction

Molecular beam epitaxy (MBE) is employed in the epitaxial growth of crystal or semiconductor films by thermal molecular or atomic beams at a crystalline surface under ultra-high vacuum (UHV) environments. MBE is often closely connected with physical evaporation and condensation of the constituent elements.

Early attempts in the 1950s to late 1960s, to overcome non-stoichiometric evaporation in the growth of various semiconductors, for example InAs, GaAs and PbS by such pioneers as Günther, Müller, Schoolar, Zemel and Steinberg were reported [12]. Günther proposed a "three- temperature" technique in which group III and V sources had different temperatures [13]. Müller tried "flash" evaporation to prevent source decomposition so that the evaporant (*e.g.* GaAs) converted to fine particles and dropped into a resistively heated tantalum bowl [14]. By way of using

single crystalline substrates, Schoolar and Zemel succeeded in forming epitaxial PbS on rock salt, and then Steinberg and his colleague Scruggs accomplished GaAs growth on (110) oriented GaAs substrates [15, 16].

Nevertheless, these investigations could report only crystal structures by electron and X-ray diffraction, because the grown films were too poor to evaluate carrier mobilities or optical properties. In general, epitaxial films of the III–V compounds cannot be obtained without rigorous high vacuum conditions and clean single crystal substrates, which were not readily available in this early work. In the 1970s, genuine MBE was pursued under ultra high vacuum conditions (around 10^{-9} torr), utilising a liquid-nitrogen (77 K) shroud surrounding the evaporation sources [17].

In situ monitoring of crystal growth by reflection high energy electron diffraction (RHEED) led to an understanding of the importance of substrate condition, deposition rate and substrate growth temperature [18]. Research by Cho and Arthur of Bell Laboratories was especially notable [19]. Especially they established the surface morphology and carrier concentration of doped n- or p- type GaAs by reducing contamination of the growth chamber using apparatus such as shown in figure 2.6 [19, 20].

Through the innumerable studies of various compounds of III-V semiconductors, MBE technologies advanced into II-VI and IV-VI semiconductors for new scientific areas such as quantum devices, photo-voltaic cells and electro-magnetic materials [21].

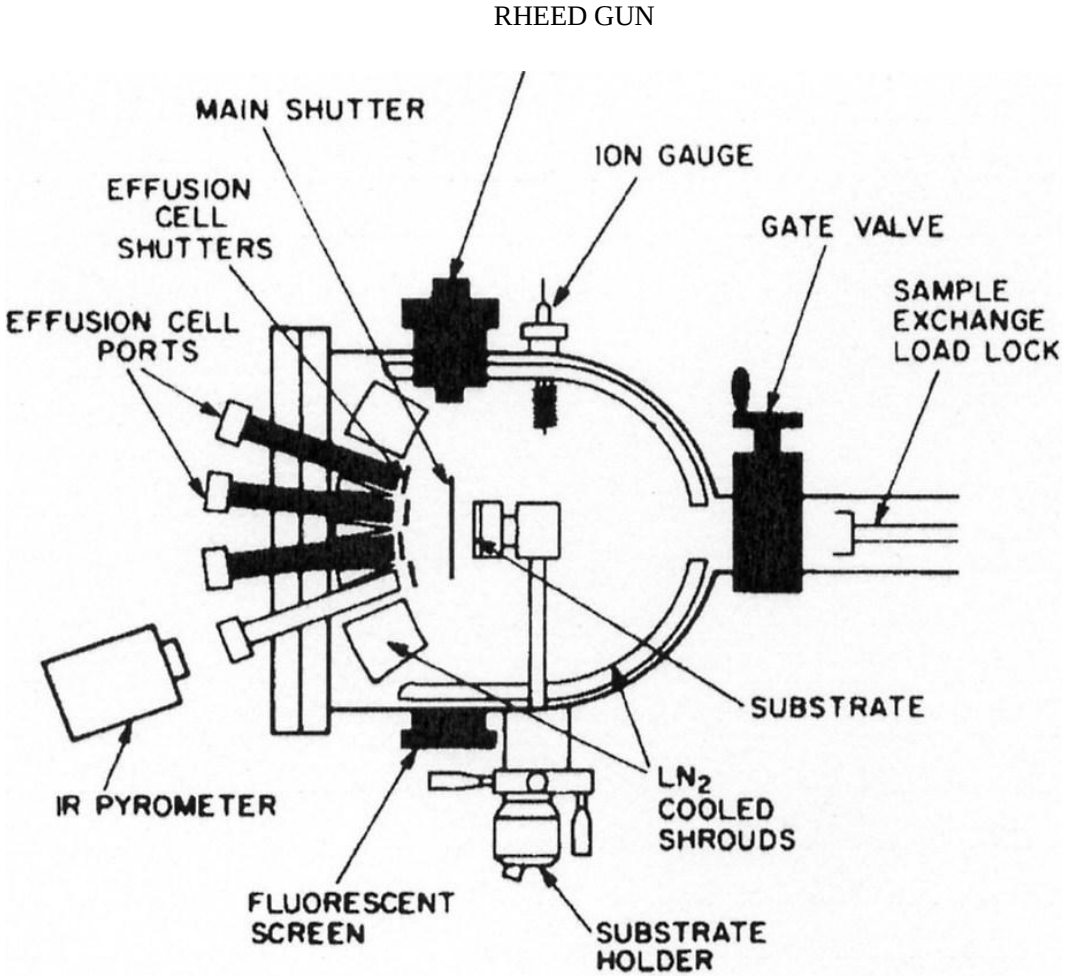


Figure 2.6. A schematic view of a commercially available MBE chamber at Bell Laboratories, Murray Hill, New Jersey, USA. The system incorporates a sample exchange airlock and a magnetically coupled transfer mechanism for preventing air contamination. (adapted from ref. 20)

2.2.2 Ultra-High Vacuum (UHV)

From gas kinetic theory, it is known that the arrival rate R of atoms at a surface is defined by the molecular density n and the mean speed of molecules υ under the pressure p. $R = p/(2\pi mkT)^{1/2} = n\upsilon/4$ per unit area. (It can be noted $n = p/kT$ and $\upsilon =$

$(8kT/\pi m)^{1/2}$) To enable clean growth conditions, background pressures need to be below 10^{-9} mbar, to minimise the molecular bombardment of the surface by unwanted species [2].

A vacuum system has a volume V at pressure p and some leak rate Q, as shown in figure 2.7 and is pumped by a pump with a pumping speed S. The equation of pump-down can be written as $pS = -V\mathrm{d}p/\mathrm{d}t + Q$. The leak rate Q consists of the true leak Q_1 added to a virtual leak Q_0. The virtual leak is caused by degassing from the inside walls or trapped volumes whereas true leaks arise for example, from small pinholes in chamber components [2].

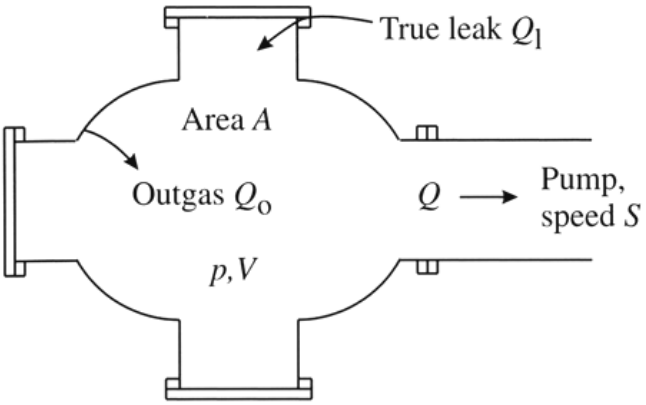


Figure 2.7. Diagram of systematic pumping chamber, is composed of the volume V, internal area A, pumping speed S and the true leak Q_1 and outgas Q_0 at pressure p. (adapted from ref. 2)

The pumping equation can be separated into two cases, assuming everything but the pressure is constant. The first is $p = p_0\exp(-t/\tau)$ at a short time limit, with $\tau = V/S$ where the leak rate is negligible. Typically τ is a few seconds for modern pumping systems. Second is the ultimate pressure $p_u = Q/S$ which is reached at a long time limit. The true leak rate can be made to be negligible using modern materials and

designs, so the ultimate pressure is largely determined by the outgassing Q_0 which is proportional to the surface area A of the system. By using modern high pumping speed pumps, ensuring the vacuum system is free from volatile materials such as grease, fingerprints etc. and baking out the system to minimise outgassing, UHV conditions of around 10^{-10} mbar are easily reached enabling ultra-clean crystal growth experiments to be carried out [2].

2.2.3 MBE Beam Sources

Beams for MBE can be produced by sources such as Knudsen effusion cells (K-cells), cracker cells, gas sources, ionized beam sources, electrochemical cells and electron beam evaporators [22].

Knudsen effusion cells should ideally comprise the condensed phase and its vapour in equilibrium, enabling the beam flux to be readily predicted [23, 24]. Using gas kinetic theory considerations noted above, the flux is given by [23]

$$J = (1.118 \times 10^{22}) \{pA/l^2(MT)^{1/2}\} \text{ molecules cm}^{-2}\text{s}^{-1} \qquad (2.8)$$

where A (cm^2) is the cell orifice area located a distance l (cm) from the substrate with an operating temperature T (K). p is the source pressure (torr) and M denotes the molecular weight of source. For example, in the typical growth of GaAs semiconductors, the calculated arrival rate of Ga atoms is 3.33×10^{15} atoms $cm^{-2}s^{-1}$ on a GaAs substrate at 1000^oC cell temperature at a distance of 15 cm from the cell [22].

The simplest concept of a K-cell comprises the solid or molten materials to be evaporated in an inert crucible, which is heated by radiation and controlled using some thermocouple feedback system. The preferred crucible material is often such phases as pyrolytic boron nitride (PBN) or graphite. The essential requirement is that

they are inert with regard to reaction with the evaporant, and show negligible outgassing of contaminants at the required operating temperature. Early forms of heater involved heated wires, but foil heaters are now common since these better surround the crucible surface, leading to smaller temperature differentials between the two [22]. To minimise heating of surrounding components water-cooling and radiation shields are often incorporated, and beam shutters can be used to better control the on-off performance. A typical K-cell is shown in figure 2.8.

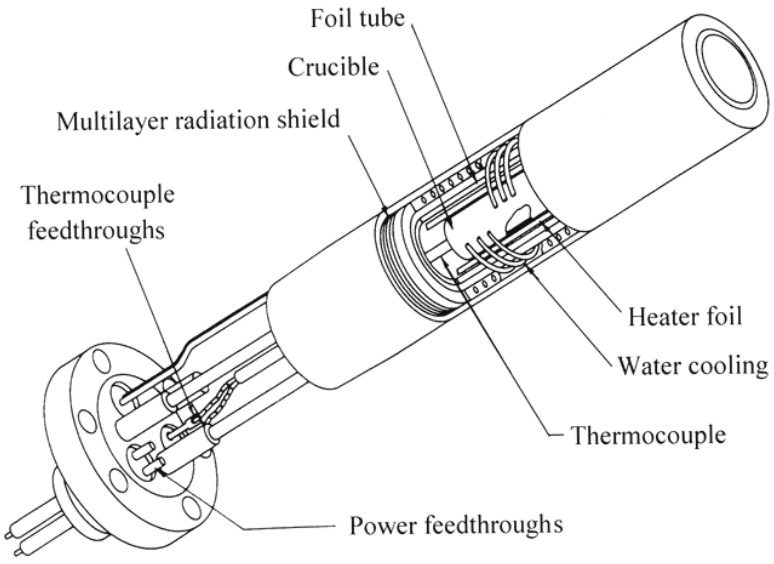


Figure 2.8. A cutway diagram of a small effusion source in a MBE furnace using graphite crucible or PBN oven (After G. J. Davies and D. Williams 1985, adapted from ref. 22)

More complicated versions of the K-cell exist. Cracker cells are modified types of K-cells which have a high temperature region to decompose the evaporant into more dissociated species. [25]. Gas sources instead of evaporating solids can be used [26]. The beams themselves can also sometimes be ionised –for example low-energy Zn^+ ions (about 1 keV) for *p*-type doping, although the majority of dopants employed in III-V MBE growth use a neutral source [27, 28]. Electrochemical cells within the vacuum

chamber have also been employed producing group VI species such as sulphur for doping purposes [29].

For some elements, the temperatures required for thermal evaporation in the conventional K-cell configuration are impractically high. Under these circumstanced direct electron beam heating is employed such as in Si-MBE. This technology has now been expanded into applications such as the sequential evaporation of metal contact layers, particularly in the case of low-vapour-pressure and refractory metals like tungsten (W) [30-32] .

2.2.4 Oxygen Plasma Assisted Atomic Beam Epitaxy (OPABE)

Thin film metal oxides are conventionally grown in many ways, including pulsed laser deposition (PLD), gas phase or liquid phase chemical vapour deposition (CVD), DC magnetron sputtering and spray pyrolysis [33]. Under optimal conductions these techniques, especially PLD, can yield highly textured or even truly monocrystalline oxide thin films. However a more controlled and versatile approach for preparation of the best quality single crystal epilayers is provided by deposition of metal atoms from a thermal source onto a growing surface simultaneously exposed to a plasma rich in oxygen atoms.

This technique has been referred to as *oxygen plasma assisted molecular beam epitaxy*, however because the beams are atoms and not molecules, it is preferred to call the technique *oxygen plasma assisted atomic beam epitaxy*, with the acronym OPABE [34].

This approach in principle offers the best prospects for true atomic layer control of oxide thin films, needed for example in the growth of single and double heterojunctions, periodic alloy systems and modulation doped heterostructures.

Growth can be achieved at much lower temperatures than with CVD techniques as there is no need for precursor decomposition, thus minimising problems arising from interdiffusion [35]. Beam source technology naturally lends itself to scaling up to production processes using large wafers much more so than with pulsed laser deposition. It can be noted that simple GSMBE (Gas Source MBE) of metal oxides, using K-cell deposition of metals and an O_2 gas source is unlikely to be successful since molecular oxygen has a relatively low sticking probability to form oxide lattice oxygen in such an experiment. O atoms are much more reactive so alleviate this problem.

2.2.5 The SVT UHV-OPABE System

A facility for oxide MBE (SVT, USA) using an radiofrequency (RF) atom oxygen source (see figure 2.9) has been established in the Department of Chemistry at Oxford University as shown in figure 2.10 and this facility provided the key resource for implementation of the experiments in this thesis.

The system utilises mains three-phase electrical power for operation. Cooling water is required for the operation of the system to cool turbo pumps, source cooling shrouds, the RF plasma source cooling, the e-beam source and the substrate manipulator. The system also incorporated liquid nitrogen cooled cryopanels, and needed dry air or nitrogen to operate the gate valves, shutters and pneumatic shut-off valves [36].

An ultra high vacuum growth chamber with a base pressure of $5x10^{-9}$ torr is sustained by 38,000 revolutions per minute (RPM) turbo-pump. The manufactures volume chamber incorporated the cryopanels, Knudsen cells and a radiofrequency plasma oxygen atom source operated at maximum 250W RF power with oxygen

background pressure of up to about 2.0~3.0 x 10^{-5} torr. The MBE system includes five Knudsen cells (typically Cu, In, Sn, Cr and Ga in this work), a five pocket electron beam evaporator and diagnostic capabilities with *in situ* RHEED, LEED, XPS and Auger electron spectroscopy. The nominal deposition rate was typically adjusted to about 0.1 Å/s using a digital quartz crystal thickness monitor (QCM) offset at the substrate position.

A QCM measures a mass per unit area by measuring the change in frequency of a quartz crystal resonator. The resonance is disturbed by the addition or removal of a small mass due to oxide growth/decay or film deposition at the surface of the acoustic resonator. The QCM can be used under vacuum, in gas phase ("gas sensor", first use described by King [37]) and more recently in liquid environments. It is useful for monitoring the rate of deposition in thin film deposition systems under vacuum. Frequency measurements are easily made to high precision; hence, it is easy to measure mass densities down to a level of below 1 μg/cm^2. In addition to measuring the frequency, the dissipation factor (equivalent to the resonance bandwidth) is often measured to help analysis. The dissipation factor is the inverse quality factor of the resonance, $Q^{-1} = w/f_r$; it quantifies the damping in the system and is related to the sample's viscoelastic properties. For thin films, the resonance frequency is usually inversely proportional to the total thickness of the plate [38, 39].

A graphite substrate heater controlled by a calibrated thermocouple was used to control the substrate temperature. A side view of the chamber is shown in Figure 2.10 and picture of the internal components is shown in Figure 2.9.

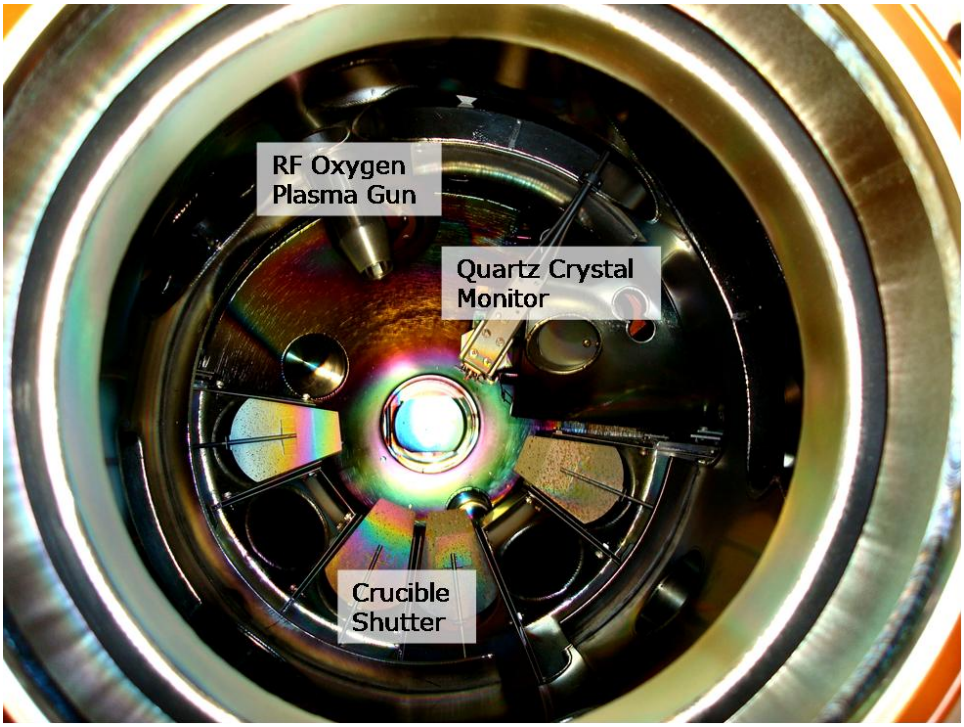


Figure 2.9. The top view of inside of the growth chamber of UHV-OPABE system at Chemistry Research Laboratory, University of Oxford (The chamber made by SVT Associates, Inc. Eden Prairie, MN, USA)

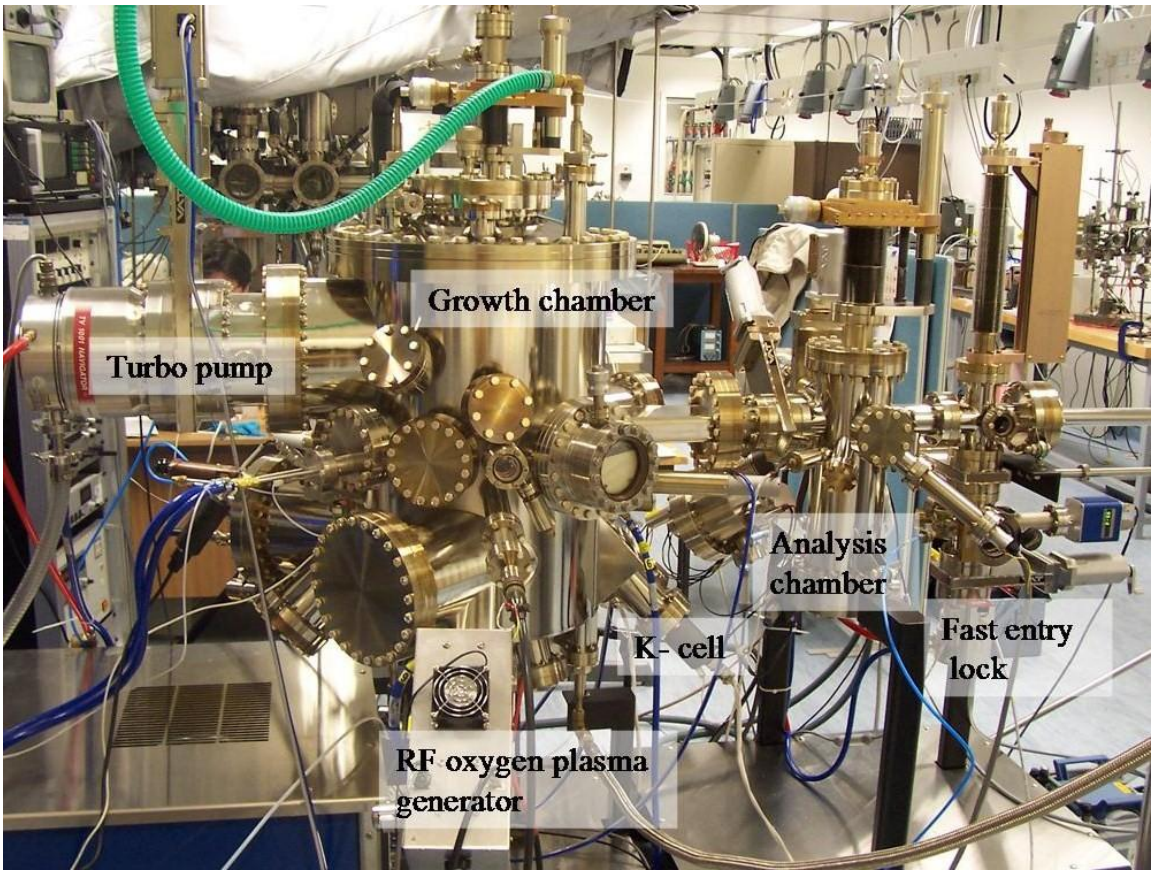


Figure 2.10. A side view of the UHV-Oxygen Plasma assisted Atomic Beam Epitaxy (OPABE) system at Chemistry Research Laboratory, University of Oxford (The chamber made by SVT Associates, Inc. Eden Prairie, MN, USA)

2.3 X-ray Spectroscopies

2.3.1 Introduction to Spectroscopic Methods

Spectroscopic techniques are able to provide a lot of information on the electronic energy levels of atoms, molecules and solids and several were used in the course of this work. Optical absorption in the visible or ultraviolet (UV) range is very widely known as a representative electronic spectroscopy [40]. The absorption spectra are caused by the transition of an electron from filled to empty bands in solids, or for

molecules arise from transitions from occupied to unoccupied valence states. On the other hand, photons in the X-ray region, which can excite core levels as well as valence levels, can also be used to provide a wealth of information on electronic states [40]. A schematic diagram of several spectroscopic techniques is shown in figure 2.11 which provide insights into the filled levels, empty levels, band gap and conduction electrons of materials.

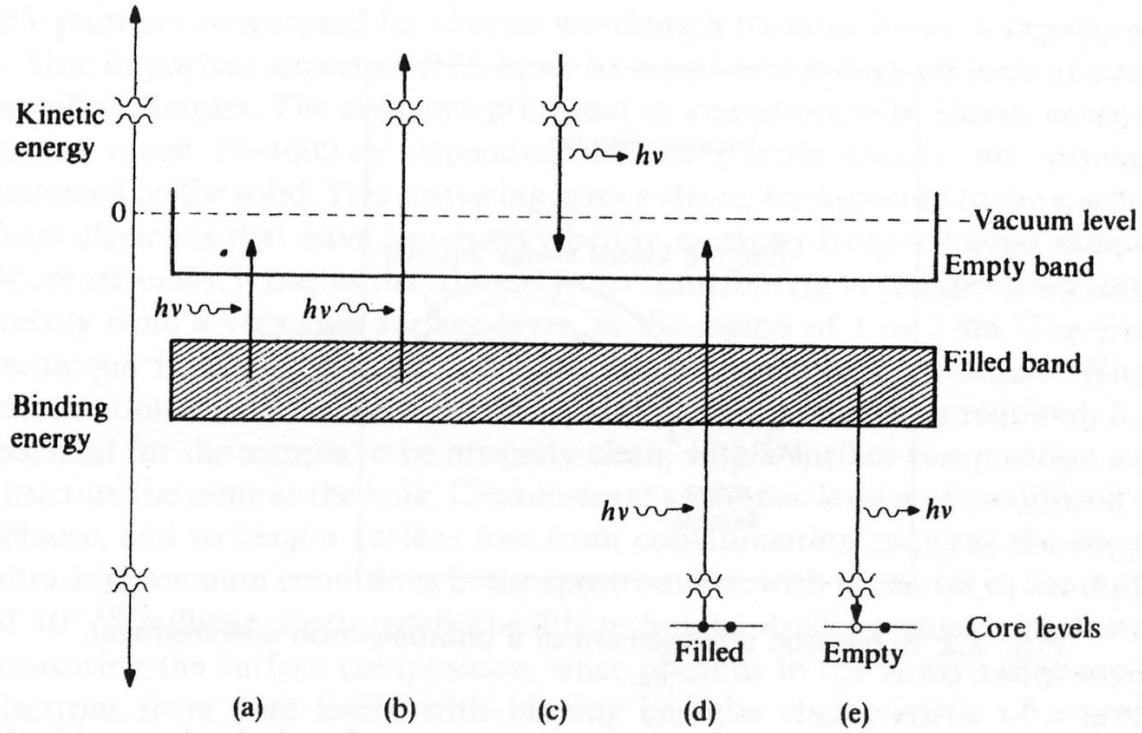


Figure 2.11. A schematic diagram of the spectroscopic techniques. (a) UV-Visible optical absorption; (b) photoelectron spectroscopy; (c) inverse photoelectron spectroscopy; (d) X-ray absorption; (e) X-ray emission. (adapted from ref. 40)

2.3.2 X-ray Photoelectron Spectroscopy (XPS)

Extensive use of XPS was made in this project so a detailed presentation of this technique is given.

(a) Fundamentals

Surface analysis by X-ray photoelectron spectroscopy (XPS), or electron spectroscopy for chemical analysis (ESCA) [41] is accomplished by irradiating a solid material with monoenergetic soft X-rays and energy analysing the electrons emitted, through the photoelectric effect [42].

$$E_{kin} = h\nu - E_B - e\varphi_{sp} \qquad (2.9)$$

where $h\nu$ is the energy of the photon, E_B is the binding energy of the atomic orbital from which the electron originates, and $e\varphi_{sp}$ is called the work function of the spectrometer according to the schematic energy diagram in Figure 2.12 [43].

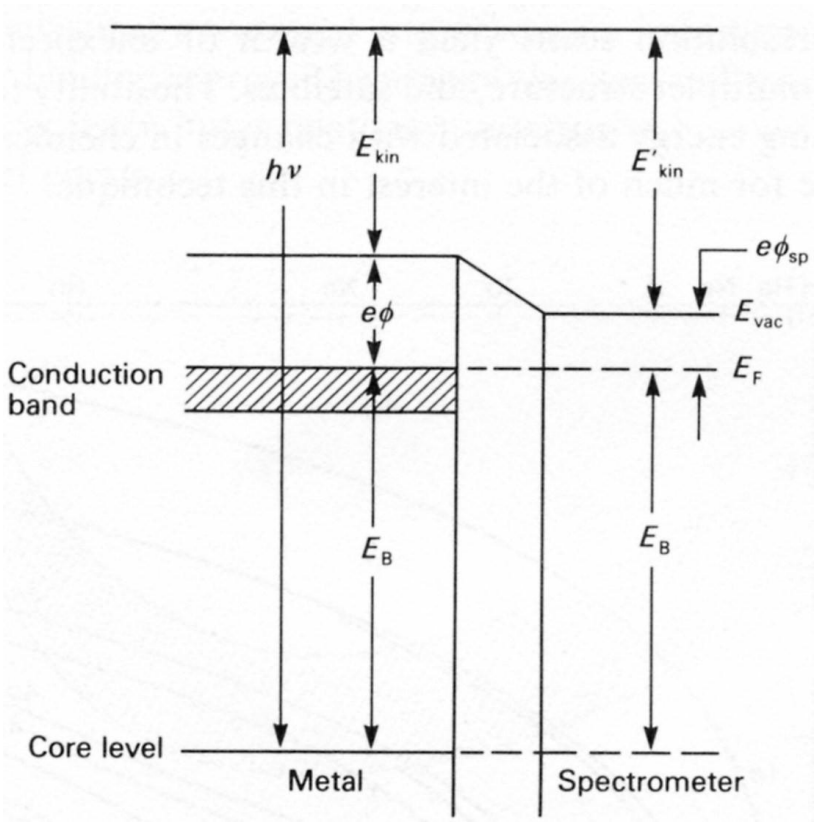


Figure 2.12. Energy level diagram for photoemission. Note that the contact potential between the sample and the spectrometer, $e(\varphi-\varphi_{sp})$, changes the kinetic energy of the electron as it enters the spectrometer. As a result only the spectrometer work function is needed to calculate E_B from the measured kinetic energy. (adapted from ref. 43)

The first demonstration of practical X-ray photoemission was by Siegbahn and his collaborators at the University of Uppsala in Sweden in the middle of 20th century [41].

At its simplest, the fundamental principle of photoelectron spectroscopy (PES) is based on the classical photoelectric effect, first discovered by Hertz in 1887 and explained by Einstein in 1905 [42], whereby an electron is emitted from a solid upon light-matter interaction. As shown schematically in Figure 2.13 a material is illuminated with a flux of photons with a specific energy (designated hγ in this figure, although more conventionally the photon energy is designated as hν) from an x-ray tube, gas discharge lamp or a synchrotron radiation source [44, 45].

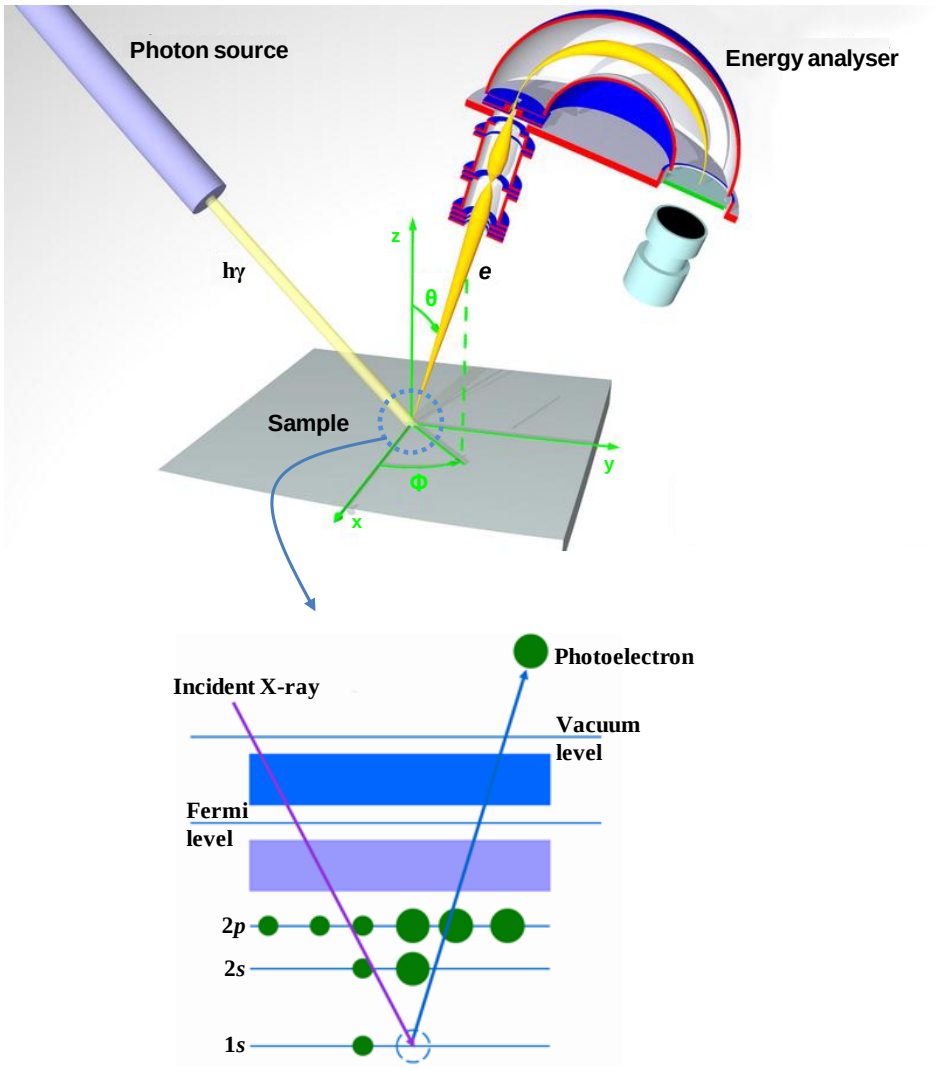


Figure 2.13. Schematic representation of PES showing the angle of photoelectron emission referenced to the sample coordinate system (top) and photoemission from core and valence states (bottom). (adapted from ref. 45)

The electrons in the materials that occupy a certain initial energy state (E_i) can absorb the photon and are excited as free electrons by the photoelectric effect. The photoelectrons are then analysed with respect to their kinetic energy (E_k) and their momentum $\boldsymbol{p}$ in an electrostatic analyser. The binding energy relative to the Fermi energy E_b is given by the energy difference of total energies between the final state

N-1 electrons after ejection of the photoelectron and the initial *N* electron ground state of the system [9]:

$$E_b = E_{f,tot\,(N-1)} - E_{i,tot\,(N)} \qquad (2.10)$$

The momentum ***p*** of the photoemitted electron is determined from its kinetic energy by [9]:

$$E_k = p^2/2m \qquad (2.11)$$

where p is $(2mE_k)^{1/2}$.

The direction of momentum is obtained from polar (θ) and azimuth (φ) angles of the electron detected. Figure 2.14 shows schematically the relation between energy levels and electron distribution in a solid state sample, which consists of core levels and a valence band. Thus PES basically reflects the electronic eigenstates of the solid [46].

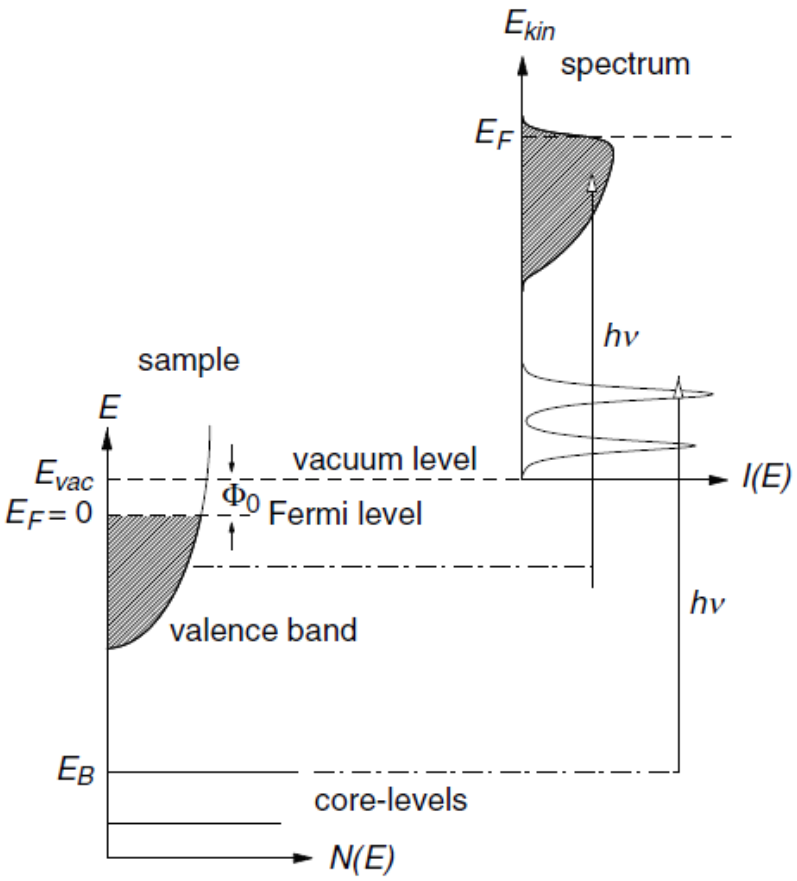


Figure 2.14. Schematic view of the photoemission process in the single-particle picture. Electrons with binding energy E_b can be excited above the vacuum level E_{vac} by photons with energy $h\gamma > E_b + \Phi_0$. The photoelectron distribution $I(E_{kin})$ can be measured by the analyser and is an image of occupied density of states $N(E_b)$ in the sample. (Figure adapted from ref. 46)

(*b) Components of the photoelectron process*

XPS experiments show very useful results, the simplest of which is provided by a wide "survey" scan which provides immediate identification of the chemical composition, since the binding energy of core electrons, which is easily measured

from the spectrum, is characteristic of the emitting atom as shown in figure 2.15 [41, 43, 47].

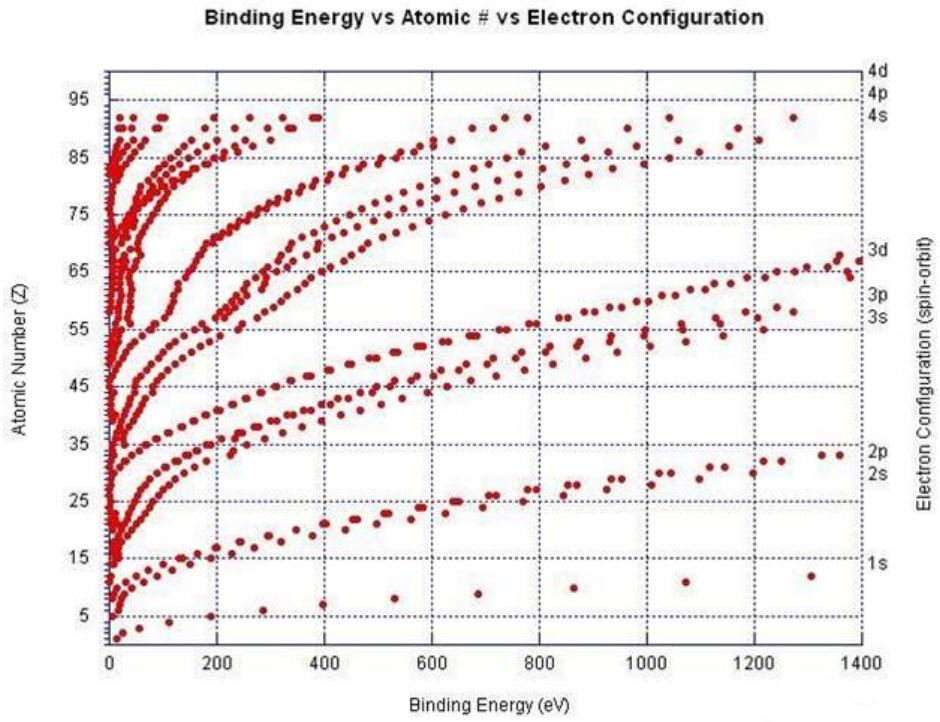


Figure 2.15. A diagram of core electron binding energy of elements, including transition metals, rare earths, and actinides. Below 10 eV chemical effects are omitted to allow a universal plot. (adapted from ref. 41, 43, 47)

To interpret such data, the absorption length of the X-rays, 10^3 to 10^4 Å, must be considered, so that photoelectrons are generated with significant intensity to that depth within the solid. Most photoelectrons are inelastically scattered however as they propagate towards the surface. The mean-free-path of electrons with energies of the order of < 1.5 keV typical of XPS is about 15 Å as shown in figure 2.16 [48]. The detected elastic electrons thus arise close to the surface hence the method is surface

sensitive, although the probe depth does depend on the kinetic energy of the emitted electrons.

The dominant scattering mechanism involves interaction with valence or conduction electron plasmons with energies typically of the order of 20 eV. The scattering is characterised by an inelastic mean free path λ and a flux I_0 of photoelectrons created at a depth d, beneath the surface is attenuated to a value I at the surface according to [41]:

$$I = I_0 \exp^{-d/\lambda} \qquad (2.12)$$

Electron pathlengths are quite long at energies below that of the scattering plasmons and reach a minimum value of around ~5 Å at around 50 eV kinetic energy, which is about two or three typical plasmon energies, as shown in figure 2.16. This means that spectroscopy involving electrons collects only electrons from a very thin layer of the sample. It can be seen that if one wishes to learn about the bulk electronic structure of the solid, atomically clean surfaces must be prepared in ultra-high vacuum (UHV) conditions (~10^{-10} mbar) to minimize surface – gas interactions [48, 49].

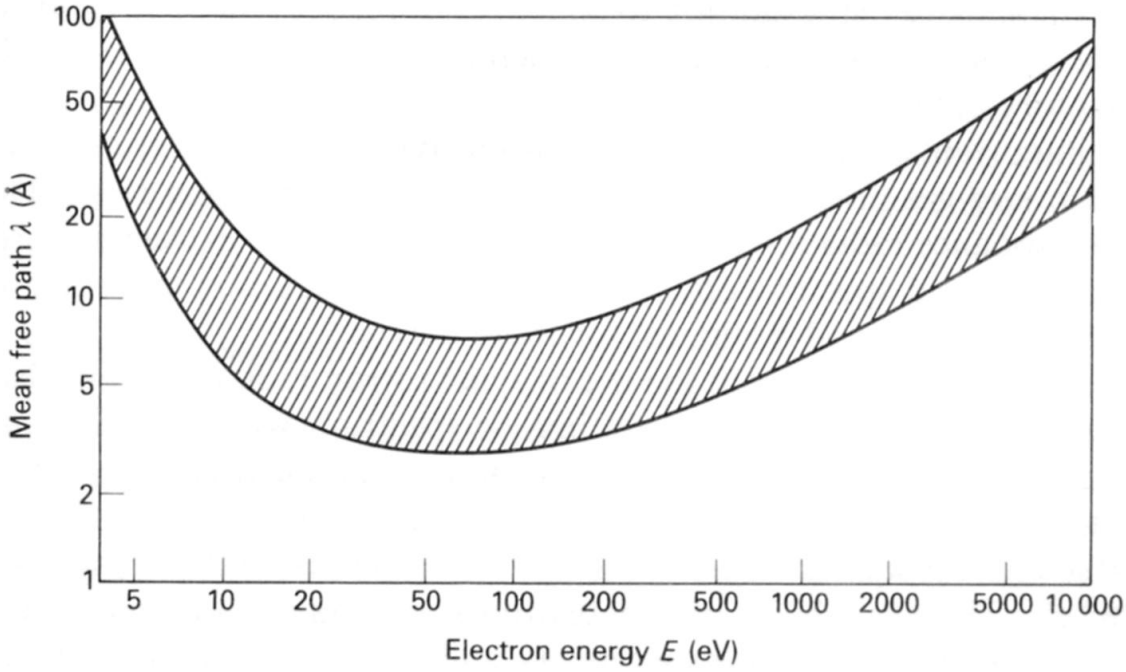


Figure 2.16. Electron mean-free-paths as a function of kinetic energy. The majority of reported values involved in the shaded region. (adapted from ref. 48)

In general, the experiment of photoelectron spectroscopy requires (1) a source of monochromatic radiation such as Mg *Kα* (1253.6 eV) or Al *Kα* (1486.6 eV), (2) an electron spectrometer, such as a hemispherical analyser, (3) an adequate vacuum, to enable recording of the spectrum without gross sample contamination. Typical line X-ray sources as noted above have a natural line width of ~1 eV so recorded spectra typically show this type of resolution, unless an X-ray monochromator is used [43] in which case resolutions of ~0.3 eV are commonly displayed.

A special surface preparation is often required to investigate bulk composition in view of the surface sensitivity. For example, crushing a crystalline material in an

inert gas in order to expose fresh surfaces can be used, or alternatively the outermost layers of the sample can be etched away with a noble gas ion beam [43]. Surface contaminants can also be removed by this way or chemically removed by for example annealing at high temperature or in an oxygen environment [50].

(c) Electron analyser

X-ray photoelectron spectroscopy ordinarily requires a deflection spectrometer to enable energy measurement of the emitted electrons. The comparatively low kinetic energy ~1 keV means that electrostatic analysers are preferable to magnetic ones. The electrostatic energy analyser (see figure 2.17) is the most widely used detector at present, in which electrons of a selected kinetic energy only display trajectories between the entrance and exit slits, and is normally operated in the fixed analyser transmission mode [51].

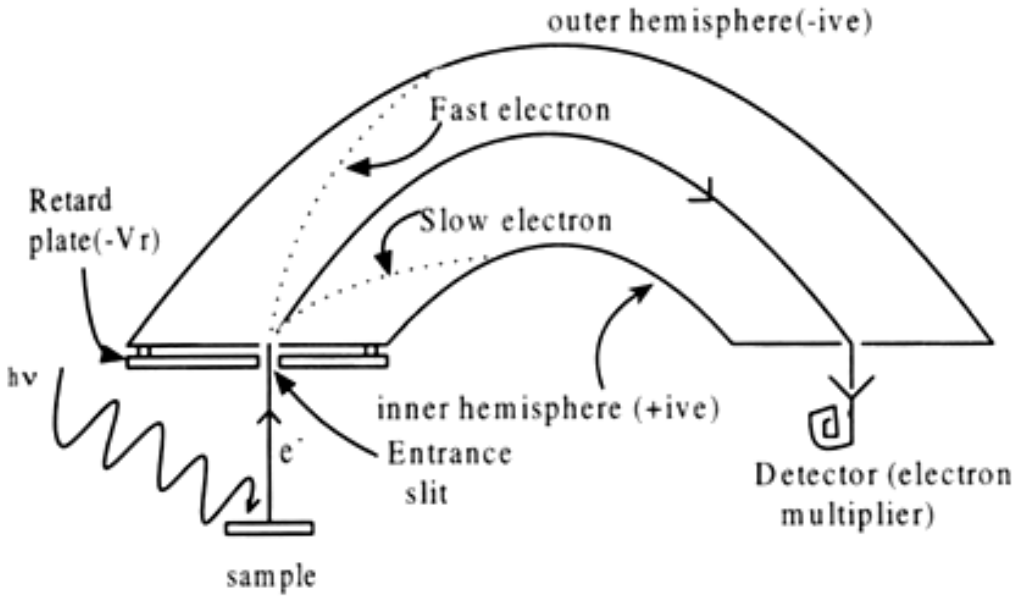


Figure 2.17. Electrostatic energy analyser used in electron/ion spectroscopic analysis of surfaces. (adapted from ref. 52)

(d) Chemical shifts

Although the simplest interpretation of XPS assumes core level binding energies are completely characteristic of a particular atom, this is an oversimplification since small energy shifts – "chemical shifts" – arise when the chemical state is changed [41, 53]. In general, a distinguishable photoemission peak can appear for every chemically distinct state (see figure 2.18). The gas phase C 1*s* spectrum of ethyl trifluoroacetate shows four separate lines with regards to different chemical circumstances [44]. In molecules, the core binding energy is enhanced with increasing partial charge on the atom concerned. However, chemical shifts in solids are often unforseeable due to a diversity of final state screening effects and Madelung potential effects which vary from material to material [43, 54]. Nonetheless chemical shifts provide a useful empirical guide to determining chemical states.

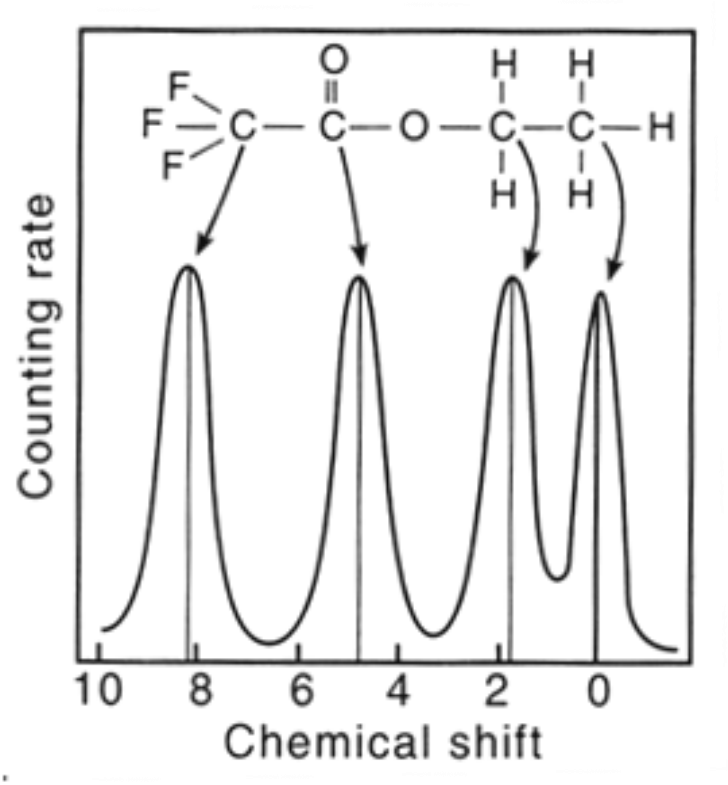


Figure 2.18. Spectrum of the gas phase carbon 1*s* of ethyl trifluoroacetate in which there are four kinds of environment for carbon core levels. (adapted from ref. 44)

(e) Valence-level photoemission

Ultraviolet photoemission spectroscopy (UPS) is often used in the study of solids to study occupied valence levels of a material [43] but can be difficult to interpret since the spectra do not simply reflect the occupied density of states [43]. Although the spectra are relatively weak, XPS (< 0.05eV) and hard X-ray photoelectron spectroscopy (HXPS, $h\nu$ > 5 keV) also provide well-defined valence band spectra which can be easier to understand [55-56], even though the spectra do not totally reflect the one-electron density of states due to lifetime broadening effects, cross-sections, multi-electron excitations etc [43, 57]. The spectra can often be related directly to band structure calculations to help clarify the understanding of the occupied band structure e.g. [58, 59].

(f) The appearance of spectral lines

As discussed so far, the XPS spectrum of a solid should simply consist of a number of peaks, corresponding to the valence band and the various atomic core levels which can be ionised by the radiation used. In actual fact, this is an oversimplification since peak splittings and additional peaks often appear in spectra. For example, the XPS spectrum of samples containing C and Sn are shown below in figure 2.19 relating to ionisation of the C 1*s* and Sn 3*d* electrons. The sharp line of C 1*s* at 284.5 eV is apparent corresponding to the core orbital of graphite. However the long tail towards bigger binding energy is due to the creation of plasmons and other excitations, which accompany the ionisation process, or take place as the photoelectron is transported to the surface. This reduces the energy of the emitted electron, so peaks appear to higher binding energy. In the lower panel, the Sn 3*d* spectrum shows photoemission from an electron state with non-zero orbital angular momentum, which generates a spin-orbit doublet. The predominant two lines coincide with the final states with $j_+ = l + s$ and $j_- = l - s$ where j is the total angular momentum of the ionised core hole, within the $j - j$ coupling scheme equivalent to the vector sum of its spin and orbital momenta [43].

The intensity ratio of these lines is calculated by the $(2j_- + 1)/(2j_+ + 1)$, for example *p*, *d* and *f* levels become spilt upon ionisation, leading to vacancies in the $p_{1/2}$, $p_{3/2}$, $d_{3/2}$, $d_{5/2}$, $f_{5/2}$ and $f_{7/2}$ in the ratio 1/2 for *p* subshells, 2/3 for *d* subshells, and the 3/4 for *f* subshells.

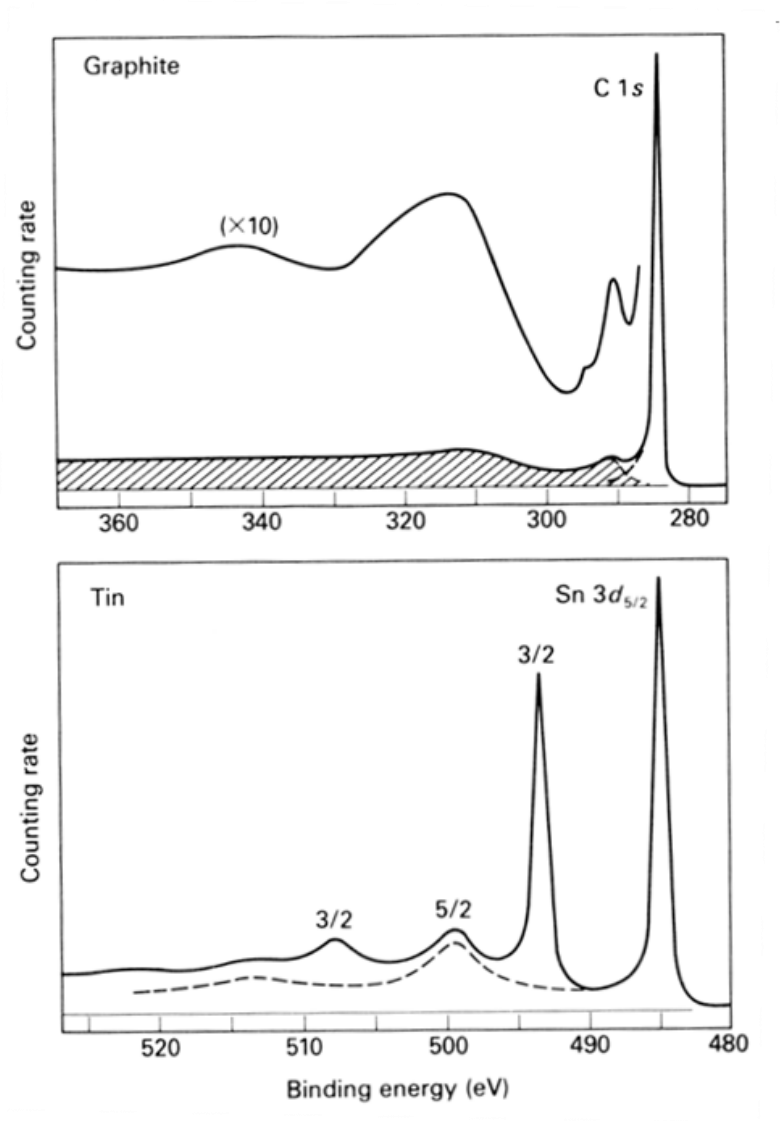


Figure 2.19. Photoemission spectra from graphite (upper panel) and tin (lower panel) with monochromated Al *Kα* radiation. (adapted from ref. 43)

Auger electrons are emitted additionally within the photoelectric process, because of relaxation of the energetic ions left after photoemission.

The Auger electron process is seen in figure 2.20. An incident photon induces a "hole" by core photoemission (electron 1). An outer electron (electron 2) relaxes into the hole (or electron vacancy), and a third electron (Auger electron) is finally emitted carrying away the excess energy [52]. The kinetic energy of the Auger electron process is equivalent to the gap between the energy of the primary ion and the doubly-charged final ion. The quantum energy ΔE can be expressed by [52]:

$$\Delta E_{kin} = E_K - E_{L1} - E_{L2,3} - \varphi \quad \text{(Auger transition termed } KL_1L_{2,3}) \quad (2.13)$$

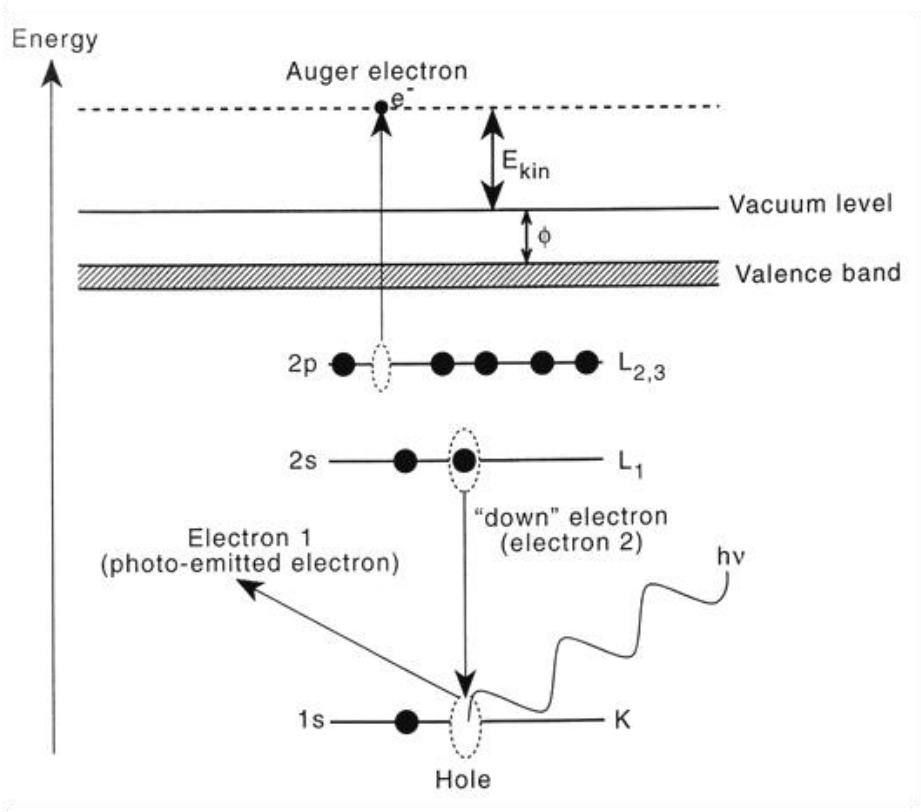


Figure 2.20. Schematic diagram of energetic the Auger process after the 'hole' creation by photoemission. (adapted from ref. 52)

The quantitative treatment of the intensity of Auger transitions is complicated not only by inelastic scattering but also backscattering effects. First, consider the geometry of excitation and detection as shown in figure 2.21 [9]. Some of the electrons from the primary excitation beam excite the emission of Auger electrons, and some are backscattered after elastic or inelastic scattering from the sample [9]. Auger Electron Spectroscopy (AES) is an analytical technique that uses a primary electron beam to probe the surface of a solid material. Secondary electrons that are emitted as a result of the Auger process are analyzed and their kinetic energy is determined. The identity and quantity of the elements are determined from the kinetic energy and intensity of the Auger peaks. The nature of the Auger surface analysis process is such that Auger electrons can only escape from the outer 5-50 Å of a solid surface at their characteristic energy [52, 60]. This effect makes AES an extremely surface sensitive technique. A finely focused electron beam can be scanned to create secondary electron and Auger images, or the beam can be positioned to perform microanalysis of specific sample features. Applications include materials characterization, failure analysis, thin film analysis, and particle identification for semiconductor and thin film head manufacturing.

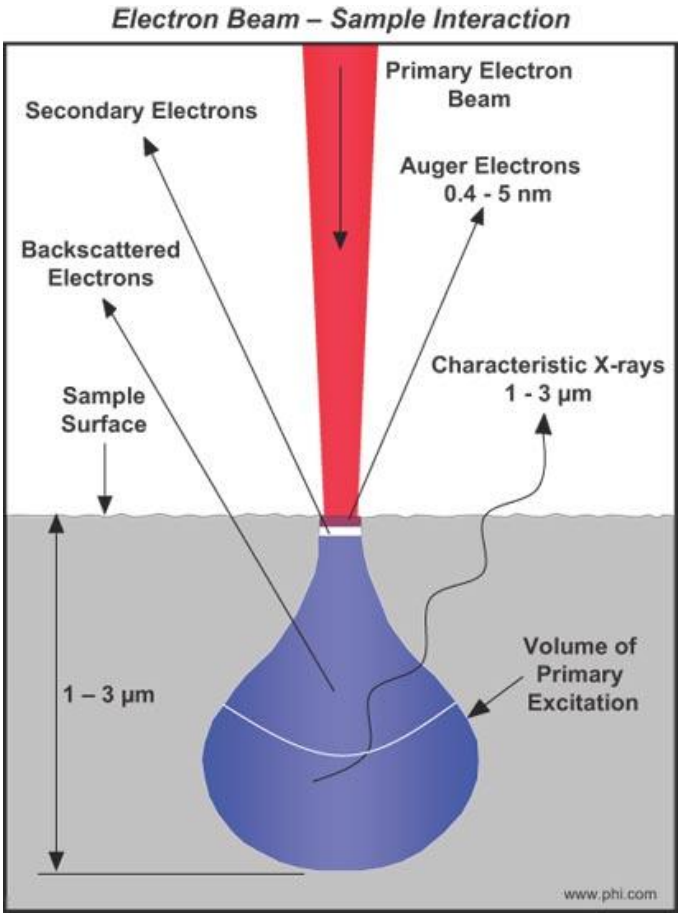


Figure 2.21. The geometry of Auger electron spectroscopy. (adapted from ref. 9 and www.phi.com)

When non-monochromatic X-ray sources are used, extra photon lines are present in the exciting radiation giving rise to extra weak peaks in the spectrum (see figure 2.22) [61] and contamination of the X-ray anode can arise.

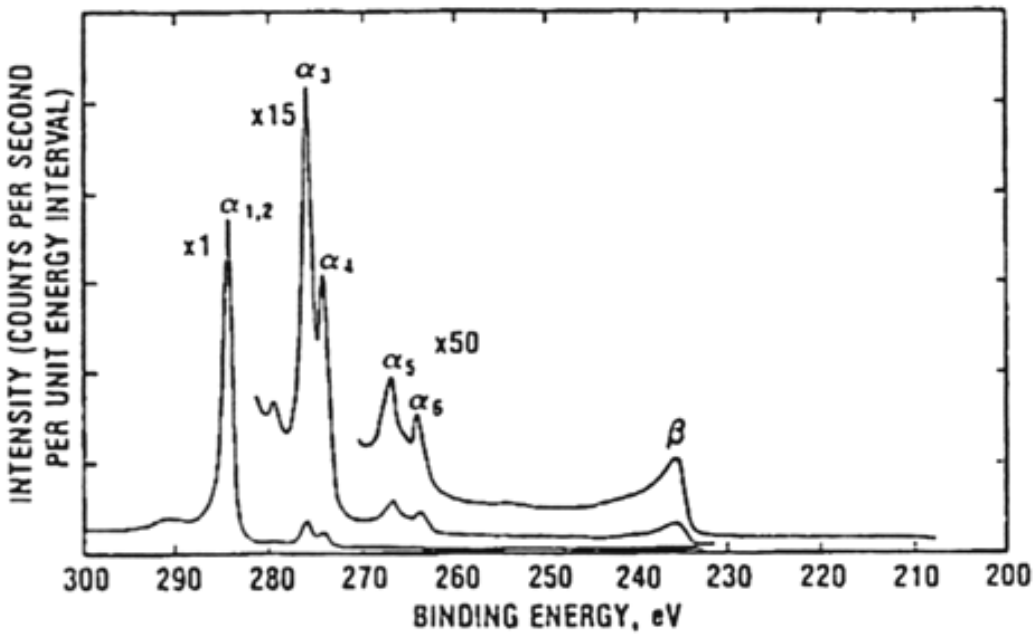


Figure 2.22. X-ray satellites for Mg Anode. (Spectrum of C 1*s* graphite, adapted from ref. 61)

Shake-up satellites may exist when the outgoing photoelectron at the same time interacts with a valence electron which is excited to a higher orbital [41].The kinetic energy of the outgoing electron is thus reduced correspondingly. Commonly, very strong shake-up satellite peaks arise when paramagnetic compounds such as Cu (II) are studied. Several kinds of shake-up line of Cu are shown in figure 2.23.

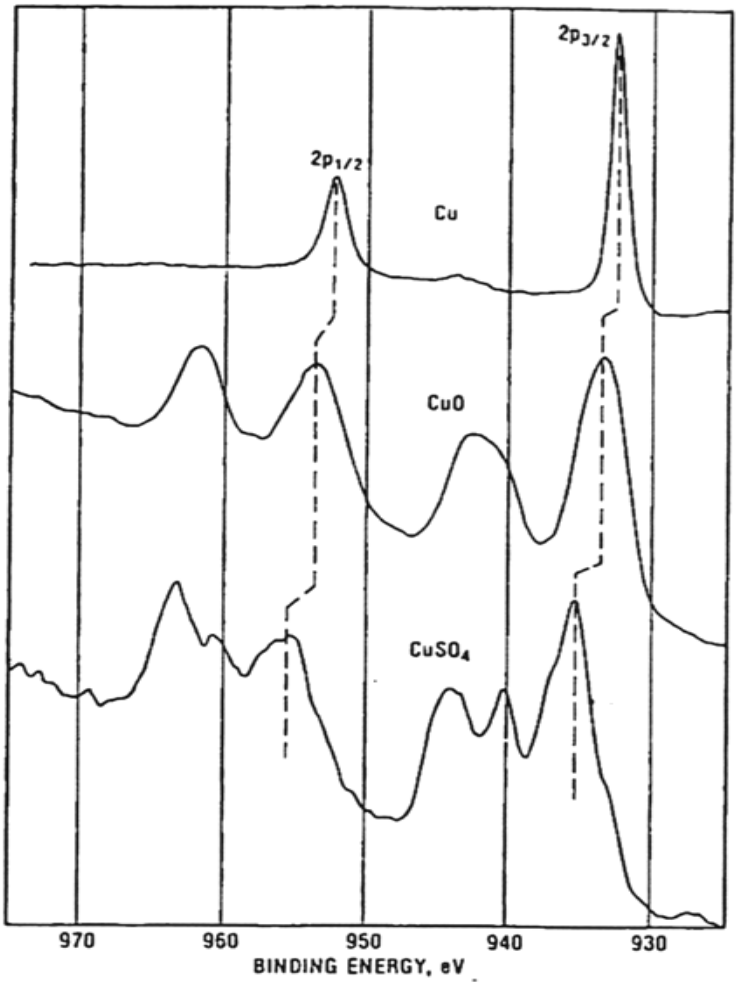


Figure 2.23. Shake-up satellite lines of the Cu 2*p* spectrum. Shake-up process involves variable energy transition states (adapted from ref. 61)

(g) Quantification and sensitivity factors

One of the main reasons for popularity of XPS is that it is the most quantitative of the commonly used methods of surface analysis, capable of providing an element analysis of a surface to within ±10 % accuracy [62]. Although the nature of the photoemission and spectral recording process can produce inherent noise in the spectrum, it is frequently found in fact that the spectrum can be recorded at an extremely high level of reproducibility. The main uncertainties in composition,

therefore arises from uncertainties in the quantification procedure itself.

From an homogeneous sample, theory [63] suggests that a simplified expression for the intensity of a spectral line can be written as

$$I_A = K\sigma_A N_A \lambda_{E_A} G_{E_A} \qquad (2.14)$$

where K is a proportionality factor, I_A is the intensity of the spectral line, sigma is the cross-section for photoemission from the relevant inner shell of atom *A*, N_A is the atomic concentration, lambda is the attenuation length of the photoelectron in the matrix and G_{E_A} is an energy dependent spectrometer transmission function. The expression shows the measured intensity is proportional to atomic concentration, is dependent on the properties of the ionised core level (through sigma) but also depends on sample properties (through lambda) and spectrometer properties (though *G*). If further simplifications are made to ignore matrix effects on atomic packing and mean free paths, then for an atomic mixture equation 2.14 becomes [63]

$$X_A = \frac{\frac{I_A}{I_A^o}}{\sum \frac{I_i}{I_i^o}} \qquad (2.15)$$

where X_A is the mole fraction and I^o_A is the spectral intensity recorded for pure *A* material. To use this equation it is necessary to have a set of sensitivity factors, representing I^o_A to account for the variation in relative sensitivities of the different chemical elements.

There are a number of such databases in the literature, which can be adapted for use with any XPS e.g. [64-66] and the most commonly used of these databases is that by Wagner *et al.* [67]. The sensitivity factors in theory depend on the fundamentals of the photoionisation process, and the electron mean free path [62, 68]. There are many problems and approximations involved in the use of this equation. Matrix effects as noted above are ignored, and it is assumed that surface segregation and the presence of attenuating contaminant films on the surface are absent. Measurement of spectral intensity from the peak area requires accurate background subtraction and may require effects due to energy loss processes to be taken into account. The standard sensitivity factors used may not be accurately applicable to the spectrometer and conditions used in recording the spectrum.

Equation 2.15 was used in this thesis to determine thin film composition from XPS data. Bearing in mind the discussion above, it is unlikely that absolute mole fractions deduced are accurate to better than 10% [62] and probably significantly worse. However given the precision with which the spectrum is recorded, trends in relative composition within a series of samples of otherwise similar properties made on the same spectrometer are probably detected within a factor of a few percent.

2.3.3 XPS Implementation

Many of the XPS spectra recorded in this thesis employed the Scienta ESCA300 spectrometer based at Daresbury Laboratory as illustrated in Figure 2.24. A 300 mm diameter coated alloy disc (see figure 2.24) is used for the UHV rotating anode X-ray source producing Al $K\alpha$ ($h\nu$ = 1486.6eV) or Cr $K\beta$ ($h\nu$ = 5946.7 eV) radiation [69]. The X-rays emitted are monochromated by double focusing quartz crystals to a focal

spot of 0.5 mm wide x 6 mm long [70]. Photoelectrons from the sample are collected using a multi-element lens and focussed into a slit/aperture at the entrance region of the hemispherical electron energy analyser of a large mean radius of 300 mm. A chevron type microchannel plate in conjunction with a phosphor screen enables the signal to be read out on a CCD camera.

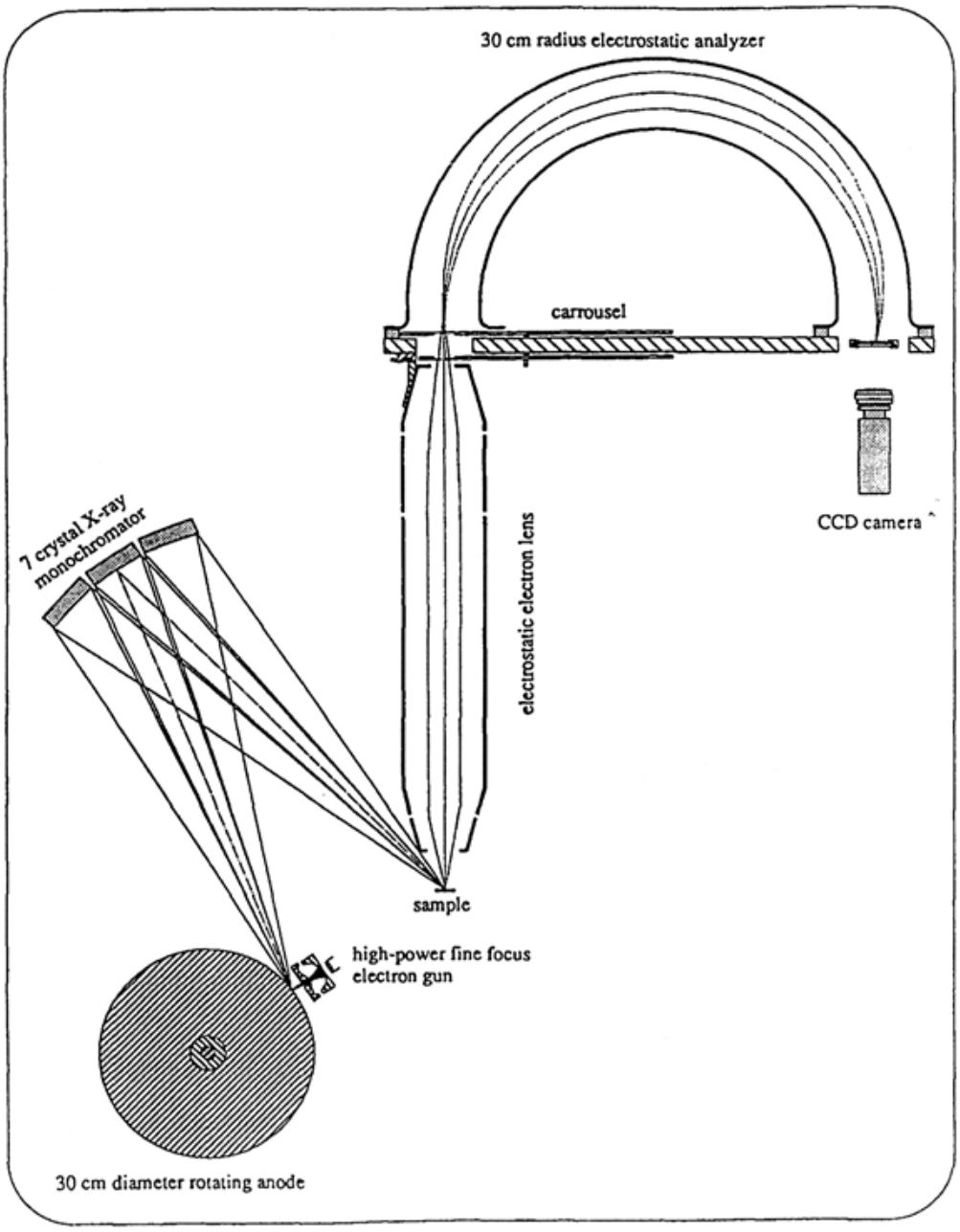


Figure 2.24. Schematic diagram of the Scienta ESCA300 spectrometer. (adapted from ref. 69)

Samples are introduced to the spectrometer via a turbo-molecular pumped fast entry airlock (base pressure 1 x 10^{-6} mbar) and preparation chamber. Ar ion sputtering and sample heating can be used to remove contaminants. Figure 2.25 shows the front view image of the ESCA300 instrument, containing all of the components.

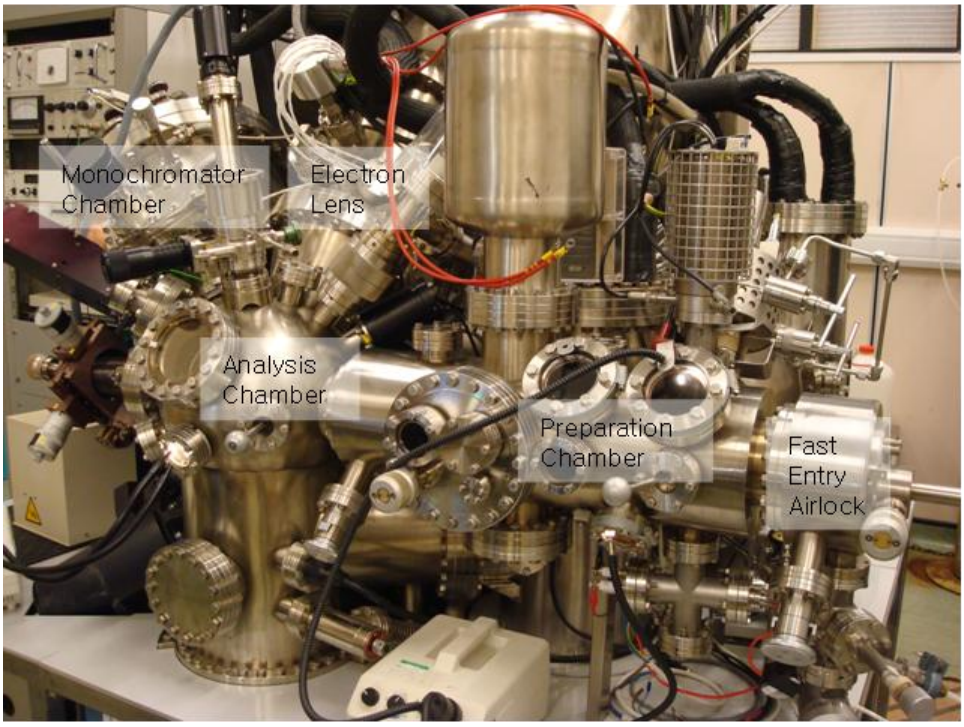


Figure 2.25. Front view photograph of the *Scienta ESCA300* instrument, NCESS, Daresbury Laboratory, UK.

The characteristics of the instrument are that high quality, high resolution spectra can be readily recorded. When the Daresbury instrument was not available, XPS spectra were recorded using a more conventional instrument based on a non-monochromatised Al X-ray source, 100 mm radius hemispherical analyser and

multichannel detector. This produced spectra qualitatively similar to the Scienta, but with inferior energy resolution and signal:noise ratio.

2.3.4 X-ray Emission Spectroscopy (XES)

(a) History of X-ray emission

The first pioneer of X-ray emission spectroscopy was Moseley in the early 20th century who found that the most intense wavelength spectral line in the X-ray range for a particular element is actually related to the element's atomic number, Z in the periodic table by a relationship later called Moseley's law [71, 72]. Karl Manne Siegbahn at Uppsala University developed X-ray emission spectroscopy. He analysed the X-ray wavelength of various elements using high precision X-ray fluorescence spectroscopy, excited by high-energy electrons [73].

(b) Valence-level X-ray emission

Valence shell XES is particularly useful for the investigations of chemical bonding and elemental analysis, because of the entanglement of core levels (localized states of well separated energies) with those of valence electrons responsible for chemical bonding.

Valence X-ray emission often has very weak cross-sections and requires strong X-ray sources to induce the initial core hole state such as the 3rd generation synchrotron undulator beam line [49, 74]. The partial density of states (PDOS) thus provided enables insights into the electronic structure of the valence band.

XES has two schematic types of emission, resonant and non-resonant. Photon-in-photon-out processes can be considered a scattering event. If the X-ray energy matches with the excitation energy of a core electron, the scattering process is then

enhanced resonantly ("resonant inelastic X-ray scattering", RIXS) providing convolved information concerning the occupied and vacant valence states [75].

Non-resonant XES is accomplished when the excitation energy exceeds the core ionisation threshold. The schematic diagram of non-resonant X-ray emission is shown as figure 2.26. After photoionisation, a valence electron decays into the core hole, leading to photon emission in a single photon process. This emission process has the selection rules as $\Delta n \geq 1$; $\Delta l = \pm 1$; $\Delta j = 0, \pm 1$ [49].

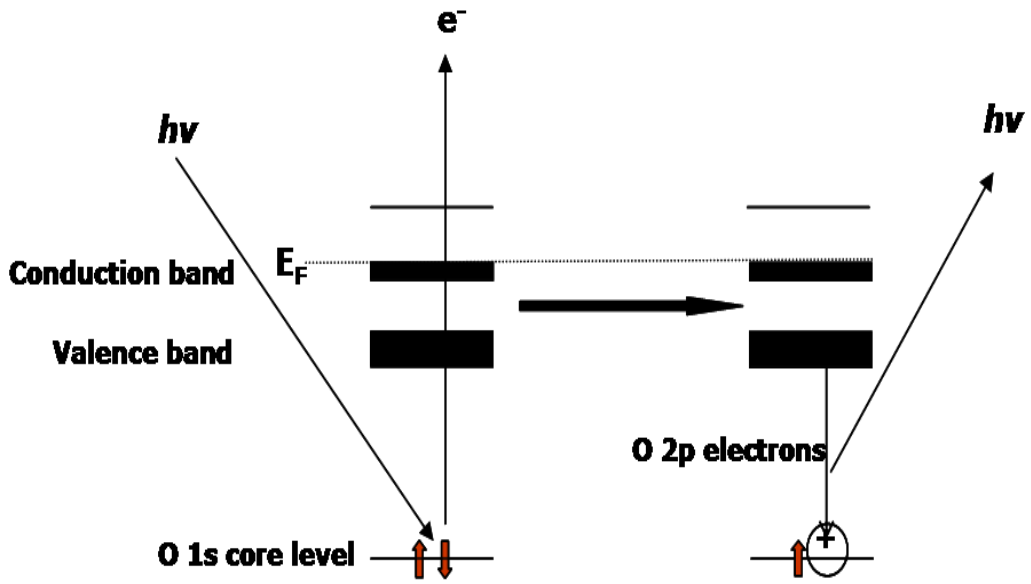


Figure 2.26. Schematic diagram of non-resonant O *K*-shell X-ray emission.

2.3.5 X-ray Absorption Spectroscopy (XAS)

X-ray absorption spectroscopy is an effective analytical tool for probing the local geometric bonding or electronic structure of a material [76]. Absorption of an X-ray photon by an atom takes place if the photon energy exceeds the ionisation energy (E_0) for a core electron in the material. There is an *absorption edge* at certain energies

where the absorption enhances drastically. The edges occur broadly at energies where the creation of photoelectrons by the absorbed radiation becomes possible corresponding to the continuum states from the *K*, *L*, *M*, etc, shells of the absorbing elements. These absorption edges following a sequence of increasing energy, *K*, L_1, L_2, L_3, M_1…, associated with each orbital of $1s$ ($^2S_{1/2}$), $2s$ ($^2S_{1/2}$), $2p$ ($^2P_{1/2}$), $2p$ ($^2P_{3/2}$), $3s$ ($^2S_{1/2}$)…, respectively.

The XAS technique is best performed by synchrotron beamlines, where tunable intense X-rays can be easily produced. The 'absorption edge' in XAS is often divided into four sections as shown in figure 2.27 [76]: (1) pre-edge ($E < E_0$), (2) X-ray absorption near-edge structure, XANES ($E = E_0 \pm 10$ eV), (3) near edge X-ray absorption fine structure, NEXAFS ($E = E_0 + 10$ eV~50 eV), (4) extended X-ray absorption fine structure, EXAFS ($E = E_0 + 50$ eV~1000 eV) [76].

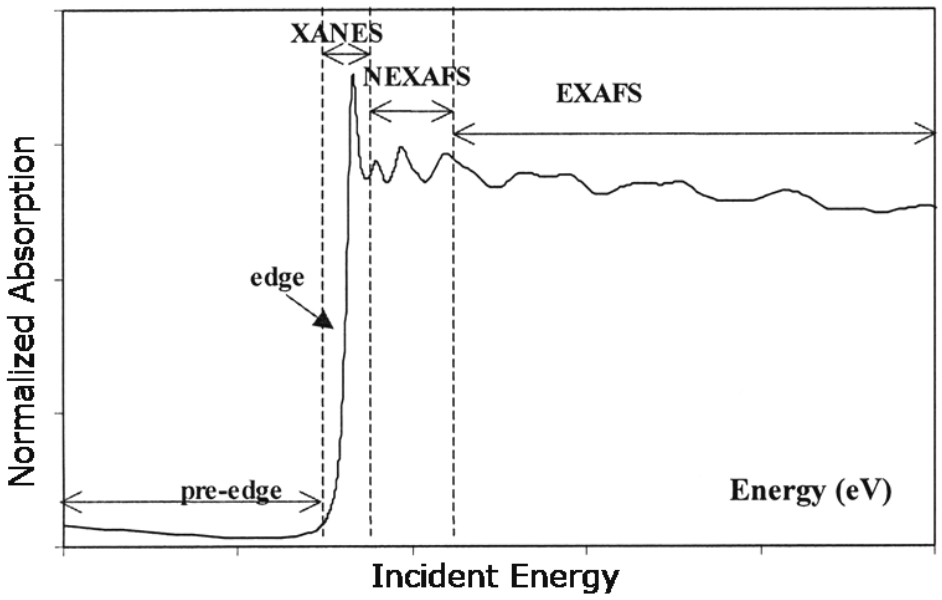


Figure 2.27. Schematic diagram of three regions of XAS data, XANES, NEXAFS and EXAFS. (adapted from ref. 76)

The pre-edge region is caused by electron transitions from the core level to higher partially occupied bound orbitals, for example, $s \rightarrow p$, or $p \rightarrow d$. The XANES region comprises transitions of core electrons to non-bound levels close to threshold. In the NEXAFS area, the ejected photoelectrons have a small kinetic energy and undergo strong multiple scattering. Finally in the EXAFS region, the photoelectrons have substantial kinetic energy, that means $E - E_0$ is large, and simple scattering due to the nearest neighbouring atoms takes place.

2.3.6 XES, XAS Implementation

High-resolution X-ray emission and absorption spectroscopy (XES and XAS) were implemented at the synchrotron beamline 7.0.1 at the 3rd-generation Advanced Light Source (ALS), Lawrence-Berkeley National Laboratory (LBNL), California (USA) [77]. The ALS includes 35 operational beamlines, incorporating super bend magnets, wigglers and undulators, offering high gains in flux and brightness. XES and XAS characterisations are performed at the endstation of 7.0.1 on beamline 7.0. A schematic flow chart of the beamline is shown in figure 2.28 [78].

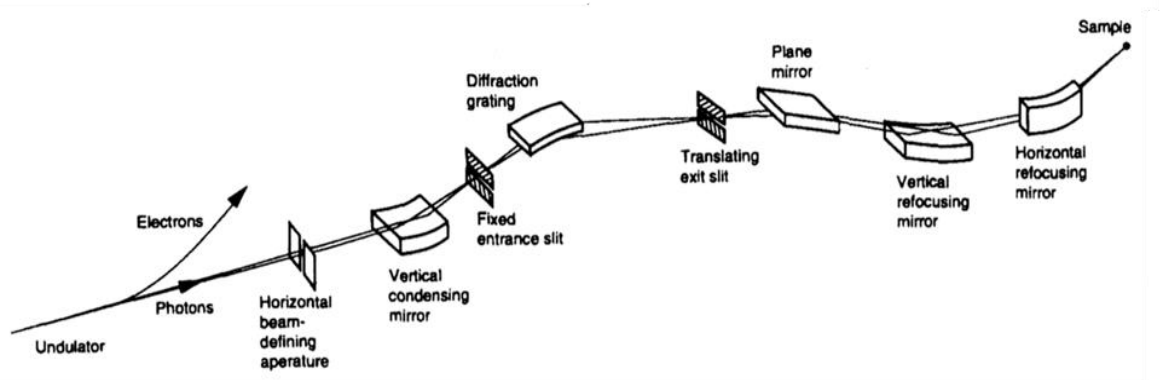


Figure 2.28. Optical geometry layout of beamline 7.0.1 at the ALS. (adapted from ref. 78)

Beamline 7.0 uses a state of the art undulator source consisting of 89 magnetic periods each 5 cm in length. The beamline can be operated with the appropriate the undulator gap, for example, the gap of about 23 mm, which is in accordance with deflection parameter value K = 0.5 ~ 2.2. The beamline utilises a spherical grating monochromator (SGM) between the entrance slit and the sliding exit slit [79]. The SGM and the other optics are cooled due to the high power energy. After the slits the monochromatic beam is deflected downwards by a plane mirror and then vertical and horizontal refocusing mirrors to deflect the light to two separate experimental end-stations. The detector is composed of multi-channel plates for high efficiency.

2.4 X-ray Diffraction and Surface Morphology

2.4.1 X-ray Diffraction (XRD)

The simplest and most obvious method to identify a crystalline substance is probably X-ray diffraction combined with chemical analysis. If the substance is a crystalline material, X-ray crystallography is one of the best ways to obtain information such as the crystal structure, the bonding present and the crystal defects [80]. An XRD experiment normally involves the generation of X-rays, the utilisation of a sample, and the imaging of the diffracted beams. X-rays are traditionally produced by accelerating electrons (to about 30 kV) which then bombard a metal target, often Cu or Mo. (see figure 2.29(a)) The typical spectra of X-rays thereby produced has two origins, a broad background known as 'white radiation' and monochromatic wavelengths, as shown in figure 2.29(b).

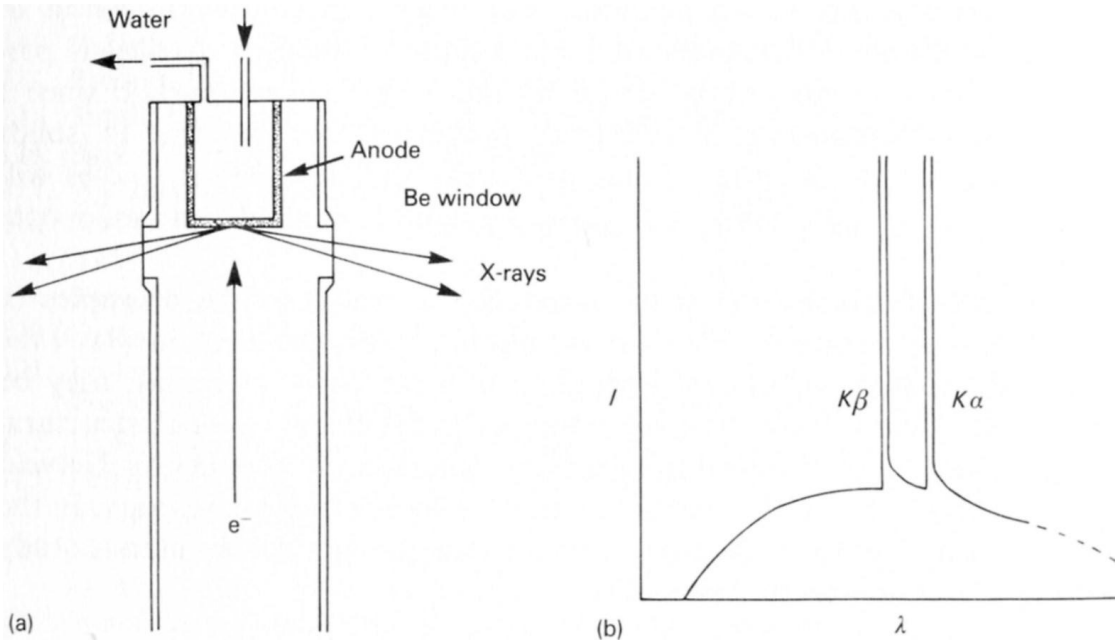


Figure 2.29. (a) Schematic cross-section view of X-ray tube, (b) X-ray emission spectrum. (adapted from ref. 43)

The diffraction of X-rays occurs as a result of the scattering by the repeating atomic crystal structure. Diffraction theory can be illustrated for a hypothetical 1-dimensional crystal, which suggests the equation [80]

$$a \sin\varphi = n\lambda \qquad (2.16)$$

where a is the separation of the atoms in the row with wavelength (λ) and the diffraction angle (φ). The *Laue equations* for a 3-dimensional arrangement of atoms for a real crystal, may be written [43, 80]:

$$a_1 \sin\varphi_1 = n\lambda \qquad (2.17)$$

$$a_2 \sin\varphi_2 = n\lambda \qquad (2.18)$$

$$a_3 \sin\varphi_3 = n\lambda \qquad (2.19)$$

Bragg's law considers diffraction by repeating crystal layers or planes. The derivation of Bragg's law deals with two X-ray beams as shown in figure 2.30. The relationship between pairs of planes is expressed by [43, 80]

$$\text{AB} = 2d_{hkl} \sin\theta, \text{ (path difference)} \qquad (2.20)$$

$$n\lambda = 2d_{hkl} \sin\theta, \text{ (for constructive interference)} \qquad (2.21)$$

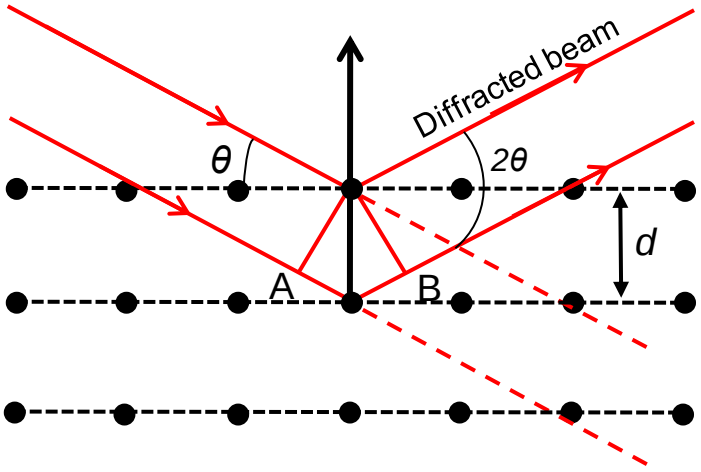


Figure 2.30. Derivation of Bragg's law for X-ray diffraction. Bragg reflection is shown by crystal planes with spacing d_{hkl}. (adapted from ref. 43, 80)

2.4.2 XRD Implementation

Monochromatic X-ray diffractograms were produced by using a PANalytical X'Pert PRO powder diffractometer. A monochromatic Cu *Kα* X-ray source generated a wavelength of 1.5418 Å. The entrance slit of the diffracted X-ray beams was set at 0.25 mm. The scan range, on a goniometer axis, was between 3.00~120.00^{o} (2θ). The scan step size was 4.1778 x 10^{-3} ^{o} (2θ), with a 2.545 sec dwell time.

2.4.3 Scanning Probe Microscopies

(a) Introduction

In 1982, Gert Binnig and Heinreich Röhrer invented the scanning tunnelling microscope (STM), for which they won the Novel Prize for Physics in 1986. The basic principle of STM is fairly simple. A sharp metal tip is manoeuvred to within a

few nanometers of an electrically conducting surface and a small electrical potential difference is applied between the tip and surface of the material. This results in the onset of electron tunnelling between the tip and the surface, as suggested by figure 2.31 [52]. The tunnelling current (*I*) can be expressed in terms of the tip-surface gap (*W*) and the sample work function (φ) [52],

$$I(W) = C\exp(-W\sqrt{\varphi}) \qquad (2.22)$$

where C is a constant.

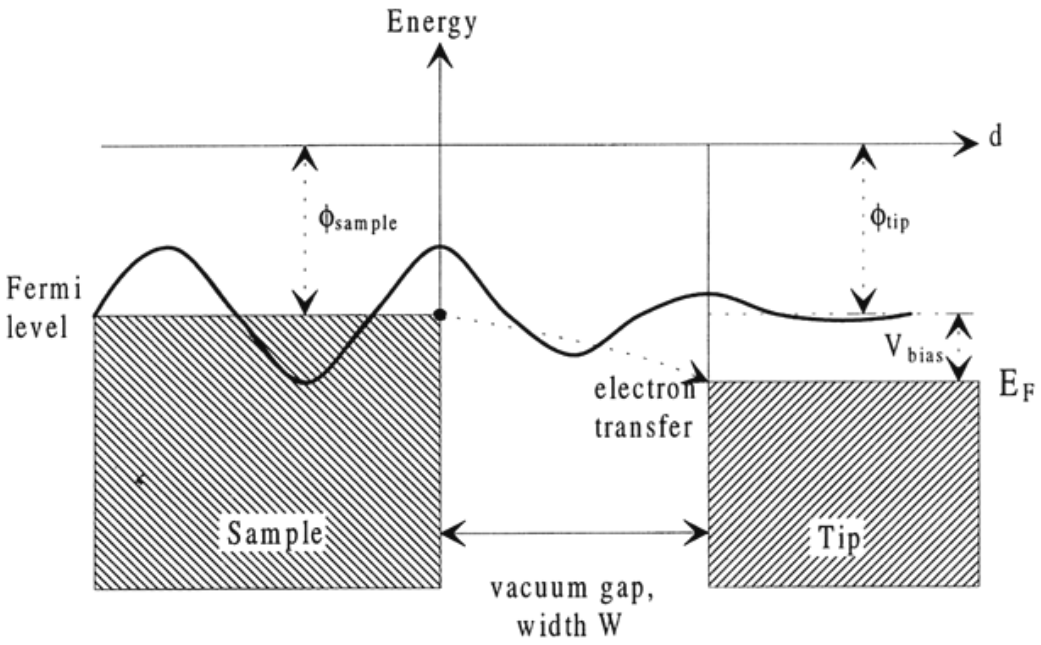


Figure 2.31. Energy diagram explaining electron tunnelling phenomena between tip and sample in SPM. (adapted from ref. 52)

Thus, if a tip is scanned at constant height above a surface the tunnelling current will increase in areas where protrusions exist because of a lowering in the gap distance. By applying a bias voltage (tens of *m*V to several V) between the tip and the sample,

small tunnelling currents (0.01 nA-50 nA) can flow from the sample to the tip or vice versa (Figure 2.31). Two modes of scanning may be employed. A measurement of the current at constant voltage (constant voltage imaging mode) or of the voltage at constant current (constant current imaging mode) is then made while the tip is scanned across the surface. As always, we set up a co-ordinate system in which the *x* and *y* axis lie in the plane of the surface and the *z* axis is direct away from the surface [9].

Since the current is a very sensitive function of the tip-surface separation, it can be used to image the atoms present at the surface, if the tunnelling current is measured as the tip is scanned over the surface with atomic precision using for example piezoelectric scanners, as indicated in figure 2.32 [81]. Figure 2.33 also shows a schematic feedback loop of a scanning tunnelling microscope with components.

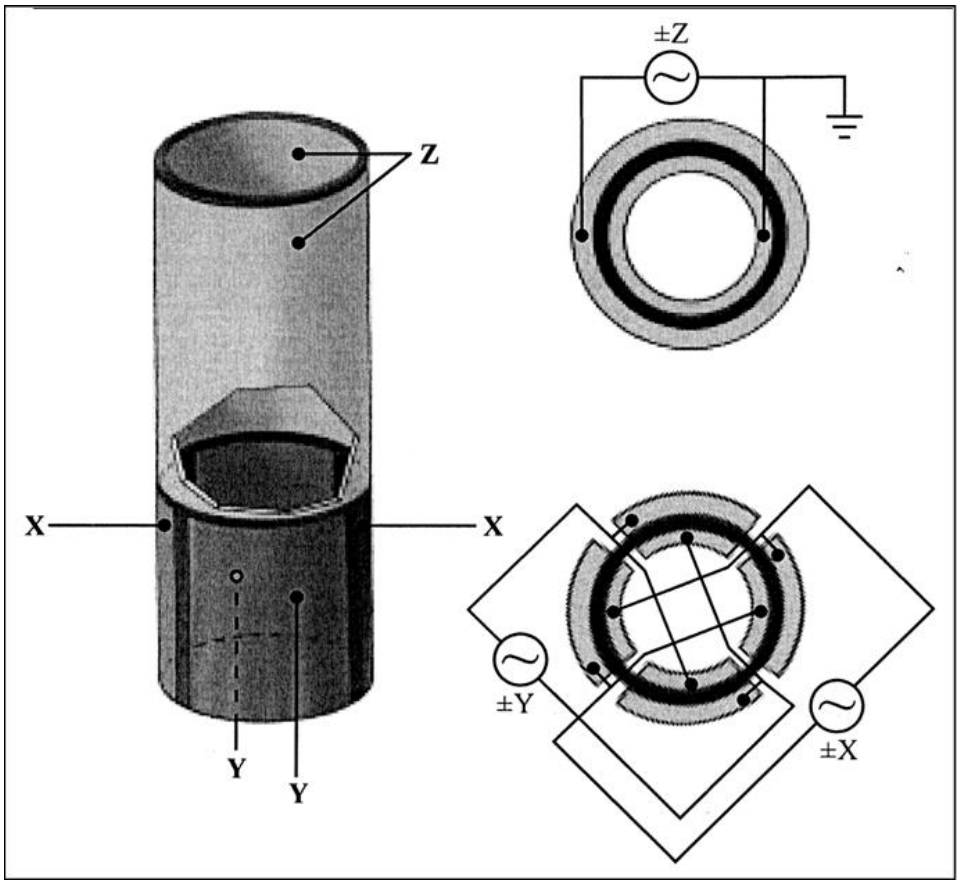


Figure 2.32. Typical scanner piezo tube and X-Y-Z electrical configurations. AC signals applied to conductive areas of the tube create piezo movement along the three major axes [81].

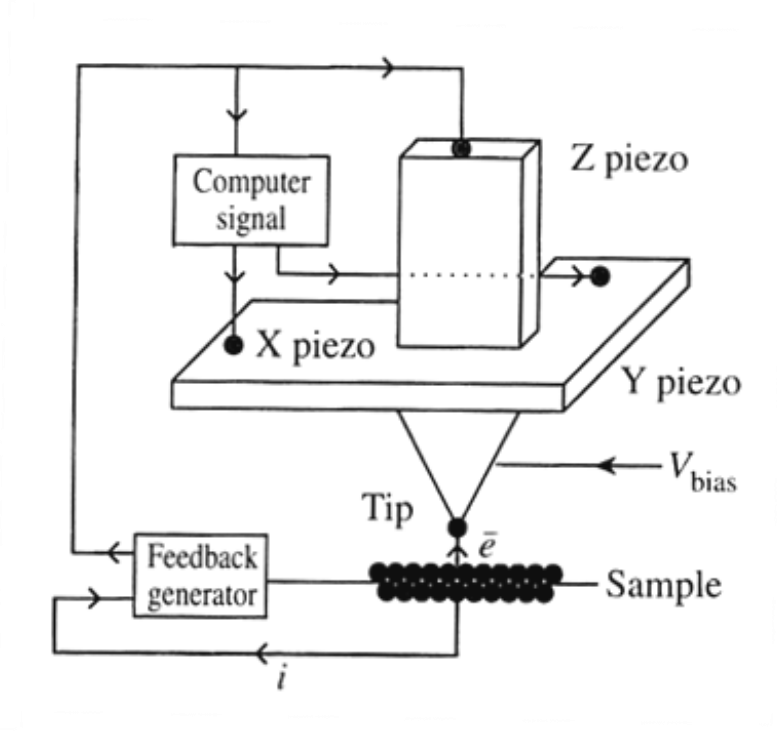


Figure 2.33. Schematic diagram of the components and feedback loop of a scanning tunnelling microscope. (adapted from ref. 52)

The development of STM has provided the basis for a whole range of "scanning probe" techniques. For insulating materials, STM cannot be applied, and the most important technique for these materials is known as atomic force microscopy (AFM). The method is similar to STM, except the interaction involves a force between the AFM tip and the surface. Figure 2.34 schematically illustrates the principle of operation of one form of AFM. A cantilever tip, typically made by silicon nitride with diameter under 20 um, oscillates close to the surface in question and the force between the tip and surface is judged from the measurement of its resonance frequency.

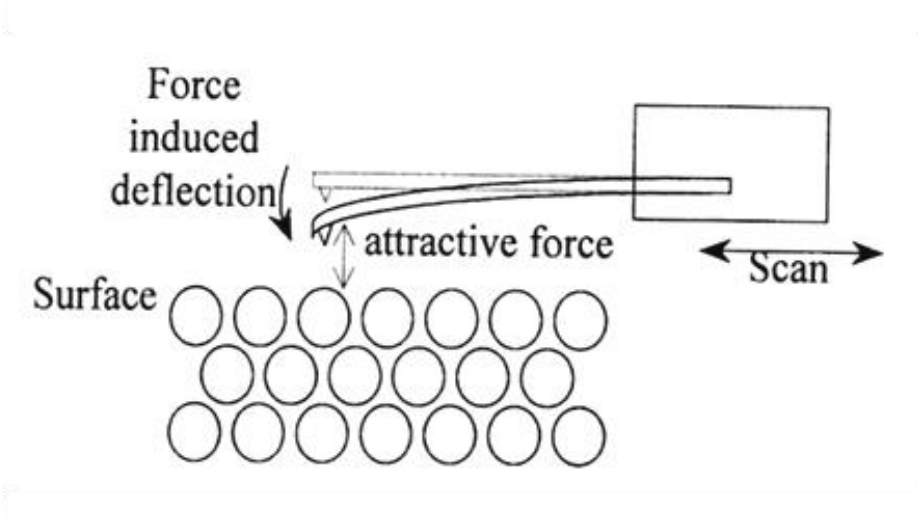


Figure 2.34. Schematic diagram of the principle of atomic force microscopy. (adapted from ref. 52).

The resonant frequency (v) of the cantilever is provided as following equation [52],

$$v = 1/(2\pi)\ \sqrt{(K/m)} \qquad (2.23)$$

where K is the cantilever force constant and m is its mass. There are however several different ways of imaging the surface with AFM involving both contact and non-contact modes. The method is now widely used for the high resolution topography analysis of the surfaces of materials, and this was the application of the method in the present work.

Figure 2.35 above shows a typical multi-mode SPM head which can be used for AFM. The tip scans over the sample surface, and the motion of it is tracked via a laser beam which reflects from the back surface. The quad photodiode detector with four elements provides different signal information depending on the running mode.

Figure 2.36 shows the arrangement of the photodetector elements in the MulitMode head [81].

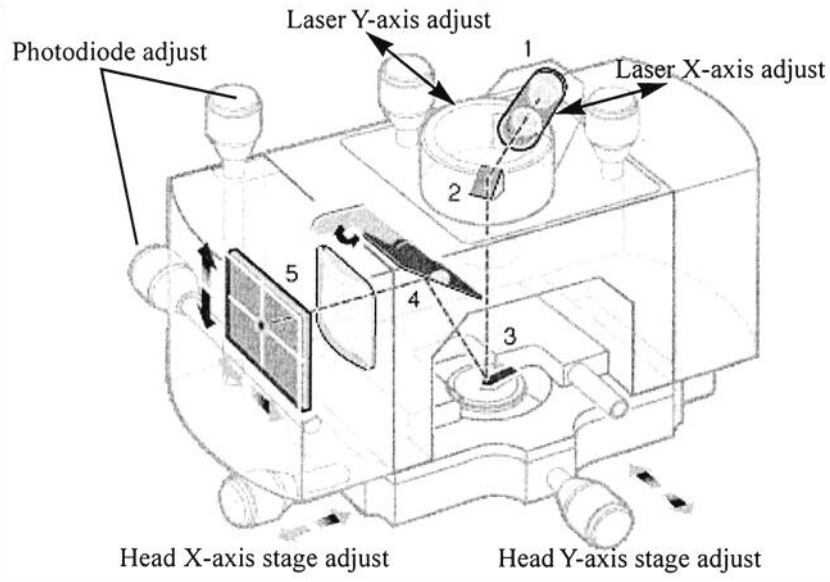


Figure 2.35. MultiMode SPM head and main parts: (1) laser, (2) mirror, (3) cantilever, (4) tilt mirror, (5) photodetector. (adapted from ref. 81)

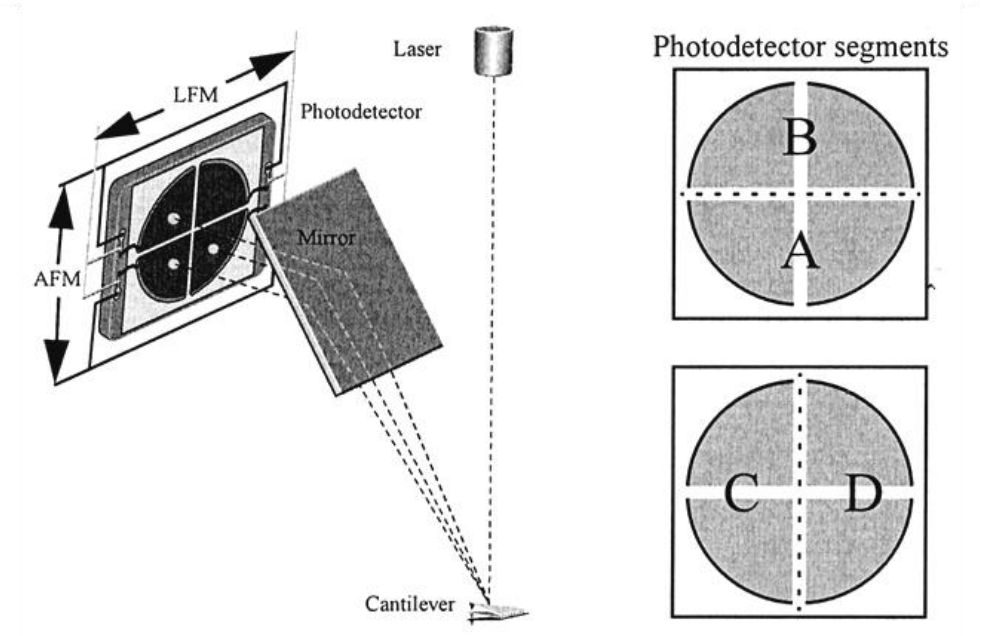


Figure 2.36. The arrangement of quad photodetector. Generating AFM signals are provided by different segments of the photodiode. (adapted from ref. 81)

2.4.4 Implementation

Atomic force microscopy (AFM) was carried out using a Digital Instruments Nanoscope™ Scanning Probe Microscope at the surface analysis facility (SAF) in the Chemistry Research Laboratory (CRL), University of Oxford, as shown in Figure 2.37. Measurements were made using Contact Mode AFM, which operates by scanning a tip of platinum across the sample surface, using laser tracking as described above.

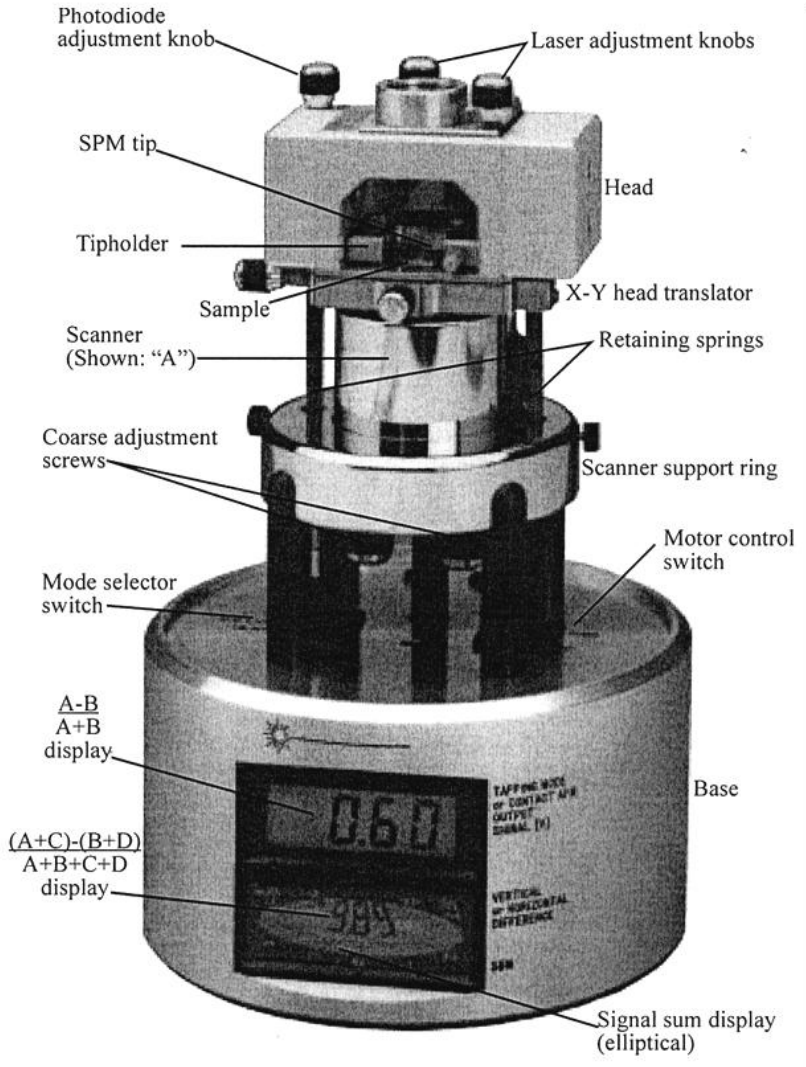


Figure 2.37. Image of DI Nanoscope ™ MultiMode SPM. (adapted from ref. 81)

2.4.5 Optical band gap

Optical absorption measurements of the band gap energy of the grown thin films were made using UV-Visible spectroscopy. In order to directly measure the optical band gap, the Tauc relationship, $\alpha h\nu = A(\hbar\nu - E_g)^n$ was employed [82, 83]. A Tauc plot (see figure 2.38) is a convenient way of displaying the optical absorption spectrum of a material, pioneered by Jan Tauc, who proved that momentum is not conserved even in a direct optical transition [82].

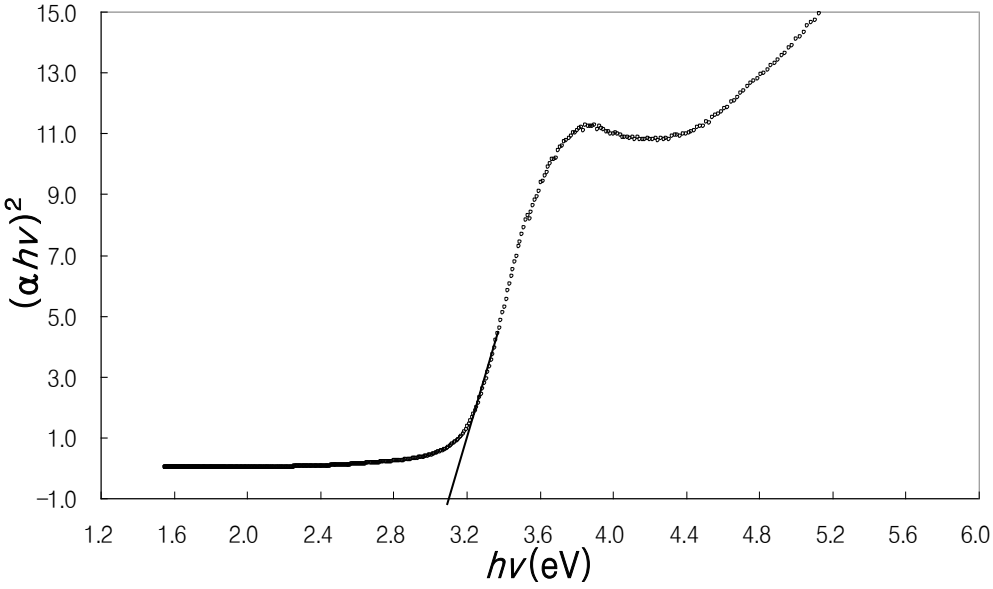


Figure 2.38. An example of Tauc plot. Direct optical band gap energy evaluation of 5% Sn-doped $CuCrO_2$ ($h\nu$ = 3.1 eV) thin film by $h\nu$ vs. $(\alpha h\nu)^2$ approximation (adapted from chapter 6)

Typically, a Tauc plot shows the quantity $h\nu$ (the energy of the light) on the abscissa and the quantity $(\alpha h\nu)^{1/n}$ on the ordinate, where α is the absorption coefficient of the material. The value of the exponent n denotes the nature of the transition [84]:

- n = 1/2 for direct allowed transitions
- n = 3/2 for direct forbidden transitions.
- n = 2 for indirect allowed transitions
- n = 3 for indirect forbidden transitions

The resulting plot has a distinct linear regime which denotes the onset of absorption. Thus, extrapolating this linear region to the abscissa yields the energy of the optical band gap of the material.

For a direct band gap, the absorption coefficient α is related to light frequency according to the following formula [85, 86]:

$$\alpha \approx A^* \sqrt{h\nu - E_g}, \text{ with } A^* = \frac{q^2 x_{vc}^2 (2m_r)^{3/2}}{\lambda_0 \epsilon_0 \hbar^3 n} \quad (2.24)$$

where α is the absorption coefficient, a function of light frequency. ν is light frequency. h is Planck's constant, is reduced Planck's constant ($\hbar = h/2\pi$). E_g is the band gap energy. A^* is a certain frequency-independent constant, with formula above.

- $m_r = m_h^* m_e^* / (m_h^* + m_e^*)$, where m_e^* and m_h^* are the effective masses of the electron and hole, respectively (m_r is called a "reduced mass")
- q is the elementary charge
- n is the (real) index of refraction
- ε_0 is the vacuum permittivity

- x_{vc} is a "matrix element", with units of length and typical value the same order of magnitude as the lattice constant.

This formula is valid only for light with photon energy larger, but not too much larger, than the band gap (more specifically, this formula assumes the bands are approximately parabolic), and ignores all other sources of absorption other than the band-to-band absorption in question, as well as the electrical attraction between the newly created electron and hole (see exciton). It is also invalid in the case that the direct transition is forbidden, or in the case that many of the valence band states are empty or conduction band states are full [86].

On the other hand, for an indirect band gap, the formula is [86]:

$$\alpha \propto \frac{(h\nu - E_{\mathrm{g}} + E_{\mathrm{p}})^2}{\exp(\frac{E_{\mathrm{p}}}{kT}) - 1} + \frac{(h\nu - E_{\mathrm{g}} - E_{\mathrm{p}})^2}{1 - \exp(-\frac{E_{\mathrm{p}}}{kT})} \qquad (2.25)$$

where:

- E_{p} is the energy of the phonon that assists in the transition
- k is Boltzmann's constant
- T is the thermodynamic temperature

(This formula involves the same approximations mentioned above.)

Therefore, if a plot of $h\nu$ versus α^2 forms a straight line, it can normally be inferred that there is a direct band gap, measurable by extrapolating the straight line to the $\alpha = 0$ axis. On the other hand, if a plot of $h\nu$ versus $\alpha^{1/2}$ forms a straight line, it can normally be inferred that there is an indirect band gap, measurable by extrapolating the straight line to the $\alpha = 0$ axis (assuming $E_{\mathrm{p}} \approx 0$).

References

1. J. W. Gibbs, *Scientific papers*. (Dover Publications, New York,, 1961).

2. J. Venables, *Introduction to surface and thin film processes*. (Cambridge University Press, Cambridge, UK ; New York, 2000).

3. Z. f. Kristallographie, *not everything was done last year, and the most thorough description is in Herring's 1953 article*. (Zeitschrift für Kristallographie, 1901).

4. W. Kossel, Nach. Ges. Wiss. Göttingen (1927).

5. I. N. Stranski, Z. Phys. Chem. **136,** 259-278 (1928).

6. J. D. Weeks and G. H. Glimer, Advances in Chemical Physics **40** 157-228 (1979).

7. W. K. Burton, N. Cabrera and F. C. Frank, Philosophical Transactions of the Royal Society of London Series a-Mathematical and Physical Sciences **243** (866), 299-358 (1951).

8. I. V. Markov, *Crystal growth for beginners: fundamentals of nucleation, crystal growth and epitaxy*. (World Scientific, Singapore, 2003).

9. K. W. Kolasinski, *Surface Science, Foundations of Catalysis and Nanoscience*, 3rd edition ed. (A John Wiley & Sons, Ltd., 2012).

10. Z. Y. Zhang and M. G. Lagally, *Morphological organization in epitaxial growth and removal* (World Scientific, Singapore, 1998).

11. Z. Y. Zhang and M. G. Lagally, Science **276** (5311), 377-383 (1997).

12. American Vacuum Society. and American Institute of Physics., *Papers from the ... North American Conference on Molecular Beam Epitaxy*. (Published for the American Vacuum Society by the American Institute of Physics, Woodbury, NY, 1994).

13. K. G. Gunther, Zeitschrift Fur Naturforschung Part a-Astrophysik Physik Und Physikalische Chemie **13** (12), 1081-1089 (1958).

14. E. K. Muller, Journal of Applied Physics **35** (3), 580-585 (1964).

15. R. B. Schoolar and J. N. Zemel, Journal of Applied Physics **35** (6), 1848-1851 (1964).

16. R. F. Steinber and D. M. Scruggs, Journal of Applied Physics **37** (12), 4586-4589 (1966).

17. P. A. Barnes and A. Y. Cho, Applied Physics Letters **33** (7), 651-653 (1978).

18. A. Y. Cho, Thin Solid Films **100** (4), 291-317 (1983).

19. A. Y. Cho and J. R. Arthur, Prog. Solid-State Chem. **10,** 157-192 (1975).

20. T. J. Drummond, H. Morkoc and A. Y. Cho, Journal of Applied Physics **52** (3), 1380-1386 (1981).

21. A. Y. Cho, D. L. Sivco, H. M. Ng, C. Gmachl, A. Tredicucci, A. L. Hutchinson, S. N. G. Chu and F. Capasso, Journal of Crystal Growth **227**, 1-7 (2001).

22. E. H. C. Parker, *The Technology and physics of molecular beam epitaxy*. (Plenum, New York, 1985).

23. M. Knudsen, Ann. Phys. **4,** 75 (1909).

24. N. Ramsey, *Molecular beams* (Clarendon Press, Oxford, 1956).

25. W. T. Tsang, Journal of Crystal Growth **95** (1-4), 121-131 (1989).

26. E. Veuhoff, W. Pletschen, P. Balk and H. Luth, Journal of Crystal Growth **55** (1), 30-34 (1981).

27. M. Naganuma and K. Takahashi, Applied Physics Letters **27** (6), 342-344 (1975).

28. N. Matsunaga, T. Suzuki and K. Takahashi, Journal of Applied Physics **49,** 5710 (1978).

29. G. J. Davies, D. A. Andrews and R. Heckingbottom, Journal of Applied Physics **52** (12), 7214-7218 (1981).

30. J. C. Bean and E. A. Sadowski, Journal of Vacuum Science & Technology **20** (2), 137-142 (1982).

31. U. Koenig, H. J. Herzog, H. Jorke, E. Kasper and H. Kibbel, Proc. 2nd Int. Symp. Molecular Beam Epitaxy and Related Clean Surface Techniques, Tokyo, 193 (1982).

32. A. R. Calawa, *Private Communication with E. H. C. Parker* (1990).

33. S. Beke, Thin Solid Films **519** (6), 1761-1771 (2011).

34. A. Bourlange, D. J. Payne, R. G. Egdell, J. S. Foord, P. P. Edwards, M. O. Jones, A. Schertel, P. J. Dobson and J. L. Hutchison, Applied Physics Letters **92** (9), 092117 (2008).

35. H. B. Kang, K. Nakamura, K. Yoshida and K. Ishikawa, Japanese Journal of Applied Physics Part 2-Letters, **36** (7B), L933-L935 (1997).

36. SVTA, *Oxygen Plasma Assisted Atomic Beam Epitaxy Oxide Growth System*. 1. (2005).

37. W. H. King, Analytical Chemistry. **36** (9), 1735-1739 (1964).

38. G. Sauerbrey, Z. Phys. **155** (2), 206-222 (1959).

39. J. W. Grate, Chemical Reviews. **100** (7), 2627–2648 (2000).

40. P. A. Cox, *The electronic structure and chemistry of solids*. (Oxford University Press, Oxford, 1987).

41. K. Siegbahn, *ESCA; atomic, molecular and solid state structure studied by*. (Almqvist & Wiksells, Uppsala, 1967).

42. A. Einstein, Ann. Physik. **17,** 132-148 (1905).

43. A. K. Cheetham and P. Day, *Solid state chemistry : techniques*. (Clarendon Press, Oxford, 1987).

44. K. Siegbahn, Philosophical Transactions of the Royal Society of London Series a-Mathematical and Physical Sciences **268** (1184), 33 (1970).

45. K. H. L. Zhang, Thesis D. Phil. University of Oxford (2011).

46. F. Reinert and S. Hüfner, New J. Phys. **7**, 97 (2005).

47. J. A. Bearden and A. F. Burr, Rev. Modern Phys. **39** (1), 125-142 (1967).

48. S. Hagstrom, C. Nordling and K. Siegbahn, Zeitschrift Fur Physik **178** (5), 439-444 (1964).

49. D. J. Payne, Thesis D. Phil. University of Oxford (2008).

50. S. Gan, L. Li, T. Nguyen, H. Qi, R. F. Hicks and M. Yang, Surf. Sci. **395** (1), 69-74 (1998).

51. Casa, *XPS Instrumentation*. 1. (2005).

52. G. Attard and C. Barnes, *Surfaces*. (Oxford University Press, Oxford, 1998).

53. O. Nilsson, C. H. Norberg, J. E. Bergmark, A. Fahlman, C. Nordling and K. Siegbahn, Helvetica Physica Acta **41** (6-7), 1064 (1968).

54. J. W. Davenport, R. E. Watson, M. L. Perlman and T. K. Sham, Solid State Communications **40** (11), 999-1002 (1981).

55. Proceedings of the Workshop on Hard X-ray Photoelectron Spectroscopy, HAXPES: European Synchrotron Radiation Facility, Grenoble, France. September 11 - 12, 2003. Elsevier (2005).

56. S. Thiess, C. Kunz, B. C. C. Cowie, T. L. Lee, M. Renier and J. Zegenhagen, Solid State Communications **132** (9), 589-594 (2004).

57. P. Glans, R. E. Lavilla, M. Ohno, S. Svensson, G. Bray, N. Wassdahl and J. Nordgren, Physical Review A **47** (2), 1539-1542 (1993).

58. X. L. Nie, S. H. Wei and S. B. Zhang, Physical Review Letters **88** (6), 066405 (2002).

59. J. Robertson, P. W. Peacock, M. D. Towler and R. Needs, Thin Solid Films **411** (1), 96-100 (2002).

60. D. Briggs and M. P. Seah, *Practical Surface Analysis by Auger and X-ray Photoelectron Spectroscopy*. (John Wiley & Sons Ltd., 1984).

61. C. D. Wagner and G. E. Muilenberg, *Handbook of x-ray photoelectron spectroscopy : a reference book of standard data for use in x-ray photoelectron spectroscopy*. (Perkin-Elmer Corp., Physical Electronics Division, Eden Prairie, Minn, 1979).

62. R. J. Ward and B. J. Wood, Surface and Interface Analysis **18** (9), 679-684 (1992).

63. D. Briggs and M. P. Seah, *Practical surface analysis*. (Chichester, New York, 1990).

64. H. Berthou and C. K. Jorgensen, Analytical Chemistry. **47** (3), 482-488 (1975).

65. C. K. Jorgensen and H. Berthou, Chemical Physics Letters **31** (3), 416-418 (1975).

66. C. D. Wagner, Analytical Chemistry **49** (9), 1282-1290 (1977).

67. C. D. Wagner, L. E. Davis, M. V. Zeller, J. A. Taylor, R. H. Raymond and L. H. Gale, Surface Interface Analysis **3** (5), 211-225 (1981).

68. R. F. Reilman, A. Msezane and S. T. Manson, Journal of Electron Spectroscopy and Related Phenomena **8** (5), 389-394 (1976).

69. G. Beamson, D. Briggs, S. F. Davies, I. W. Fletcher, D. T. Clark, J. Howard, U. Gelius, B. Wannberg and P. Balzer, Surface Interface Analysis **15** (9), 541-549 (1990).

70. U. Gelius, B. Wannberg, P. Baltzer, H. Fellnerfeldegg, G. Carlsson, C. G. Johansson, J. Larsson, P. Munger and G. Vegerfors, Journal of Electron Spectroscopy and Related Phenomena **52**, 747-785 (1990).

71. H. G. J. Moseley, Philosophical magazine 26, London (1912).

72. H. G. J. Moseley, *High frequency spectra of elements*, (Philosophical magazine, 27, London, 1913).

73. M. Siegbahn, *Spektroskopie der Röntgenstrahlen*. (J. Springer, Berlin,, 1931).

74. J. L. Hazemann, O. Proux, V. Nassif, H. Palancher, E. Lahera, C. Da Silva, A. Braillard, D. Testemale, M. A. Diot, I. Alliot, W. Del Net, A. Manceau, F. Gelebart, M. Morand, Q. Dermigny and A. Shukla, Journal of Synchrotron Radiation **16**, 283-292 (2009).

75. A. Kotani, European Physical Journal B **47** (1), 3-27 (2005).

76. F. Jalilehvand, D.Spångberg, P. Lindqvist-Reis, K. Hermansson, I. Persson and M. Sandström, "Hydration of the Calcium Ion. An EXAFS, Large Angle X-ray Scattering and Molecular Dynamics Simulation Study", Journal of American Chemical Society 123, 431-441 (2001)

77. J. Nordgren and J. H. Guo, Journal of Electron Spectroscopy and Related Phenomena **110** (1-3), 1-13 (2000).

78. H. A. Padmore and T. Warwick, Journal of Electron Spectroscopy and Related Phenomena **75**, 9-22 (1995).

79. T. Warwick, P. Heimann, D. Mossessian, W. Mckinney and H. Padmore, Review of Scientific Instruments **66** (2), 2037-2040 (1995).

80. A. R. West, *Basic solid state chemistry*, 2nd ed. (John Wiley & Sons, New York, 1999).

81. *MultimodeTM SPM Instruction Manual, Ver.4.31ce*. (1997).

82. J. Tauc, Grigorov.R and A. Vancu, Physica Status Solidi **15** (2), 627 (1966).

83. J. Tauc, Materials Research Bulletin **3**, 37-46 (1968).

84. E. A. Davis and N. F. Mott, Philosophical Magazine A **22** (179), 903–922 (1970).

85. E. Rosencher, Optoelectronics equation 7.25 (2002).

86. J. I. Pankove, *Optical Processes in Semiconductors*. (Dover, 1971).

3 Epitaxial Growth of p-Type TCO Cu_2O Thin Films by Oxygen Plasma Assisted Atomic Beam Epitaxy

3.1 Introduction

3.1.1 Background

Copper oxide based materials form a range of metal oxide semiconductors and should be a good starting point for alternative p-type transparent conducting oxides (TCOs) such as $CuAlO_2$, $CuGaO_2$, $CuInO_2$ and $SrCu_2O_2$ [1-4]. Their abundance, low economic cost, low hazard and electrical performance gives rise to growing interest in the developments of electronic and optoelectronic applications [5-7]. Especially thin film type copper oxides have been in the limelight as catalysts, photovoltaic devices, low-friction materials, solar cells, electrochromic layers and quantum dots [8-12]. Copper oxide shows two stable common forms that is cuprous oxide (Cu_2O) and cupric oxide (CuO). The energy band gaps of Cu_2O (cubic lattice) and CuO (monoclinic) are 2.1~2.6 and 1.3~2.1 eV, respectively [13-15]. Cuprous oxide, Cu_2O is known to be a semiconductor material with p-type conductivity because of metal vacancies from doping or annealing. Acceptor energy levels of Cu_2O are situated about the range 0.12~0.7 eV above the valence band maximum (VBM) of a Cu_2O single crystal prepared by oxidation treatment of copper [16, 17]. In contrast to many other oxide materials, the highest states of the valence band in Cu_2O come from the entirely occupied orbital states of Cu $3d^{10}$ which are not localized permitting hole conductivity [18]. However, these states have brought various arguments. For example, the presence of hole acceptors has sometimes been asserted to be 0.45~0.55 eV above the valence band edge, as suggested by deep level transient spectroscopy (DLTS), but this may be caused by structural aberrations such as CuO byproducts [19-21].

3.1.2 Crystal Structure and Electronic Configuration of Cu_2O

Crystalline Cu_2O of the cuprite structure is defined by a body centred cubic (BCC) arrangement of oxygen atoms with copper atoms inserted. When each copper atom is linearly bonded with two oxygen atoms, forming linear O-Cu-O dumbbell units which resemble a delafossite framework [22].

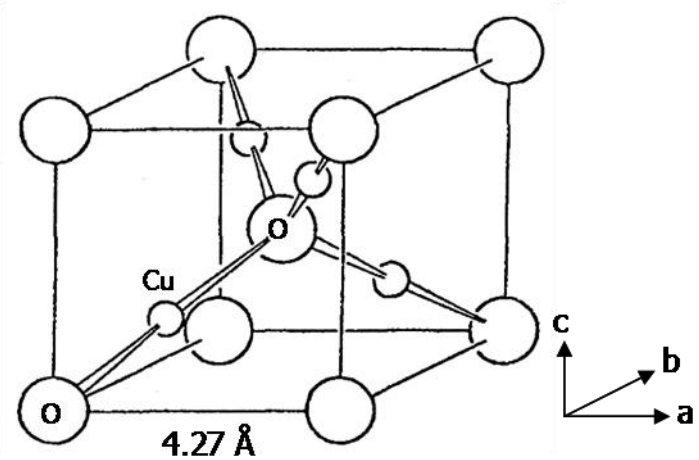


Figure 3.1. Crystal unit structure of Cu_2O. Large spheres - oxygen atoms; small spheres - copper atoms. (adapted from ref. 23)

The unit cell of Cu_2O could be considered to be a clear ionic compound, as shown in figure 3.1, consisting of Cu^+ cations with a $3d^{10}$ configuration and O^{2-} anions. This ionic model may not interpret either the low coordination number 2 for Cu or the short distance of Cu – O, which is not reconcilable with the sum of any pair of the ionic radii for Cu^+ and O^{2-} given by several theorists: Cu^+ : r = 0.96 Å (Pauling, Ahrens), O^{2-} : r = 1.32 Å (Goldschmidt), 1.40 Å (Pauling, Zachariasen). Thus the total sum of the ionic radii of Cu^+ and O^{2-} could be 2.28 or 2.36 Å, whilst the distance

of Cu – O in Cu_2O is 1.85 Å [24]. Up to the middle of the 1980s, a lot of theoretical attempts to calculate the electronic structure and bonding mechanism of Cu_2O were made such as a non-self-consistent APW band structure, self-consistent Gaussian-orbitals, tight-binding band structure and a cluster model by Nagel [25-28]. Among the theoretical models, only a cluster model dealt with the question of chemical bonding in earnest, and showed that the ionic model was not appropriate; the bonding has significant covalent character involving substantial charge transfer from O^{2-} to Cu^{+}. Subsequently, a self-consistent Gaussian-orbitals model correctly described the hybridisation of Cu 3*d* and Cu 4*s* states [29]. The non-relativistic linearised augmented plane wave (LAPW) method was used for this more advanced band structure calculation. For this calculation, the local-density approximation (LDA) treated the exchange and correlation effects.

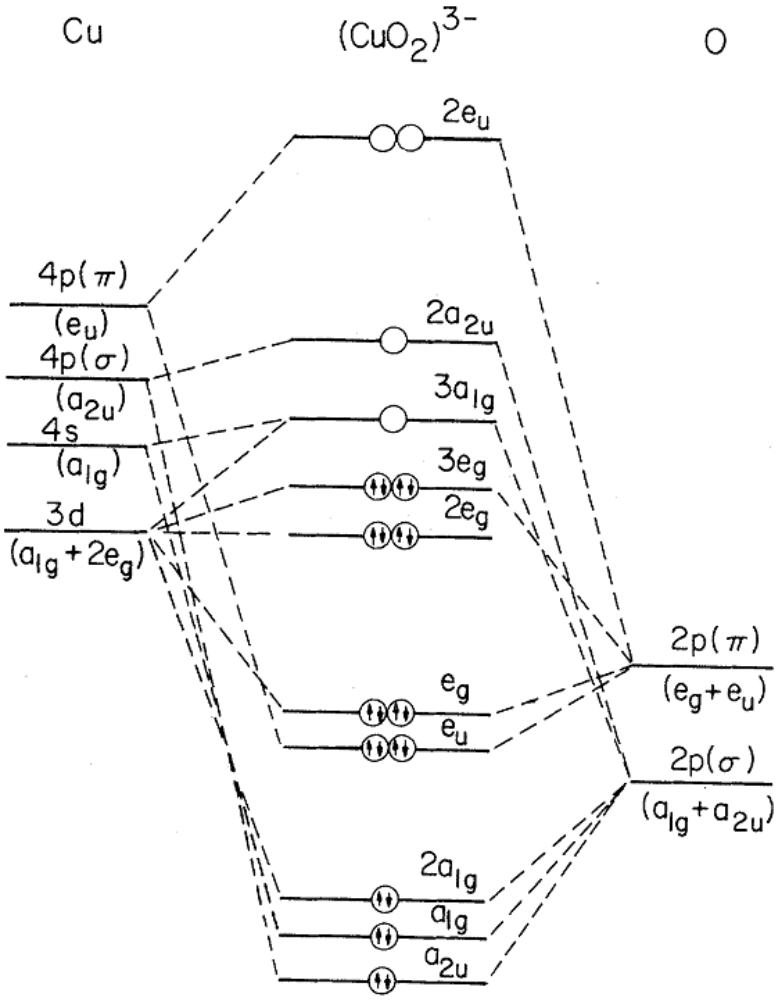


Figure 3.2. Molecular orbital diagram for Cu_2O showing Cu and O atomic orbitals and the resultant molecular orbitals and their occupations in the ground state. The symmetry of the full lattice at the Cu site in Cu_2O is D_{3d}. (adapted from ref. 30)

Figure 3.2 shows that mixing the atomic orbitals of each symmetry using a linear combination of atomic orbitals produces the provisional molecular-orbital diagram for $(CuO_2)^{3-}$. The ten electrons of Cu^+ and twelve O^{2-} "2*p*" valence electrons fill the bonding, e_g nonbonding $2e_g$, and $3e_g$ hybrid antibonding molecular orbitals, leaving the antibonding $3a_{1g}$, $2a_{2u}$, and $2e_u$ molecular orbitals unfilled [30].

The existence of weak homoatomic $d^{10}\cdots d^{10}$ interactions between linear $[O\text{-}Cu\text{-}O]^{3-}$ units was found in Cu_2O as well as $CuMO_2$ (where M = III~V element). The relevant molecular orbitals for these fragments, estimated by the extended Hückel model, are shown in figure 3.3. The property of the valence and conduction bands in this solid would be intrinsically related to the orbital ordering shown in this molecular orbital diagram.

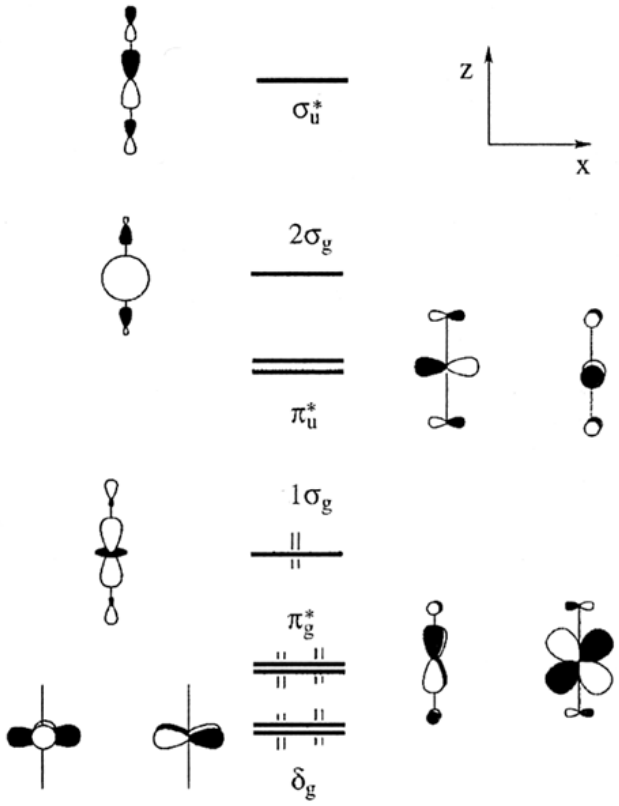


Figure 3.3. Molecular orbitals hybridisation of Cu 3*d* and O 2*p* in linear $[O\text{-}Cu\text{-}O]^{3-}$ fragment. (adapted from ref. 22)

The top of the valence band is supposed to be of Cu $3d_z^2$ character, which is due to a interaction with O *sp* hybrids. The carrier transport that can be generated by extrinsic doping will rely on the dispersion obtained from these orbitals by forming a band through interaction between adjacent copper atoms. The relative disposition of $[O\text{-}Cu\text{-}O]^{3-}$ is different in Cu_2O and $CuMO_2$, but this distinction does not affect the

dispersions of the band created from the d_z^2 orbital characters in the two compounds because the interaction is insensitive to rotation about the Cu···Cu axis [22].

3.1.3 Evolution of The Crystal Growth of Cu_2O and Aims of The Present Work

In the 1920s, work with cuprous oxide, Cu_2O, as a semiconductor first began with the creation of the Cu_2O rectifier by Grondhal [31]. Lange *et al*. reviewed Cu_2O as the base material of photosensitive devices [32]. Two related projects on Cu_2O photovoltaic cells began in the 1970s, looking at Schottky diode, metal-insulator-semiconductor (MIS) and heterojunction photovoltaic cells established on high-temperature prepared Cu_2O substrates [8]; this yielded a small amount of data on low-temperature synthesis methods such as electrodeposition, chemical oxidation, reactive sputtering and anodic oxidation which were used to grow the polycrystalline thin and thick films that were formed by these aforementioned methods.

In contrast to polycrystalline films, single crystal Cu_2O has been prepared by a melting method, a grain growth technique and the float zone technique [33-35]. Since the 1990s, higher quality epitaxial films have been grown by advanced techniques such as magnetron sputtering, pulsed laser deposition and advanced molecular beam epitaxy with a low-energy oxygen ion source [36, 37]. Although this latter approach is related to the present work, the use of an ion source gives rise to ion bombardment of the growing film, leading to the likely introduction of crystal defects.

The aim of the present work was to explore for the first time if Cu_2O could be grown with OPABE. Typical expected experimental conditions for copper oxide growth can be judged from the pressure-temperature phase diagram of Rakhashni [8] using data taken from the literature [38-40] which is illustrated in figure 3.4. Although this is thermodynamic in origin so not directly applicable to OPABE growth, which

also involves kinetics, nevertheless it does provide a useful starting point for the work. In particular it highlights there could be a problem with getting the desired copper (I) oxidation state, which is a relatively new feature in this field, since most OPABE studies have focussed on problems where formation of one phase is the expected thermodynamic outcome. OPABE uses atomic oxygen which has a much higher chemical potential than molecular oxygen under normal conditions, so the pressures shown on this plot are not applicable. The implications are if CuO is the product observed a reduction in the O flux or an increase in the growth temperature are likely to be needed to obtain the desired cuprous phase; careful control of the temperature as well as the oxygen partial pressure will probably thus be required.

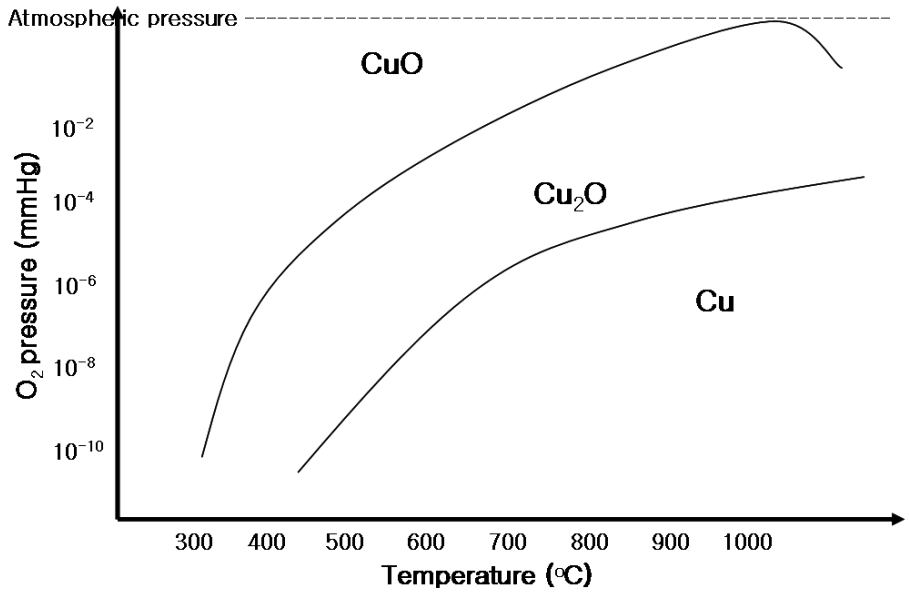


Figure 3.4. Pressure-Temperature relationship diagram of Cu-Cu_2O-CuO system. (adapted from ref. 8, 38-40)

3.2 Experimental Details

The Cu_2O thin films were grown on MgO (100) and (110)-oriented 10 x 10 mm^2 both side polished substrates in an UHV oxygen plasma-assisted atomic beam epitaxy (OPABE) system (SVT, Eden Prairie, MN) with a base pressure of 5.0 x 10^{-9} mbar as described in the previous chapter. A hot lip copper Knudsen cell at *K*-cell temperature of 1100 ^{o}C was used in conjunction with a radio frequency plasma oxygen atom source operated typically at 150~200 W RF power with an oxygen background 2.5~3.0 x 10^{-5} mbar. The nominal growth rate was 0.1~0.2 Å/sec as judged using a quartz crystal monitor (QCM, see section 2.2.5 of chapter 2) offset from the sample position. Quoted film thicknesses (F/T) are as stated from the QCM but in reality are probably up to a factor of 4 greater, as determined from measurements of actual film thicknesses of other materials in this growth system, which suggest the QCM underestimates the growth flux in the reactor. The MgO substrates were pretreated by ultra-sonication in solvents, (acetone and 2-propanol) and heating to 850^{o}C using the substrate heater in the growth chamber, respectively. After that, films were grown to a thickness of 100~1200 Å at a substrate temperature of 400~800^{o}C using OPABE.

High-resolution Al *Kα* X-ray photoemission spectra excited at *hv* =1486.6 eV were recorded in a Scienta ESCA 300 spectrometer or in-house XPS system, to record either survey scans or high resolution spectra. X-ray emission spectra were measured for ceramic cuprite on beamline 7.0.1 at the Advanced Light Source (ALS), Lawrence Berkeley National Laboratory in collaboration with the groups of Egdell (University of Oxford) and Smith (Boston University), who recorded the spectra used in this work. The beamline had an energy resolution of 500 meV at the O *K*-edge and

the emission spectrometer was set to have a resolution of 350 meV. The O *K* emission spectra were calibrated relative to Zn $L_{1,2}$ emission lines of Zn metal. X-ray diffraction (XRD) profiles of Cu_2O films were obtained from a PANalytical X'Pert PRO diffractometer using monochromatic Cu $K\alpha$ radiation. Direct optical band gaps of grown films were measured using a Shimadzu UV-2401 PC (λ=230~800 nm) spectrometer and analysed using the Tauc relationship. AFM images were recorded *ex situ* with a Digital Instruments Multimode SPM instrument with silicon nitride probes.

3.3 Results

3.3.1 XRD analysis

Initial experiments focussed on XRD analysis of thin films grown by OPABE to assess the phases formed during the growth experiments, and the textures of the deposited films.

(a) Cu_2O from continuous Cu and O adsorption on MgO (100)

XRD data for the grown films using the reactant flux conditions described above are shown in figure 3.5, from which it is immediately apparent that the structure and chemical properties of the grown layers are sensitive to growth conditions through the substrate temperature. At 400 ^oC substrate temperature for "standard" operational conditions of the oxygen plasma source: film thickness (F/T) = 330 Å, rate = 0.109 Å/sec, CuO seems to be a prominent phase, as see in figure 3.5(a). For these films, the plasma source and Cu source were switched off at the end of the growth run, and the oxygen valve closed and the samples were then allowed to cool.

As the substrate growth temperature is raised to 600 ^oC; F/T = 100 Å , rate =0.1 Å , the structure changes to a mixture of CuO and Cu_2O resulting in a complicated diffraction pattern as in figure 3.5(b) which shows various crystal reflections and orientations. This changeover in stoichiometry becomes more apparent as the growth temperature rises to 700^oC, when the peaks due to CuO disappear, although at least two crystallographic orientations, (111) and (110) are suggested by the XRD pattern in figure 3.5(c). This is clearly suggestive of no unique epitaxial relationship under these conditions.

Other experimental variables also were examined. Since the tendency to produce Cu (II) seems to exist, especially at low temperatures, film growth was attempted at lower oxygen beam pressures and plasma powers (e.g. $<1.5x10^{-5}$ mbar and <150 W radiofrequency power) and at higher temperatures. In addition because of the danger of surface oxidation, post growth annealing in vacuum was attempted compared to cooling in the ambient oxygen in the chamber. Typical results with these changed conditions are shown in figure 3.5(d); F/T = 100 Å , rate = 0.1 Å , which illustrates loss of the unwanted (111) oriented component, although both (110) as well as the expected (100) oriented crystal orientations still seem to be present. The shift from CuO to Cu_2O at increased growth temperatures is as suggested from phase stability diagrams of Rakhshani *et al*. from sputtering studies of Cu-CuO-Cu_2O phases [8], although the thermodynamic "conditions" used in the present work do not enable direct comparisons to be made with other growth approaches. A surprise of the work is that the (110) orientation of cuprous oxide is seen instead of the lattice matched (100) orientation. This probably reflects the tendency to "match" non-polar surfaces of the overlayer (the (110) of cuprous oxide) to non-polar substrate surfaces (the (100) plane of MgO) [41].

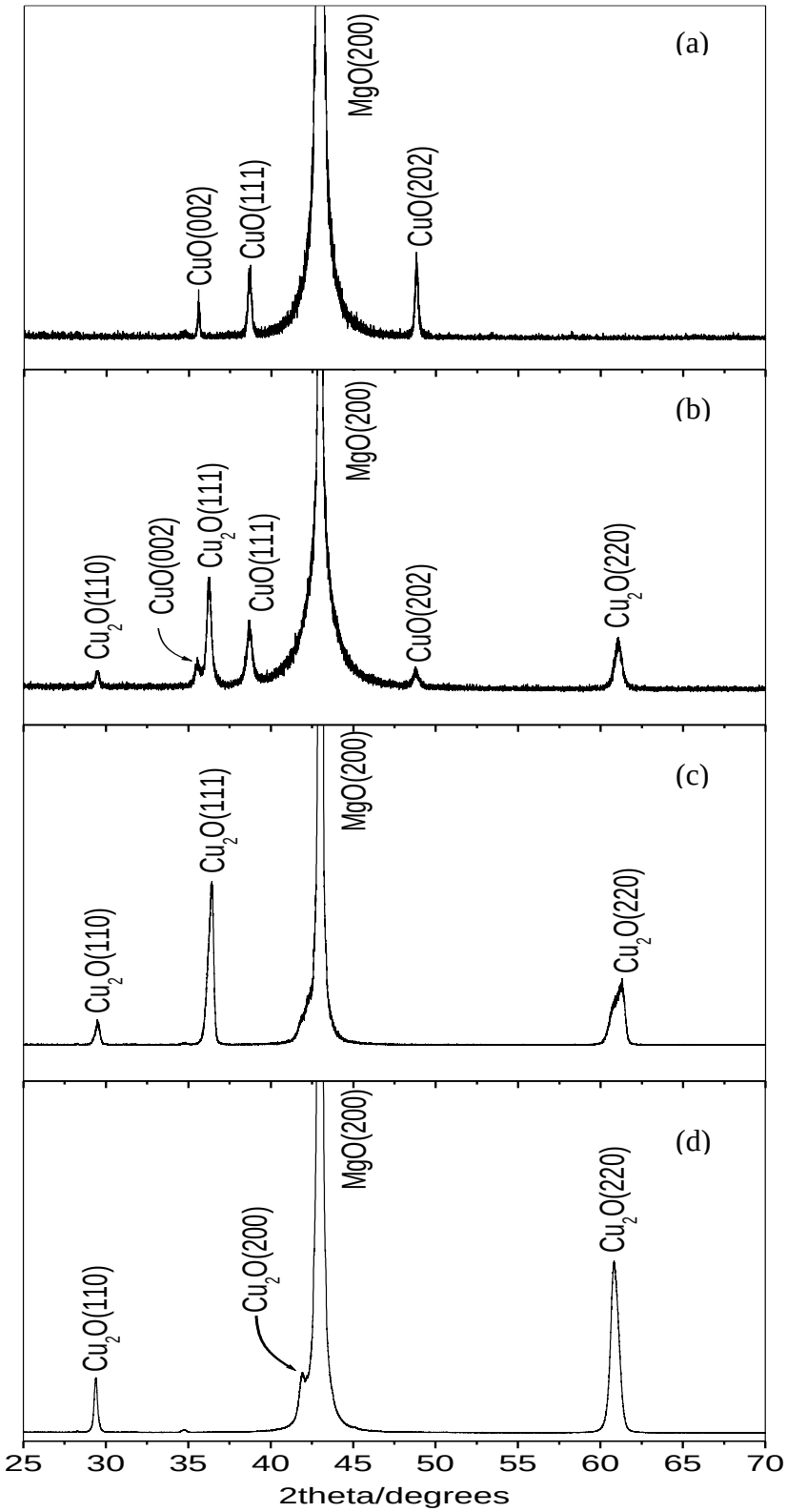


Figure 3.5. 2theta (θ) monochromatic X-ray diffraction profile of an OPABE copper oxide films on MgO (100) substrate. (a) G.T. (growth temperature) 400 ^{o}C, (b) 600 ^{o}C, (c) 700 ^{o}C, (d) 800 ^{o}C

(b) Cu_2O from Cu/CuO bilayer by the diffusion method on MgO (100)

OPABE of Cu_2O is clearly complicated because of the mixed Cu (I) and Cu (II) phases which can form, and although results could be obtained at high growth temperatures which showed only Cu (I) in XRD, XPS results often indicated the presence of Cu (II) (XPS results are discussed below). An alternative approach was therefore explored to overcome "over-oxidation" by evaporating Cu onto the surface at the end of Cu oxide growth followed by annealing, with a view to reducing any CuO formed to Cu_2O by inter-diffusion. Figure 3.6 shows the schematic interdiffusion effect model of Cu_2O from the Cu/CuO bilayer on the substrate.

It is expected the amount of Cu evaporated will be a key parameter in the success of this, since on simple chemical grounds the amount of Cu required will need to match the amount of CuO formed on the surface during the initial deposition of the copper oxide in comparison to Cu_2O.

Some results using this approach at high growth temperatures of 800 ^oC are shown in figure 3.7. This film was grown to an initial cupric oxide thickness of 100 Å over a period of 1000 sec as rate of 0.1 Å/sec, after which Cu was deposited for the same rate and same time and substrate temperature, after which the sample cooled in vacuum after annealing for 1 hr to complete the inter-diffusion at 800 ^oC. The XRD data show enhanced intensity of the (200) reflection compared to the single layer growth at this temperature, but clearly the (110) orientation is still occurring.

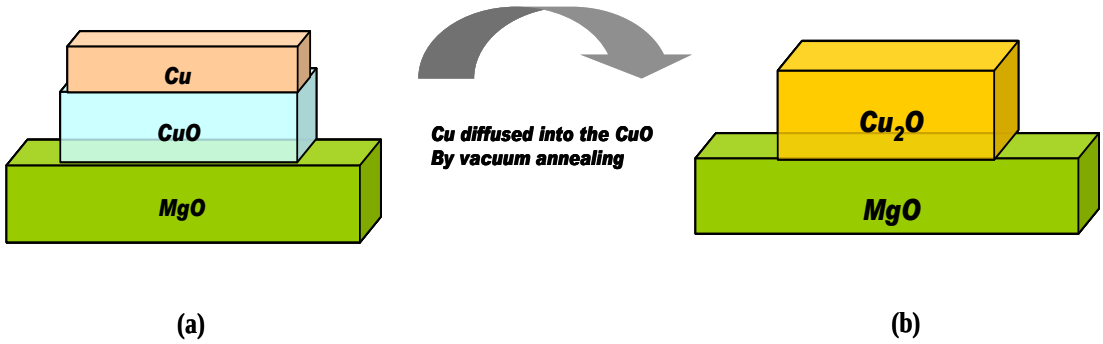


Figure 3.6. Schematic interdiffusion effect model of Cu_2O from the Cu/CuO bilayer.

(a) Cu metal/ CuO on substrate, (b) inter diffusive Cu_2O film on substrate

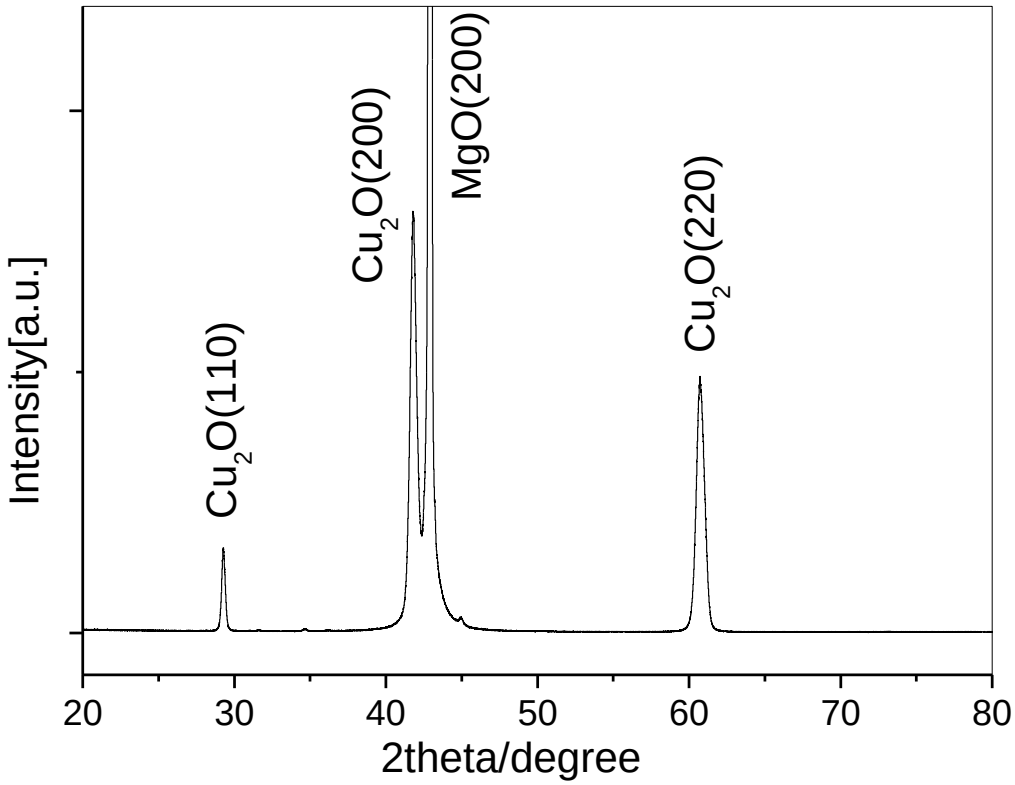


Figure 3.7. θ-2θ monochromatic X-ray diffraction profiles of an OPABE cuprous oxide film: Cu_2O (100) and (110) mixture on MgO (100) from Cu/CuO (1:1) bilayer annealing. Film was grown at 800 ^{o}C for F/T = 200 Å .

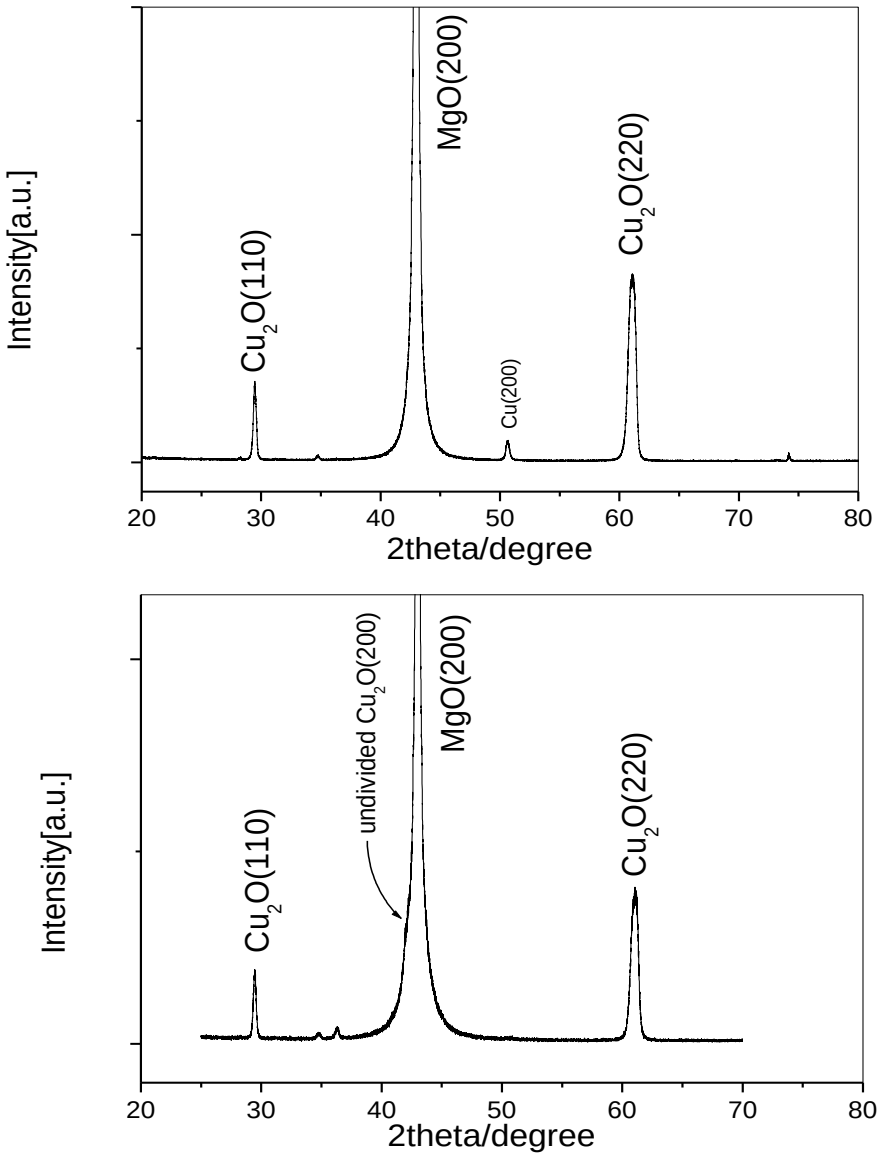


Figure 3.8. θ-2θ monochromatic X-ray diffraction profiles of an OPABE cuprous oxide film. Upper panel: Cu/CuO (1:1) bilayer with annealing, F/T 100 Å . Lower panel: Cu/CuO (1:4) bilayer through annealing, F/T 125 Å . These films were grown at 650^{o}C.

In contrast, at a lower temperature of 650 ^{o}C, the (110) reflections become dominant as seen in figure 3.8 for which conditions are similar to those described above except the oxide growth and Cu deposition utilised a deposition temperature of 650 ^{o}C. It can be seen in the upper panel that a weak Cu (200) reflection is visible in the XRD

data. This suggests too much Cu was deposited on the surface. The experiment was therefore repeated but by reducing the amount of Cu deposited so that the Cu deposition phase was reduced. Experiments were repeated so that the Cu deposition phase varied from 1:1 to 1:8 Cu deposition time: oxide deposition time.

Results for 1:2 were rather similar to those seen from 1:1 reported above. For the 1:4 experiment shown in the lower panel of figure 3.8, the Cu reflection is now absent from the XRD pattern suggesting a better film stoichiometry had been reached. Experiments were also repeated at ratios of 1:6 and 1:8 using the growth temperature of 650^{o}C. For both of these conditions data as shown in figure 3.9 were observed. The film now appears to consist of a (100)-textured layer. Calculated lattice parameters from figure 3.9 yield a lattice mismatch of 1.53 % which is in good agreement with published values of 1.33 % for the bulk crystal structures.

Overall, it thus appears that several differing orientations and stoichiometries are possible for the growing layer in these experiments. By subtle variations in growth conditions the initially desired (100) layer can be obtained.

(c) Cu_2O from Cu/CuO bilayer by the diffusion method on MgO(110)

In view of the observation of (110) orientations in the results described above, growth studies were also tried on MgO (110) substrate. All growth runs used the bilayer method described using a 1:6 Cu deposition time as described above, and a post-annealing step of 800 ^{o}C for 1 hr, again as described above. Typical growth data at 650 ^{o}C using normal oxygen plasma (pO_2 = 2.4 x 10^{-5} mbar with 200 W) for a F/T = 225 Å : are shown in figure 3.10(a). Clearly a variety of crystallite orientations are observed, spanning (100), (110) and (111).

The results described in the previous section suggested that the film stoichiometry played a crucial role in obtaining good epitaxial orientation, although the method is seemingly less successful on the (110) plane. It proved difficult in all these experiments to run the oxygen source under low flux, low power conditions because of plasma instability. In an effort to reduce the oxygen flux, nitrous oxide was used instead of oxygen (2.1×10^{-5} mbar, 200 W) otherwise the growth conditions were as described above. XPS analysis showed the absence of N from the layer. Nonetheless the use of N_2O seems to have a desirable effect in terms of obtaining the desired (110) film texture. Some similarities exist with the work of Yin *et al*. who demonstrated the role of argon (Ar) addition to the oxygen supply for magnetron sputtered Cu_2O. They find that a ratio of 1:16 yields provide the desired oxidation state of Cu [42, 43].

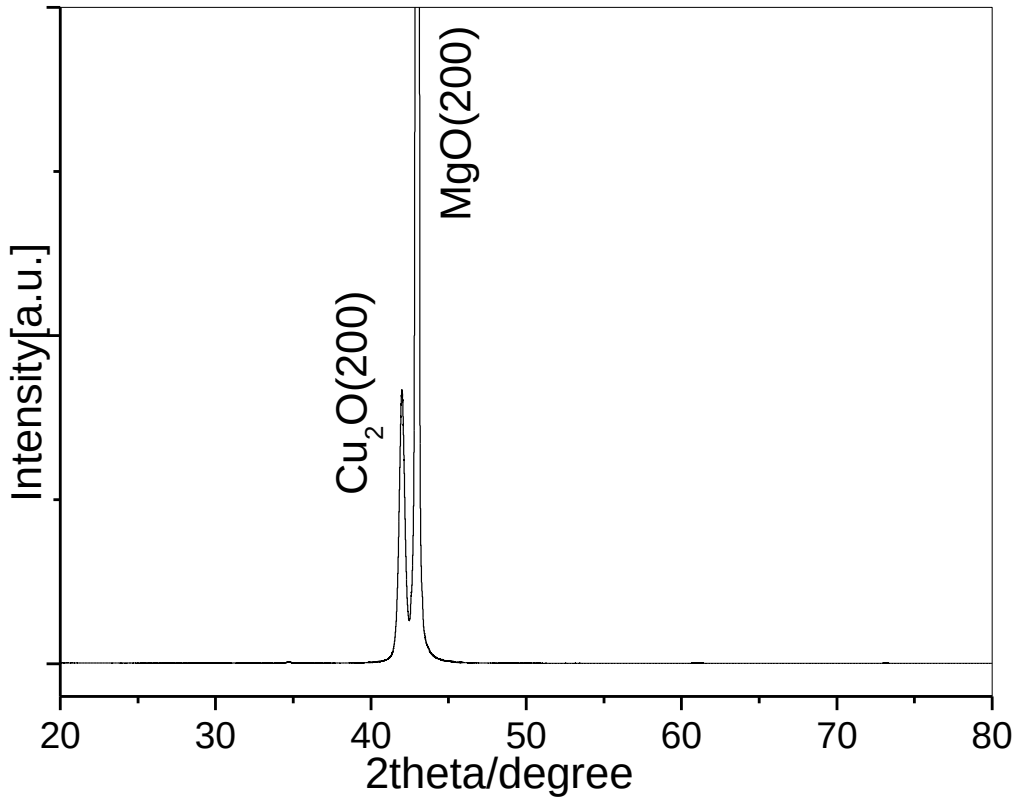


Figure 3.9. θ-2θ monochromatic X-ray diffraction profiles of an OPABE cuprous oxide film: Cu_2O (100) (F/T = 225 Å) on MgO (100) from Cu/CuO bilayer annealing at 800 ^oC/hr.

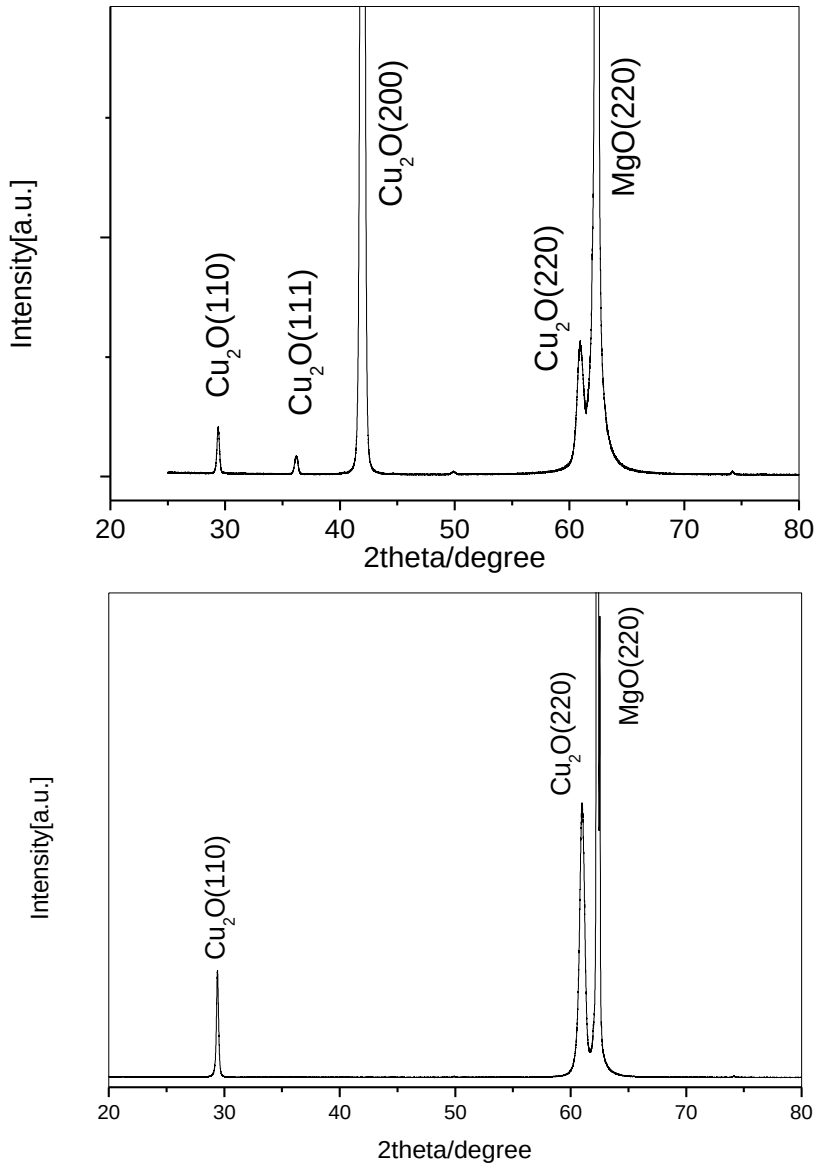


Figure 3.10. θ-2θ monochromatic X-ray diffraction profiles of an OPABE cuprous oxide films. (upper) polycrystalline Cu_2O (F/T = 225 Å) on MgO (110), (lower) single crystalline Cu_2O (110) (F/T = 225 Å) on MgO (110) under plasma by pure N_2O gas in growth chamber. These films were obtained from Cu/CuO (1:6) bilayer diffusion at 800 ^oC/hr.

3.3.2 Survey XPS Scan of OPABE Films

Although XRD provides a good indication of crystalline structure and phase, it is unlikely to be sensitive to the exact stoichiometry of the grown layer. XPS experiments were therefore carried out *ex situ* to gain further insights into film stoichiometry, although it should be born in mind it has its own limitations since it is highly surface sensitive so only reflects the surface condition of the sample.

A survey XPS spectrum of thin films grown using the experimental approach noted above is shown in figure 3.11. The spectrum is from a sample using the "single layer" oxide growth approach at 800 ^{o}C substrate temperature for "normal" operational conditions of the oxygen plasma source (pO_2 = 2.1 x 10^{-5} mbar, 200 W) resulting in a F/T = 400 Å and growth rate = 0.10 Å/sec, followed by vacuum annealing at 800^{o}C/1hour for which the XRD was suggestive of a polycrystalline cuprous oxide phase. The survey spectrum shows the expected transitions for a thin film based on copper oxide(s), as well as lines due to the MgO substrate from the edge of the sample. A carbon peak can be seen in the survey scan and figure 3.12(a). This seemed to be due to air contamination after the films were withdrawn from the OPABE system since it could be readily removed by sample heating, which would not be expected if the carbon was incorporated in the layer. Also simple XPS spectra could be recorded *in situ* by annealing at temperatures up to 350 ^{o}C in the UHV spectrometer which showed the absence of C. The XPS data are therefore consistent with the growth of a pure phase containing Cu and O as the matrix elements. Shown in figure 3.12(b) is the O 1*s* line for the Cu_2O phase which showed 2 peaks. This could be due again to some surface contamination, for example due to adsorbed water

vapour [12], but overall the simple XPS spectra enabled it to be concluded that some form of copper oxide could be grown using OPABE.

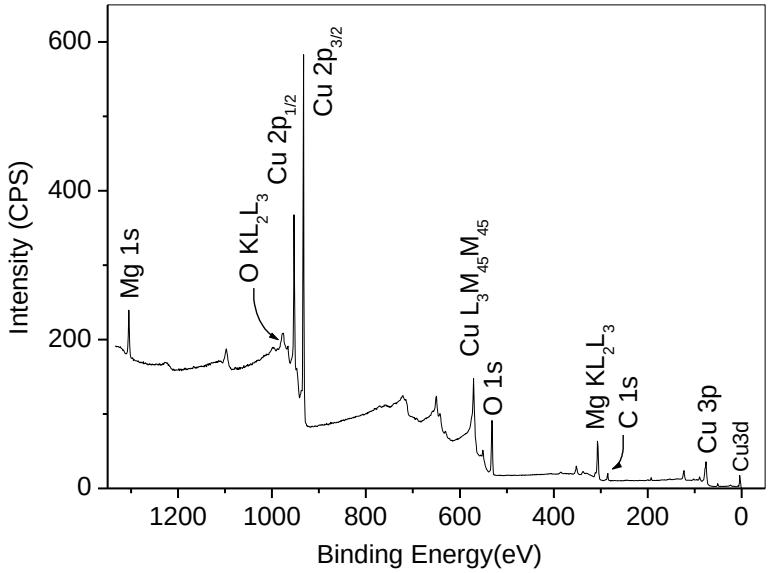


Figure 3.11. XPS survey scan of single crystalline Cu_2O (110) thin film on MgO (100) substrate by UHV-OPABE (see text 3.3.2).

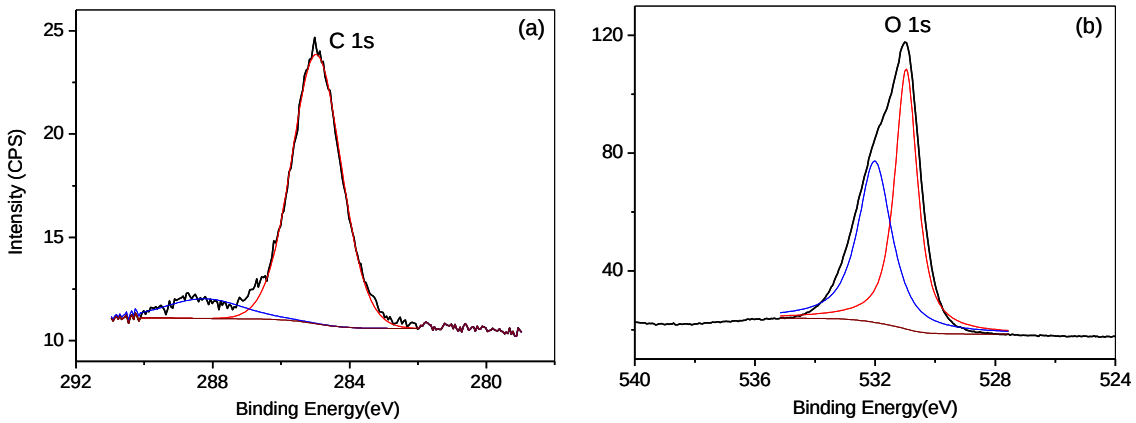


Figure 3.12. XPS spectra of (a) C 1*s* and (b) O 1*s* core line for an as-presented crystalline Cu_2O thin film by UHV-OPABE.

3.3.3 High Resolution XPS Analysis of Grown Films

A key issue in OPABE growth of Cu_2O as mentioned above is achieving the correct oxidation state since both monovalent and divalent oxidation states are clearly achievable using this approach. Cu 2*p* core level photoemission spectra were thus recorded to look at this in detail for differing growth conditions since such spectra are very diagnostic in determining oxidation state although it should be born in mind that XPS is a surface technique so primarily probes the outermost layers. The previous reported values of the binding energy are listed in table 3.1 [12] for the differing copper oxides which shows small differences between the two forms suggesting binding energy measurement could be useful. However the chemical form can be more reliably diagnosed since pronounce shake-up satellites at around 9 eV higher binding energy (BE) than the parent 2*p* line are seen [44] for Cu_2O but not CuO. Data for the O 1*s* line also shown in the table suggests this signal is not useful to diagnose oxidation state, especially as adsorbed water or hydroxide can contribute to the measured signal [44].

Table 3.1 Reference values of the XPS binding energies (BE) and full-width at half maximum (Γ) of copper oxides in the Cu $2p_{3/2}$ and O 1*s* core orbital regions. (adapted from ref. 12)

Peak	Type	Material	BE (eV)	Ref.	Γ (eV)	Ref.
Cu $2p_{3/2}$	Film	Cu_2O	932.4-933.7	45-47	-	-
		CuO	933.6-934.8	45-48	-	-
	Bulk	Cu_2O	932.4-933.3	44, 47, 49	1.9	47
		CuO	933.6-933.8	44, 47, 49	3.4	47
O 1*s*	Film	Cu_2O	530.4	50	-	-
		CuO	529.8-530.8	48	-	-
	Bulk	Cu_2O	530.4	49	1.2	49
		CuO	529.6-530.0	45, 49	1.3	49

Cu 2*p* spectra of the grown films are shown in figure 3.13 and binding energies are noted in table 3.2, recorded using the in-house XPS system. The binding energies were referenced to the small residual C 1*s* peak, which was assigned to a binding energy of 285.0 eV. The value of copper oxide binding energies in table 3.2 are slightly increased compared with the reference BE in table 3.1. Possibly this is because of some differential charging between the film and the C 1*s* reference, which clearly makes spectral assignment difficult. However the prominent shake-up satellites seen in figure 3.13 (b) clearly show the presence of Cu (II) under the corresponding growth conditions: G.T. = 400 ^{o}C, F/T = 330 Å , rate = 0.109 Å /sec, pO_2 = 2.1 x 10^{-5} mbar, 200 W). The spectrum also is different to that seen in figure 3.13(a) under the growth conditions: G.T. = 800 ^{o}C, F/T = 300 Å , rate = 0.100 Å /sec, pO_2 = 2.1 x 10^{-5} mbar, 200 W) where the shake-up fine structure is much weaker, indicating a reduced concentration of Cu (II) species. Overall it can be concluded that CuO seems to be formed in high concentration when films at a substrate temperature around 400 ^{o}C are used, and with the Cu (II) concentration being much lower (although still significant) in the film formed when growth is carried out at much higher substrate temperatures of over 600 ^{o}C. This is again in line with the XRD results.

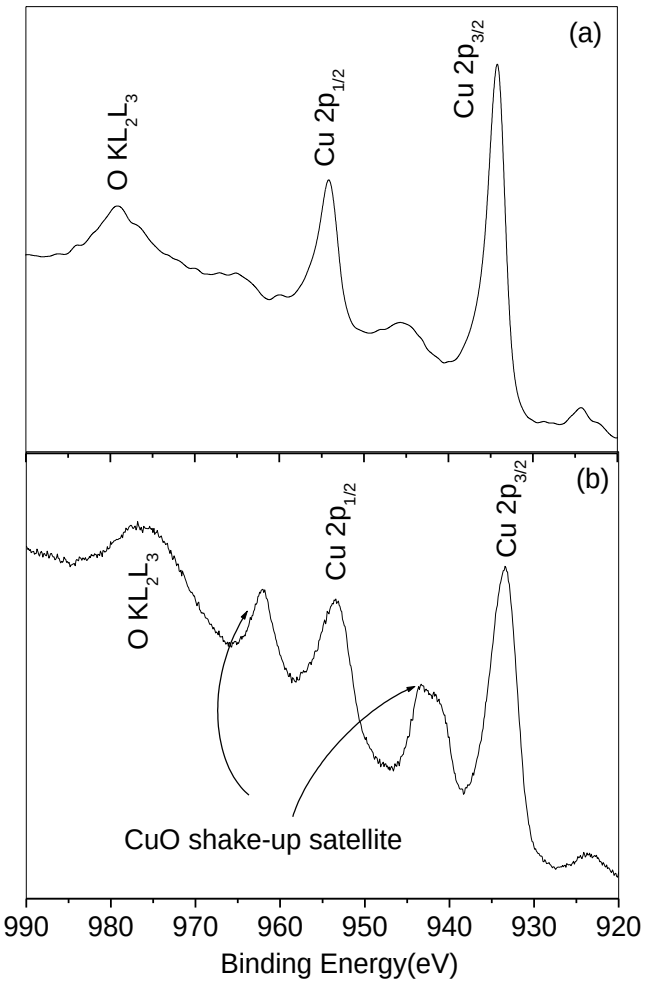


Figure 3.13. XPS (Al *K*α, *hv*=1486.6 eV) spectra of (a) Cu 2*p* region of Cu_2O growth film: G.T. = 800 ^oC, F/T = 300 Å , pO_2 = 2.1 x 10^{-5} mbar, 200 W), (b) Cu 2*p* region of CuO growth film: G.T. = 400 ^oC, F/T = 330 Å , pO_2 = 2.1 x 10^{-5} mbar, 200 W)

Table 3.2 Experimental data of the XPS binding energies (BE) and full-width at half maximum (Γ) of copper oxides in the Cu $2p_{3/2}$ and O 1*s* core orbital regions. The in-house XPS used for the measurements.

Peak	Type	Material	BE (eV)	Γ (eV)
Cu$2p_{3/2}$	OPABE Film	Cu_2O CuO	934.2 933.1	1.6 3.5
O 1*s*	OPABE Film	Cu_2O CuO	531.5 531.4	2.4 4.1

To examine if the XPS spectrum for the films grown at higher temperature is consistent with a pure cuprous oxide phase, better quality XPS spectra for a high deposition temperature film were recorded on the high quality Scienta ESCA300 instrument. Figure 3.14 shows the Cu core level photoelectron spectra of such a film (G.T. = 700 ^{o}C, F/T = 100 Å , rate = 0.098 Å /sec, $pO_2 = 2.1 \times 10^{-5}$ mbar, 200 W). An electron flood gun (8 eV) is used to minimise charging. The values of Cu $2p_{3/2}$ and O 1*s* BEs(see figure 3.11(b)) are 932.9 eV (*FWHM* = 1.24 eV) and 531.0 eV (*FWHM* = 1.92 eV), respectively, which is slightly on the low side from the tabulated data above but more consistent with cuprous rather than cupric oxide forms.

The spectral components were mathematically fitted using a Gaussian/Lorentzian mixed function after Shirley background correction [51] to better define the weak features which are observed in the spectrum.

Apart from the simple spin-orbit doublet expected for a *p*–orbital core ionisation which dominate the spectra, it can be seen that weak features labelled M2 , s1* and s1 appear in the spectrum so it is important to understand if these peaks come from Cu (I) or Cu (II) species.

The $2p_{3/2}$ component which labeled M1 in figure 3.14, corresponds to a Cu $3d^{10}$ electron configuration in the final state coming from Cu (I) [52]. A weak and somewhat broader peak M2 also coincides with Cu $3d^{10}$ terminal state, however this is reported to be associated with the Cu (II) occurring from introduction of holes into the Cu 3*d* bands. The final state of the $3d^{10}$ configuration originates from the Cu (II) $3d^9$ initial state by core hole screening by transfer of an electron into the 3*d* orbital of the ionised atom [18, 53-55]. In particular, the M2 peak is not associated with simple Cu (II) oxidation products.

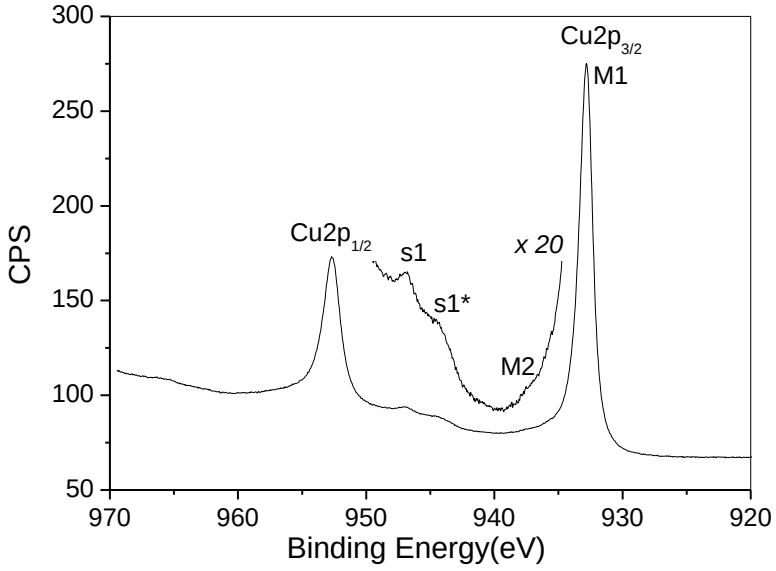


Figure 3.14. XPS (Al *K*α, hv=1486.6 eV) spectra in the Cu 2*p* region of OPABE Cu_2O (110) film on MgO (100) measured by ESCA300 in Daresbury Laboratory, UK. BE regions (934~951 eV) are 20 times magnified its added spectrum.

Satellites labeled s1 and $s1^*$ also appear in the illustrated spectrum in figure 3.14. These two satellites have binding energies of 946.9 and 944.6 eV. Again these are known to be associated with Cu_2O and come from $3d^9$ final states. These energies are equivalent to those of weak satellites in Cu (I) oxide arising from excitation of a

Cu 3*d* electron into the conduction band to provide a $2p^5 3d^9 \underline{L}^0$ $(4s, 4p)^1$ final state [52, 56]. Importantly there seems to be no satellites at lower binding energy, which are expected for $3d^9$ states derived from Cu (II).

Overall it can therefore be concluded that the high resolution XPS spectra are consistent with the growth of pure cuprous oxide for the high growth temperatures. Spectra were also recorded for some of the bilayer systems. The spectra recorded were very similar to those described above for the single layer growth.

3.3.4 Valence Band Spectra

The density of states expected from Cu_2O band structure calculations is shown in figure 3.15. The calculations are based on the B3LYP formalism in which the exchange energy, in this case from Becke's exchange functional, is connected with the exact energy from Hartree-Fock theory [57-59]. By comparing the total and partial densities of states, it can be seen that the lower binding energy area of the valence band is of dominant Cu 3*d* atomic character and the higher binding energy part is related to dominant of O 2*p* character. The structure in the Cu 3*d* part of the valence band comprises sharp peaks labeled *a*, *a′* and *a″* together with a weaker peak *b* in figure 3.15. The O 2*p* states are themselves separated into two components *x* and *y* at the higher binding energy region. However there also is significant covalent mixing of Cu 3*d* atomic character into both *x* and *y* of the O 2*p* states and in peak b, there also is covalent mixing of O 2*p* atomic character in the Cu 3*d* states.

Valence band X-ray photoemission spectra ($h\nu$ = 1486.6 eV) of synthesized ceramic Cu_2O are shown in figure 3.16 (upper panel) along with O *K* shell X-ray emission

spectra (lower panel) excited in the nonresonant condition ($h\nu$ = 565.7 eV) above the core threshold. The O *K* edge X-ray emission spectrum is a measure of the O 2*p* atomic states and it can be seen to be in relatively good agreement with the calculations, with a weak peak (or more accurately unresolved peaks) at low binding energy and strong emission at high binding energy, representing the involvement of the O 2*p* orbitals in the valence band. The valence band XPS spectrum matches up well to the calculations also with 4 resolved peaks being observed. The fact that bands I and II emerge at all in O *K* shell X-ray emission spectra is an immediate result of hybridisation between Cu 3*d* and O 2*p* states which presents O 2*p* atomic character into states of nominal Cu 3*d* origin. No mixing between O 2*p* states is possible for the Cu 3*d* orbitals of δ symmetry, while the mixing for the π states is weaker than for σ states [56]. The intensity differences between the XPS spectra and the X-ray emission spectra correspond to the fact that the Cu 3*d* states in band I are σ-like whereas, δ and π Cu 3*d* states fully contribute to band II.

The XPS data of OPABE Cu_2O (110) growth film on MgO (100) substrate (G.T. = 650 ^oC, F/T = 100 Å , rate = 0.098 Å /sec, pO_2 = 2.1 x 10^{-5} mbar, 200 W) are shown in figure 3.17. Four features labeled I-IV may again be identified in XPS data of the OPABE Cu_2O epitaxial film. The data are consistent with the formation of good quality Cu_2O in view of the agreement between the differing sets of experimental data and the calculations.

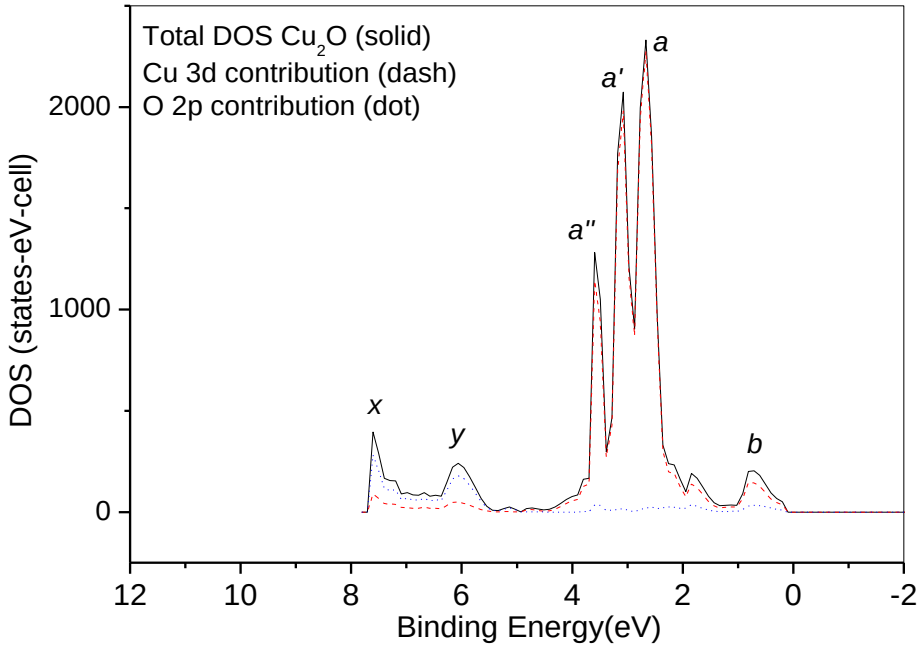


Figure 3.15. Theoretical cross section weighted density of states including Cu 3*d* and O 2*p* partial density of states (PDOS) for Cu_2O (B3LYP).

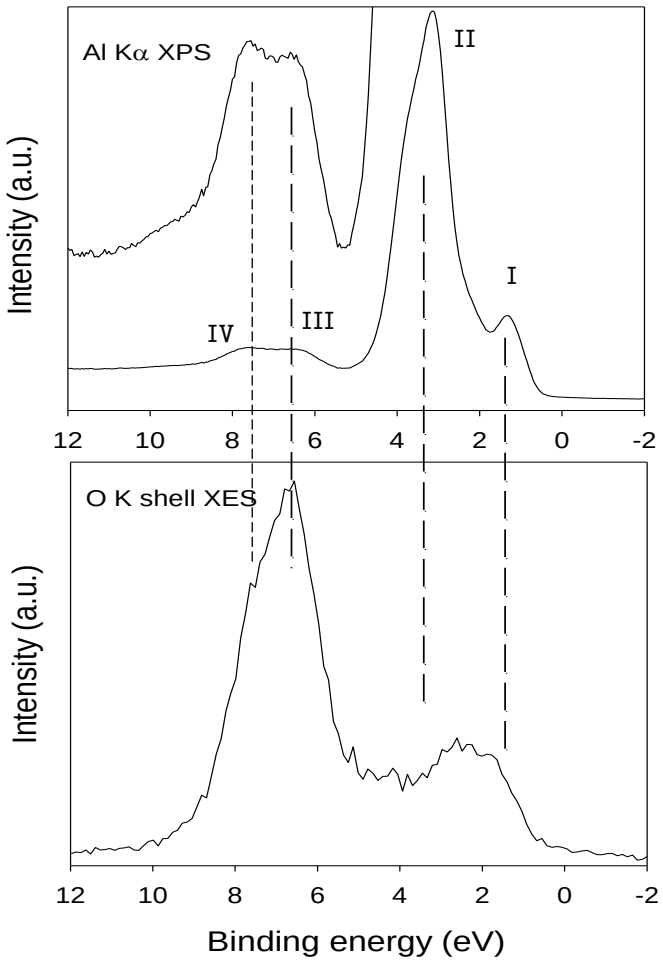


Figure 3.16. Comparison between Al *K*α XPS of ceramic Cu_2O (which measures the Cu 3*d* PDOS) and O *K* shell XES (which measures the O 2*p* PDOS). (ref. 7)

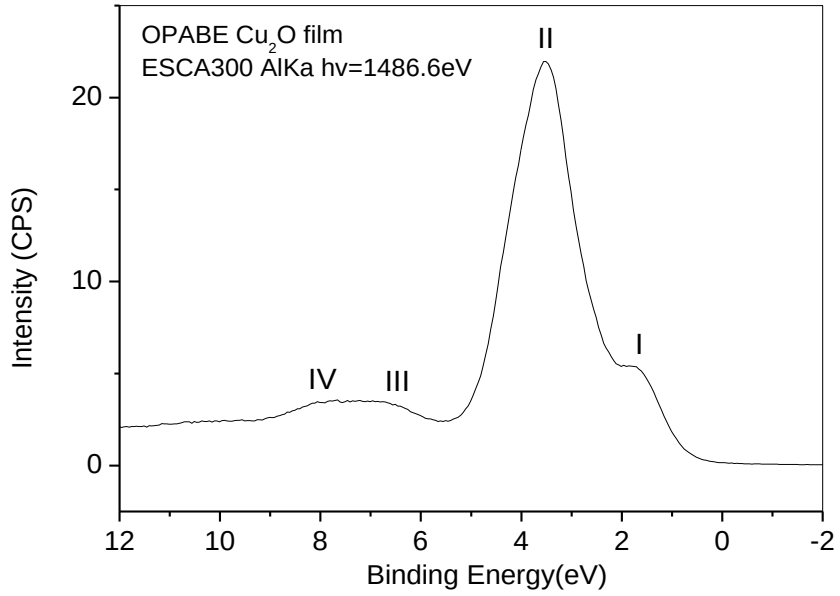


Figure 3.17. Al *Kα*, *hν*=1486.6eV excited valence band XPS (ESCA300) of OPABE Cu_2O film.

3.3.5 Optical Band Gap

Optical absorption measurements of the band gap energy of the grown thin films were made using UV-Visible spectroscopy. In order to directly measure the optical band gap, the Tauc relationship, $\alpha h\nu = A(h\nu - E_g)^{1/2}$ [60, 61] was employed. *hν* is the photon energy, E_g is the band gap, A is a constant and α is the absorbance. Reference values of Cu_2O show an optical band gap range, from 2.1 to 2.6 eV, whilst CuO has a reported band gap in the range 1.3 to 2.1 eV [13-15]. Optical data in the case of films grown at 400^{o}C using the single layer approach on MgO (100), are as shown in figure 3.18(top). The suggested band gap is about 2.0 eV, below that expected for cuprous oxide. At the higher growth temperatures of 600 ^{o}C and 800 ^{o}C, a band gap around 2.4 eV is suggested, as seen in figure 3.18(mid) and figure 3.18(bottom). These data

are again broadly consistent with the work discussed above representing the increased tendency to form cuprous oxide as the growth temperature rises.

Figure 3.19 shows the optical band gap energy of high temperature films on MgO (100) and (110) substrates, respectively, grown by the process of Cu/CuO bilayer diffusion which corresponds to the Cu_2O films. The optical band gap on MgO (100) as shown in figure 3.19(upper), reaches 2.2 eV by linear extrapolation. The optical band gap energy of the Cu_2O film on MgO (110) also was obtained to 2.1 eV by linear extrapolation, as seen in figure 3.19(lower).

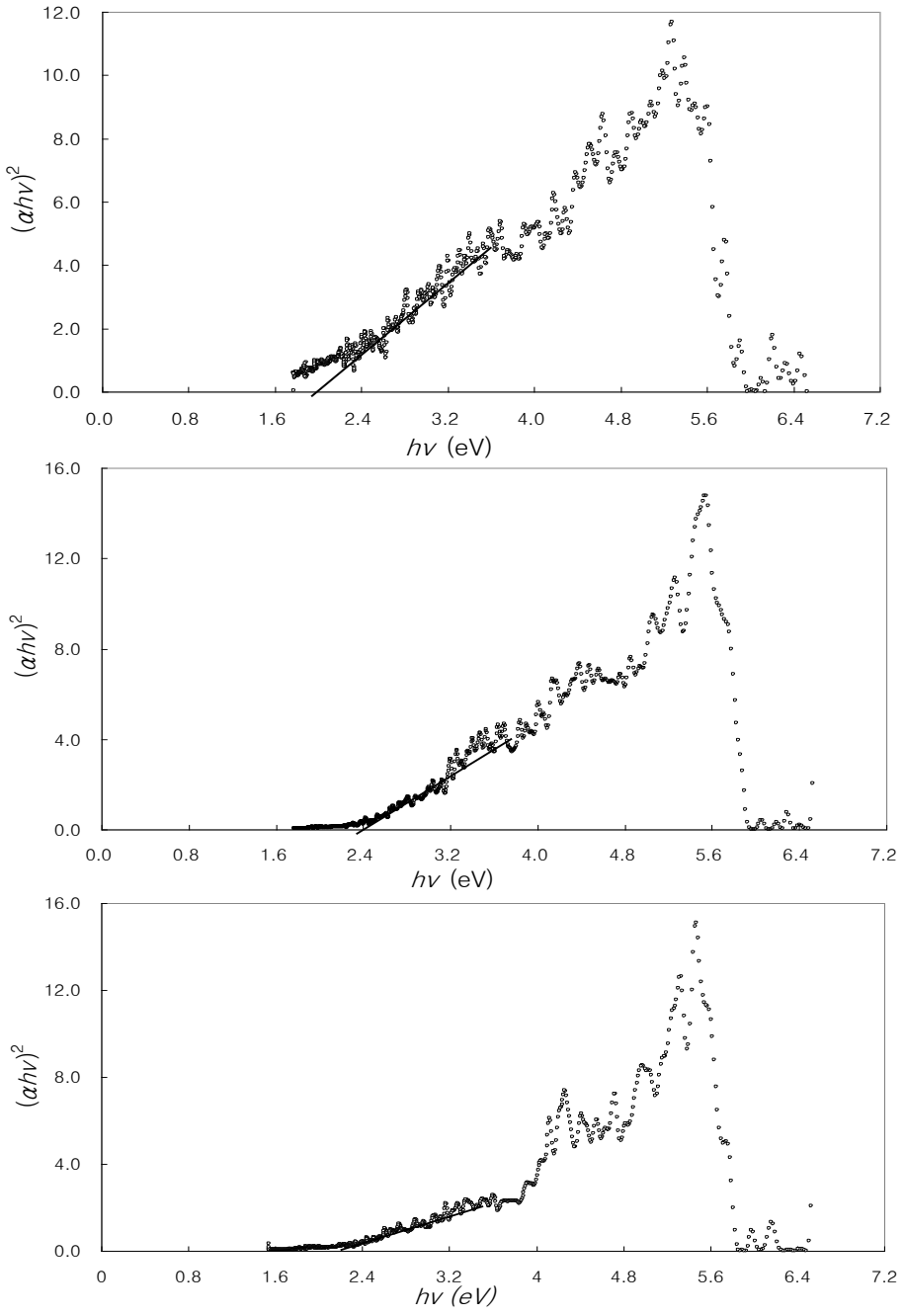


Figure 3.18. Direct optical bandgap energy evaluation by the hv vs. $(\alpha hv)^2$ approximation. (top) CuO film (hv = 1. 9 eV), G.T. 400 ^oC (mid) mixture of CuO and Cu_2O film (hv = 2.4 eV), G.T. 600 ^oC (bottom) Cu_2O film hv = 2.3 eV, G.T. 800^oC, using an MgO (100) substrate.

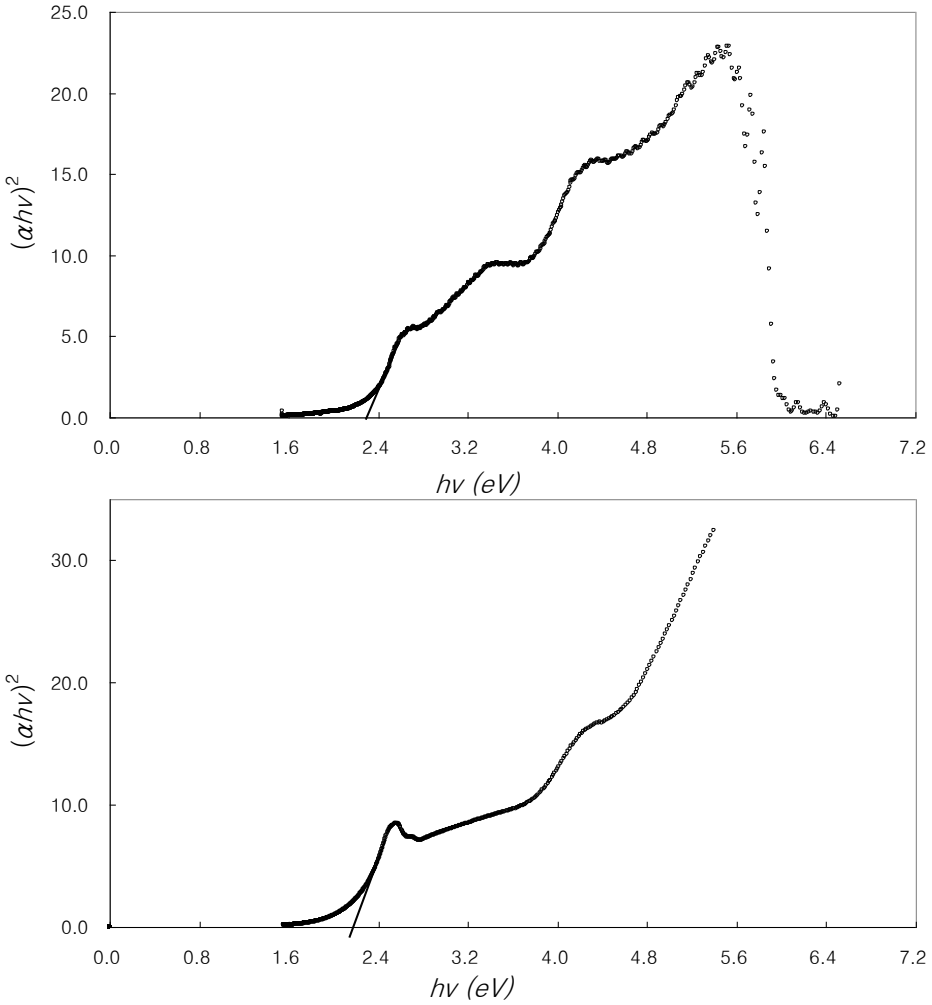


Figure 3.19. Direct optical band gap energy evaluation by the hv vs. $(\alpha hv)^2$ approximation. (upper) Cu_2O on MgO (100) hv = 2.2 eV, (lower) Cu_2O on MgO (110) hv = 2.1 eV. These Cu_2O films were obtained from the Cu/CuO bilayer layer system (G.T. 650 ^oC) with post vacuum annealing at 800 ^oC/hr.

3.3.6 Investigation of Surface Morphology by AFM

Figure 3.20 shows the surface morphology of the MgO(100) substrate (a) and some of the grown monolayers with differing growth temperature of 400 ^oC, 600 ^oC and 800 ^oC in (b), (c) and (d), respectively. Figure 3.20(e) shows the image of post-annealed samples grown at a substrate temperature of 800 ^oC. The films were grown to a similar thickness of 100~200 Å as judged by QCM using the single growth layer approach, although as noted previously actual film thicknesses are up to 4 times bigger. The size of grains on (e) appear bigger than film (d), however surface roughness (root mean square, RMS) is not very different between films (d) and (e). Overall, the layers are all relatively rough, of a similar magnitude to the actual film thickness suggesting that the growth mechanism involves 3D nucleation and island growth, rather than the smooth layer-by-layer growth seen often in conventional MBE studies, with the island size increasing at higher temperatures.

In addition, figure 3.21 shows the corresponding image using the bilayer growth approach at a substrate temperature of 800 ^oC for 1:1 copper : oxide growth. Images are shown at differing resolutions. The RMS roughness is equal to 24.5 ±0.5 nm on 5 x 5 μm^2 which should be compared to the single layer approach (see figure 3.20 (d) and (e)).

The morphology of the roughness formed in the two cases seems to be different. Whereas the single layer approach indicates a fairly uniform roughness across the surface, the bilayer approach seems to produce films with fairly smooth regions mixed into areas showing increased roughness.

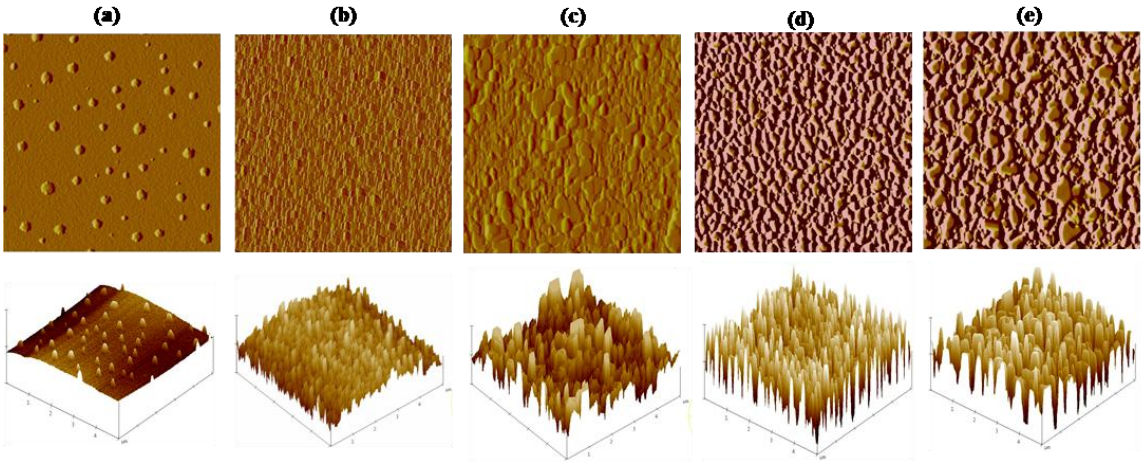


Figure 3.20. AFM images (normalised thickness 100~200 Å). (a) MgO (100), RMS 3.3 ±0.5 nm (b) CuO, G.T. 400 ^{o}C, RMS 19.9 ±0.5 nm (c) CuO and Cu_2O mixture, G.T. 600 ^{o}C, RMS 17.3 ±0.5 nm (d) Cu_2O, G.T. 800 ^{o}C, RMS 20.4 ±0.5 nm (e) Cu_2O, G.T. 800 ^{o}C and vacuum annealed at 800 ^{o}C/1hr, RMS 19.0 ±0.5 nm. AFM images were evaluated on 50 nm Z-scale and 5 x 5 μm^2 viewing area.

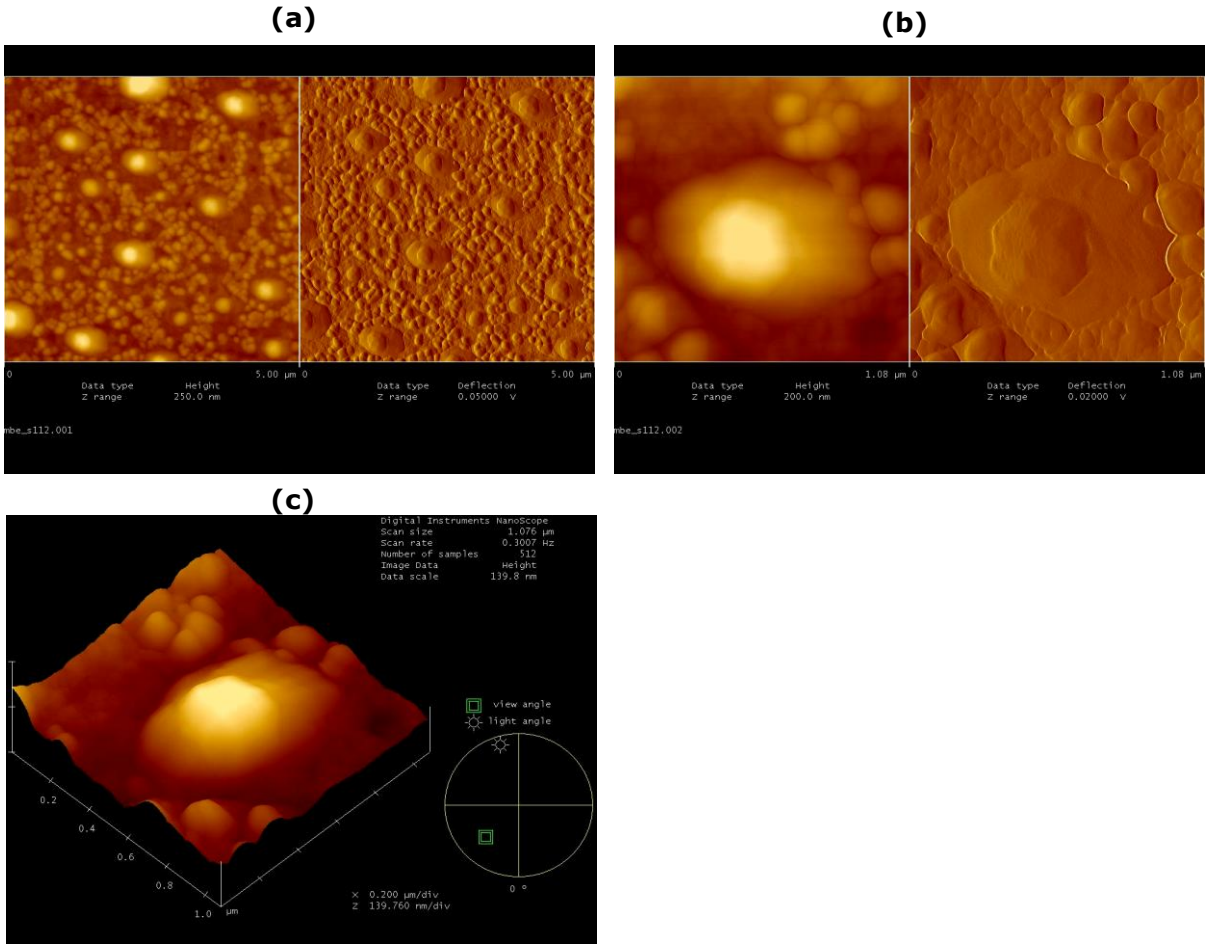


Figure 3.21. AFM images (normalised thickness 200 Å) of OPABE grown Cu_2O on MgO (100) using the bilayer approach: (a) Scan size of 5x5 μm^2, Z-range 250 nm, in the height and deflection detection modes, RMS = 24.5 ±0.5 nm (b) Scan size of 1.08x 1.08 μm^2, Z-range 200 nm, (c) 3D image of crystal, scan size of 1.078 x 1.078 μm^2, Z-range of 139.8 nm

3.4 Summary

The first studies of the growth of Cu_2O by OPABE have been carried out. This system poses new problems in OPABE, where the normal approach is to choose an excess oxygen atom flux to minimise oxygen vacancies in the grown structure in systems where there is little chemical ambiguity in the oxidation state of the incorporated metal atoms. For the Cu system, there is the problem of forming the CuO phase in competition with Cu_2O.

This problem is indeed realised in practice since the first phases formed in growth experiments which were carried out at comparatively low temperatures seemed predominantly CuO when studied by XRD or XPS. Attempts to tune in to the desired oxidation state by controlling the oxygen atom flux were relatively unsuccessful since the oxygen atom source only operates stably over a narrow range of conditions. However in line with thermodynamic predictions the choice of high growth temperatures favoured the formation of Cu_2O.

Film texture for the high growth temperatures using this conventional approach showed that the (110) orientation seemed to dominate the diffraction profile, over the expected epitaxially matched (100) crystal orientation. This could result from two factors. The (100) surface of MgO is non-polar so it might be reasonably expected that matching to a non-polar surface of Cu_2O might be favoured [41]. In addition, calculations on the surface energies of Cu_2O show the (100) orientation to be less stable than the (110) orientation, again favouring the latter [62]. That it is not the dominant factor however is suggested by the growth experiments on MgO (110)

which also failed in general to produce the epitaxially matched (110) surface orientation.

Since the tendency to form Cu (II) exists in this system, an alternative approach was realised involving the growth and interdiffusion of copper:oxide bilayers. The best (100) textured films were grown using this techniques at lower growth temperatures than for the single layer approach. In contrast on the (110) MgO surface, unique epitaxial orientation could still not be obtained using such conditions, although experiments using N_2O instead as the oxygen source did improve this situation.

XPS spectra as well as optical absorption studies were consistent with the formation of cuprous oxide under optimised conditions. Valence band spectra of the grown films were also consistent with corresponding spectra measured for ceramic samples and are consistent with calculations and X-ray emission spectra which indicate substantial hybridisation at the top of the valence band between Cu 3*d* and O 2*p* orbitals.

AFM measurements showed the films were relatively rough, consistent with the coalescence of 3D islands.

References

1. B. J. Ingram, G. B. Gonzalez, D. R. Kammler, M. I. Bertoni and T. O. Mason, Journal of Electroceramics **13** (1-3), 167-175 (2004).

2. A. N. Banerjee and K. K. Chattopadhyay, Progress in Crystal Growth and Characterization of Materials **50** (1-3), 52-105 (2005).

3. S. Sheng, G. J. Fang, C. Li, S. Xu and X. Z. Zhao, Physica Status Solidi a-Applications and Materials Science **203** (8), 1891-1900 (2006).

4. M. Nolan, Thin Solid Films **516** (22), 8130-8135 (2008).

5. E. M. Alkoy and P. J. Kelly, Vacuum **79** (3-4), 221-230 (2005).

6. V. Figueiredo, E. Elangovan, G. Goncalves, P. Barquinha, L. Pereira, N. Franco, E. Alves, R. Martins and E. Fortunato, Applied Surface Science **254** (13), 3949-3954 (2008).

7. J. P. Hu, D. J. Payne, R. G. Egdell, P. A. Glans, T. Learmonth, K. E. Smith, J. Guo and N. M. Harrison, Physical Review B **77** (15), 155115 (2008).

8. A. E. Rakhshani, Solid-State Electronics **29** (1), 7-17 (1986).

9. M. Goto, A. Kasahara, T. Oishi, Y. Konishi and M. Tosa, Tribology Letters **17** (1), 51-54 (2004).

10. H. Derin and K. Kantarli, Applied Physics a-Materials Science & Processing **75** (3), 391-395 (2002).

11. B. Balamurugan, B. R. Mehta and S. M. Shivaprasad, Applied Physics Letters **79** (19), 3176-3178 (2001).

12. M. F. Al-Kuhaili, Vacuum **82** (6), 623-629 (2008).

13. S. C. Ray, Solar Energy Materials and Solar Cells **68** (3-4), 307-312 (2001).

14. B. Balamurugan and B. R. Mehta, Thin Solid Films **396** (1-2), 90-96 (2001).

15. A. A. Ogwu, E. Bouquerel, O. Ademosu, S. Moh, E. Crossan and F. Placido, Journal of Physics D-Applied Physics **38** (2), 266-271 (2005).

16. G. P. Pollack and D. Trivich, Journal of Applied Physics **46** (1), 163-172 (1975).

17. D. O. Scanlon, B. J. Morgan, G. W. Watson and A. Walsh, Physical Review Letters **103** (9), 096405 (2009).

18. J. Ghijsen, L. H. Tjeng, J. Vanelp, H. Eskes, J. Westerink, G. A. Sawatzky and M. T. Czyzyk, Physical Review B **38** (16), 11322-11330 (1988).

19. L. Papadimitriou, Solid State Communications **71** (3), 181-185 (1989).

20. L. Papadimitriou, Solid-State Electronics **36** (3), 431-434 (1993).

21. A. E. Rakhshani, Y. Makdisi and X. Mathew, Thin Solid Films **288** (1-2), 69-75 (1996).

22. A. Buljan, M. Llunell, E. Ruiz and P. Alemany, Chemistry of Materials **13** (2), 338-344 (2001).

23. P. Marksteiner, P. Blaha and K. Schwarz, Zeitschrift Fur Physik B-Condensed Matter **64** (2), 119-127 (1986).

24. L. Pauling, *The nature of the chemical bond and the structure of molecules and crystals; an introduction to modern structural chemistry*, 3d ed. (Cornell University Press, Ithaca, N.Y., 1960).

25. J. P. Dahl and Ac. Switendi, Journal of Physics and Chemistry of Solids **27** (6-7), 931-942 (1966).

26. L. Kleinman and K. Mednick, Physical Review B **21** (4), 1549-1553 (1980).

27. J. Robertson, Physical Review B **28** (6), 3378-3385 (1983).

28. S. Nagel, Journal of Physics and Chemistry of Solids **46** (6), 743-756 (1985).

29. D. D. Koelling and G. O. Arbman, Journal of Physics F-Metal Physics **5** (11), 2041-2054 (1975).

30. S. L. Hulbert, B. A. Bunker, F. C. Brown and P. Pianetta, Phys Rev B **30** (4), 2120-2126 (1984).

31. L. O. Grondahl, Reviews of Modern Physics **5** (2), 141 (1933).

32. B. Lange and A. St. John, *Photoelements and their application*. (Reinhold Publishing Corporation, New York, 1938).

33. R. S. Toth, R. Kilkson and D. Trivich, Journal of Applied Physics **31** (6), 1117-1121 (1960).

34. A. S. Kakar, Thesis (Ph. D.), Wayne State University (1978).

35. D. Trivich and G. P. Pollack, Journal of the Electrochemical Society **117** (3), 344-345 (1970).

36. K. Kawaguchi, R. Kita, M. Nishiyama and T. Morishita, Journal of Crystal Growth **143** (3-4), 221-226 (1994).

37. S. B. Ogale, P. G. Bilurkar, N. Mate, S. M. Kanetkar, N. Parikh and B. Patnaik, Journal of Applied Physics **72** (8), 3765-3769 (1992).

38. M. R. Wright, Thesis, Wayne State University, Dept. of Chemistry (1962).

39. J. R. Coughlin, U.S. Bur. Mines Bull. **542** (1954).

40. M. O'Keeffe and W. J. Moore, J. Chem. Phys. **36** (1962).

41. M. Causa, R. Dovesi, E. Kotomin and C. Pisani, Journal of Physics C-Solid State Physics **20** (30), 4983-4990 (1987).

42. Z. G. Yin, H. T. Zhang, D. M. Goodner, M. J. Bedzyk, R. P. H. Chang, Y. Sun and J. B. Ketterson, Applied Physics Letters **86** (6), 061901 (2005).

43. D. J. Miller, R. P. Chiarello, H. K. Kim, T. Roberts, H. You, R. T. Kampwirth, K. E. Gray, J. Q. Zheng, S. Williams, R. P. H. Chang and J. B. Ketterson, Applied Physics Letters **59** (24), 3174-3176 (1991).

44. S. Poulston, P. M. Parlett, P. Stone and M. Bowker, Surface and Interface Analysis **24** (12), 811-820 (1996).

45. K. H. Yoon, W. J. Choi and D. H. Kang, Thin Solid Films **372** (1-2), 250-256 (2000).

46. T. Maruyama, Solar Energy Materials and Solar Cells **56** (1), 85-92 (1998).

47. B. Balamurugan, B. R. Mehta, D. K. Avasthi, F. Singh, A. K. Arora, M. Rajalakshmi, G. Raghavan, A. K. Tyagi and S. M. Shivaprasad, Journal of Applied Physics **92** (6), 3304-3310 (2002).

48. Z. H. Gan, G. Q. Yu, B. K. Tay, C. M. Tan, Z. W. Zhao and Y. Q. Fu, Journal of Physics D-Applied Physics **37** (1), 81-85 (2004).

49. A. Losev, K. Kostov and G. Tyuliev, Surface Science **213** (2-3), 564-579 (1989).

50. P. D. Kirsch and J. G. Ekerdt, Journal of Applied Physics **90** (8), 4256-4264 (2001).

51. D. A. Shirley, Physical Review B **5**, 4709 (1972).

52. D. J. Aston, D. J. Payne, A. J. H. Green, R. G. Egdell, D. S. L. Law, J. Guo, P. A. Glans, T. Learmonth and K. E. Smith, Phys Rev B **72** (19) (2005).

53. G. Vanderlaan, C. Westra, C. Haas and G. A. Sawatzky, Physical Review B **23** (9), 4369-4380 (1981).

54. K. Karlsson, O. Gunnarsson and O. Jepsen, International Journal of Modern Physics B **14** (32), 3791-3830 (2000).

55. K. Karlsson, O. Gunnarsson and O. Jepsen, Journal of Physics-Condensed Matter **4** (11), 2801-2816 (1992).

56. T. Arnold, D. J. Payne, A. Bourlange, J. P. Hu, R. G. Egdell, L. F. J. Piper, L. Colakerol, A. Masi, P. A. Glans, T. Learmonth, K. E. Smith, J. Guo, D. O. Scanlon, A. Walsh, B. J. Morgan and G. W. Watson, Physical Review B **79** (7), 075102 (2009).

57. A. D. Becke, Journal of Chemical Physics **98** (7), 5648-5652 (1993).

58. C. T. Lee, W. T. Yang and R. G. Parr, Physical Review B **37** (2), 785-789 (1988).

59. J. Muscat, A. Wander and N. M. Harrison, Chemical Physics Letters **342** (3-4), 397-401 (2001).

60. J. Tauc, Grigorov.R and A. Vancu, Physica Status Solidi **15** (2), 627 (1966).

61. J. F. Pierson, A. Thobor-Keck and A. Billard, Applied Surface Science **210** (3-4), 359-367 (2003).

62. A. Soon, M. Todorova, B. Delley and C. Stampfl, Physical Review B **76** (12) (2007).

4 Epitaxial Growth of Transparent $CuInO_2$ Thin Films by Oxygen Plasma Assisted Atomic Beam Epitaxy

4.1 Introduction

The aim of this chapter is to describe experiments directed to the growth of $CuInO_2$ layers using oxygen plasma assisted atomic beam epitaxy (OPABE). This is a challenging problem which has never been addressed previously, and demands careful control of the Cu:In stiochiometry in addition to the Cu (I) oxidation state as discussed in the previous chapter.

4.1.1 Background

Optically transparent oxides generally tend to be dielectrics, due to their wide electronic band gap energy, ≥ 3.1 eV although some very famous notable exceptions exist such as n-type doped materials of the oxides ZnO, SnO_2 and In_2O_3 [1]. These n-type conductors are very useful electrodes for optoelectronic applications such as flat panel displays, along with transparent conductive coatings [2, 3]. By contrast, suitable p-type transparent oxide semiconductors are much less common. So novel devices cannot be realised such as transparent oxide p-n junctions, which could lead to a 'functional' window, allowing optical transmission of visible light and the creation of electricity by near UV radiation [1]. The rare existence of good p-type transparent conducting oxides (TCOs) can be explained to originate from a strong localization of the upper edge of the valence band to oxide ions. Several p-type TCOs, in particular delafossite type $CuMO_2$ (M = Al, Ga, In) compounds and $SrCu_2O_2$, are associated

with the modification of the energy band structure to reduce such localization behaviour [4-6].

Most delafossite-like oxides are synthesized by cation-exchange or direct reaction under high pressures/temperatures using solid materials. For example, Shannon *et al*. reported the hydrothermal synthesis of $CuMO_2$ (M = Co, Fe, Al, Ga, In, and Rh) and $AgMO_2$ (M = Co, Cr, Fe, Ga, In, and Tl), at suitable temperatures (500-700 ^oC) and pressure of 3000 atm [7-9].

In the meantime, Gessner described the preparation of $CuInO_2$ using an exchange reaction by CuCl and $NaInO_2$ [10]. In addition, good results for this compound were reported by Shimode and colleagues based on the following exchange reaction [11],

$$CuCl + LiInO_2 \rightarrow CuInO_2 + LiCl$$

They also reported that no reaction occurred in the Cu_2O-In_2O_3 and Cu_2O-$In(OH)_3$ schemes under diverse heating processes. In their report, lattice parameters of the rhombohedral $CuInO_2$ cell were provided as a = 3.2992, c = 17.388 Å , using Rietveld refinement [12].

Rietveld refinement is a technique devised by Hugo Rietveld for use in the characterisation of crystalline materials [12]. The neutron and x-ray diffraction of powder samples results in a pattern characterised by reflections (peaks in intensity) at certain positions. The height, width and position of these reflections can be used to determine many aspects of the material's structure. The Rietveld method uses a least squares approach to refine a theoretical line profile until it matches the measured profile. The introduction of this technique was a significant step forward in the

diffraction analysis of powder samples as, unlike other techniques at that time, it was able to deal reliably with strongly overlapping reflections.

The method was first reported for the diffraction of monochromatic neutrons where the reflection-position is reported in terms of the Bragg angle 2θ. This terminology will be used here although the technique is equally applicable to alternative scales such as x-ray energy or neutron time-of-flight. The only wavelength and technique independent scale is in reciprocal space units or momentum transfer Q, which is historically rarely used in powder diffraction but very common in all other diffraction and optics techniques. The relation is [12]

$$Q = \frac{4\pi \sin(\theta)}{\lambda}. \tag{4.1}$$

The shape of a powder diffraction reflection is influenced by the characteristics of the beam, the experimental arrangement, and the sample size and shape. In the case of monochromatic neutron sources the convolution of the various effects has been found to result in a reflex almost exactly Gaussian in shape. If this distribution is assumed then the contribution of a given reflection to the profile y_i at position $2\theta_i$ is [12]:

$$y_i = I_k \exp\left[\frac{-4\ln(2)}{H_k^2}(2\theta_i - 2\theta_k)^2\right] \tag{4.2}$$

where H_k is the full width at half peak height (full-width half-maximum), $2\theta_k$ is the centre of the reflex, and I_k is the calculated intensity of the reflex (determined from the structure factor, the Lorentz factor, and multiplicity of the reflection)

The width of the diffraction peaks are found to broaden at higher Bragg angles. This angular dependency was originally represented by [12]

$$H_k^2 = U\tan^2\theta_k + V\tan\theta_k + W \tag{4.3}$$

where *U*, *V* and *W* are the halfwidth parameters and may be refined during the fit.

The principle of the Rietveld Method is to minimise a function *M* which analyzes the difference between a calculated profile *y*(calc) and the observed data *y*(obs). Rietveld defined such an equation as [12]:

$$M = \sum_i W_i \left\{ y_i^{obs} - \frac{1}{c} y_i^{calc} \right\}^2 \qquad (4.4)$$

where W_i is the statistical weight and *c* is an overall scale factor such that $y^{calc} = cy^{obs}$

Thin films of Ca-doped and Sn-doped $CuInO_2$ (optical Eg = ~3.9 eV) which exhibited both *p*-type and *n*-type conduction, were grown on α-Al_2O_3 (001) single crystal substrates by pulsed laser deposition (PLD) [5]. In this technique, a $CuInO_2$ delafossite target was grown using the cation exchange reaction of Shimode *et al*. although $NaInO_2$, rather than $LiInO_2$, was employed as the precursor for the cation exchange in their preparation. Substitution for In^{3+} with Ca^{2+} or Sn^{4+} was performed to generate hole acceptor or electron donor, respectively. Yanagi *et al*. also indicate that substitution for the In^{3+} ion by both of the dopants ion is effective to enhance electrical conductivity. The electrical conductivity and the Seebeck coefficient of Ca-doped thin films at room temperature were measured to be 2.8 x 10^{-3} Scm^{-1} and +4.8 x 10^2 μVK^{-1}, respectively, indicating that the $CuInO_2$:Ca 7% thin film should be a *p*-type conductor. On the other hand, the values for the $CuInO_2$:Sn 5% thin film were 3.8 x 10^{-3} Scm^{-1} and -5.0 x 10^1 μVK^{-1}, respectively, showing that the specimen is an *n*-type conductor. Especially, the film growth of the Sn-doped films was hard as a consequence of the deposition conditions having to be restricted to a very narrow

oxygen atmosphere (1.4~1.6 Pa). The crystal quality of the films was also very poor [5]. The optical band gap of the $CuInO_2$:Ca and the $CuInO_2$:Sn PLD thin films, evaluated from a plot by Tauc relationship assuming a direct band-to-band transition, was ~3.9 eV.

Up to now, theoretical calculations were performed using such methods as local density approximation (LDA)[13] as executed by the general potential linearized augmented plane wave (LAPW)[14], generalised gradient approximation (GGA) and quasiparticle self-consistent *GW* approximation (QPsc*GW*)[15], to investigate some of the features of doping delafossite compounds [13, 14]. The LDA method confined lattice parameters and bond lengths in $CuInO_2$ to a = 3.285 Å, c = 17.270 Å, u = 0.1056 [13] and Cu-O 1.845 Å, In-O 2.17 Å, Cu-Cu 3.29 Å [14], respectively. The calculated indirect gaps were 0.41 for LDA, 0.52 eV for GGA and 2.51 eV for QPscGW [15]. The computed direct band gaps were found to be 0.73 at Γ, 1.89 at Z, 3.34 at F and 3.08 eV at L along the Brillouin-zone (BZ) [13]. Direct band gaps is 5.26 eV at L by QPsc*GW* [15]. Nevertheless, the experimental optical gap is well known to be 3.9 eV, and the consequences of the disparity between the fundamental and apparent optical gaps were discussed.

4.1.2 Band Gap Energy of Delafossite Compounds $CuMO_2$

The delafossite structure $CuMO_2$ (M=group III elements), is shown in figure 4.1 [16]. The Cu delafossites families can be classified as two groups, $CuM^{IIIA}O_2$ (M^{IIIA}=Al, Ga and In) and $CuM^{IIIB}O_2$ (M^{IIIB}=Sc, Y, and La) [17]. Despite the similar crystal structures, the $CuM^{IIIA}O_2$ and $CuM^{IIIB}O_2$ families show meaningfully different electronic properties. The optical characterizations demonstrate that the group-IIIA delafossite family has indirect band gaps [18, 19]. By contrast, the group-IIIB delafossite

family belongs to direct wide band gap classification and is able to be doped with extrinsic impurities [20, 21]. It has been commented that the $CuM^{IIIA}O_2$ shows band-gap irregularities compared to other group-III-containing semiconductors. The reported optical band gap increases from 3.5 eV ($CuAlO_2$) to 3.6 eV ($CuGaO_2$) to 3.9 eV ($CuInO_2$) whilst decreasing for the corresponding binary oxides and nitrides [17]. On the contrary, $CuM^{IIIB}O_2$ does not follow such abnormalities and shows an entirely opposite band gap trend. The decrease in optical band gap was obtained as the following sequence, 3.7 eV ($CuScO_2$) > 3.5 eV ($CuYO_2$) > 2.4 eV ($CuLaO_2$) [22-24].

4.1.3 Crystal Structure of Delafossite $CuMO_2$

Within the Cu delafossite structure, each Cu atom is linearly coordinated by two oxygen atoms, O-Cu-O dumbbells parallel to the *c*-axis. The oxygen atoms that terminate the dumbbells are also each coordinated to three M^{3+} atoms, oriented such that M^{3+}-centred octahedral shape MO_2 layers which lie parallel to the *ab* plane [5, 16, 25]. Figure 4.1 shows that two alternative layer stacking sequences ABABAB and ABCABC are possible to give hexagonal (space group $P6_3/mmc$) or rhombohedral (space group $R3m$) polymorphs, respectively [26, 27]. Within the linear O-Cu-O units the Cu $3d_z^2$ orbitals have σ-like symmetry, the Cu $3d_{xz}$ and $3d_{yz}$ orbitals π-like symmetry and the Cu $3d_{xy}$ and Cu $3d_{x^2-y^2}$ orbitals δ-like symmetry. No mixing with O 2*p* states is possible for the Cu 3*d* orbitals of δ symmetry, while the mixing for the π states is weaker than for σ states [28-32]. Linear coordination about copper is also found in the binary oxide Cu_2O as discussed in the previous chapter. However the band gap in the parent material has a much smaller value of 2.17 eV than found for the delafossites [33]. The difference can be attributed to the fact that Cu has 12 Cu next nearest neighbours

in Cu_2O, whereas there are only 6 coplanar next-nearest neighbours in the delafossite structure. This leads to a reduction in the Cu 3*d* bandwidth and a wider band gap [25].

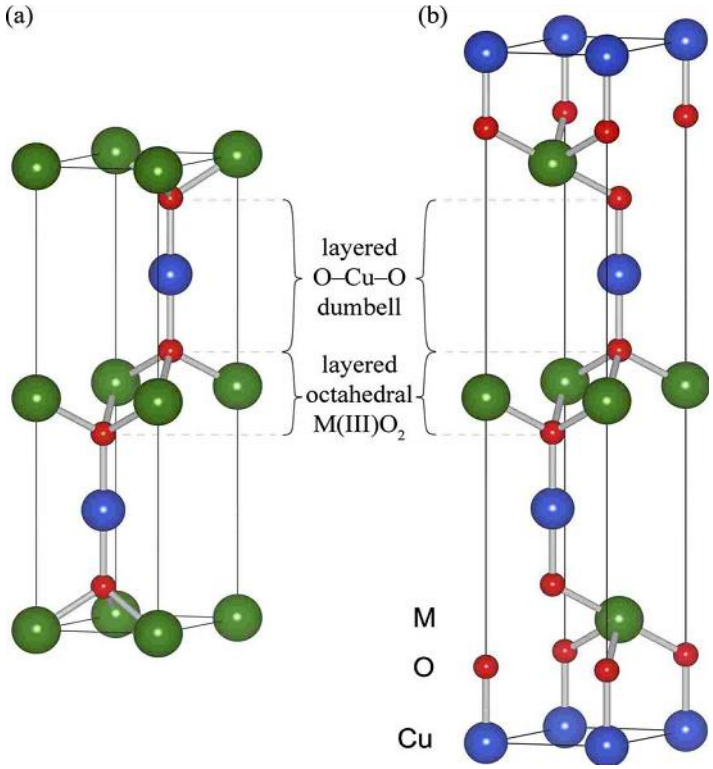


Figure 4.1. Crystal unit structure of delafossite $CuMO_2$, where M denotes trivalent cations. (a) 2H structure; (b) 3R structure. (adapted from ref. 16)

4.2 Experimental Details

Epitaxial films of nominally undoped $CuInO_2$ were grown on 1 cm ×1 cm Al_2O_3 (*c*-plane, 0001) substrate in ultrahigh vacuum oxygen plasma assisted molecular beam epitaxy (SVT, USA) system with a base pressure of $5x10^{-9}$ torr, as described in chapter 2. Conventional In, Cu, Sn K-cells and a high temperature Cr K-cell was used in these experiments and the radio frequency plasma oxygen atomic source was

operated using the "standard' conditions (200 W RF power during growth under oxygen pressure of about $2x10^{-5}$ torr). Optimised evaporation temperatures were approximately Cu 1100 ^oC, In 640 ^oC, Sn 640 ^oC, Cr 1400 ^oC. Substrate temperatures were typically 800 ^oC, although lower temperatures of 700 and 600 ^oC were also employed. The normal deposition rate was set at 0.1 Å/sec using a quartz crystal monitor offset from the sample position—the true growth rate on the sample was found to be about four times greater than this value. All growth runs used the bilayer method using a 1:6 $Cu/CuInO_2$ deposition time as described chapter 3, using a post-annealing step the same temperature as the growth temperature for around 30 min. Substrates were pretreated for cleaning and stabilizing by chemical (acetone and 2-propanol) ultra-sonication and heated radiatively at 850 ^oC using a graphite hot filament, respectively. Films were then grown to a nominal thickness of 100~1200 Å at a substrate temperature in the range 600~800 ^oC. The sample temperature was measured by a chromel-alumel thermocouple spot welded to the cradle holding the sample mounting stage. High-resolution X-ray photoemission spectra were measured in a Scienta ESCA 300 spectrometer described previously, or occasionally the in-house XPS system was employed. Binding energies are referenced to the Fermi energy of a silver (Ag) sample regularly used for spectral calibration. X-ray emission spectra were measured for ceramic Cu delafossites on beamline 7.0.1 at the Advanced Light Source (ALS), Lawrence Berkeley National Laboratory in collaboration with the K. E. Smith Group, Department of Physics, Boston University, USA. X-ray diffraction (XRD) profiles of $CuInO_2$ films were obtained from a PANalytical X'Pert PRO diffractometer using monochromatic Cu $K\alpha$ radiation and a rotating spinner stage. The direct optical band gap energies of the films were measured using a Shimadzu UV-2401 PC (λ = 230~800 nm) instrument, analysed via

the Tauc relationship. AFM images were recorded *ex situ* with a Digital Instruments Multimode SPM instrument.

4.3 Results

The growth of $CuInO_2$ requires careful control of the Cu : In stoichiometry and so initial experiments focussed on the growth of the material using conditions established first for the single metal Cu or In oxides. Surprisingly layers grown using this approach always seemed to be very significantly Cu deficient, compared to the expected relative fluxes. Apparently the In flux seemed to impede the incorporation of Cu in the growing layer. All the main experiments therefore used the bilayer method described in the previous chapter in which a Cu layer was deposited separately to maintain stoichiometry and oxidation state, as noted in the preceding experimental section. Specifically, 1:6 Cu (bottom layer)/$CuInO_2$ (top layer) deposition time as adapted from chapter 3 was employed followed by an annealing cycle to equilibrate the layer at the growth temperature.

4.3.1 Stoichiometric Proportions of $CuInO_2$ Films on Differing Fluxes

Films were grown under differing conditions and initial experiments focussed on the investigation of stoichiometry using XPS, involving especially change of K-cell conditions to optimise the stoichiometry. Typical K-cell temperatures around 1100^{o}C for copper and 640^{o}C for indium were used and small changes made in an attempt to obtain a 1:1 Cu:In ratio. Table 4.1 shows representative experimental results. Atomic

sensitivity factors for XPS were used to calculate empirical stoichiometry as follows; Cu $2p_{3/2}$ = 4.2, In $3d_{5/2}$ = 3.9, O 1s = 0.66 [34].

Table 4.1 Stoichiometries of $CuInO_2$ films as a function of growth conditions. Ratios of Cu/In/O were obtained by XPSPEAK41 software using the Cu $2p_{3/2}$, In $3d_{5/2}$ and O 1*s* regions.

Stoichiometries of OPABE $CuInO_2$ thin films

Ratio of Cu/In/O	Substrate	Growth Temp.(°C)	pO_2 (torr), RF power	Vac. Anneal (°C)	Cu temp (°C)	In temp (°C)
1.0/0.5/6.1	Al_2O_3 (0001)	350	$2.3x10^{-5}$, 200 W	350/20 min	1120	650
1.0/0.7/3.6	Al_2O_3 (0001)	570	$1.8x10^{-5}$, 150 W	570/10 min	1121	650
1.0/1.2/8.2	Al_2O_3 (0001)	570	$2.8x10^{-5}$, 200 W	570/15 min	1100	650
1.0/1.0/7.3	Al_2O_3 (0001)	570	$3.0x10^{-5}$, 200 W	570/30 min	1109	650
1.0/0.7/2.3	Al_2O_3 (0001)	600	$2.6x10^{-5}$, 200 W	700/10 min	1130	700
1.0/1.2/5.1	Al_2O_3 (0001)	700	$2.2x10^{-5}$, 200 W	800/10 min	1130	730
1.0/1.0/2.3	Al_2O_3 (0001)	800	$2.0x10^{-5}$, 200 W	800/10 min	1100	640

** See section 2.3.2 (g) for consideration of accuracy of quoted elemental compositions.*

The results showed that approximate film stoichiometries relevant to $CuInO_2$ could be obtained although it was clear that deviations rather sensitive to the growth conditions were occurring. Occasionally very high oxygen levels were seen in the XPS spectra – attributable either to contamination in the atmosphere by water vapour, or the presence of O from the underlying substrate due to inadequate thin film coverage. Nevertheless the preliminary data suggested that some success might be possible using OPABE in this materials system.

4.3.2 X-ray Photoemission Spectra of Core Level and Occupied Valence Band States

A survey scan XPS spectrum of a $CuInO_2$ thin film is shown in figure 4.2. This film (nominal film thickness = 200 Å) was grown at 800 °C using the optimum

conditions in the final entry in table 4.1. Apart from a small C 1*s* signal, all of the other peaks are consistent with the elemental formulation of the target compound.

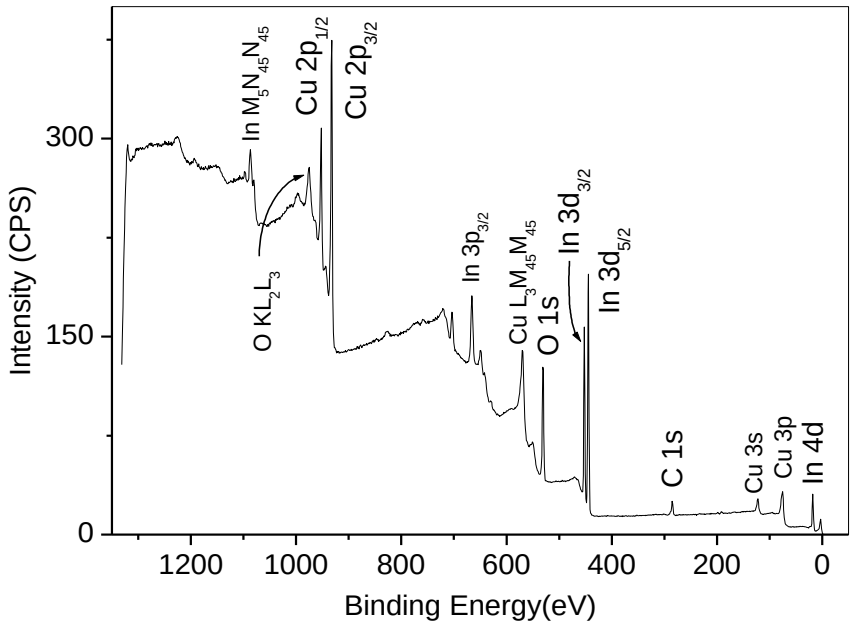


Figure 4.2. XPS (ESCA300) survey scan of undoped $CuInO_2$ thin film of OPABE on sapphire substrate, Al_2O_3 (0001).

The measured experimental valence band X-ray photoemission spectrum of this sample is compared to the density of states (DOS) result of $CuInO_2$ from band structure calculations and the partial DOS contributions, as shown in figure 4.3 [30]. The full and partial densities of states were derived from the band structure calculations of density functional theory (DFT) code VASP [35, 36], which employs a plane wave basis set to describe the valence electronic states, as shown in figure 4.3 (lower panel). It can be seen that the lower binding energy area is of dominant Cu 3*d* atomic character and the higher binding energy part is more related to O 2*p* character. Figure 4.3 (lower panel) shows that various features are observed, which can be reasonably identified as regions I-IV in the valence band spectrum. Reference to the

band structure calculations suggests that I and II relate to states of dominant Cu 3*d* atomic character, whereas the region III and the poorly defined region IV correspond with states with significant O 2*p* character. The band width of the valence band found experimentally is broader than the calculations, but there is otherwise some agreement between theory and the result.

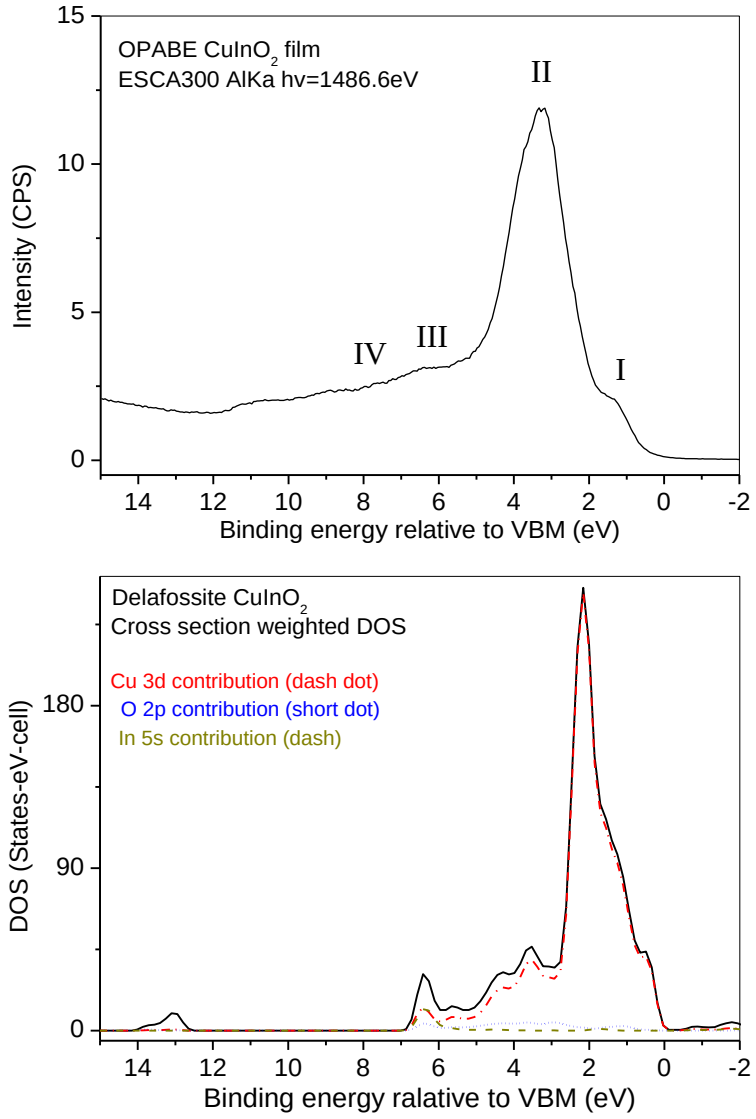


Figure 4.3. Upper panel: Al *Kα*, *hν* = 1486.6 eV excited valence band XPS (ESCA300). Lower panel: theoretical cross section weighted DOS including Cu 3*d*, O 2*p* and In 5*s* PDOS for $CuInO_2$ (DFT) [30].

The experimental Al *Kα* XPS core level spectrum for Cu 2*p* is shown in figure 4.4, which compares both Sn-doped and intrinsic $CuInO_2$ films formed by OPABE. These films were grown at 800 ^oC as described in section 4.3.1 and 4.3.2. In situ Sn doping with a Sn K-cell temperature of 640 ^oC was achieved, which should achieve an approximately 5% Sn-doped film, as judged from the estimated beam fluxes. The Sn flux was used during the $CuInO_2$ growth step of the bilayer growth, followed by the usual vacuum annealing at the growth temperature (800 ^oC) for 10 min.

First of all, it shows that the sample with incorporated Sn-doped $CuInO_2$ of OPABE growth techniques give rise to a peak shift of around 1 eV. Cu $2p_{3/2}$ peak (M1) shifted to higher binding energy with respect to the sample without Sn. (A similar valence band shift about 1 eV also can be seen at figure 4.6.) This is suggestive of *n*-type doping. The Cu $2p_{3/2}$ component (M1) in both the Sn-free sample and that containing Sn, agrees with the expected Cu $3d^{10}$ configuration in the final state arising from Cu (I), suggesting that the problem in oxidation state discussed in the previous chapter is not seen in the present case using the bilayer approach. In particular the features M2, s1, s2, s1* and s2* can be observed, as discussed in 3.3.3 entirely consistent with the presence of Cu (I) species [37-39]. The Cu (II) content in the $CuInO_2$ film as judged from the absence of the characteristic satellites appears to be negligible as judged by XPS.

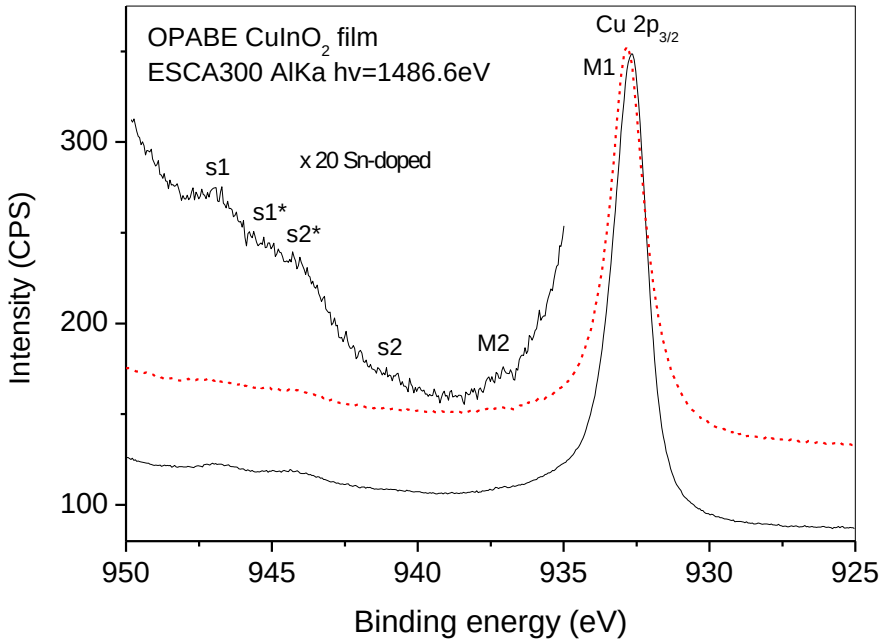


Figure 4.4. XPS (Al *Kα*, *hv* = 1486.6 eV) spectra in the Cu 2*p* region of OPABE $CuInO_2$ films by using ESCA300 in Daresbury Laboratory, UK. BE regions (935~950 eV) are 20 times magnified spectrum of Sn-doped $CuInO_2$ film. Black solid line: undoped, red dot: Sn-doped, upper zig-zag line: x 20 magnified Sn-doped film.

4.3.3 X-ray Photoemission Spectra and Valence Band Shift Concerning Bipolar Doping

To further work described above, bipolar doping by substitution of In (III) with Cr (III) or Sn (IV) was carried out to introduce acceptor or donor states, respectively. Figure 4.5 shows survey XPS spectra for Sn incorporation (upper panel) and Cr incorporation (lower panel) for $CuInO_2$.

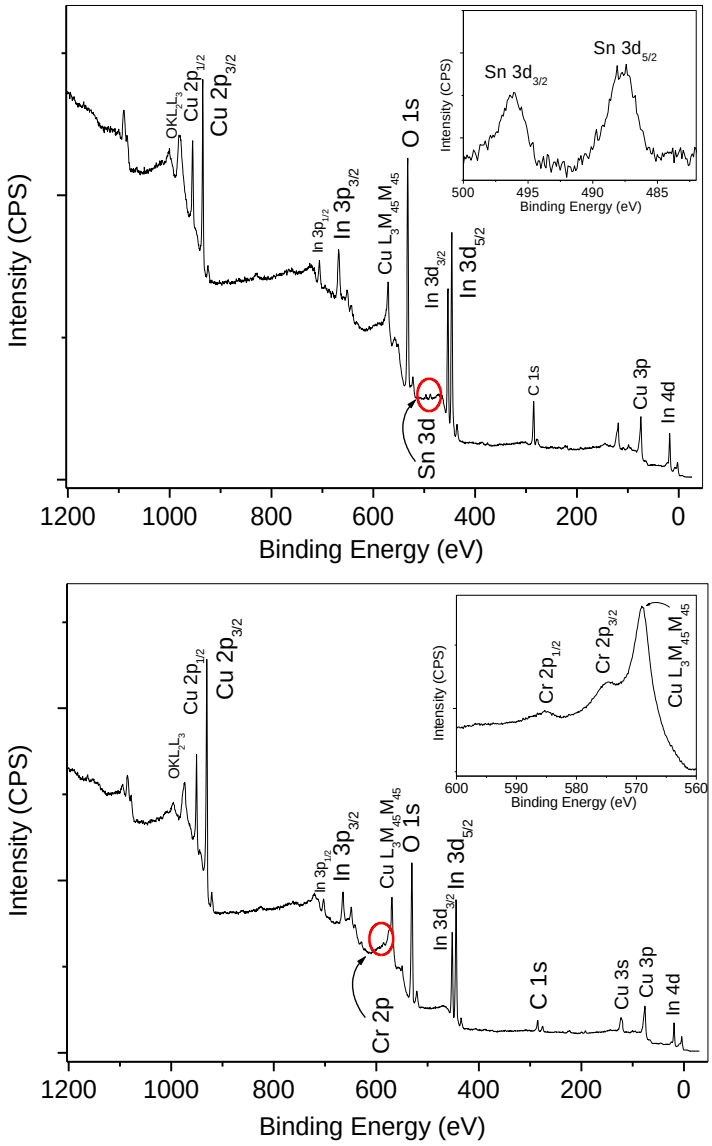


Figure 4.5. Upper panel: XPS (Al *Kα*, *hν* = 1486.6eV) spectra of 5% Sn-doped $CuInO_2$ in OPABE growth film. Lower panel: XPS spectra of 3% Cr-doped $CuInO_2$ in OPABE film.

The Sn-doped film was grown at 800 ^{o}C as described in the preceding section. The Sn 3*d* core level photoemission spectrum doublet was observed, as shown in inset of figure 4.5 (upper panel).

The calculated stoichiometric ratio of Sn/Cu/In/O is 0.05/1.0/1.0/6.5 (*See section 2.3.2 (g) for consideration of accuracy of quoted elemental composition*) from the elemental core level peak areas using atomic sensitivity factors [34] Cu $2p_{3/2}$ = 4.2, In $3d_{5/2}$ = 3.9, O 1s = 0.66, Sn $3d_{5/2}$ = 4.3. The unusually high level of oxygen is difficult to reconcile with lattice oxygen, suggesting some atmospheric contaminant.

The Cr-doped film was formed under similar conditions, except using a Cr K-cell temperature of ca. 1400^{o}C. The Cr 2*p* core line also spilt into two sublevels: Cr $2p_{3/2}$ and Cr $2p_{1/2}$, as shown in inset figure 4.5 (lower panel). The elemental ratio of Cr/Cu/In/O is obtained as 0.03/1.1/1.0/5.0 (*See section 2.3.2 (g) for consideration of accuracy of quoted elemental composition*), respectively, using the elemental sensitivity factors noted above along with Cr $2p_{3/2}$ = 1.5 [34].

The core level spectra are thus in agreement with the concept that Cr and Sn can be readily incorporated in the growing layer.

The valence band X-ray photoemission spectra of the OPABE grown $CuInO_2$ films containing Cr and Cu are shown in figure 4.6. The Fermi level in nominally undoped $CuInO_2$ lies above the valence band maximum. A significant shift is seen for the incorporation of Sn, consistent with the expected electrical n-type doping of this material [40]. In contrast the peak shift seen for Cr is much less significant. Nevertheless, some valence band shift is seen up to about 0.3 ± 0.05 eV, again suggestive of electrical (p-type) doping.

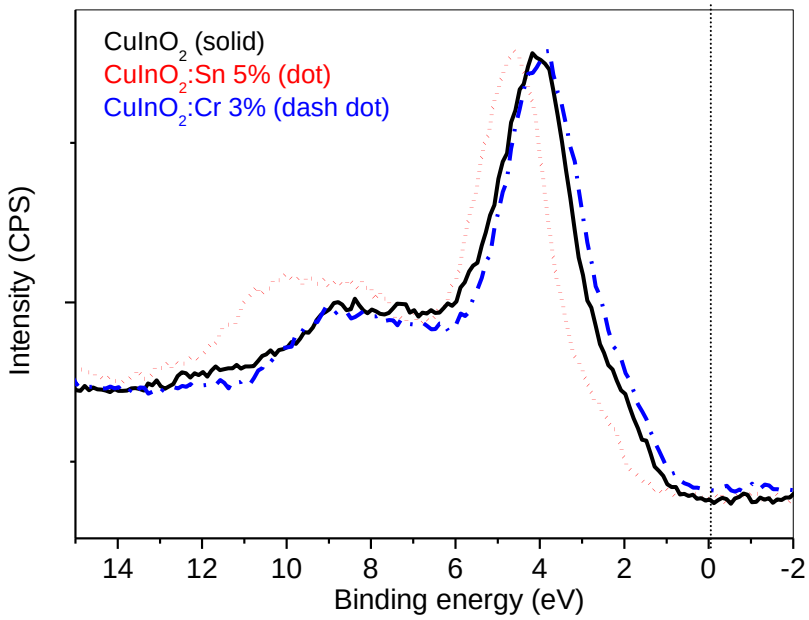


Figure 4.6. Note the shift binding energy with p- and n- dopants. Valence band X-ray photoemission spectra of $CuInO_2$ (Al *Kα*, *hν* = 1486.6 eV); undoped (black solid), 5% Sn-doped (red dot), 3% Cr-doped (blue dash dot)

4.3.4 X-ray Diffraction of OPABE $CuInO_2$ Films

The XRD analysis of bulk $CuInO_2$ powders has been carried out previously [11, 41] enabling comparison with the recorded patterns for the grown films.

Figure 4.7 shows the XRD patterns of OPABE grown Sn-doped $CuInO_2$ films for temperatures ranging from 600 ^oC to 800 ^oC. At the optimised effusion rate of OPABE system as judged from the XPS analysis above (evaporation temp. Cu 1100 ^oC, In 640 ^oC, Sn 640 ^oC, pO_2 2.0 x 10^{-5} torr (≈ 2.67 x 10^{-3} Pa) with 200 W of RF power, F/T around 200 Å, the (006) reflection of $CuInO_2$ is observed confirming

formation of the delafossites. However a range of other compounds are suggested by other reflections observed which can be linked to $Cu_2In_2O_5$, In_2O_3 and Cu_2O [42]. These extra reflections particularly dominate at the lower growth temperatures 4.7 (b) and (c) respectively, and similar results were also observed in the absence of Sn. Somewhat similar behaviour has been seen in previous thin film studies by pulsed laser deposition which showed the presence of $Cu_2In_2O_5$ or In_2O_3, depending on the partial pressure [43]. A notable difference is the crystallite orientation with the PLD films tending to share variable crystallite orientation [5, 11, 42, 43]. In contrast, OPABE shows the pure (001) reflections such as (003), (006) and (0012) indicative of O-Cu-O frame work lying parallel to the Al_2O_3 (0001) substrate.

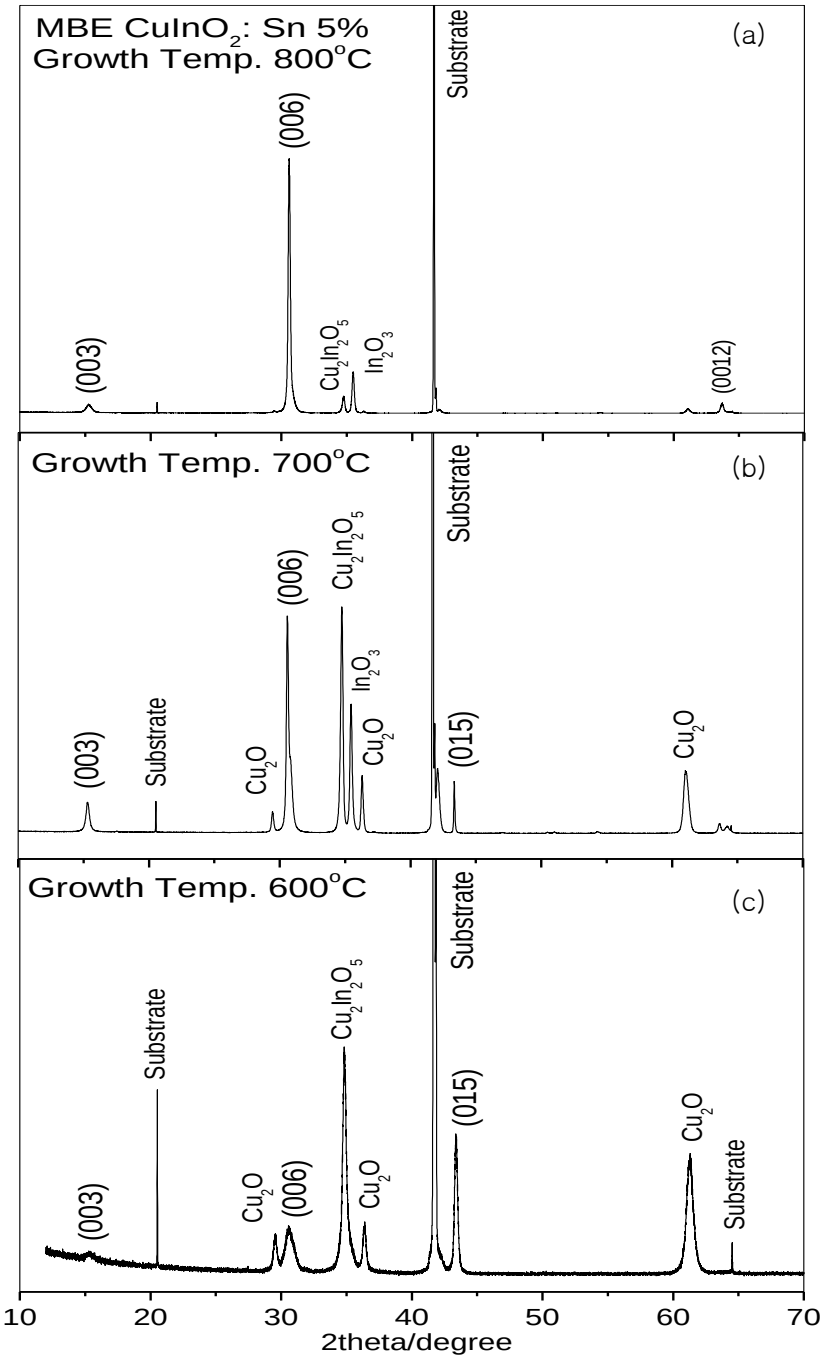


Figure 4.7. X-ray diffraction (monochromatic Cu Kα radiation λ = 1.5418 Å) patterns of oxygen plasma assisted atomic beam epitaxial $CuInO_2$, (a) 5% Sn-doped film at growth temperature of 800 ^{o}C, (b) 700 ^{o}C, (c) 600 ^{o}C, Note the effusion Knudsen-cells were optimised.

4.3.5 Optical Band Gap of OPABE $CuInO_2$ Films

OPABE $CuInO_2$ films as described above were evaluated to establish the optical absorption band gap energy by UV-Visible spectroscopy. These films were grown at 800^{o}C with 200 W oxygen plasma source for the bilayer system (1:6 Cu/$CuInO_2$) as described in sections 4.3.1 and 4.3.2. Furthermore, in situ doping by Sn or Cr doping with 640^{o}C or 1400 ^{o}C, was also employed to produce ca. 5% Sn-doped or 3% Cr-doped films as described above.

In order to directly measure the optical bandgap, the Tauc relationship, $\alpha h\nu = A(\hbar\nu - E_g)^n$ [44] was employed. A is a constant, n depends on the nature of the transition (n = 1/2 for the direct allowed transition, n = 3/2 for the direct forbidden transition, n = 2 for the indirect allowed transition and n = 3 for the indirect forbidden transition), $\hbar\nu$ is the photon energy, E_g is the band gap and α is the absorbance. To analyse the UV-visible measurement result, a graph is plotted for $(\alpha h\nu)^{1/n}$ vs. $h\nu$ for different values of n, and values which yield the best linear graph extrapolation are taken as the correct values n [45]. Figure 4.8 suggests indirect allowed transitions for range of $h\nu \leq 3.6$ eV, with an indirect gap around 2.8 eV, and a direct allowed transition in the range of $h\nu$ = 3.6 ~ 4.4 eV, described by n=1/2. The intercept of the straight line on the $h\nu$ axis gives the direct optical band gap of 3.8 eV for the undoped $CuInO_2$ film. Reference values of $CuInO_2$ films with bipolar doping have shown an optical band gap range about 3.9 eV [5].

In the same manner, the Sn-doped $CuInO_2$ films showed slightly decreased direct optical band gap energies of about 3.7 eV and an indirect band gap of 2.4 eV compared with undoped film, as seen in figure 4.9(a); the Cr-doped films have much

reduced direct optical band gap energies of around 3.4 eV and an indirect band gap of 2.4 eV and 2.9 eV, as shown in figure 4.9(b).

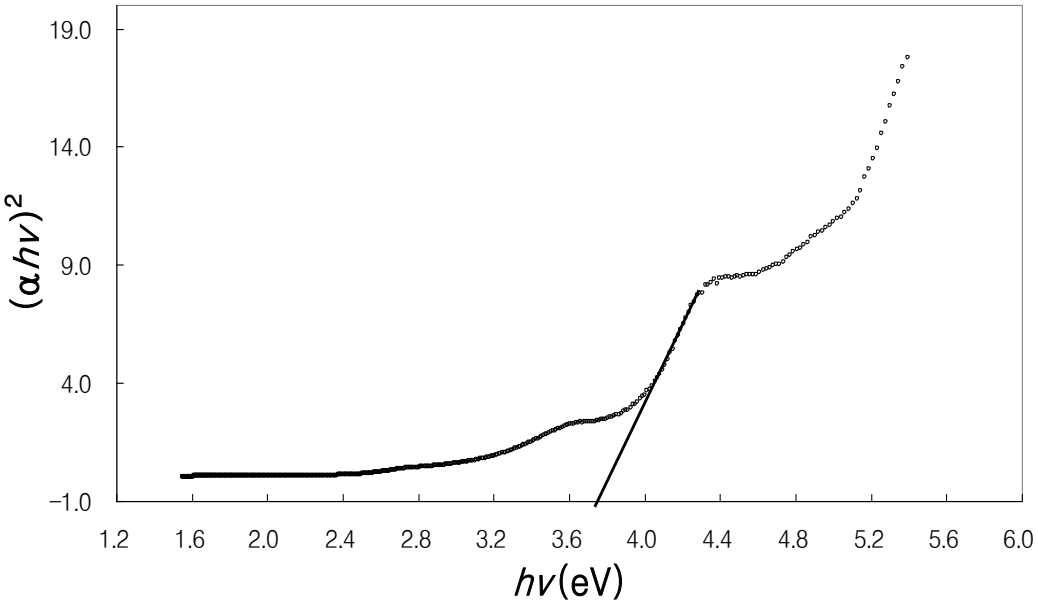


Figure 4.8. Direct optical band gap energy evaluation by hv vs. $(\alpha hv)^{1/n}$ approximation. undoped $CuInO_2$ on Al_2O_3 (0001), hv = 3.8 eV

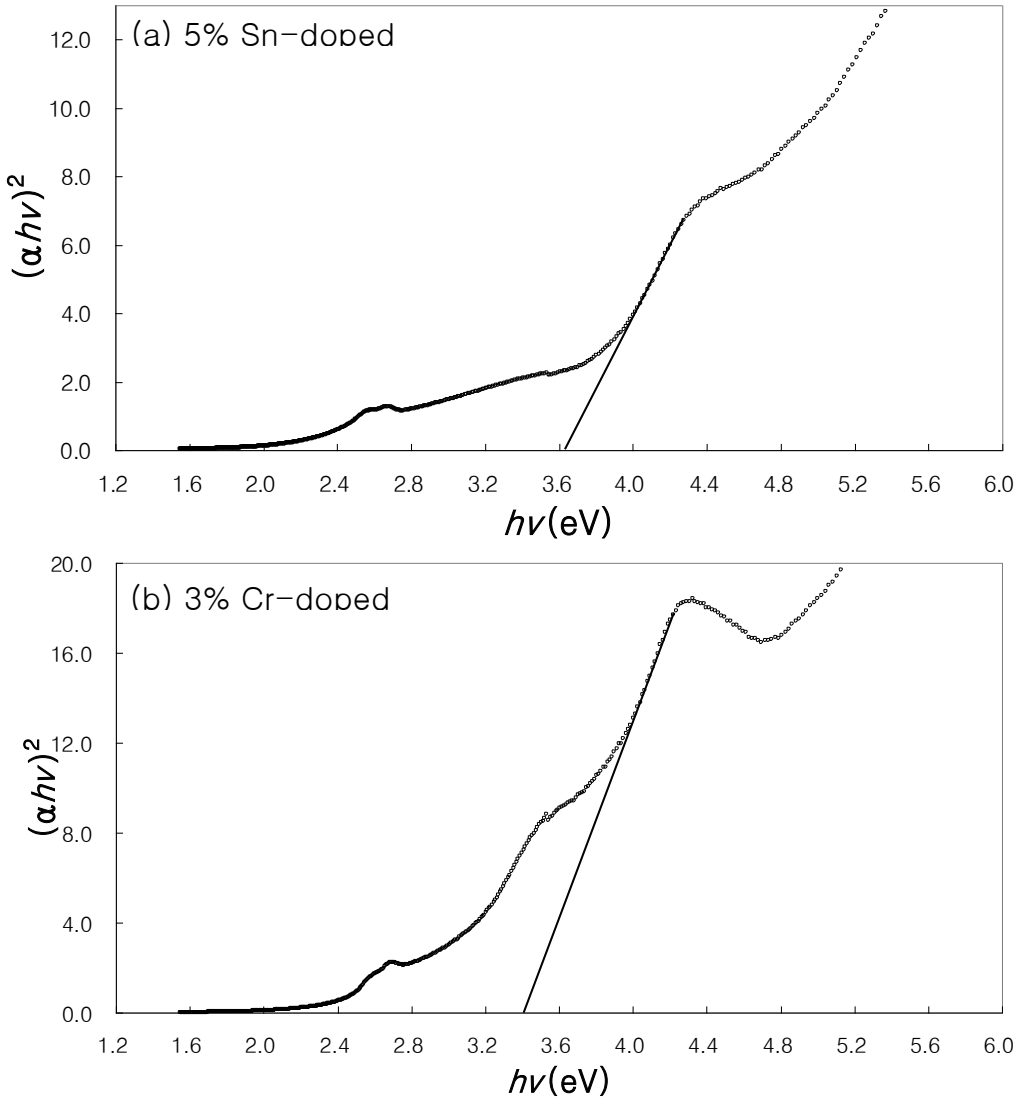


Figure 4.9. Direct optical band gap energy evaluation by hv vs. $(\alpha hv)^{1/n}$ approximation.

(a) 5% Sn-doped $CuInO_2$ hv = 3.65 eV (b) 3% Cr-doped $CuInO_2$ hv = 3.4 eV on *c*-plane Al_2O_3 (0001) substrate. Indirect band gap energies are 2.4 eV and 2.9 eV are in (b).

4.3.6 Surface Morphology Investigation by AFM

Figure 4.10 shows atomic force microscope surface morphology (scan size of 1.0 x 1.0 μm^2) of undoped $CuInO_2$ films grown by the bilayer method, using a 1:6 $Cu/CuInO_2$ deposition time ($CuInO_2$ on Cu bottom layer) at a growth temperature of 650 ^oC. These films were then treated by post thermal annealing at 800 ^oC for 20 min in vacuum (about 10^{-8} torr) to improve the phase purity, as suggested by the XRD data noted above.

The films are rough on the atomic scale with the surface roughness (root mean square, RMS) increasing along with film thickness: (a) film thickness (F/T) = 200 Å, RMS = 4.9 ±0.5nm, (b) F/T = 300 Å, RMS = 7.6 ±0.5nm (c) F/T = 350 Å, RMS = 10.2 ±0.5nm. This suggests limited surface diffusion under these growth conditions.

In contrast, figure 4.11 shows very good evidence for the evolution of 3D island growth of $CuInO_2$ at substrate growth temperatures of 800 ^oC: The images correspond to (a) 3% Cr-doped $CuInO_2$ film with F/T = 1300 Å, RMS = 26.0 ±0.5nm (b) 5% Sn-doped $CuInO_2$ with F/T = 800 Å, RMS = 17.9 ±0.5nm (c) $CuInO_2$ with F/T = 200 Å, RMS = 4.9 ±0.5nm. The shape of crystal seems to be a square pillar, as seen in figure 4.11(a) and (b), respectively.

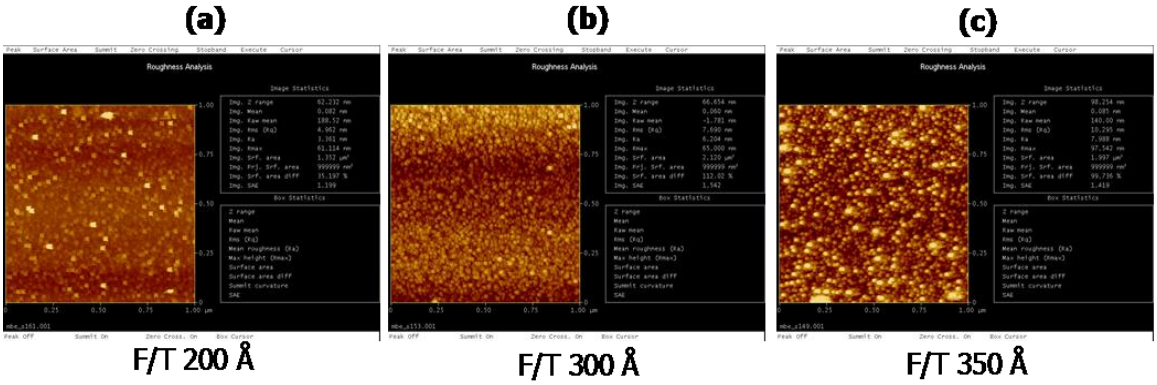


Figure 4.10. AFM images of $CuInO_2$ thin films, scan size of 1.0 x 1.0 μm^2 (a) film thickness (F/T) = 200 Å , RMS = 4.9 ±0.5nm (b) F/T = 300 Å , RMS = 7.6 ±0.5nm (c) F/T = 350 Å , RMS = 10.2 ±0.5nm. All of AFM images have been evaluated under 100 nm Z-scale sensitivity. These films were grown at substrate temperature of 650 ^oC.

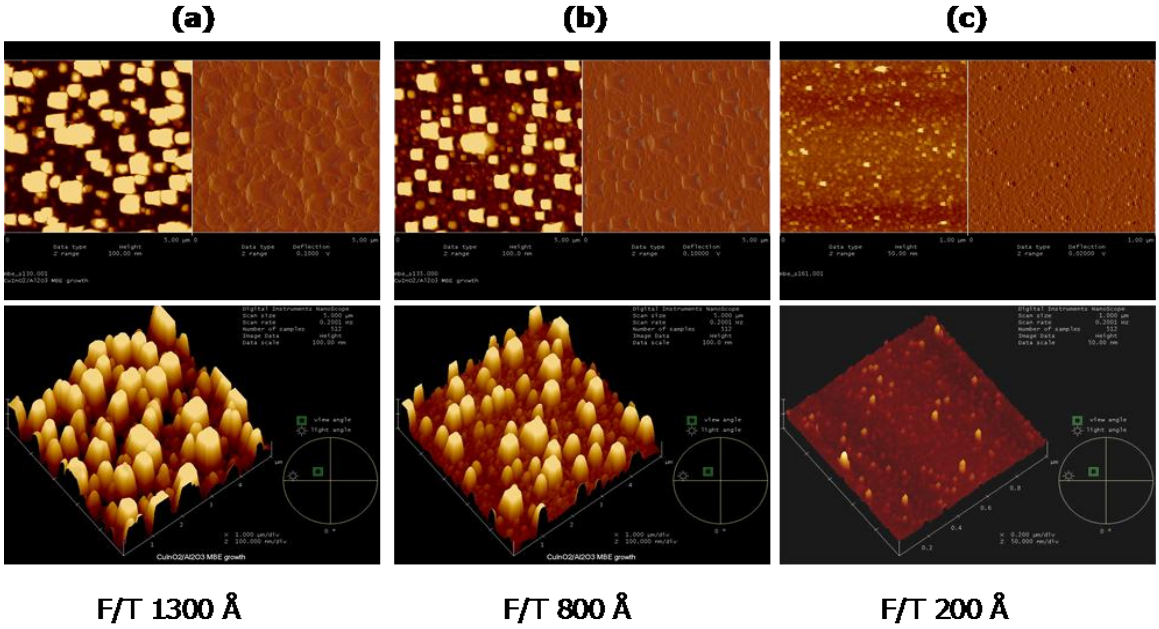


Figure 4.11. AFM images of $CuInO_2$ and bipolar doped film, scan size of 5.0 x 5.0 μm^2 except (c). (a) 3% Cr-doped $CuInO_2$ film with F/T = 1300 Å , RMS = 26.0 ±0.5nm (b) 5% Sn-doped $CuInO_2$ with F/T = 800 Å , RMS = 17.9 ±0.5nm (c) $CuInO_2$ with F/T = 200 Å , RMS = 4.9 ±0.5nm. All of AFM images have been evaluated under 50 nm Z- range for (a) and (b), 100 nm Z-scale for (c). These films were grown at substrate temperature of 800 ^oC.

4.4 Summary

The first studies of the growth of $CuInO_2$ thin films using OPABE are reported, and a number of conclusions can be drawn.

- The successful formation of pure $CuInO_2$ clearly requires the careful control of Cu : In ratio. During simultaneous beaming of Cu, In, O onto the substrate, XPS measurements seemed to indicate that the general incorporation of Cu into the grown layers was inhibited by the presence of In. The bilayer diffusion method developed in chapter 3 was helpful in overcoming this problem, enabling reasonable control of the Cu : In stoichiometry in the film. With improved system design to focus on this feature (e.g. addition of beam flux monitors to the K-cells) the results suggest this control of stoichiometry is entirely feasible.
- As expected given the results in the previous chapter, the use of the bilayer approach also enables the achievement of the required Cu (I) oxidation state, as judged by XPS.
- XPS core level and valence band data are consistent with the formation of $CuInO_2$. XRD data also showed this to be the dominate phase at higher growth temperatures (800 ^oC) although, as is common with other approaches such as pulsed laser deposition (PLD), small amounts of other phases such as $Cu_2In_2O_5$ and Cu_2O are suggested which increase in concentration as the growth temperature is lowered.
- AFM measurements show a disordered rough film morphology at lower growth temperatures, whereas the formation of 3D islands can be seen at

800 ^{o}C growth temperature, suggesting that surface diffusion is significant at these higher temperatures. A unique film texture in which the copper oxide framework lies parallel to the substrate is suggested from XRD data, which differs significantly from that seen in PLD.

- It has been confirmed that Cr and Sn can also be incorporated into the grown films, and XPS peak shifts in the core levels and the valence band are consistent with *p*-type and *n*-type dopant modification of the electronic properties of the layers.
- Optical absorption measurements are consistent with a direct band gap of around 3.8 eV for the grown Cu-In oxide layers, in agreement with literature data on $CuInO_2$.

References

1. H. Kawazoe, M. Yasukawa, H. Hyodo, M. Kurita, H. Yanagi and H. Hosono, Nature **389** (6654), 939-942 (1997).

2. I. Hamberg and C. G. Granqvist, Journal of Applied Physics **60** (11), R123-R159 (1986).

3. K. L. Chopra, S. Major and D. K. Pandya, Thin Solid Films **102** (1), 1-46 (1983).

4. K. Ueda, T. Hase, H. Yanagi, H. Kawazoe, H. Hosono, H. Ohta, M. Orita and M. Hirano, Journal of Applied Physics **89** (3), 1790-1793 (2001).

5. H. Yanagi, T. Hase, S. Ibuki, K. Ueda and H. Hosono, Applied Physics Letters **78** (11), 1583-1585 (2001).

6. A. Kudo, H. Yanagi, H. Hosono and H. Kawazoe, Applied Physics Letters **73** (2), 220-222 (1998).

7. R. D. Shannon, D. B. Rogers and C. T. Prewitt, Inorganic Chemistry **10** (4), 713-718 (1971).

8. C. T. Prewitt, R. D. Shannon and D. B. Rogers, Inorganic Chemistry **10** (4), 719-723 (1971).

9. D. B. Rogers, R. D. Shannon, C. T. Prewitt and J. L. Gillson, Inorganic Chemistry **10** (4), 723-727 (1971).

10. W. Gessner, Silik at technik **21** (2), 45 (1970).

11. M. Shimode, M. Sasaki and K. Mukaida, Journal of Solid State Chemistry **151** (1), 16-20 (2000).

12. H. M. Rietveld, Journal of Applied Crystallography **2** (2), 65-71 (1969).

13. X. L. Nie, S. H. Wei and S. B. Zhang, Physical Review Letters **88** (6), 066405 (2002).

14. J. Robertson, P. W. Peacock, M. D. Towler and R. Needs, Thin Solid Films **411** (1), 96-100 (2002).

15. A. Thatribud and T. Pengpan, Physical Review B **90**, 115150 (2014).

16. T. Arnold, D. J. Payne, A. Bourlange, J. P. Hu, R. G. Egdell, L. F. J. Piper, L. Colakerol, A. Masi, P. A. Glans, T. Learmonth, K. E. Smith, J. Guo, D. O. Scanlon, A. Walsh, B. J. Morgan and G. W. Watson, Physical Review B **79** (7), 075102 (2009).

17. M. N. Huda, Y. F. Yan, A. Walsh, S. H. Wei and M. M. Al-Jassim, Physical Review B **80** (3), 035205 (2009).

18. J. Pellicer-Porres, A. Segura, A. S. Gilliland, A. Munoz, P. Rodriguez-Hernendez, D. Kim, M. S. Lee and T. Y. Kim, Applied Physics Letters **88** (18), 181904 (2006).

19. S. Gilliland, J. Pellicer-Porres, A. Segura, A. Munoz, P. Rodriguez-Hernandez, D. Kim, M. S. Lee and T. Y. Kim, Physica Status Solidi B-Basic Solid State Physics **244** (1), 309-314 (2007).

20. M. Younsi, S. Saadi, A. Bouguelia, A. Aider and M. Trari, Solar Energy Materials and Solar Cells **91** (12), 1102-1109 (2007).

21. S. Saadi, A. Bouguelia, A. Derbal and M. Trari, Journal of Photochemistry and Photobiology a-Chemistry **187** (1), 97-104 (2007).

22. Y. Kakehi, K. Satoh, T. Yotsuya, K. Masuko and A. Ashida, Japanese Journal of Applied Physics Part 1-Regular Papers Brief Communications & Review Papers **46** (7A), 4228-4232 (2007).

23. M. Trari, A. Bouguelia and Y. Bessekhouad, Solar Energy Materials and Solar Cells **90** (2), 190-202 (2006).

24. N. Koriche, A. Bouguelia and M. Trari, International Journal of Hydrogen Energy **31** (9), 1196-1203 (2006).

25. D. Shin, J. S. Foord, D. J. Payne, T. Arnold, D. J. Aston, R. G. Egdell, K. G. Godinho, D. O. Scanlon, B. J. Morgan, G. W. Watson, E. Mugnier, C. Yaicle, A.

Rougier, L. Colakerol, P. A. Glans, L. F. J. Piper and K. E. Smith, Physical Review B **80** (23), 233105 (2009).

26. O. Crottaz and F. Kubel, Zeitschrift Fur Kristallographie **211** (7), 481 (1996).

27. O. Crottaz and F. Kubel, Zeitschrift Fur Kristallographie **211** (7), 482 (1996).

28. J. Nordgren and R. Nyholm, Nuclear Instruments & Methods in Physics Research Section a-Accelerators Spectrometers Detectors and Associated Equipment **246** (1-3), 242-245 (1986).

29. J. Nordgren, G. Bray, S. Cramm, R. Nyholm, J. E. Rubensson and N. Wassdahl, Review of Scientific Instruments **60** (7), 1690-1696 (1989).

30. J. J. Yeh and I. Lindau, Atomic Data and Nuclear Data Tables **32** (1), 1-155 (1985).

31. P. Marksteiner, P. Blaha and K. Schwarz, Zeitschrift Fur Physik B-Condensed Matter **64** (2), 119-127 (1986).

32. D. J. Aston, D. J. Payne, A. J. H. Green, R. G. Egdell, D. S. L. Law, J. Guo, P. A. Glans, T. Learmonth and K. E. Smith, Physical Review B **72** (19), 195115 (2005).

33. S. Nikitine, J. B. Grun and M. Sieskind, Journal of Physics and Chemistry of Solids **17** (3-4), 292-300 (1961).

34. C. D. Wagner, L. E. Davis, M. V. Zeller, J. A. Taylor, R. H. Raymond and L. H. Gale, Surface and Interface Analysis **3** (5), 211-225 (1981).

35. G. Kresse and J. Furthmuller, Computational Materials Science **6** (1), 15-50 (1996).

36. G. Kresse and J. Hafner, Physical Review B **49** (20), 14251-14269 (1994).

37. M. A. Vanveenendaal and G. A. Sawatzky, Physical Review Letters **70** (16), 2459-2462 (1993).

38. T. Boske, K. Maiti, O. Knauff, K. Ruck, M. S. Golden, G. Krabbes, J. Fink, T. Osafune, N. Motoyama, H. Eisaki and S. Uchida, Physical Review B **57** (1), 138-141 (1998).

39. A. Koitzsch, J. Fink, M. S. Golden, K. Karlsson, O. Jepsen, O. Gunnarsson, L. L. Miller, H. Eisaki, S. Uchida, G. Yang and S. Abell, Physical Review B **66** (2), 024519 (2002).

40. C. C. B. Lynch, R. G. Egdell and D. S. L. Law, Chemical Physics Letters **401** (1-3), 223-226 (2005).

41. M. Sasaki and M. Shimode, Journal of Physics and Chemistry of Solids **64** (9-10), 1675-1679 (2003).

42. I. Konovalov, L. Makhova, D. Wett and M. Lorenz, Physica Status Solidi a-Applications and Materials Science **203** (11), 2861-2866 (2006).

43. C. W. Teplin, T. Kaydanova, D. L. Young, J. D. Perkins, D. S. Ginley, A. Ode and D. W. Readey, Applied Physics Letters **85** (17), 3789-3791 (2004).

44. J. Tauc, Grigorov.R and A. Vancu, Physica Status Solidi **15** (2), 627-637 (1966).

45. K. Santra, C. K. Sarkar, M. K. Mukherjee and B. Ghosh, Thin Solid Films **213** (2), 226-229 (1992).

5 $CuInO_2$ Thin Films by Pulsed Laser Deposition

One aim of this chapter is to characterise pulsed laser deposition (PLD) $CuInO_2$ layers and compare them with the films formed in the previous chapter. This provides greater insight into the characteristics of the differing methods. In addition, various results which provide insight into the electronic structure of the deposited layers are given, to enable understanding of the extent to which the electronic properties of the grown layers compare with theoretical calculation, and the properties of other copper-oxide-based materials.

5.1 Introduction

5.1.1 Background

In the past 25 years, pulsed laser deposition (PLD) has developed as an effective growth method for a wide range of thin films for current and future technologies. The judicious use of this technique provides versatility, flexibility, and rapid processing of many materials such as metals, binary compounds and especially multi-component phases such as complex chemical compounds [1].

In 1986, the discovery of high-temperature superconductors induced the predominant development of laser ablation techniques obtained from the invention of high power PLD light sources in the 1960s [2].

The work of Dijkamp and coworkers on high-temperature superconductors, $YBa_3Cu_3O_7$, can be traced back to early work from Smith and Turner in 1965 for the preparation of semiconductors and dielectric thin films [3, 4].

In the present day, the PLD technique is being applied to a broad range of material growth problems from single atomic layer to quasi-bulk crystalline materials with

thickness over 100 μm, and is used both for fundamental and applied research applications.

This chapter investigates the properties of $CuInO_2$ films prepared under a range of conditions using the PLD method. The films were prepared in a scientific collaboration with co-workers (A. Rougier group) who prepared the films [5]. In preliminary characterisation, they report that a higher pressure of oxygen introduces an increase in the oxygen content leading to a $CuInO_{2.1}$ composition for the thin film deposited at 5 Pa (5×10^{-2} mb) and a progressive loss of the delafossite structure., with a (012) preferred crystal orientation, as was remarked in the previous chapter with regard to PLD layers.

5.1.2 Typical Experimental Set-Up Used for PLD

With the PLD apparatus, materials are ablated from a target and deposited onto a relevant substrate in a vacuum chamber with a controlled atmosphere to form stoichiometric layers which characteristically are often found to closely match the target material. The basic PLD system at the Department of Physics at Colorado State University is shown schematically in figure 5.1 as being typical of the art [6, 7]. A focussed krypton fluoride (KrF) excimer laser with a wavelength of 248 nm is used as the light source and can be rastered over a rotating target. Material can be ablated from the target onto the substrate of interest which is situated in the vicinity and with line of sight to the target. The experiment is carried out at low pressure, either in vacuum or in the presence of some low pressure gas such as oxygen. The basis of the experiment is that material is moved with maintained stoichiometry from target to

substrate, although in the case of oxides, oxygen can be lost in the transfer so background oxygen is useful to help restore stoichiometry.

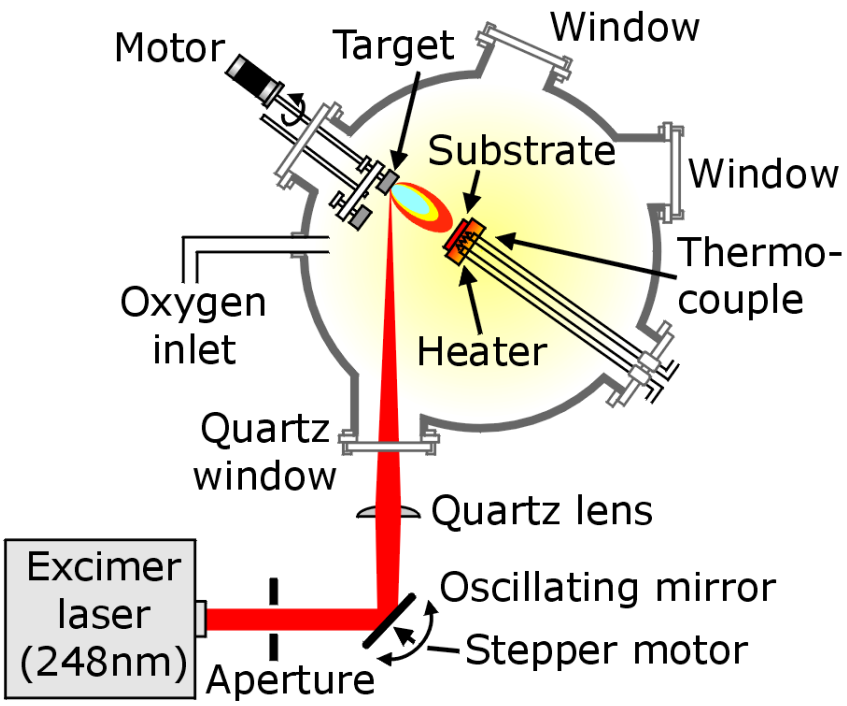


Figure 5.1. A schematic view of the typical available PLD set-up at the Magnetization Dynamics Group, Department of Physics, Colorado State University, USA. (adapted from ref. 6, 7)

5.2 Experimental Details

5.2.1 Synthesis of Target

As described in chapter 4, although delafossite-like oxides can be synthesized by cation-exchange or direct reaction under high pressure from solid materials, the preparation of bulk ceramic materials such as $CuInO_2$ is found to be rather

challenging, fundamentally since other compounds of these elements are easily formed or produced by decomposition of the desired material at the temperatures used. [8-10].

For this PLD film project, a $Cu_2In_2O_5$ target was therefore used rather than $CuInO_2$ as it is generally easier to synthesise [5, 11]. In contrast to $CuInO_2$ which undergoes decomposition, it can be formed by the simple heating of the relevant oxide mixtures, in this case In_2O_3 and CuO [12]. Since it has the correct Cu:In stoichiometric proportions, $Cu_2In_2O_5$ has the potential to be an appropriate target for $CuInO_2$ PLD, especially as the excess oxygen in the target compared to the desired product might easily be lost during the ablation process. Doping studies utilised targets in which CaO or SnO_2 was mixed in with the $Cu_2In_2O_5$ phase at varying concentrations (2 %, 5 % and 10 %) [13].

5.2.2 Film Preparation and Characterisation

The films were grown by PLD by Rougier group [5], using KrF excimer laser (Lambda Physik Compex 102, λ=248 nm) with 1-2 Jcm^{-2} flux and repetition rate of 1-20 Hz for 1hour. The base pressure in the chamber was in the order of 10^{-4} Pa (10^{-6} mbar). The substrate (Al_2O_3 (0001)) temperature was fixed at 550 ^oC. Oxygen was added to the vapour phase to compensate stoichiometric loss during ablation, and three differing oxygen pressures were used 1 x 10^{-2}, 2 x 10^{-3} and 5 x 10^{-4} mbar for the deposition. The substrate - target was set at a distance of 4 cm. Film thicknesses were in the range 1000-30,000 Å corresponding to deposition rates in the 0.6-0.8 Å/pulse [5]. High-resolution X-ray photoemission spectra were measured in the Scienta ESCA 300 spectrometer described previously. Binding energies are referenced to the Fermi energy of the silver (Ag) sample regularly used to calibrate the

spectrometer. X-ray emission spectra were measured for Cu delafossite on beamline 7.0.1 at the Advanced Light Source (ALS), Lawrence Berkeley National Laboratory by Smith group, Department of Physics, Boston University. X-ray diffraction (XRD) profiles of $CuInO_2$ films were obtained from a PANalytical X'Pert PRO diffractometer using monochromatic Cu Kα (λ=1.5418 Å) radiation and rotating spinner stage. Direct optical band gap energy of the films was measured in Shimadzu UV-2401 PC (λ=230~800 nm) with the Tauc relationship. AFM images were recorded ex-situ with a Digital Instruments Multimode SPM instrument.

5.3 Results

5.3.1 Stoichiometries of PLD $CuInO_2$; Effect of Oxygen Pressure

Undoped and bipolar doped $CuInO_2$ deposition films were formed by using the KrF PLD system as described above with a film thickness of about 350 nm using differing oxygen pressures of 5 x 10^{-4}, 2 x 10^{-3} and 1 x 10^{-2} mbar. Visually, the films show a slight golden colour. The deposited samples were analysed by XPS to determine stoichiometry via the Cu $2p_{3/2}$, In $3d_{5/2}$, O 1*s*, Sn $3d_{5/2}$ and Ca 2*p* transitions. Atomic sensitivity factors for XPS peaks were used to calculate empirical stoichiometries by division of the measured peak areas by the appropriate sensitivity factors; Cu $2p_{3/2}$ = 4.2, In $3d_{5/2}$ = 3.9, O 1*s* = 0.66, Sn $3d_{5/2}$ = 4.3 and Ca 2*p* = 1.58 [14]. As possibly expected if ablation results in loss of oxygen, an increase in oxygen pressure in the growth chamber is associated with an increase in the oxygen composition of the films, as shown in Table 5.1. Some variation in the composition ratio is also seen in the films, which appears reduced in Cu/In ratio (0.73 at 5 x 10^{-4} mbar, 0.57 at 2 x 10^{-3} mbar, 0.54 at 1 x 10^{-2} mbar) as well as In/O ratio (0.77 at 5 x 10^{-4} mbar, 0.59 at 2 x 10^{-3} mbar, 0.47 at 1 x 10^{-2} mbar). This trend continues again with an increase in

oxygen pressure. It suggests that either surface segregation of In is occurring, or that Cu is systematically lost from the growing layer.

Table 5.1 Stoichiometries of undoped films are determined by using XPSPEAK41 software with ESCA300 measurement data.

pO_2(mbar)	Thin Film Composition
$5x10^{-4}$	$Cu_{1.0}In_{1.4}O_{1.8}$
$2x10^{-3}$	$Cu_{1.0}In_{1.8}O_{3.0}$
$1x10^{-2}$	$Cu_{1.0}In_{1.9}O_{3.9}$

** See section 2.3.2 (g) for consideration of accuracy of quoted elemental compositions.*

Results in the presence of Ca or Sn are shown in table 5.2. Again fluctuations in stoichiometry are observed, with clear depletion of Cu being detected. Enrichment in the dopants is also seen, especially at high oxygen concentrations. It seems unlikely that metallic elements would be lost during the ablation process, since volatile metal reaction products are not obvious, so the overall conclusion probably is that significant surface segregation takes place during ablation.

Table 5.2 Stoichiometries of doped $CuInO_2$ films regarding growth conditions. Ratios of doped $CuInO_2$ were obtained by XPSPEAK41 software using the Cu $2p_{3/2}$, In $3d_{5/2}$ and O 1*s* regions with Sn $3d_{5/2}$ or Ca 2*p*.

PLD $CuInO_2$ films with bipolar doping by Sn (n-type) and Ca (p-type)

Target doping level	pO_2(mbar)	Sn-doped	Ca-doped
2 %	$5x10^{-4}$	$Sn_{0.02}Cu_{1.0}In_{1.1}O_{2.0}$	$Ca_{0.15}Cu_{1.0}In_{2.3}O_{3.3}$
	$2x10^{-3}$	$Sn_{0.03}Cu_{1.0}In_{1.7}O_{2.5}$	$Ca_{0.16}Cu_{1.0}In_{2.7}O_{3.8}$
	$1x10^{-2}$	$Sn_{0.02}Cu_{1.0}In_{1.2}O_{2.0}$	$Ca_{0.1}Cu_{1.0}In_{1.7}O_{4.1}$
5 %	$5x10^{-4}$	$Sn_{0.03}Cu_{1.0}In_{0.5}O_{1.1}$	$Ca_{0.2}Cu_{1.0}In_{1.8}O_{2.7}$
	$2x10^{-3}$	$Sn_{0.1}Cu_{1.0}In_{2.1}O_{3.3}$	$Ca_{0.3}Cu_{1.0}In_{2.7}O_{3.9}$
	$1x10^{-2}$	$Sn_{0.05}Cu_{1.0}In_{1.1}O_{2.3}$	$Ca_{0.11}Cu_{1.0}In_{1.6}O_{3.2}$
10 %	$2x10^{-3}$	$Sn_{0.3}Cu_{1.0}In_{3.0}O_{5.1}$	$Ca_{0.19}Cu_{1.0}In_{1.3}O_{5.7}$
	$1x10^{-2}$	$Sn_{0.2}Cu_{1.0}In_{2.2}O_{4.3}$	$Ca_{0.27}Cu_{1.0}In_{2.0}O_{5.4}$

** See section 2.3.2 (g) for consideration of accuracy of quoted elemental compositions.*

5.3.2 X-ray Photoemission Spectra and the Occupied Density of States

Figure 5.2 shows a typical survey scan X-ray photoemission spectra of $CuInO_2$ grown film by pulsed laser deposition with oxygen pressure of 5×10^{-4} mbar. In this survey scan, expected core and Auger peaks associated with the matrix elements are observed suggestive of phase purity although a C 1*s* line is seen which probably arises from adventitious carbon picked up during sample exposure to atmosphere.

Valence band X-ray photoemission spectra of $CuInO_2$ are shown as figure 5.3 (a) and (b) with respect to oxygen pressure of 1×10^{-2} and 5×10^{-4} mbar. These spectra also are compared with the density of states result of $CuInO_2$ from the band structure calculations with the partial contributions, as shown in figure 5.3(c) [15]. Figure 5.3 (a) and (b) show that four features labeled I-IV may be identified in ESCA300 data of the PLD $CuInO_2$ epitaxial film. The data seems better defined at the lower oxygen pressures and is consistent with the formation of $CuInO_2$ and resembles the valence band spectra of the films grown by OPABE as discussed in the previous chapter.

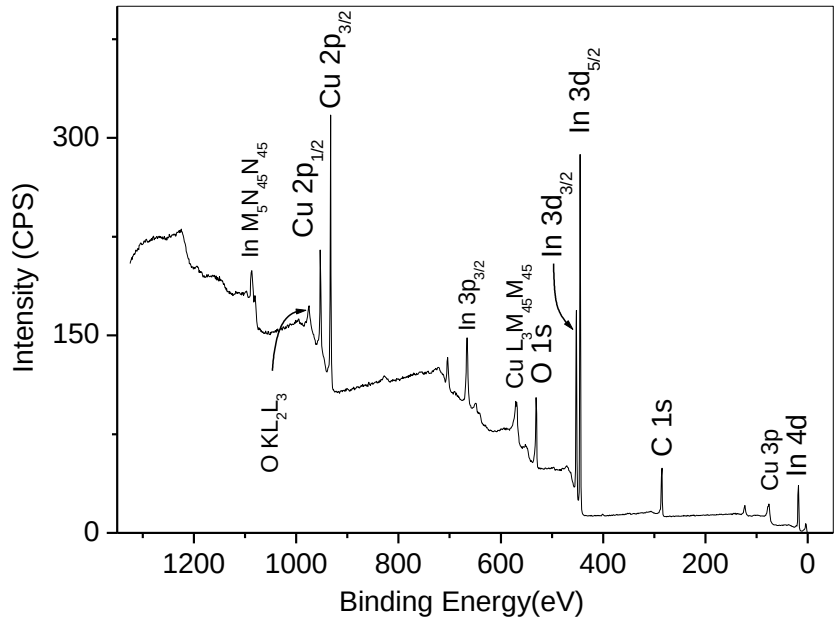


Figure 5.2. XPS (ESCA300) survey scan of undoped $CuInO_2$ thin film on sapphire (*c*-axis Al_2O_3, (0001)) substrate by PLD growth. Film thickness and oxygen pressure are 350 nm and 5 x 10^{-4} mbar, respectively.

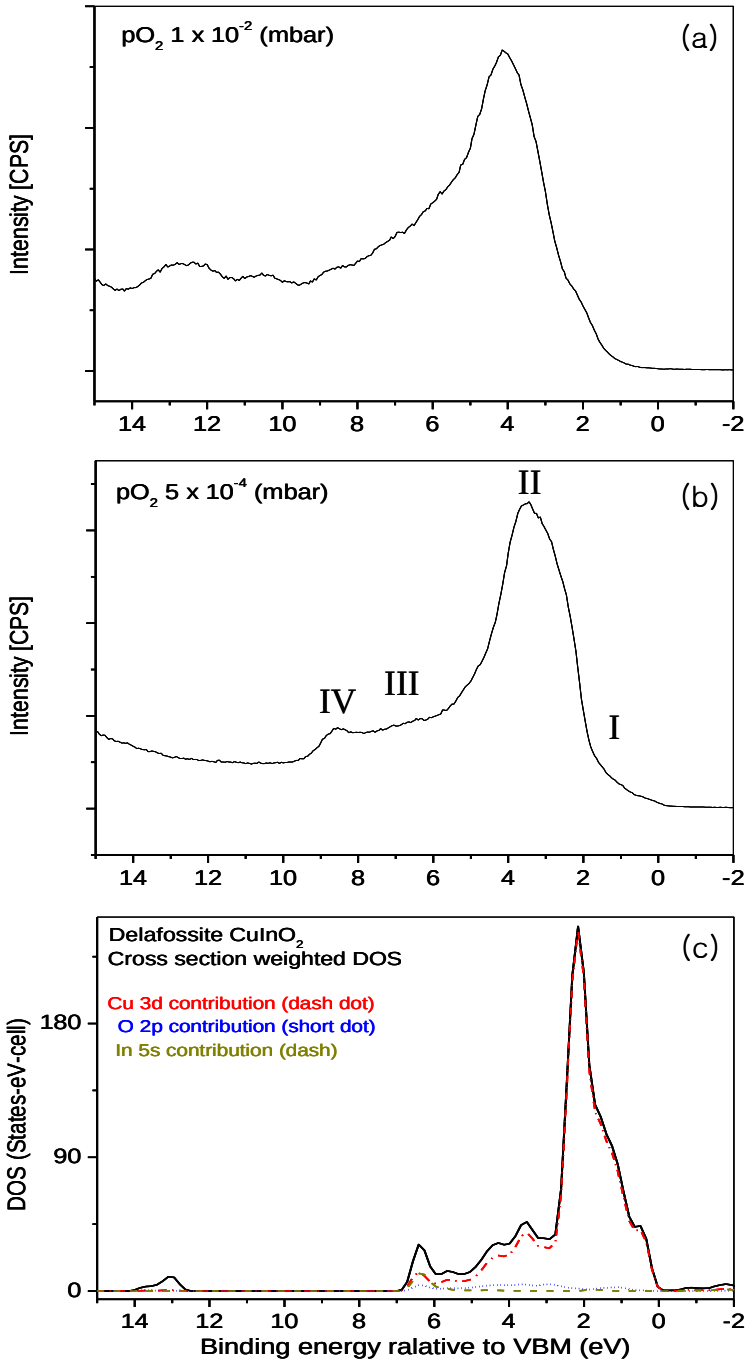


Figure 5.3. Al Kα, $h\nu$ = 1486.6 eV excited valence band XPS (ESCA300) with pO_2 : (a) 1 x 10^{-2} mbar, (b) 5 x 10^{-4} mbar and (c) theoretical cross section weighted DOS including Cu 3*d*, O 2*p* and In 5*s* PDOS for $CuInO_2$ (DFT) [15].

Experimental core level data for Cu 2*p* Al Kα XPS are shown in figure 5.4, which includes comparison between the 5% Sn-doped and intrinsic $CuInO_2$ films grown by PLD. These films of undoped and Sn-doped $CuInO_2$ were grown by pulsed laser deposition with oxygen pressure of 5 x 10^{-4} mbar which seemed to produce the best results for the valence band spectra as discussed above. The spectrum of the undoped material is very similar to that presented in the previous chapter and confirms that Cu (I) is the predominant oxidation state, even though Cu (II) was present in the target spectrum.

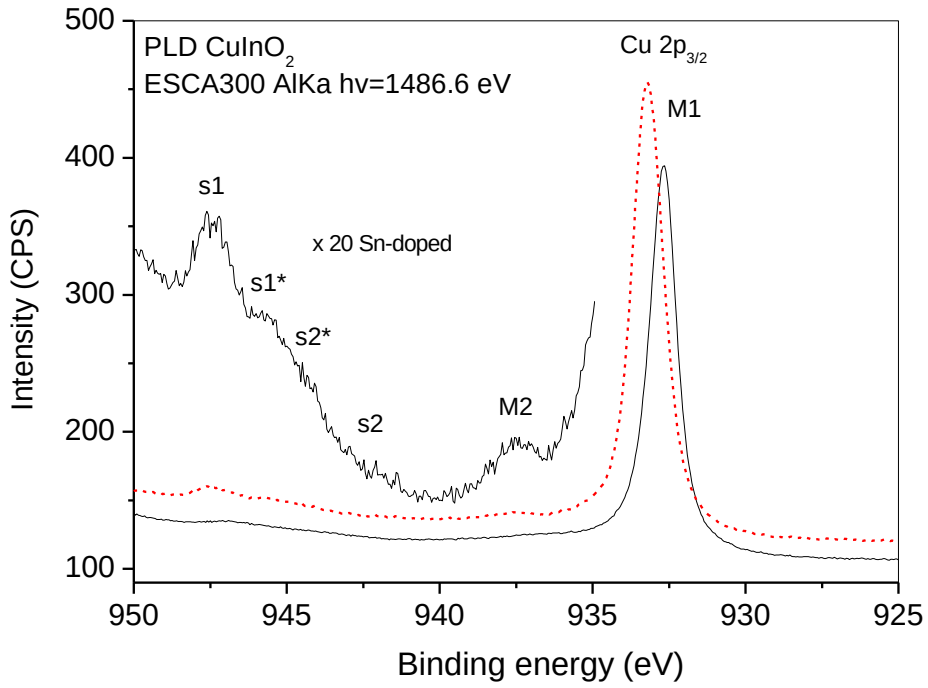


Figure 5.4. XPS (Al *K*α, hv=1486.6 eV) spectra in the Cu 2*p* region of PLD $CuInO_2$ films using ESCA300 in Daresbury Laboratory, UK. The BE regions with 935~950 eV shows the 20 times magnified spectrum of 5% Sn-doped $CuInO_2$ film. These thin films (thicknesses = 350 nm) were prepared with pO_2 of 5 x 10^{-4} mbar or 0.05 Pa. Black solid line: undoped, red dot: Sn-doped, upper zig-zag line: x 20 magnified Sn-doped film

As explained in chapter 3, the Cu $2p_{3/2}$ component (M1) agrees with a Cu $3d^{10}$ configuration in the final state arising from Cu(I),with the expected satellite peaks M2, S1, S2, S1*,S2*. The shift in the M1 feature which can be seen in the figure above using the Sn-containing target is consistent with n-type doping producing an upward shift in the Fermi level for this sample, as discussed further below.

5.3.3 X-ray Emission Spectra with PDOS of Cu 3*d* and O 2*p*

The non resonant Cu L_3 X-ray emission spectrum of PLD $CuInO_2$ and the calculation of the Cu 3*d* PDOS are compared in figure 5.5. The $CuInO_2$ films were prepared under an oxygen ambient with $pO_2 = 5 \times 10^{-3}$ mbar. . The Cu L_3 XES spectrum excited well above the absorption threshold consists of a single peak with broad wings. Fundamentally, the radiative decay spectrum is expected to contain contributions from both the Cu 4*s* and Cu 3*d* partial density of states, but the matrix elements connecting the Cu 2*p* core hole with the Cu 4*s* states are expected to be very much smaller than the corresponding matrix elements for Cu 3*d* states [16-18]. The spectra are lined up at maximum peak height. The Cu L_3 emission spectrum corresponds to the valence band XPS data as described below, in terms of the Cu 3*d* state peak II, but the low binding energy peak I and the O 2*p* valence band peaks III and IV seem to make a small contribution to the Cu L_3 XES. The oxygen *K* shell emission spectra and O 2*p* partial density of states are shown in figure 5.6 [15]. The O *K* XES data are dominated by the O 2*p* PDOS due to strong dipole selection rules for the decay of the core hole [16-18]. The O *K* XES spectrum can also be compared with the valence band XPS; the low binding energy peaks I and II are observed in reduced intensity in O *K* emission, but the spectrum is dominated by bands III and IV

connected with O 2*p* states. The change of intensity between XES and XPS thus demonstrates that the states in the upper part of valence band which gives rise to peaks I and II are of dominant Cu 3*d* character, whereas the states in the bottom half of the valence band associated with III and IV are of dominant O 2*p* character. The nonvanishing intensity of I in O *K*-edge XES is a direct consequence of hybridisation between Cu 3*d* and O 2*p* states arising from σ and π overlap within the O-Cu-O dumbbells. Conversely most of the intensity of peaks III and IV in XPS arises not from the O 2*p* states themselves but from the hybridisation of Cu 3*d* state with O 2*p* states in the bottom half of the valence band. The energy shift between peak I and II arises from the fact that the latter is associated with nonbonding Cu 3*d* states of δ symmetry within the linear O-Cu-O units [17]. Unlike the σ and π states, the δ states cannot hybridise with O 2*p* states and do not appear in XES [19, 20].

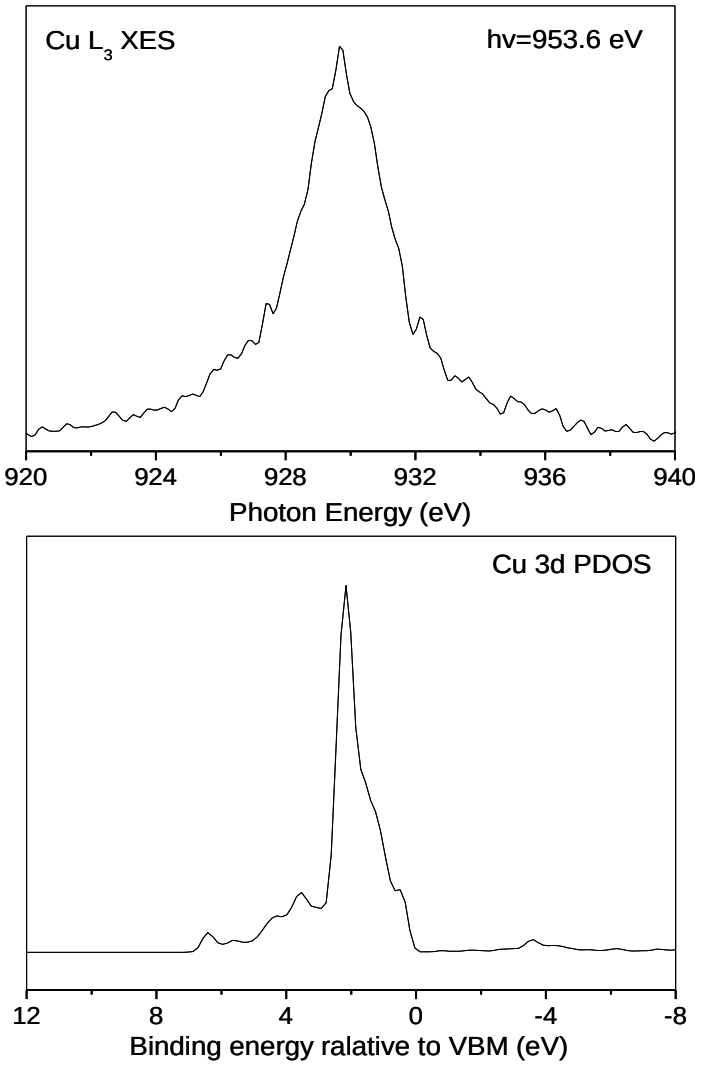


Figure 5.5. Upper panel: non resonant Cu L_3 X-ray emission spectrum of PLD $CuInO_2$. Lower panel: calculated Cu 3*d* partial density of states aligned highest peak to Cu L_3 XES highest intensity [15].

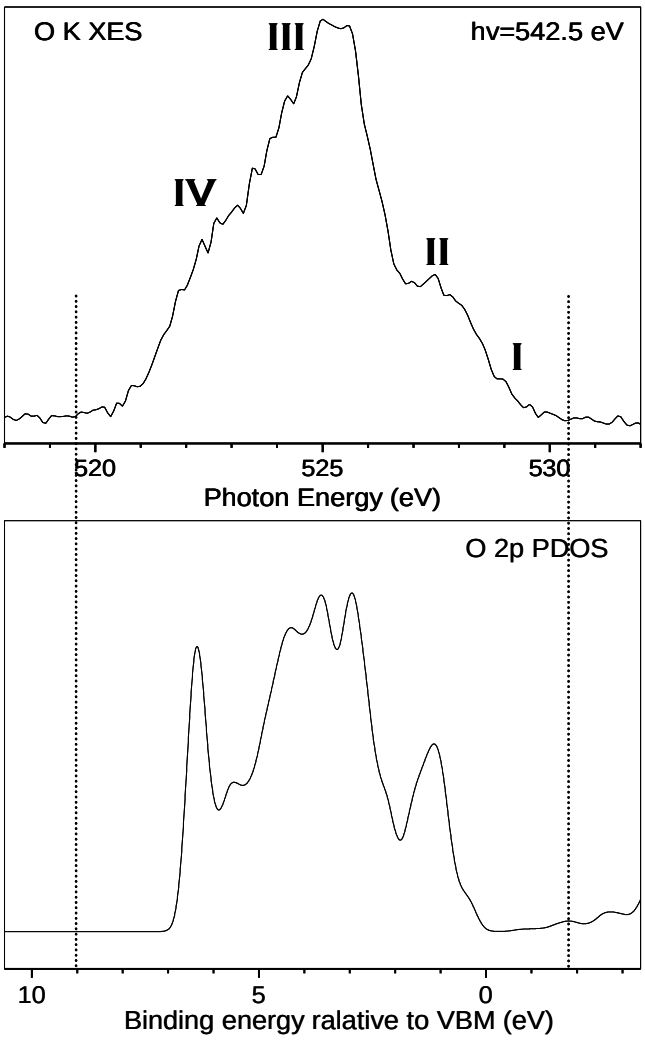


Figure 5.6. Upper panel: non resonant O *K* X-ray emission spectrum of PLD $CuInO_2$. Lower panel: calculated O 2*p* partial density of states adjusted maximum peak to O *K* XES highest intensity [15].

5.3.4 X-ray Absorption Spectra and Resonant X-ray Emission Spectra

The Cu L_3 absorption spectrum of $CuInO_2$ is shown in figure 5.7(a). The $CuInO_2$ films again were prepared by pulsed laser deposition under an oxygen ambient with $pO_2 = 5 \times 10^{-3}$ mbar [5]. The spectrum has two sharp peaks at 931.2 eV and 933.8 eV. The first strong peak labeled *p* at 931.2 eV is associated with the Cu (II) $3d^9$ state, hole in the Cu 3*d* valence band. This peak *p* is very close to the photon energy of the main peak of 931.3 eV in the Cu L_3 XAS spectrum of CuO [21]. It also could be considered due to oxidation due to air contamination of the surface on the PLD film, although the sample was assigned as entirely Cu (I) oxidation state by XPS. The main asymmetric Cu L_3 peak labeled *m* of 933.7 eV is located in same place as in Cu_2O of 933.7 eV [20]. The Cu L_3-edge XAS of this film shows at least three leading shoulders *A*, *B* and *C* with 937.6 eV, 941.1 eV and 944.6 eV, respectively. The leading peaks correspond to mixing with Cu 3*d*, 4*s*, 4*p* and O 2*p* character [21].

Near resonant Cu L_3 X-ray emission spectra are shown in figure 5.7(b) corresponding to excitation photon energies in the range 931 eV to 944.5 eV. Single broad peaks are observed that gradually move to higher photon energy area with increasing excitation energy for the smaller excitation energies. This energy shift is evidence of inelastic scattering phenomena like that seen in the Cu L_3 edge XES of Cu_2O [20], $CuAlO_2$ [18] and $CuCrO_2$ [16] associated with energy losses of 4.5 eV, 5.4 eV and 4.7 eV, respectively. These loss energy values demonstrate that both 3*d* to 4*s* and 3*d* to 3*d*, the inter band excitations are allowed by the $\Delta l = 0, \pm 2$ selection rule [16, 20].

The results of O *K*-edge X-ray absorption spectroscopy of PLD $CuInO_2$ film are shown in figure 5.8(a). The vertical dotted line indicates the photon energies used in excitation of resonant X-ray emission spectra. The three lowest energy features (a) are associated with antibonding conduction band states of the mixed Cu $3d_z^2$, Cu 4*s*

and O 2p_z orbitals characteristic of linear O-Cu-O coordination, in other related oxide materials.[16, 18, 20] The two higher energy peaks with maxima at 538.5 and 542.5 eV involve the antibonding states derived from the mixing between O 2*p* and In 5*s*, 5*p* states of InO_2 coordination [16, 18, 20]. Resonant O *K* shell X-ray emission spectra excited over the range of photon energies close to threshold are shown in figure 5.8(b). There is a slight change in the spectra along with varying photon energy suggestive of a simple emission process dominated by inelastic X-ray scattering and the occupied O 2*p* partial density of states [16, 20].

In conclusion, the electronic properties of the grown PLD layers seem to be fully consistent with the expected properties, based on calculation and results recorded in analogous copper oxide based materials [16, 22, 23].

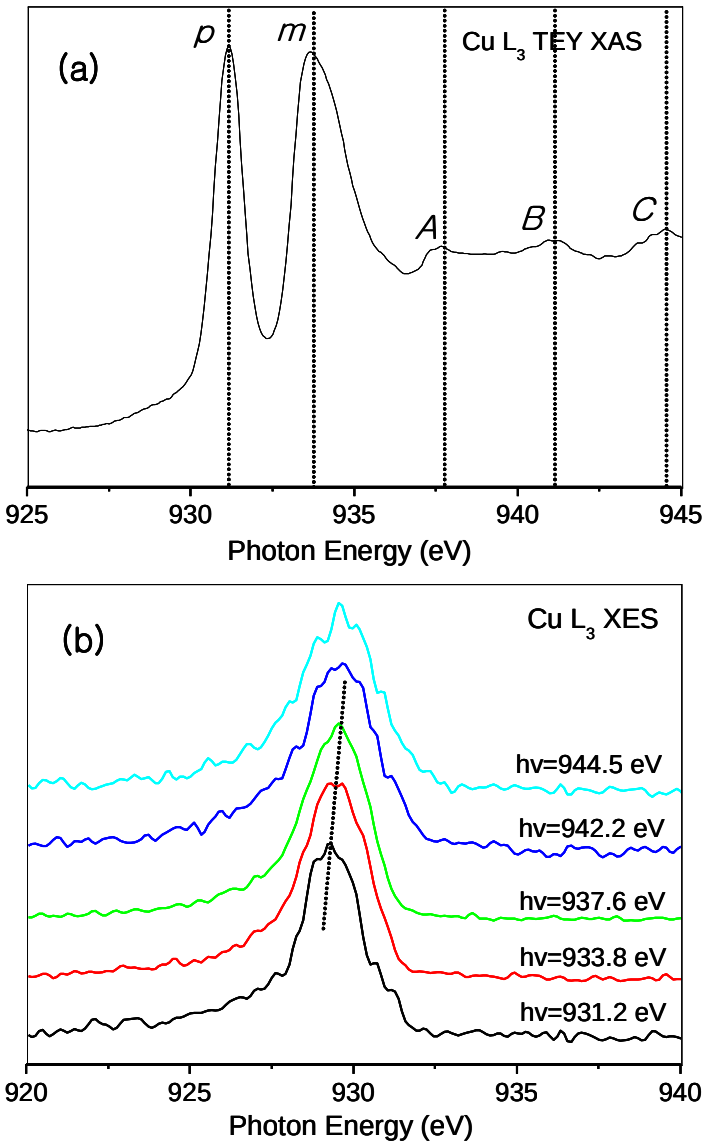


Figure 5.7. (a) Total electron yield (TEY) Cu L_3 X-ray absorption spectrum of PLD $CuInO_2$ film. The vertical dotted line indicates the photon energies used in excitation of resonant X-ray emission spectra. (b) Cu L_3 X-ray emission spectra of $CuInO_2$ film excited at the indicated photon energies. Single broad peak gradually moves to higher photon energy with increasing excitation energy.

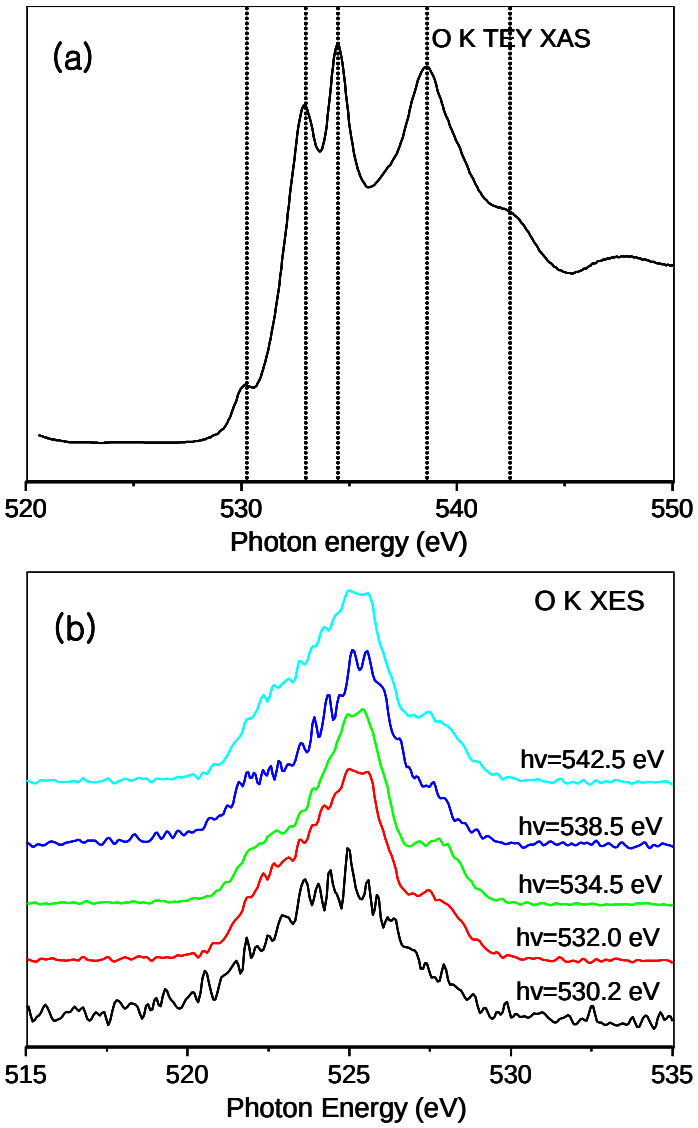


Figure 5.8. (a) Total electron yield (TEY) O *K* shell X-ray absorption spectrum of PLD $CuInO_2$ film. The vertical dotted line indicate the photon energies used in excitation of resonant X-ray emission spectra (b) O *K* shell X-ray emission spectra of $CuInO_2$ film excited at the indicated photon energies.

5.3.5 Bipolar Doping for PLD $CuInO_2$ Thin Films

Analysis of $CuInO_2$:Ca and $CuInO_2$:Sn thin films deposited with oxygen pressure of 5 x 10^{-4}, 2 x 10^{-3} and 1 x 10^{-2} mbar, was carried out using samples of film thickness about 350 nm.

Figure 5.9 shows XPS spectra of samples prepared with 5% Ca target (upper panel) and 5% Sn target doping (low panel) . However actual Ca doping levels in pO_2 5 x 10^{-4} mbar are estimated to be 11.1 % (ratio of Ca 2*p*/In 3$d_{5/2}$, $Ca_{0.20}Cu_{1.0}In_{1.8}O_{2.7}$). Probably surface segregation is responsible for the disparity. In the same manner, the measured Sn doping level in pO_2 2 x 10^{-3} mbar, shows about 4.8 % (ratio of Sn 3$d_{5/2}$/In 3$d_{5/2}$, $Sn_{0.10}Cu_{1.0}In_{2.1}O_{3.3}$) somewhat similar to the target at this low oxygen pressure. See section 2.3.2 (g) for consideration of accuracy of quoted elemental compositions.

The valence band X-ray photoemission spectra of the PLD $CuInO_2$ films noted above are shown in figure 5.10, along with the undoped layer. The Fermi level in nominally undoped $CuInO_2$ lies in above the valence band maximum. In these valence band spectra, both Ca-doped and Sn-doped $CuInO_2$ films show changes in binding energies as compared with the undoped film. For the Ca-doped $CuInO_2$ film, the valence band level shift is quite clear of the order of 1.1 ± 0.05 eV, suggestive of p-type doping [24]. In a similar manner, the Sn-doped $CuInO_2$ film shows an apparent shift in binding energies in the opposite direction of the order of 0.5 ± 0.05 eV.

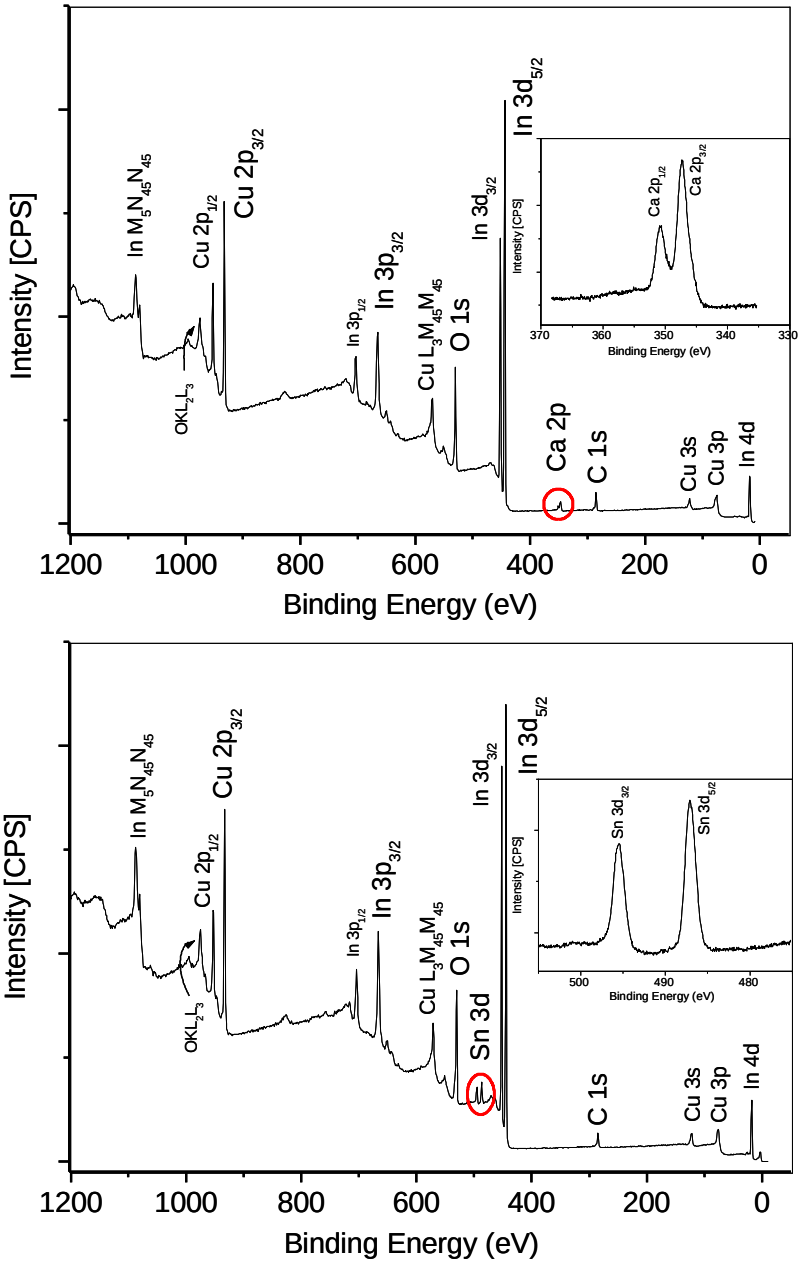


Figure 5.9. Upper panel: XPS (Al *K*α, *hv*=1486.6 eV) spectra of 5% targeted Ca-doped $CuInO_2$ in PLD growth film, pO_2 = 5 x 10^{-4} mbar, F/T = 350 nm. Lower panel: XPS spectra of 5% targeted Sn-doped $CuInO_2$ in PLD film, pO_2 = 2 x 10^{-3} mbar, F/T = 350 nm. These spectra were obtained by using the ESCA300 spectrometer at Daresbury Laboratory. Actual doping levels were identified to be 11.1 % and 4.8 % for Ca and Sn, respectively.

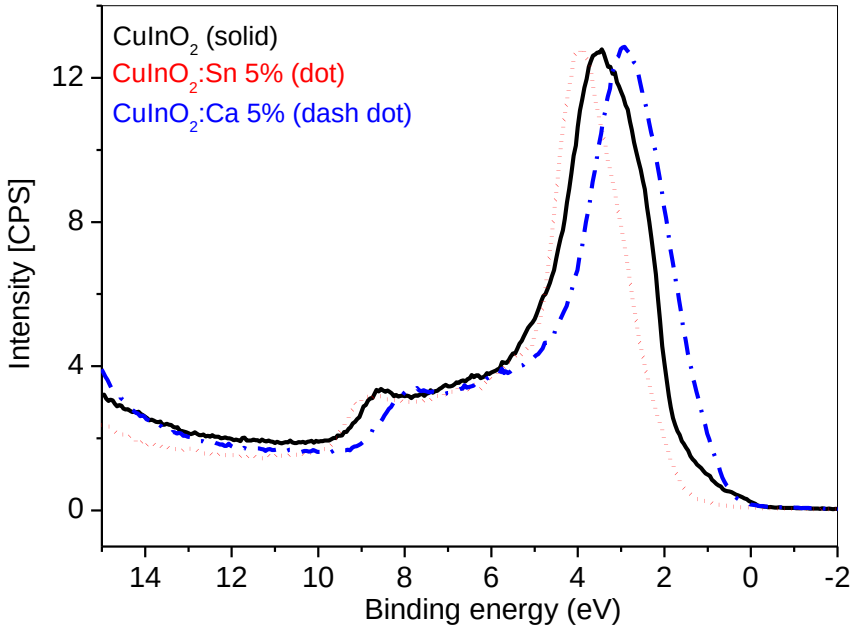


Figure 5.10. Valence band X-ray photoemission spectra of $CuInO_2$ (Al *K*α, *hν* = 1486.6 eV); undoped (black solid, $pO_2 = 5 \times 10^{-4}$ mbar, F/T = 350 nm), 5% targeted Sn-doped (red dot, 2×10^{-3} mbar, F/T = 350 nm), 5% targeted Ca-doped (blue dash dot, $pO_2 = 5 \times 10^{-4}$ mb, F/T = 350 nm). Actual doping levels were identified to be 11.1 % and 4.8 % for Ca and Sn, respectively.

5.3.6 X-ray Diffraction of PLD $CuInO_2$ Thin Films

Figure 5.11 shows XRD patterns of $CuInO_2$:Ca and $CuInO_2$:Sn polycrystalline thin films and the Ca-doped target for pulsed laser deposition. The peaks observed index with those from $CuInO_2$ delafossite, except for those due to the sapphire substrate [11, 13]. The films with Sn doping show preferential orientation along the *c*-axis. By contrast, no preferred orientation was observed for the thin films with Ca doping [13].

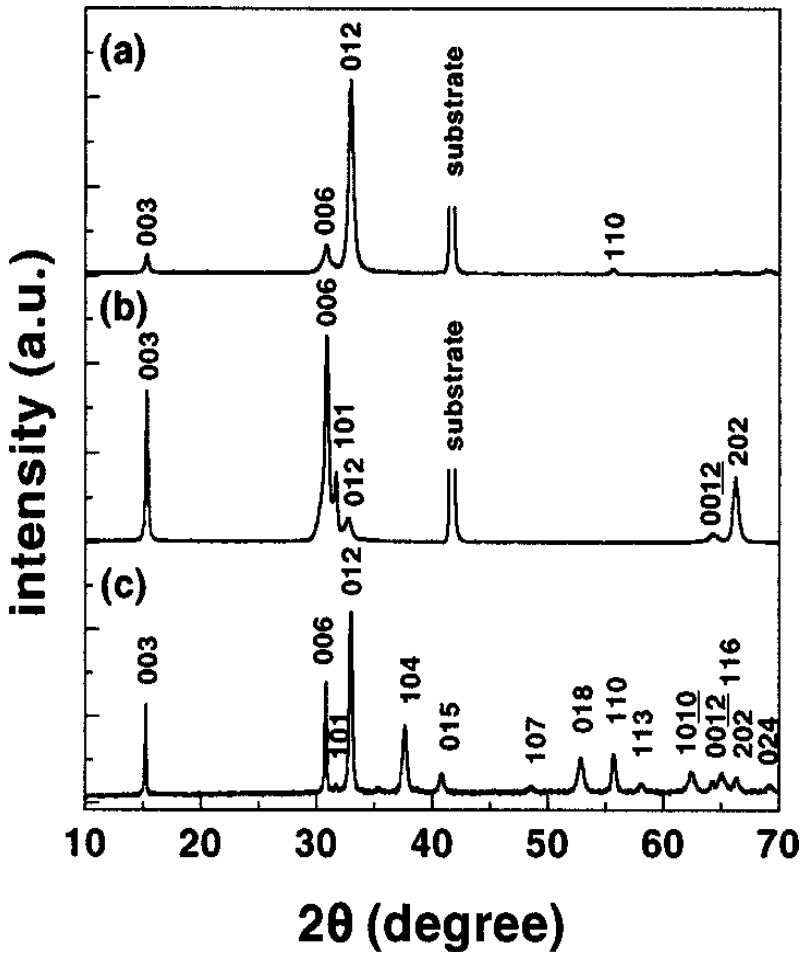


Figure 5.11. X-ray patterns of (a) Ca 7% -doped $CuInO_2$ thin film, (b) Sn 5% -doped $CuInO_2$ thin film, and (c) ceramic pellet. (Cu *Kα* radiation λ=1.5418 Å, RIGAKU: Rint-2500) oxygen pressure of (a) 1.0 Pa (1.0 x 10^{-3} mb), (b) 1.4 Pa (1.4 x 10^{-3} mb), and (c) the disk sintered at 673 K for 24 h in vacuum (~ 10^{o} Pa). (adapted from Yanagi *et al.* [13])

The structure and crystallinity of the PLD $CuInO_2$ films are very strongly dependent on the growth conditions. Figure 5.12 shows the evolution of the X-ray diffraction (XRD) patterns with decreasing oxygen pressure. Decreasing oxygen pressure is associated with an enhancement in crystallinity with films showing a (006) preferred direction. Unfortunately, low oxygen pressures result in the appearance of indium oxide and copper oxide.

Figure 5.13 shows XRD profiles of p-type $CuInO_2$ films with 2%, 5% and 10% Ca doping with oxygen pressure of 1 x 10^{-2} mbar. Actually, these films show different stoichiometry, as seen in table 5.2. A larger amount of the Ca dopant is consistent with improving the (012) reflection, tilted 23.7^o to the *c*-axis [25]. In case of 10% Ca doping, there is near perfect single crystalline in the film, as seen in figure 5.13 (c). This change is not seen for the Ca doped films as the Ca concentration increases.

Figure 5.14 also shows XRD patterns of *n*-type $CuInO_2$ films with 2%, 5%, and 10% Sn for doping with oxygen pressure of 1 x 10^{-2} mbar. In the same manner as p-type films, the Sn dopant gives rise to an enhanced (012) reflection.

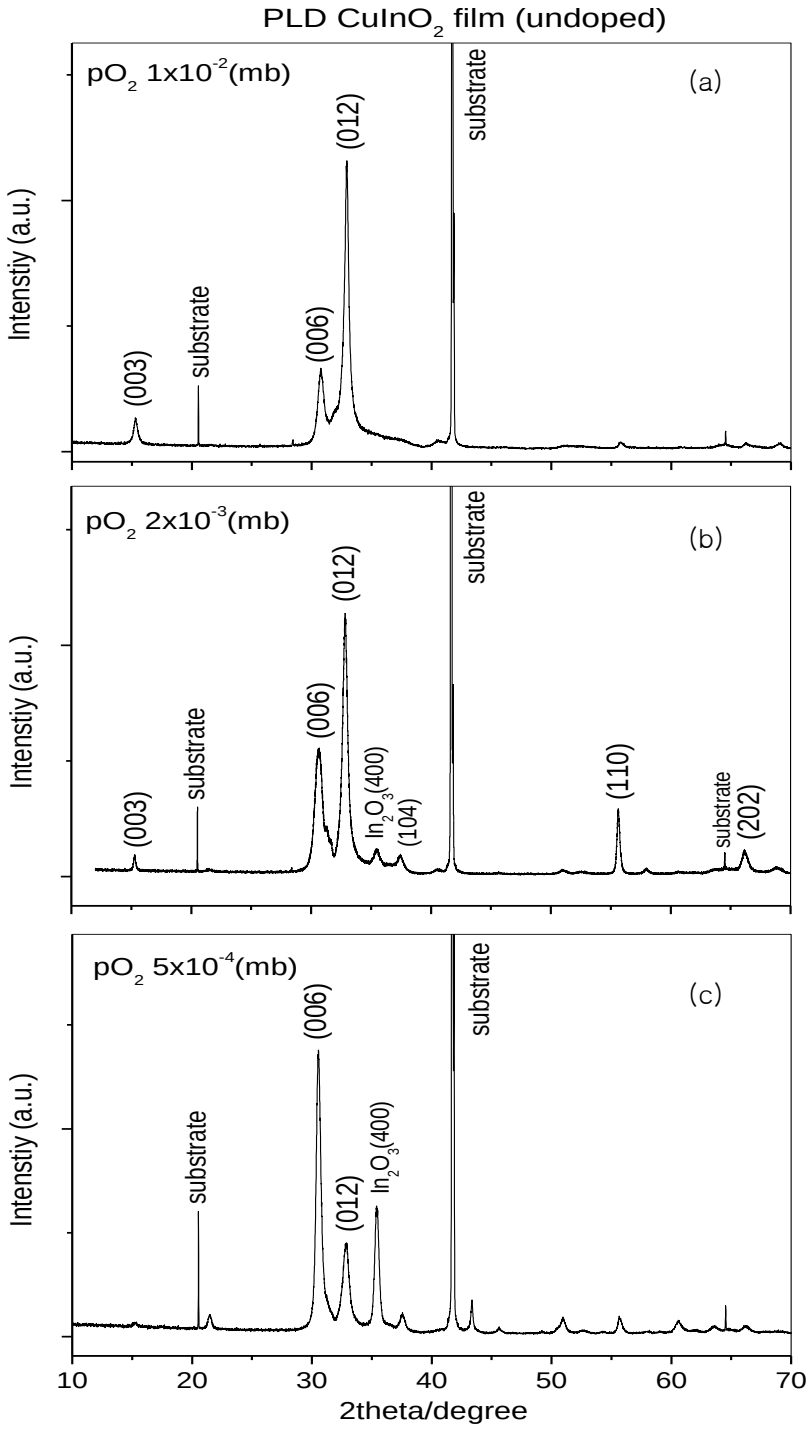


Figure 5.12. X-ray diffraction (monochromatic Cu *Kα* radiation λ = 1.5418 Å) patterns of pulsed laser deposited $CuInO_2$ films under oxygen pressure of (a) 1 x 10^{-2} mbar, (b) 2 x 10^{-3} mbar, and (c) 5 x 10^{-4} mbar.

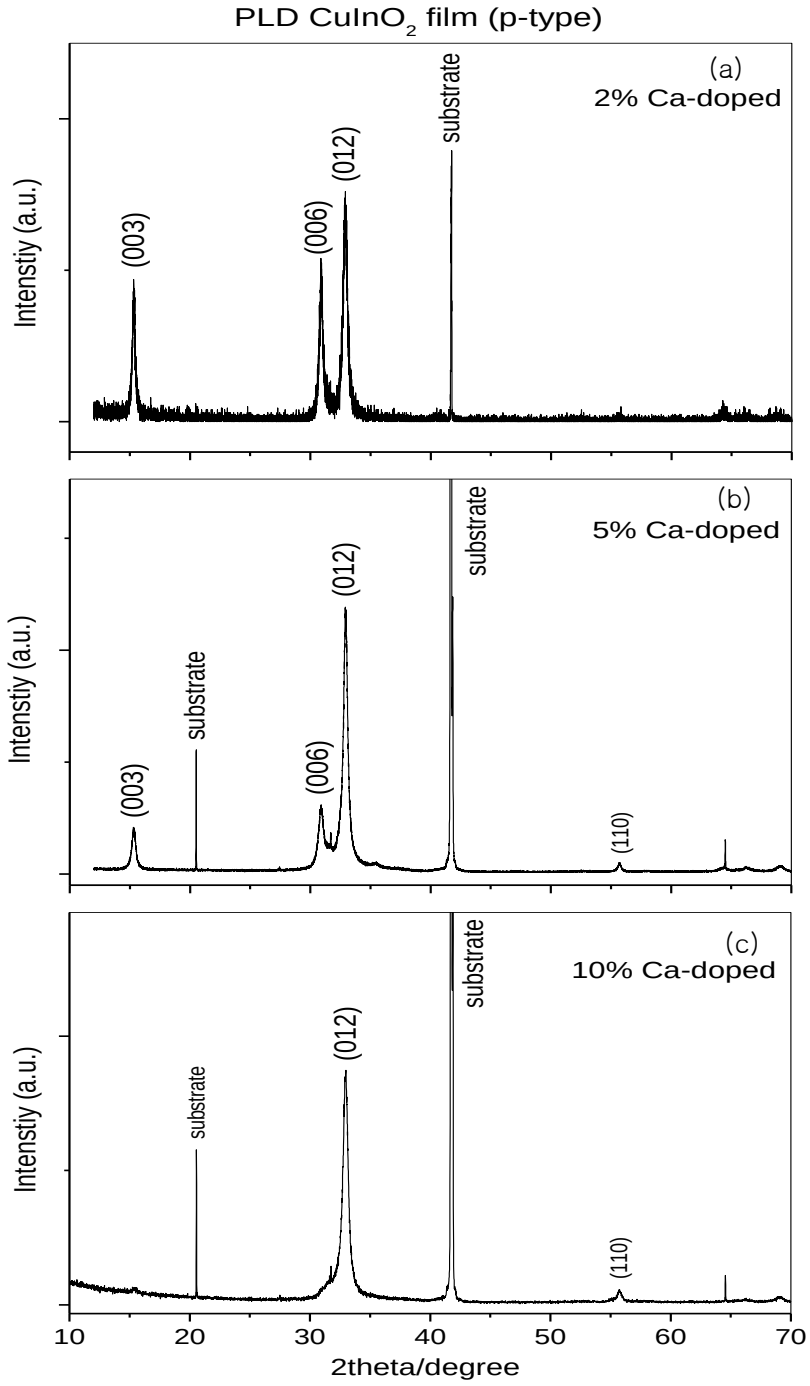


Figure 5.13. X-ray diffraction (monochromatic Cu *Kα* radiation λ = 1.5418 Å) patterns of pulsed laser deposited p-type $CuInO_2$ films under pO_2 of 1 x 10^{-2} mbar. Ca doping with (a) 2%, (b) 5%, and (c) 10% for the synthetic targets

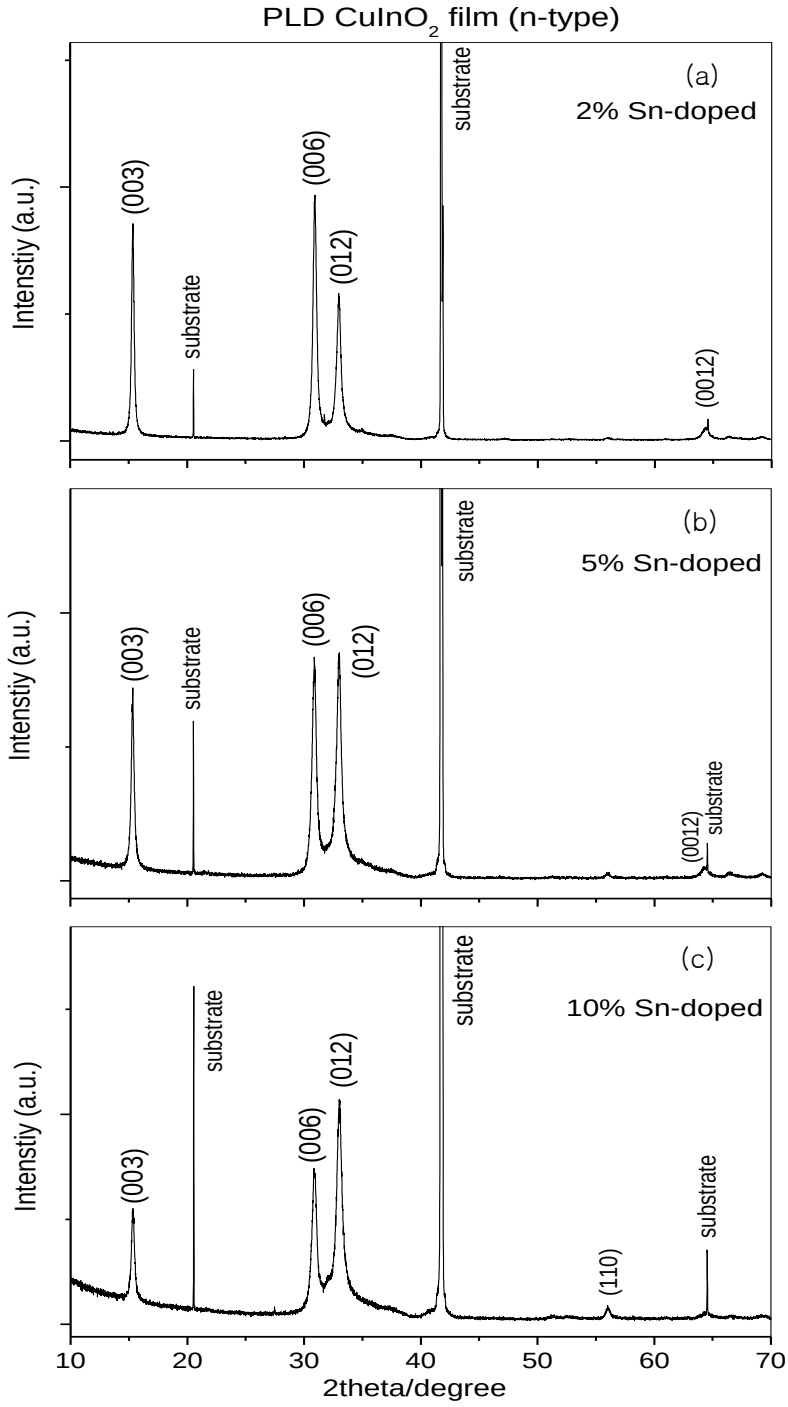


Figure 5.14. X-ray diffraction (monochromatic Cu *Kα* radiation λ = 1.5418 Å) patterns of pulsed laser deposited n-type $CuInO_2$ films under pO_2 of 1 x 10^{-2} mbar. Sn doping with (a) 2%, (b) 5%, and (c) 10% for the synthetic targets

5.4 Summary

Analysis of $CuInO_2$ thin films prepared by PLD was carried out. XPS suggested that significant changes in stoichiometry were occurring in the deposited layers, in particular enrichment of Ca and Sn dopants and Cu depletion, with the results being sensitive to oxygen partial pressure. It is suggested this arises simply from surface segregation of particular species to the surface, which might reasonably be thought to depend on the oxygen pressure. However it should be borne in mind that the cation ratio deviations in PLD can also be caused by a fluence dependence of the ablation rate of species from the target [26] and also by target inhomogeneities and differential scattering in the PLD plume [27].

- Overall the conclusion is that the greatest strength of PLD – stoichiometric transfer – cannot be readily confirmed from the available data.
- XRD results indicate also that the films deposited at low growth oxygen pressure show the existence of other phases in the deposited films, namely indium and copper oxides, in addition to the dominant parent phase. Differing crystal orientation dependencies are seen depending on growth conditions, and are also different to those seen by OPABE as discussed in the preceding chapter. XPS also indicated that Cu (I) was the dominant oxidation state.
- Detailed valence band XPS, XES and XAS measurements were used to demonstrate that the electronic properties of the deposited layers were consistent both with calculations, and with the known electronic properties of other copper based oxide materials. XPS energy shifts were also consistent

with use of Ca and Sn in the ablation target as p-type and n-type dopant, proving bipolar doping can be achieved using this approach.

It is interesting to compare the results with those provided by OPABE in the previous chapter. Both PLD and OPABE can clearly be used for the growth of $CuInO_2$. Complications, such as control of stoichiometry, seem to exist with both approaches. The advantage with OPABE would appear to be that large changes in process conditions such as metal flux to the surface can readily be achieved to enable such factors to be controlled. In addition, sample size of OPABE could be formed than PLD. Conversely, the disadvantage of OPABE is that the all the variables *do* need to be carefully controlled. This is much less the case in PLD, where at least approximate control of stoichiometry is achievable, but where otherwise the variation in experimental variables which can be exploited is more limited.

References

1. R. Eason, *Pulsed laser deposition of thin films : applications-led growth of functional materials*. (Wiley-Interscience, Hoboken, N.J., 2007).

2. J. G. Bednorz and K. A. Muller, Zeitschrift Fur Physik B-Condensed Matter **64** (2), 189-193 (1986).

3. H. M. Smith and A. F. Turner, Applied Optics **4** (1), 147-148 (1965).

4. D. Dijkkamp, T. Venkatesan, X. D. Wu, S. A. Shaheen, N. Jisrawi, Y. H. Minlee, W. L. Mclean and M. Croft, Applied Physics Letters **51** (8), 619-621 (1987).

5. C. Yaicle, A. Blacklocks, A. V. Chadwick, J. Perriere and A. Rougier, Applied Surface Science **254** (4), 1343-1346 (2007).

6. Y. Y. Song, S. Kalarickal and C. E. Patton, Journal of Applied Physics **94** (8), 5103-5110 (2003).

7. C. A. Carosella, D. B. Chrisey, P. Lubitz, J. S. Horwitz, P. Dorsey, R. Seed and C. Vittoria, Journal of Applied Physics **71** (10), 5107-5110 (1992).

8. R. D. Shannon, D. B. Rogers and C. T. Prewitt, Inorganic Chemistry **10** (4), 713-718 (1971).

9. C. T. Prewitt, R. D. Shannon and D. B. Rogers, Inorganic Chemistry **10** (4), 719-723 (1971).

10. D. B. Rogers, R. D. Shannon, C. T. Prewitt and J. L. Gillson, Inorganic Chemistry **10** (4), 723-727 (1971).

11. M. Shimode, M. Sasaki and K. Mukaida, Journal of Solid State Chemistry **151** (1), 16-20 (2000).

12. L. Makhova, D. Wett, M. Lorenz and I. Konovalov, Physica Status Solidi a-Applications and Materials Science **203** (11), 2861-2866 (2006).

13. H. Yanagi, T. Hase, S. Ibuki, K. Ueda and H. Hosono, Applied Physics Letters **78** (11), 1583-1585 (2001).

14. C. D. Wagner, L. E. Davis, M. V. Zeller, J. A. Taylor, R. H. Raymond and L. H. Gale, Surface and Interface Analysis **3** (5), 211-225 (1981).

15. J. J. Yeh and I. Lindau, Atomic Data and Nuclear Data Tables **32** (1), 1-155 (1985).

16. T. Arnold, D. J. Payne, A. Bourlange, J. P. Hu, R. G. Egdell, L. F. J. Piper, L. Colakerol, A. Masi, P. A. Glans, T. Learmonth, K. E. Smith, J. Guo, D. O. Scanlon, A. Walsh, B. J. Morgan and G. W. Watson, Physical Review B **79** (7), 075102 (2009).

17. D. Shin, J. S. Foord, D. J. Payne, T. Arnold, D. J. Aston, R. G. Egdell, K. G. Godinho, D. O. Scanlon, B. J. Morgan, G. W. Watson, E. Mugnier, C. Yaicle, A. Rougier, L. Colakerol, P. A. Glans, L. F. J. Piper and K. E. Smith, Physical Review B **80** (23), 233105 (2009).

18. D. J. Aston, D. J. Payne, A. J. H. Green, R. G. Egdell, D. S. L. Law, J. Guo, P. A. Glans, T. Learmonth and K. E. Smith, Physical Review B **72** (19), 195115 (2005).

19. P. Marksteiner, P. Blaha and K. Schwarz, Zeitschrift Fur Physik B-Condensed Matter **64** (2), 119-127 (1986).

20. J. P. Hu, D. J. Payne, R. G. Egdell, P. A. Glans, T. Learmonth, K. E. Smith, J. Guo and N. M. Harrison, Physical Review B **77** (15), 155115 (2008).

21. M. Grioni, J. F. Vanacker, M. T. Czyzyk and J. C. Fuggle, Physical Review B **45** (7), 3309-3318 (1992).

22. U. Fano and J. W. Cooper, Reviews of Modern Physics **40** (3), 441-443 (1968).

23. M. Grioni, J. B. Goedkoop, R. Schoorl, F. M. F. Degroot, J. C. Fuggle, F. Schafers, E. E. Koch, G. Rossi, J. M. Esteva and R. C. Karnatak, Physical Review B **39** (3), 1541-1545 (1989).

24. C. C. B. Lynch, R. G. Egdell and D. S. L. Law, Chemical Physics Letters **401** (1-3), 223-226 (2005).

25. *CrystalMaker@ Windows, Ver.4.0.8 Campus Licence (Education), CrystalMaker Software Ltd.* (2010).

26. D. S. Kan and Y. Shimakawa, Applied Physics Letters **99** (8), 018907 (2011).

27. C. B. Arnold and M.J. Aziz, Applied Physics A -Materials Science & Processing, **69**: p. S23-S27. (1999)

6 Epitaxial Growth of $CuCrO_2$ and $CuGaO_2$ Thin Films by OPABE

In previous chapters it has been demonstrated for the first time that $CuInO_2$ delafossite can be grown using OPABE. The aim of the present chapter is to further develop this work by investigating the formation of $CuCrO_2$ and $CuGaO_2$ delafossite materials using the same growth approach.

6.1 Introduction

6.1.1 Background

As discussed in previous chapters of this thesis, there is considerable interest in the development of new TCO's, especially transparent *p*-type materials to complement the existing established n-type materials such as as In_2O_3:Sn [1], SnO_2:F [2], or ZnO:Al [3], which could open up the feasibility of transparent electronic devices [4, 5]. One of the early candidates in this area was $CuAlO_2$, as an example of the general delafossite structure compound $Cu^{I}M^{III}O_2$. Since then many other p-type delafossite TCOs, including $CuInO_2$ [6], $CuScO_2$ [7], $CuGaO_2$ [8], $CuYO_2$ [9], and $CuBO_2$ [10, 11], have been explored. Mg-doped $CuCrO_2$ with conductivity up to 220 S cm^{-1} is clearly one of the attractive candidates in this area [12]. $CuCrO_2$ is also especially relevant to various application areas other than TCO electrodes such as multiferroic-magnetic matter [13, 14], catalysts in hydrogenation reactions [15], and thermoelectric materials [16].

Thin film growth of $CuCrO_2$ has been explored recently. Fang used PLD from a nanocrystalline $CuCrO_2$ target; the derived $CuCrO_2$ films were highly c-oriented at 800 K [17]. In 2012, Kim challenged that the preferential growth orientations of $CuCrO_2$ films on different substrates such as (0001) Al_2O_3 and (100) YSZ [18].

In Chiu *et al.*, *in situ* laser annealing was discovered in the PLD system of Mg-doped $CuCrO_2$ with annealing to improve their electrical and crystalline properties [19]. In 2008, the chemical spray pyrolysis technique for deposition of undoped $CuCrO_2$ films (~155 nm thick) and $CuCr_xMg_{1-x}O_2$ thin films (305 nm film thickness) was described by Rastogi *et al.* [20].

$CuGaO_2$ materials also have received some attention [8, 21-23]. In 2008, transparent p-type conducting $CuGaO_2$ thin films were prepared on sapphire (Al_2O_3 (0001)) single crystal substrates by pulsed laser deposition in the Hosono group [23].

6.1.2 Electronic Properties of $CuCrO_2$ and $CuGaO_2$

A controversy about the band gap $CuCrO_2$ also exists in the literature, whether it is direct or indirect, with typical suggestions reporting an indirect band gap around 2.6–3.0 eV and direct optical transitions around 3-3.4 eV [20, 24, 25]. Basic undoped $CuCrO_2$ is very resistive, however, substitution of p-type dopants for example, Mg, Ca, Ni for trivalent Cr in this structure induces a remarkable enhancement in electrical conductivity [12, 26-29]. Although doping the trivalent metal site for the delafossite compound with a divalent dopant can significantly improve the electrical conductivity, the trend of conductivity seen for different trivalent metal cations is controversial [30]. The increasing conductivity follows a decreasing ionic radius of the M^{III} cation in Cu delafossite structures such as $CuY_{1-x}Ca_xO_2$ to $CuSc_{1-x}Mg_xO_2$ to $CuCr_{1-x}Mg_xO_2$, and for this reason a decreasing lattice value in the Cu ion plane [12]. This induces increased Cu *d* orbital overlap yielding better hole mobility. However the data are not straightforward so for example the conductivity of $CuAl_{1-x}Mg_xO_2$, (around 4×10^{-4} S cm^{-1}) is lower than that of $CuCr_{1-x}Mg_xO_2$ with 220 S cm^{-1}, even though the ionic radius of Al is smaller than Cr [31].

The delafossites include only Cu-O-M^{III}-O-Cu linkages [9] in contrast to Cu_2O which has Cu-O-Cu linkages. The mixing with the 3*d* states on the M^{III} cation in the Cu-O-M^{III}-O-Cu linkages, could explain the higher conductivities observed in $CuCrO_2$ and $CuFeO_2$ [9]. Further theoretical investigation of $CuM^{III}O_2$ (M^{III} = Al, Cr, Y, and Sc) has indicated that the Cr 3*d* states are implicated in the valence band and mix with O 2*p*, and that this enhanced covalency in the system leads to augmented hole mobility [32]. Detailed treatments of the conductivity have focussed not only on the expected Cu^I/Cu^{II} hole mechanism but also a Cr^{III}/Cr^{IV} hole mechanism [25, 33-38].

$CuGaO_2$ has received much less attention, although first-principles calculations by the Zhang group found the direct band gap of $CuGaO_2$ to be 2.70 eV using the local density approximation (LDA) [22]. However the experimentally observed optical gaps were 3.6 eV in their report. An electrical conductivity, carrier (positive hole) density, and Hall mobility in thin films at room temperature has been reported as 6.3×10^{-2} S cm^{-1}, 1.7×10^{18} cm^{-3} and 0.23 cm^2 V^{-1} s^{-1}, respectively [8], with a conductivity increasing with oxygen partial pressure [23].

6.2 Experimental Details

Epitaxial films of nominally undoped $CuCrO_2$ and $CuGaO_2$ were grown on cleaned 10 x 10 x 0.5 mm^3 Al_2O_3(*c*-plane, (0001)) epi-polished substrates in the OPABE system described previously. All growth runs used the bilayer method using a 1:6 ratio of Cu (bottom layer thickness) /$CuCrO_2$ (top layer thickness). Substitution for Cr^{3+} with Sn^{4+} (using a K-cell of Sn (*s*) 99.999%) or Ga^{3+} with Sn^{4+} was carried out to attempt doping. Typical optimised conditions used K-cell evaporation temperatures Cu 1100 ^oC, Cr 1500 ^oC, Ga 810 ^oC, Sn 650 ^oC, at pO_2 2.0×10^{-5} torr with 200 W RF

power. Substrate growth temperatures of 800 ^oC were typically employed, although lower temperatures down to 600 ^oC were also used. Films were then grown to a nominal thickness of ~1200 Å as measured by a thickness monitor at the substrate temperature, although real thicknesses were approximately x4 larger. High-resolution X-ray photoemission spectra were measured in a Scienta ESCA 300 spectrometer. Binding energies are referenced to the Fermi energy of the silver (Ag) sample regularly used to calibrate the spectrometer. X-ray emission spectra were measured for ceramic Cu delafossite on beamline 7.0.1 at the Advanced Light Source (ALS), Lawrence Berkeley National Laboratory by the K. E. Smith Group, Department of Physics, Boston University, USA. X-ray diffraction (XRD) profiles of $CuCrO_2$ films were obtained from a PANalytical X'Pert PRO diffractometer using monochromatic Cu $K\alpha$ radiation and rotating spinner stage. The direct optical band gap energy of the films was measured in Shimadzu UV-2401 PC (λ=230~800 nm) with the Tauc relationship. AFM images were recorded *ex situ* with a Digital Instruments Multimode SPM instrument.

6.3 Results

6.3.1 XRD Analysis of $CuCrO_2$ and $CuGaO_2$ Thin Films

(a) $CuCrO_2$ from the bilayer inter-diffusion method

Initial experiments focussed on establishing fluxes to obtain 1:1 Cu:Cr stoichiometry which suggested K-cell temperatures of Cu 1100 ^oC, Cr 1500 ^oC. However, as noted previously in chapter 4, XPS showed significant depletion of Cu for one-stage growth runs using these cell temperatures, so the bilayer method (1:6 ratio of Cu (bottom layer)/$CuCrO_2$ (upper layer) was again employed, using a post-

annealing process at growth temperature for 10~15 min, respectively after growth was completed. XRD data at differing growth temperatures are shown in Figure 6.1. The data confirm that $CuCrO_2$ is formed since the only reflections observed (apart from substrate reflections) are associated with this compound. At the higher 800 ^oC growth temperature, the films show reflections due to (001) crystallite orientation (such as (003), (006) and (0012)) corresponding to a parallel structure of the O-Cu-O framework with the *c*-axis of the Al_2O_3 (0001) substrate. For a decreasing growth temperature from 750 ^oC to 700 ^oC, a clear switchover to the (015) orientation occurs, which is inclined at 41.516^o to the *c*-axis.

Figure 6.2 shows similar data, but with films prepared to incorporate 5~6% Sn doping from the nominal growth fluxes. The results are essentially the same as in the absence of Sn.

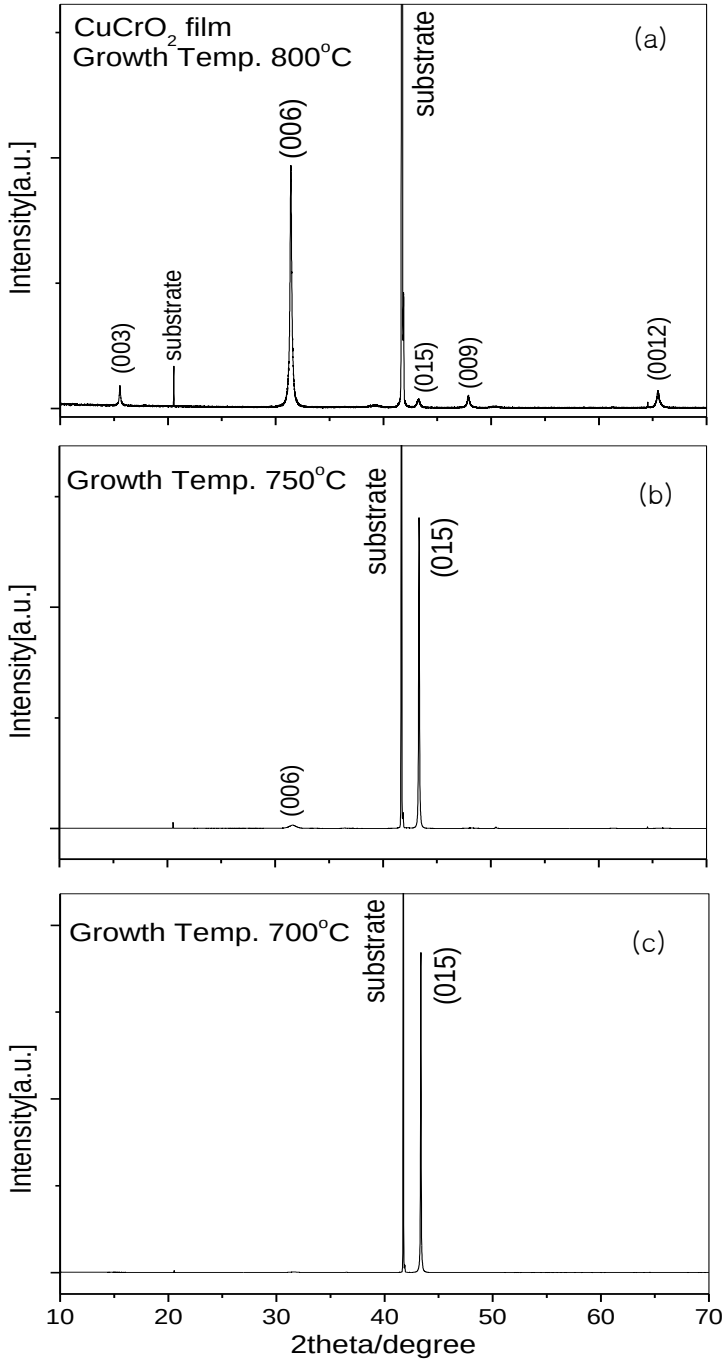


Figure 6.1. 2theta (θ) monochromatic X-ray diffraction (Cu *Kα* radiation λ=1.5418 Å) profile of OPABE $CuCrO_2$ films (F/T = 1000 Å) on *c*-plane Al_2O_3 (0001) substrate. G.T. (growth temperature) of (a) 800 °C, (b) 750 °C, (c) 700 °C

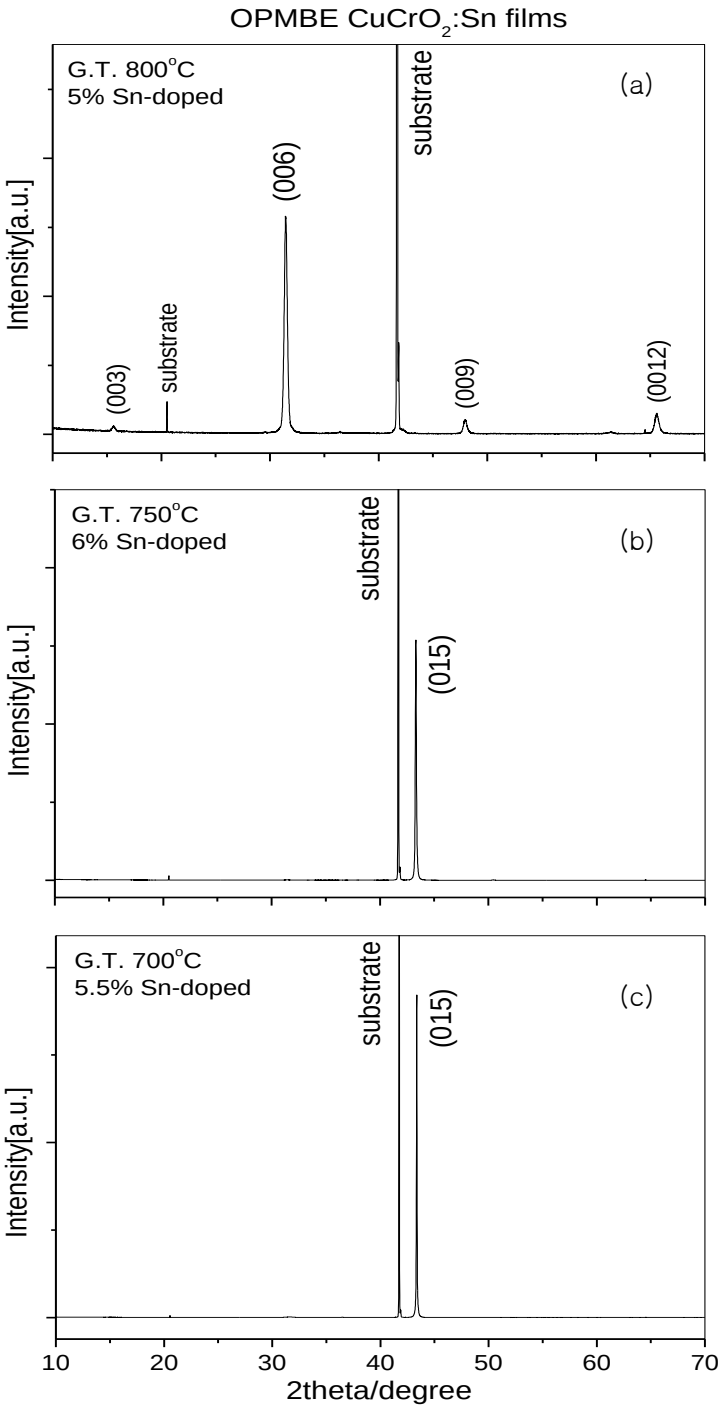


Figure 6.2. 2theta (θ) monochromatic X-ray diffraction (Cu *Kα* radiation λ = 1.5418 Å) profile of OPABE Sn-doped $CuCrO_2$ films (F/T = 1100 Å) on *c*-plane Al_2O_3 (0001) substrate. G.T. (growth temperature) of (a) 800 ^oC, (b) 750 ^oC, (c) 700 ^oC

(b) Undoped and Sn-doped $CuGaO_2$ from the bilayer inter-diffusion method in OPABE

The same bilayer growth method was also used to attempt to prepare $CuGaO_2$ layers. Approximate K-cell temperatures were Cu 1100 ^oC, Ga 810 ^oC, and substrate temperatures were varied between 600~800 ^oC. XRD results are shown in Figure 6.3 and 6.4 for the growth of undoped $CuGaO_2$ and doped material respectively. For both situations, the XRD data confirm the formation of the pure compound at the 800 ^oC growth temperature, with the crystal texture (015). This orientation persists over the whole temperature range, in contrast to the situation noted above for $CuCrO_2$. A second difference is that Cu phases (Cu or CuO) appear in the XRD spectra at the lower temperature, suggestive that interdiffusion of the bilayer does not take place readily in this materials system.

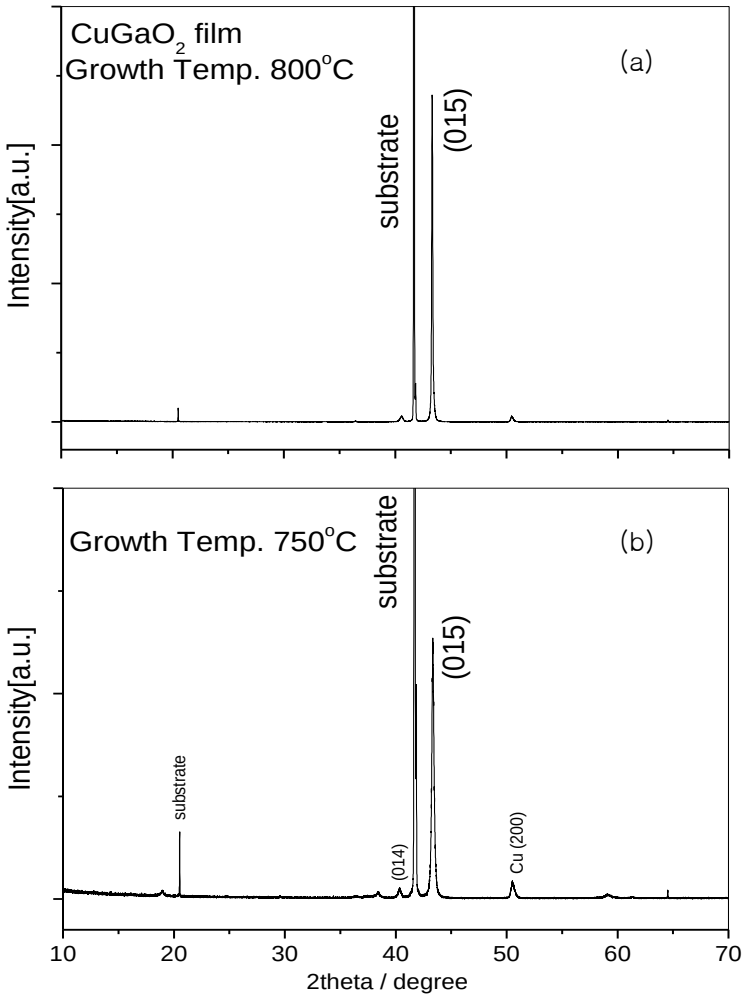


Figure 6.3. 2theta (θ) monochromatic X-ray diffraction (Cu *Kα* radiation λ = 1.5418 Å) profile of OPABE $CuGaO_2$ thin films on *c*-plane Al_2O_3 (0001) substrate. G.T. (growth temperature) of (a) 800 °C with F/T = 1200 Å , (b) 750 °C with F/T = 980 Å .

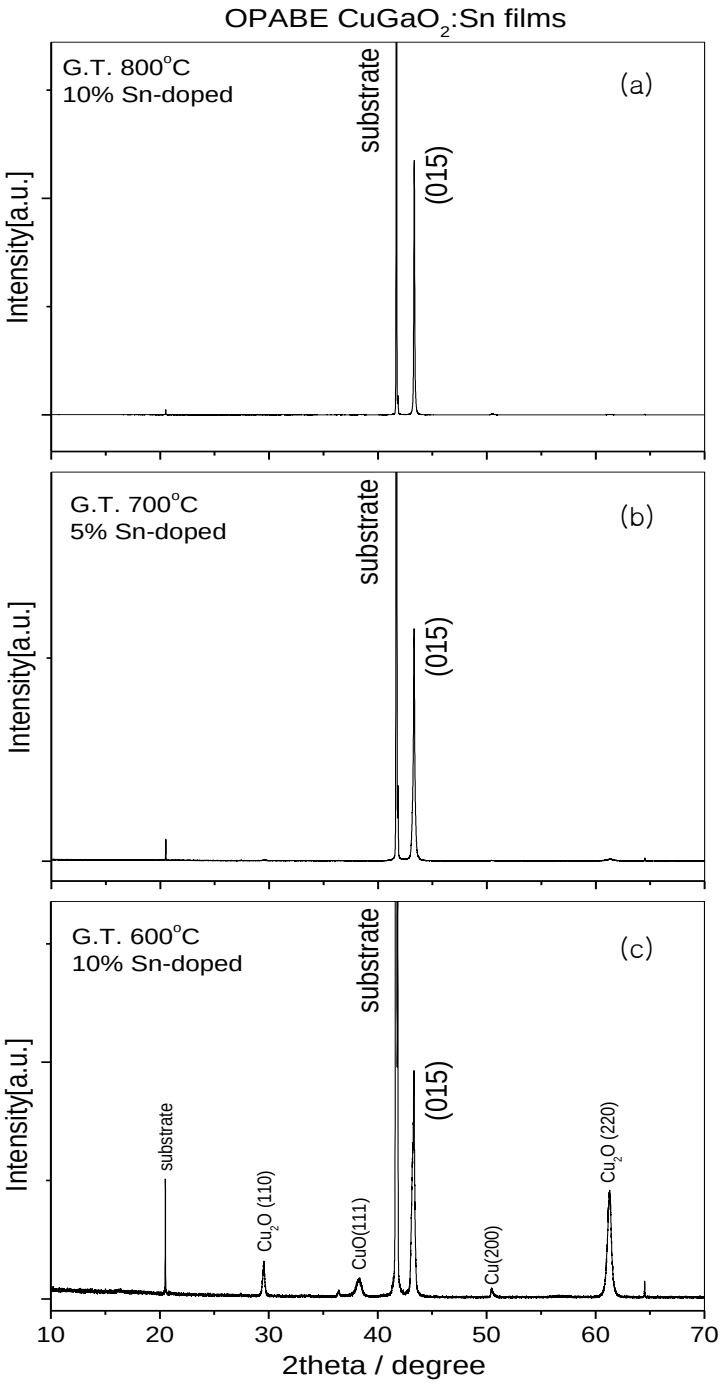


Figure 6.4. 2theta (θ) monochromatic X-ray diffraction (Cu *Kα* radiation λ = 1.5418 Å) profile of OPABE Sn-doped $CuGaO_2$ films on *c*-plane Al_2O_3 (0001) substrate. G.T. (growth temperature) of (a) 800 °C with F/T = 1200 Å , (b) 700 °C with F/T = 750 Å , (c) 600 °C with F/T = 300 Å .

6.3.2 Stoichiometric Proportions of $CuCrO_2$ and $CuGaO_2$ in the Thin Films under Differing Growth Conditions

XPS studies were carried out to probe the stoichiometries of the $CuCrO_2$ and $CuGaO_2$ films grown under differing conditions, in particular varying K-cell temperatures and substrate temperatures. Tables 6.1 and 6.2 show the stoichiometries of undoped and Sn-doped $CuCrO_2$ thin films and undoped and Sn-doped $CuGaO_2$, respectively. Atomic sensitivity factors for XPS peaks were used to calculate empirical stoichiometries by division of the measured peak area by the appropriate sensitivity factors; Cu $2p_{3/2}$ = 4.2, Cr $2p_{3/2}$ = 1.5, Ga $2p_{3/2}$ = 5.4, O 1*s* = 0.66, Sn $3d_{5/2}$ = 4.3 [39]. Stoichiometric values of elemental composition were obtained by calculations as following; for example, Cu = [integrated peak area of Cu $2p_{3/2}$]/[sensitivity factor].

Large oxygen signals, probably associated with atmospheric contamination, or some interference from the substrate, are seen. However the relative metal concentrations are relatively consistent with the elemental formulations deduced by XRD above, although the Cu XPS signal seems to lie systematically below that expected, possibly due to surface segregation effects,

Table 6.1 Stoichiometries of undoped and Sn-doped $CuCrO_2$ films on *c*-plane Al_2O_3 (0001) substrate regarding growth conditions. Ratios of Cu/Cr/O with Sn were obtained by XPSPEAK41 software using the Cu $2p_{3/2}$, Cr $2p_{3/2}$ and O 1*s* regions with Sn $3d_{5/2}$.

Stoichiometry of OPABE $CuCrO_2$ thin films

Ratio	Growth temp (°C)	O_2 (torr), RF power	Vac. Anneal(°C)	Cu temp(°C)	Cr temp(°C)	Sn temp(°C)
$Cu_{0.85}Cr_{1.0}O_{3.9}$	800	2.6×10^{-5} 200 W	800/10 min	1100	1500	-
$Cu_{0.79}Cr_{1.0}O_{5.1}$	750	2.6×10^{-5} 200 W	750/10 min	1100	1500	-
$Cu_{0.72}Cr_{1.0}O_{7.5}$	700	2.2×10^{-5} 200 W	700/10 min	1100	1500	-
$Cu_{1.1}Cr_{1.0}O_{6.7}Sn_{0.06}$	800	2.5×10^{-5} 200 W	800/10 min	1100	1500	650
$Cu_{9.8}Cr_{1.0}O_{6.8}Sn_{0.07}$	750	2.5×10^{-5} 200 W	750/10 min	1100	1500	650
$Cu_{0.91}Cr_{1.0}O_{7.5}Sn_{0.07}$	700	2.5×10^{-5} 200 W	700/10 min	1100	1500	650

** See section 2.3.2 (g) for consideration of accuracy of quoted elemental compositions.*

Table 6.2 Stoichiometries of undoped and Sn-doped $CuGaO_2$ films on *c*-plane Al_2O_3 (0001) substrate regarding growth conditions. Ratios of Cu/Ga/O with Sn were obtained by XPSPEAK41 software using the Cu $2p_{3/2}$, Ga $2p_{3/2}$ and O 1*s* regions with Sn $3d_{5/2}$.

Stoichiometry of OPABE $CuGaO_2$ thin films

Ratio	Growth temp(°C)	O_2 (torr), RF power	Vac. Anneal(°C)	Cu temp(°C)	Ga temp(°C)	Sn temp(°C)
$Cu_{0.78}Ga_{1.0}O_{4.2}$	800	2.4×10^{-5} 200 W	800/10 min	1098	810	-
$Cu_{0.79}Ga_{1.0}O_{5.1}$	750	2.6×10^{-5} 200 W	750/10 min	1100	810	-
$Cu_{0.76}Ga_{1.0}O_{8.2}Sn_{0.10}$	800	2.7×10^{-5} 200 W	800/10 min	1095	810	650
$Cu_{0.92}Ga_{1.0}O_{6.0}Sn_{0.05}$	700	2.0×10^{-5} 200 W	700/10 min	1100	810	650
$Cu_{0.91}Ga_{1.0}O_{7.5}Sn_{0.11}$	600	2.5×10^{-5} 200 W	600/10 min	1100	810	650

** See section 2.3.2 (g) for consideration of accuracy of quoted elemental compositions.*

6.3.3 X-ray Photoemission Data of $CuCrO_2$ and $CuGaO_2$ Thin Films and Comparative Study of Ceramic Sample

(i) Core Level Measurements

The experimental Al *Kα* XPS core level spectrum for Cu 2*p* is shown in figure 6.5 for both $CuCrO_2$ and $CuGaO_2$. The samples were grown at a temperature of 800 ^oC.

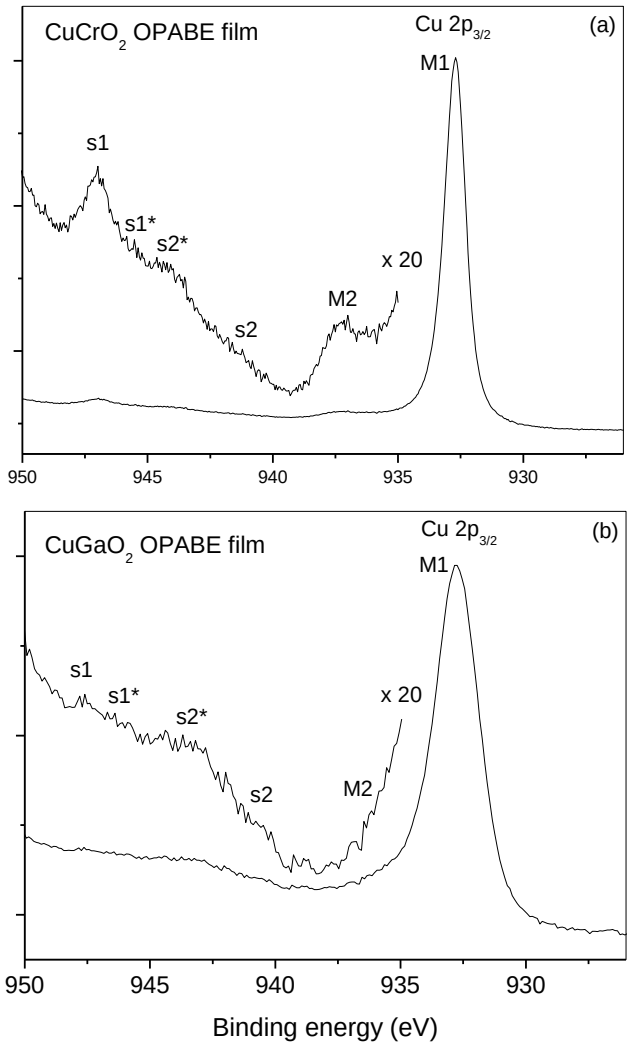


Figure 6.5. XPS (Al *K*α, hv=1486.6 eV) spectra in the Cu 2*p* region of OPABE (a) $CuCrO_2$ (ESCA300) and (b) $CuGaO_2$ (in-house XPS). The BE region 935~950 eV is 20 times magnified.

The spectra show the Cu $2p_{3/2}$ peak (M1) and weak satellite features M2, s1, s2, s1* and s2* can also be observed which, as discussed in 3.3.3, are entirely consistent with the presence of Cu (I) species, confirming the bilayer approach results in the formation of the desired Cu (I) oxidation state.

(ii) Valence Band Measurements

(a) $CuCrO_2$ thin film and ceramic sample

A survey scan X-ray photoemission spectrum of an undoped $CuCrO_2$ thin film is shown in figure 6.6 grown at 800 ^oC on the sapphire substrate. Apart from a small C 1*s* signal due to air contamination, all of the other major peaks are consistent with the elemental formulation of the target compound with stoichiometry of $Cu_{0.85}Cr_{1.0}O_{3.9}$ (*See section 2.3.2 (g) for consideration of accuracy of quoted elemental composition*), as noted above.

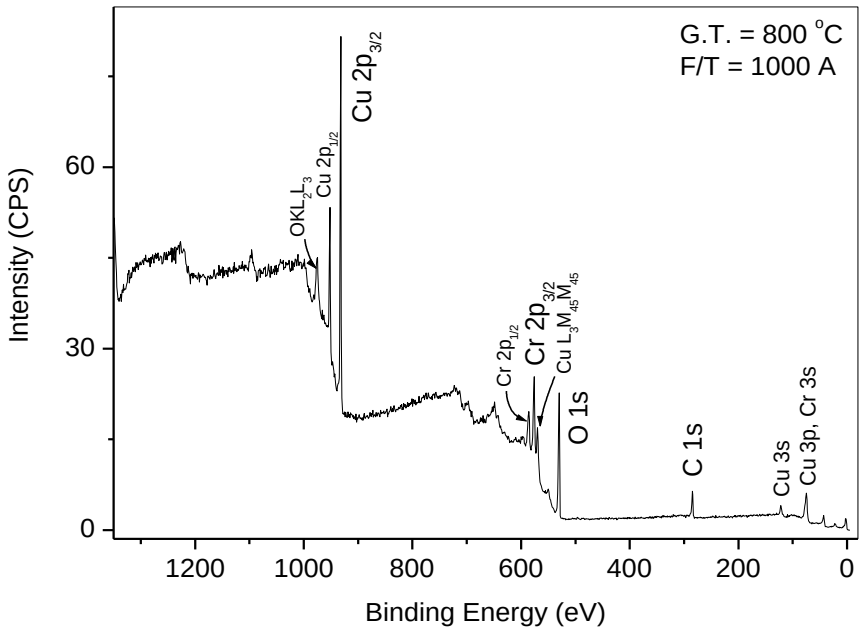


Figure 6.6. Al *Kα* XPS (ESCA300) survey scan of undoped $CuCrO_2$ thin film on sapphire substrate, Al_2O_3 (*c*-plane, (0001)) by OPABE.

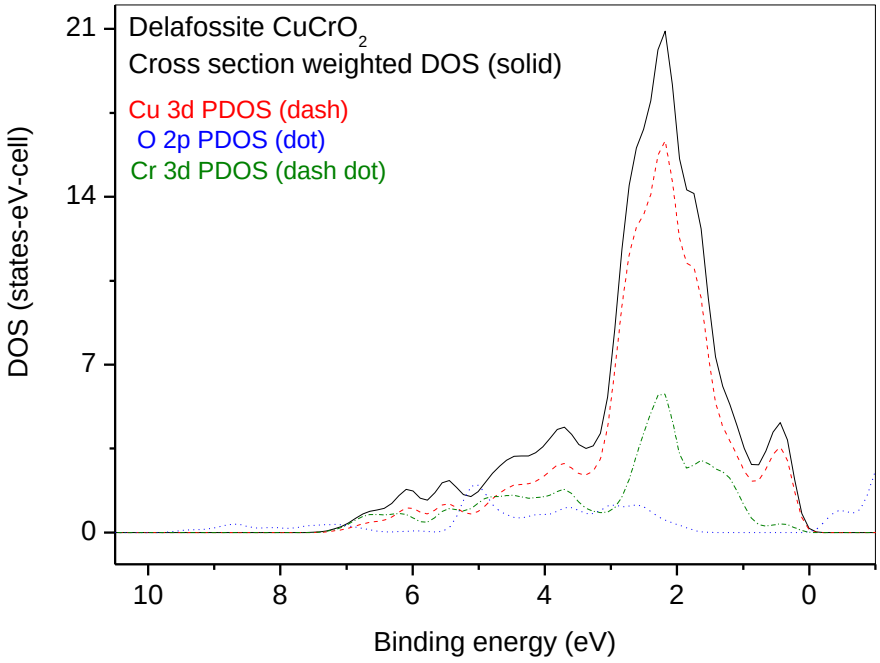


Figure 6.7. Theoretical cross section weighted DOS including Cu 3*d*, O 2*p* and Cr 3*d* PDOS for $CuCrO_2$ (DFT, GGA+U method). (adapted from ref. 40, 41)

Figure 6.7 shows the band-structure calculations of $CuCrO_2$ including Cu 3*d*, O 2*p* and Cr 3*d* partial density of states. This work was completed by the Watson group at Trinity College, Ireland. Full details of the computational approach that was adopted are given in ref. 40, 41. As shown in figure 6.7 the cross-section-weighted contribution of the Cr 3*d* partial density of states to the valence band is small compared to the Cu 3*d* contribution.

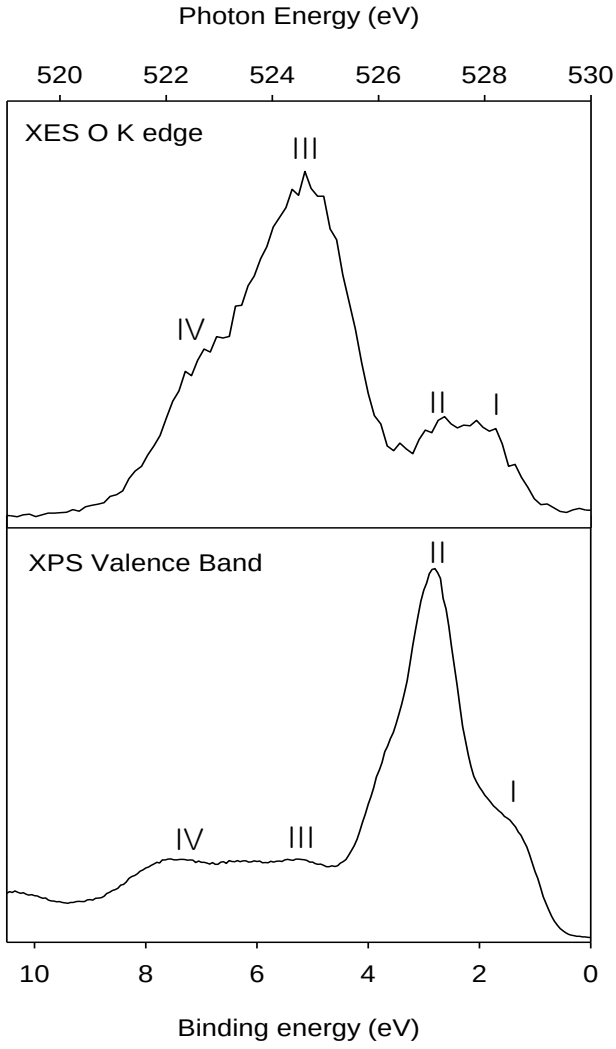


Figure 6.8. Upper panel: O *K* X-ray emission spectrum of ceramic $CuCrO_2$ pellet. Lower panel: Al *Kα* excited valence-band X-ray photoemission of ceramic $CuCrO_2$ pellet. The X-ray emission spectra have been shifted to align with the Al *Kα* XPS and are presented on a binding-energy scale [40].

For comparison with the OPABE project, the experimental O *K* X-ray emission spectrum of ceramic $CuCrO_2$ is shown in figure 6.8 along with valence-band Al *Kα* X-ray photoelectron spectrum, as provided from the Edgell group (Oxford University,

UK) in conjunction with group of Smith (Boston University, USA). This ceramic sample of $CuCrO_2$ was prepared by solid-state reaction between CuO, Cr_2O_3 [40].

The XPS data (lower panel of figure 6.8) are compared with the O *K* emission spectra. Four features labeled I-IV could be identified in the experimental spectra. Reference (Arnold *et al.* [40]) to the band structure calculations shows that I and II relate to states of dominant Cu 3*d* atomic character while III and IV are associated with states of dominant O 2*p* character. In X-ray photoemission band II is the strongest component of the experimental valence-band spectrum and I appears as an ill-resolved shoulder to low binding energy. Bands III and IV are found at higher binding energy and are also weaker than I but of comparable intensity to each other. The one-electron cross section for ionisation of Cu 3*d* states is a factor of 20 bigger than for O 2*p* states under Al *Kα* excitation so that the experimental spectrum is dominated by the Cu 3*d* partial density of states even for bands III and IV, although contributions from Cr 3d should also be taken into account. In O *K* shell X-ray emission the intensity distribution is reversed and I and II are much weaker than III and IV. There are also changes of relative intensity within the pairs I, II and III, IV. Specifically II loses intensity relative to I and IV relative to III. The fact that bands I and II appear at all in O *K* shell X-ray emission is a direct consequence of hybridisation between Cu 3*d* and O 2*p* states which introduces O 2*p* character into states of nominal Cu 3*d* parentage [40, 42, 43]. Figure 6.9 shows the various features of the Al *Kα* valence band spectrum of a $CuCrO_2$ thin film from OPABE. This is in good agreement with the results from the ceramic sample described above, consistent with the formation of the delafossite during the OPABE experiment.

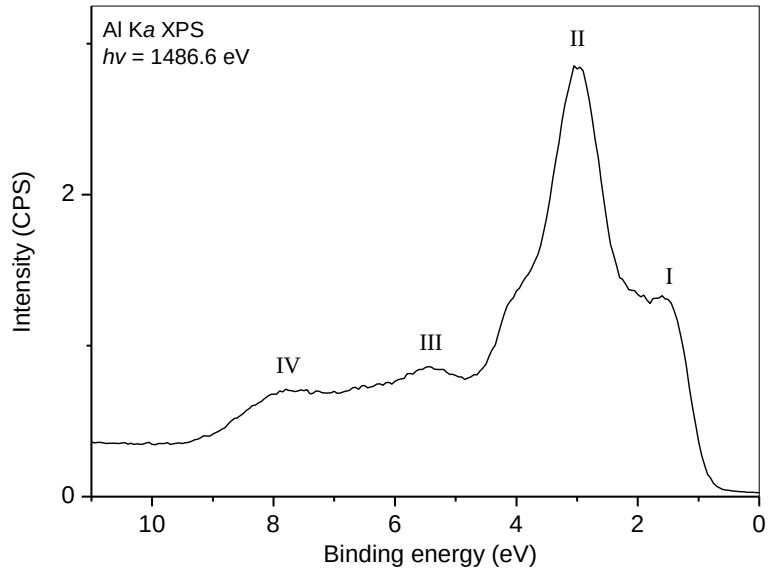


Figure 6.9. Valence-band Al *Kα* XPS (ESCA300) of $CuCrO_2$ thin film, which was grown at 800 ^oC by OPABE. Film thickness and stoichiometry are about 1000 Å and $Cu_{0.85}Cr_{1.0}O_{3.9}$, respectively.

(b) Survey scan and valence band XPS spectra of $CuGaO_2$ thin film

A survey scan X-ray photoemission spectrum of a $CuGaO_2$ thin film is shown in figure 6.10. This undoped $CuGaO_2$ film (film thickness = about 1200 Å) was grown at 800 ^oC. As noted above, the calculated stoichiometry is consistent with a surface composition of $Cu_{0.78}Ga_{1.0}O_{4.2}$ (*See section 2.3.2 (g) for consideration of accuracy of quoted elemental composition*). The valence band XPS spectrum of the $CuGaO_2$ thin film is shown in figure 6.11. Although we have no reference data, the spectrum can be seen to be consistent with the data for delafossites presented previously in this thesis, and is for example quite distinct to other possible reaction products such as Ga_2O_3 [44].

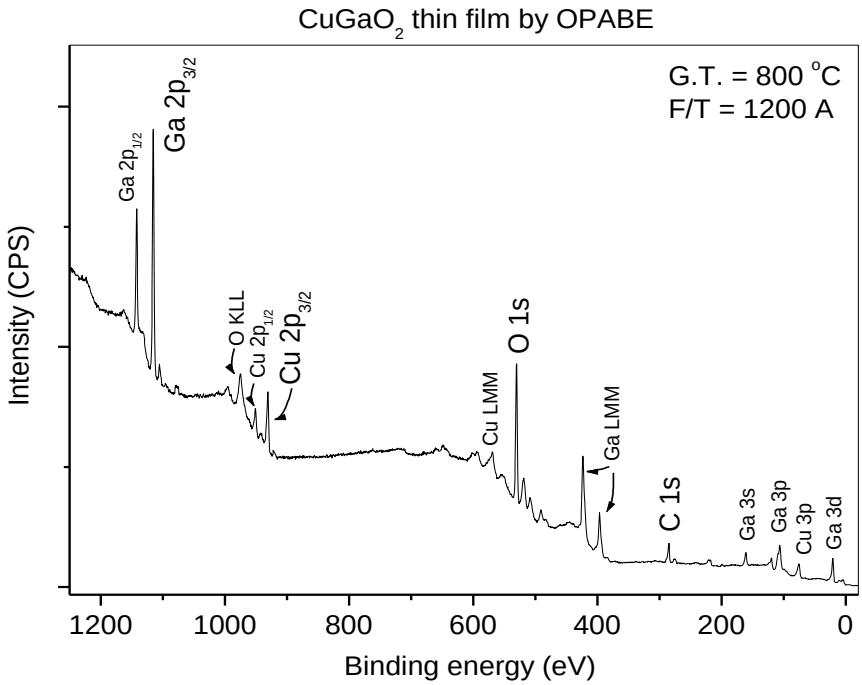


Figure 6.10. Al *Kα* XPS (in-house XPS) survey scan of undoped $CuGaO_2$ thin film on sapphire substrate, Al_2O_3 (*c*-plane, (0001)) by OPABE.

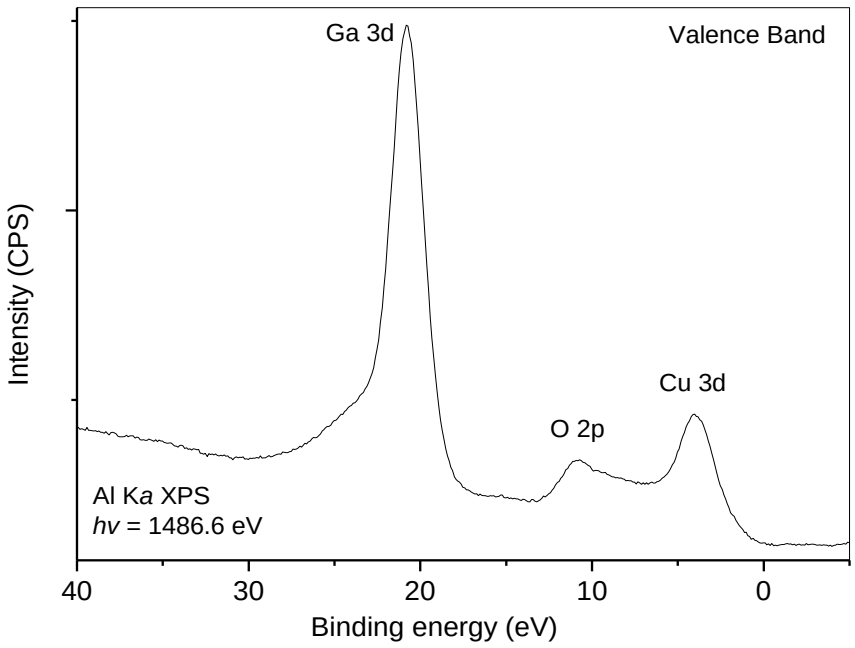


Figure 6.11. Valence-band Al *Kα* XPS (in-house XPS) of undoped $CuGaO_2$ thin film, which was grown at 800 ^{o}C by OPABE. Film thickness and stoichiometry are about 1200 Å and $Cu_{0.78}Ga_{1.0}O_{4.2}$, respectively.

6.3.4 Valence and Core Level Photoemission Spectra Shift Concerning n-Type Doping

(a) Sn-doped $CuCrO_2$ thin films

The possibility of N-type doping in OPABE growth of $CuCrO_2$ thin films by substitution of Cr (III) with Sn (IV) was investigated. Figures 6.12 and 6.13 show survey scan and valence-band XPS spectra of material incorporating Sn. The sample was grown at 800^{o}C with cell temperatures Cu 1100^{o}C, Cr 1500^{o}C, Sn 650 ^{o}C. The Sn level is about 5% as estimated from XPS sensitivity factors. Valence-band spectra in Figure 6.13 compare materials in the presence and absence of Sn. The upward shift of 0.21 eV in binding energies suggests the Fermi level is shifted commensurate with n-type behaviour. The shift in valence-band structure is accompanied by corresponding shifts in core level binding energies. Thus figure 6.14 shows the Cu $2p_{3/2}$ peaks for nominally undoped and 5% Sn-doped $CuCrO_2$. The peak maximum shifts from 932.7 ± 0.05 eV to 932.8 ± 0.05 eV with Sn doping, again indicative of small change in the Fermi level position.

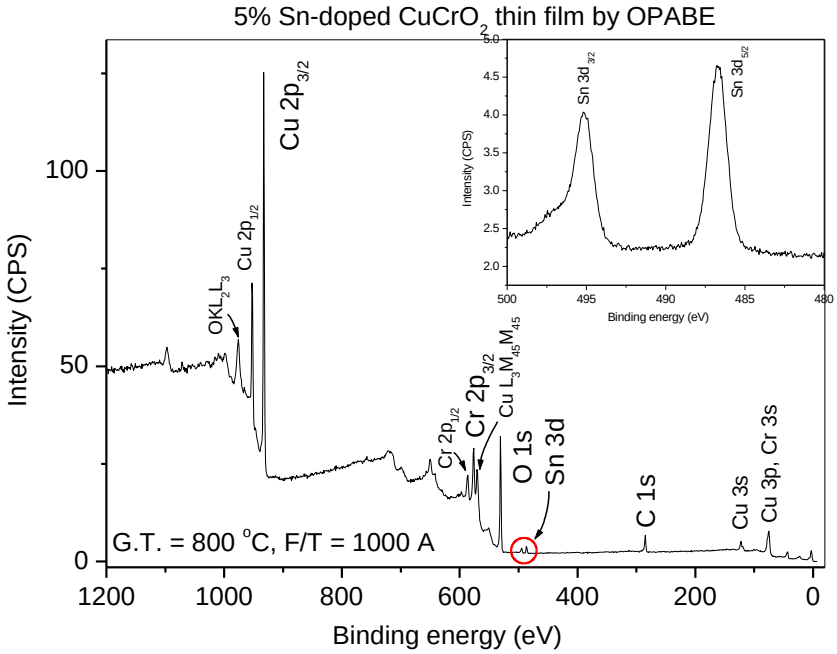


Figure 6.12. Al *Kα* XPS (ESCA300) survey scan of 5% Sn-doped $CuCrO_2$ thin film by OPABE growth on sapphire substrate, Al_2O_3 (*c*-plane, (0001)).

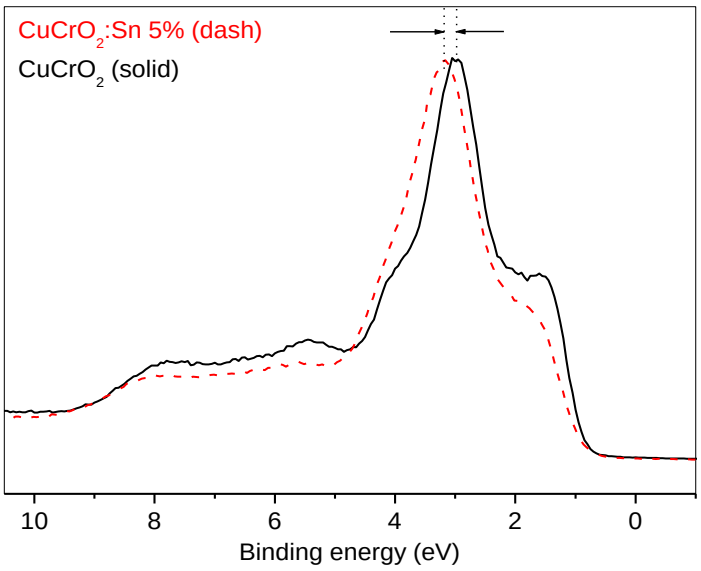


Figure 6.13. Valence band X-ray photoemission spectra of $CuCrO_2$ (Al *Kα*, *hν* = 1486.6 eV)

: undoped (black solid), 5% Sn-doped (red dot).

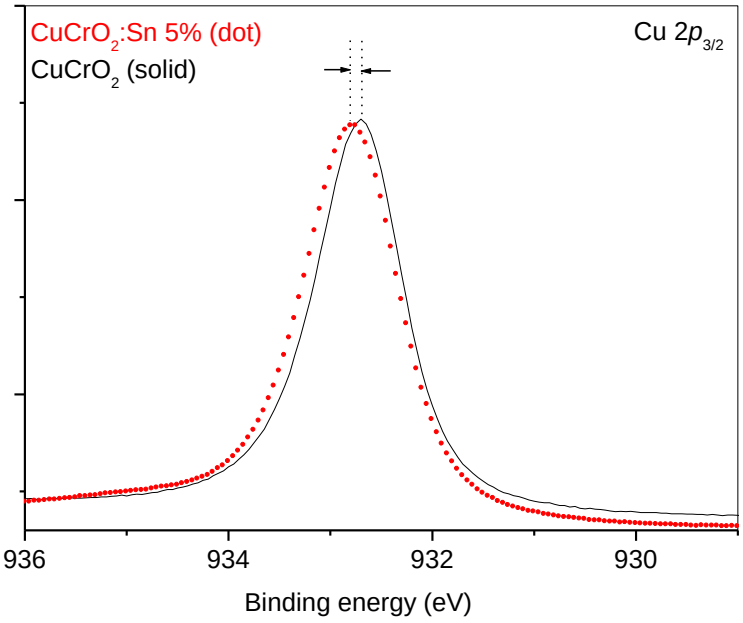


Figure 6.14. Cu $2p_{3/2}$ core line in Al $K\alpha$ excited region photoemission spectra of nominally undoped $CuCrO_2$ and 5% Sn-doped $CuCrO_2$. OPABE films: undoped (black solid), 5% Sn-doped (red dot).

(b) Sn-doped $CuGaO_2$ thin films

Figures 6.15 and 6.16 similarly show survey and valence-band XP spectra for $CuGaO_2$ films with incorporated Sn, grown at 800 ^oC. The metal cation stoichiometry is $Cu_{0.76}Ga_{1.0}Sn_{0.10}$ (*See section 2.3.2 (g) for consideration of accuracy of quoted elemental composition*). In the nominally undoped $CuGaO_2$ the peak maximum in the valence band is found at 1.7 ± 0.05 eV, while for the Sn-doped film the maximum is at 2.0 ± 0.05 eV. The upward shift of 0.3 eV is therefore again suggestive of n-type

doping. The core level Cu $2p_{3/2}$ peaks for nominally undoped and 10% Sn-doped $CuGaO_2$ are shown in Figure 6.17. The peak maximum shifts from 932.8 ± 0.05 eV to 933.3 ± 0.05 eV with Sn doping. The upward shift of 0.5 eV is somewhat bigger than valence band shift of 0.3 eV, suggesting some changes associated with valence bonding effects may also arise.

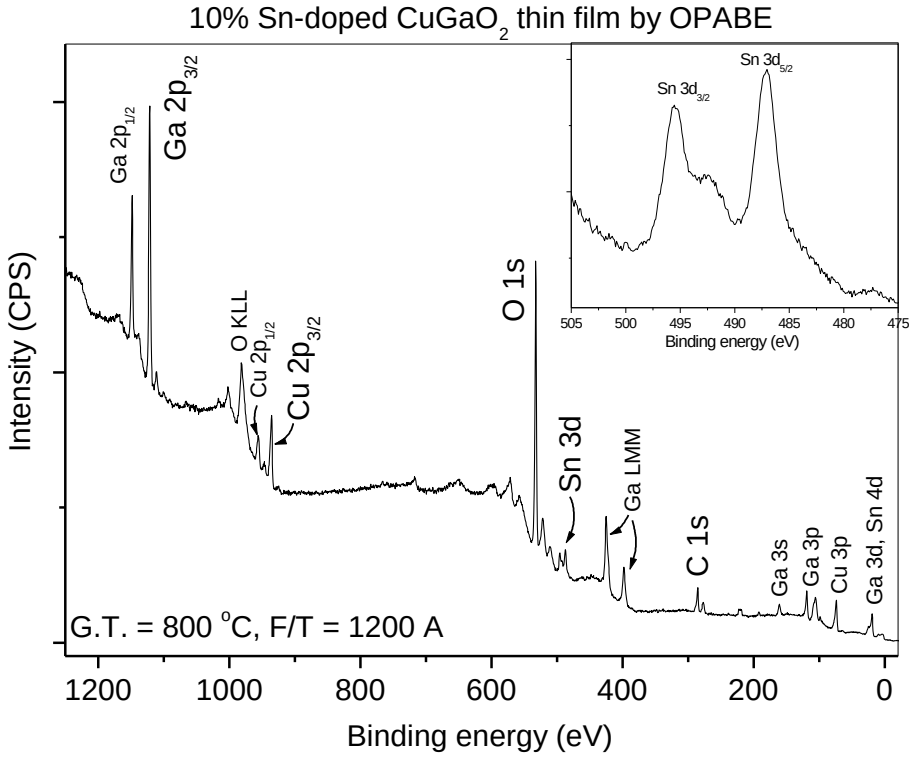


Figure 6.15. Al *Kα* XPS (in-house XPS) survey scan of 10% Sn-doped $CuGaO_2$ OPABE thin film on sapphire substrate, Al_2O_3 (*c*-plane, (0001)).

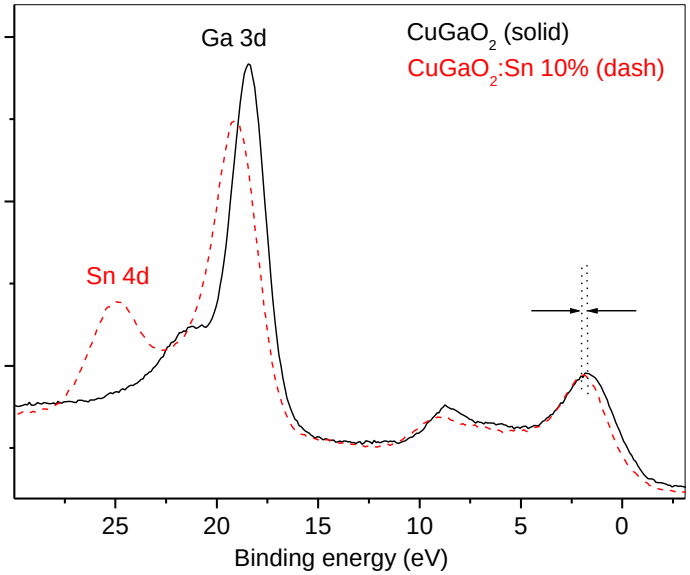


Figure 6.16. Valence band X-ray photoemission spectra of $CuGaO_2$ (Al *Kα*, *hν* = 1486.6 eV): undoped (black solid), 10% Sn-doped (red dash).

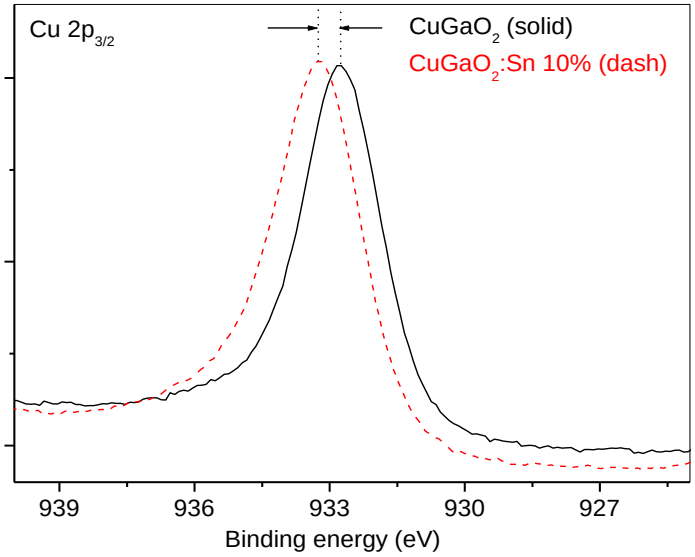


Figure 6.17. Cu $2p_{3/2}$ core line in Al *Kα* excited region photoemission spectra of nominally undoped $CuGaO_2$ and 10% Sn-doped $CuGaO_2$.OPABE films: undoped (black solid), 10% Sn-doped (red dash).

6.3.5 Optical Band Gap of $CuCrO_2$ and $CuGaO_2$ OPABE Thin Films

Undoped and Sn-doped thin films of $CuCrO_2$ and $CuGaO_2$ as described above were evaluated to establish the optical absorption band gap energy by UV-Visible spectroscopy. These films were grown at 800^oC with oxygen plasma source of 200 W for film thickness of about 1000-1200 Å. All growth runs used the bilayer diffusion method using a 1:6 Cu (bottom layer)/$CuMO_2$ (M=Cr or Ga) (upper layer) deposition time with vacuum annealing at 800 ^oC/ 10 min as described in experimental details.

In order to directly measure the optical bandgap of undoped or Sn-doped films of $CuCrO_2$ and $CuGaO_2$ thin films, the Tauc relationship, $\alpha h\nu = A\,(\hbar\nu - E_g)^n$ was employed [45, 46]. As described in chapter 2 (section 2.4.5) for optical absorption in films, A is a constant, n depends on the nature of the transition (n = 1/2 for the direct allowed transition, n = 3/2 for the direct forbidden transition, n = 2 for the indirect allowed transition and n = 3 for the indirect forbidden transition), $\hbar\nu$ is the photon energy, E_g is the band gap and α is the absorbance. To analyse our UV-visible measurement result, a graph is plotted for $(\alpha h\nu)^{1/n}$ vs. $h\nu$ for different values of n, and values which yield the best linear graph are taken as the correct values n [45]. These $CuCrO_2$ and $CuGaO_2$ thin films show the $(\alpha h\nu)^2$ vs. $h\nu$ plots suggesting that is the direct gap transitions which are being determined.

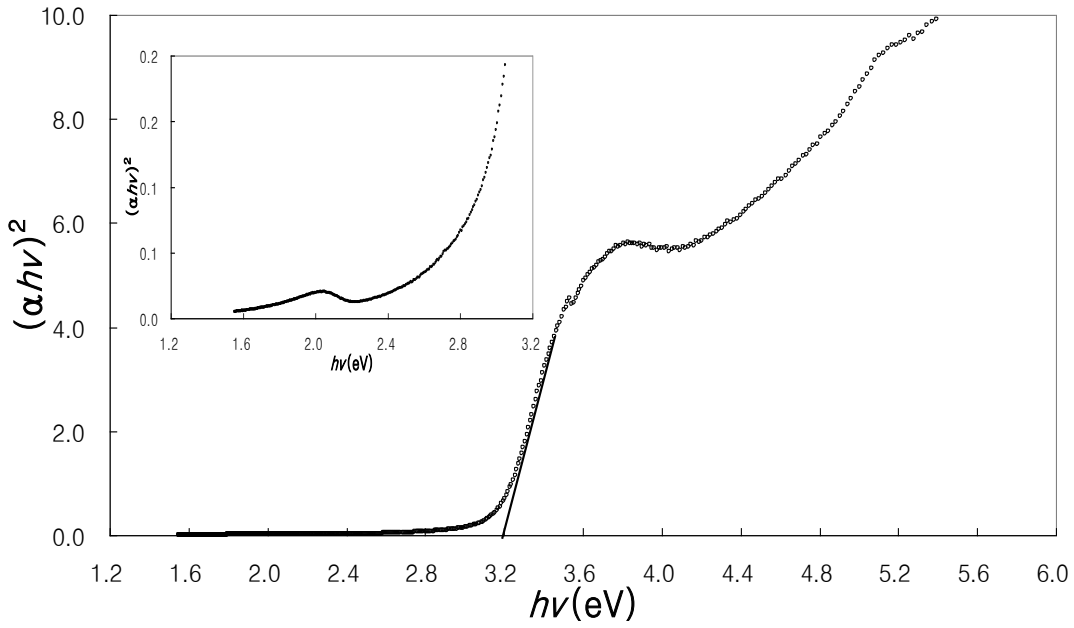


Figure 6.18. Direct optical band gap energy evaluation of undoped $CuCrO_2$ (hv = 3.2 eV) thin film by hv vs. $(\alpha hv)^2$ approximation. Insets show the indirect gap of hv = 1.7 eV.

Figure 6.18 shows an optical direct band gap of 3.2 eV for $CuCrO_2$ commensurate with the discussion at the start of this chapter. However significant absorption is seen at lower phtoton energies, down to below 2 eV, and it has been suggested this arises from an indirect band gap of 1.7 eV for $CuCrO_2$ film with excitonic effects [47] at range of 2.0~2.1 eV (see inset figure) [46]. Figure 6.19 shows somewhat similar behaviour for the Sn-doped layer although the excitonic effects at around 2 eV are no longer visible.

Comparable data for an undoped $CuGaO_2$ thin film also shows an experimental indirect band gap of 1.7 eV with excitonic effects [47] in the range 1.8~2.2 eV and an

optical direct band gap of 3.6 eV, as seen in figure 6.20. The 10% Sn-doped $CuGaO_2$ film seems to suggest direct optical band gap energy of 3.45 eV smaller compared with the undoped $CuGaO_2$ film although the indirect band gap absorptions of 2.35 eV and 2.6 eV, as seen in figure 6.21, seems to be shifted to higher energy.

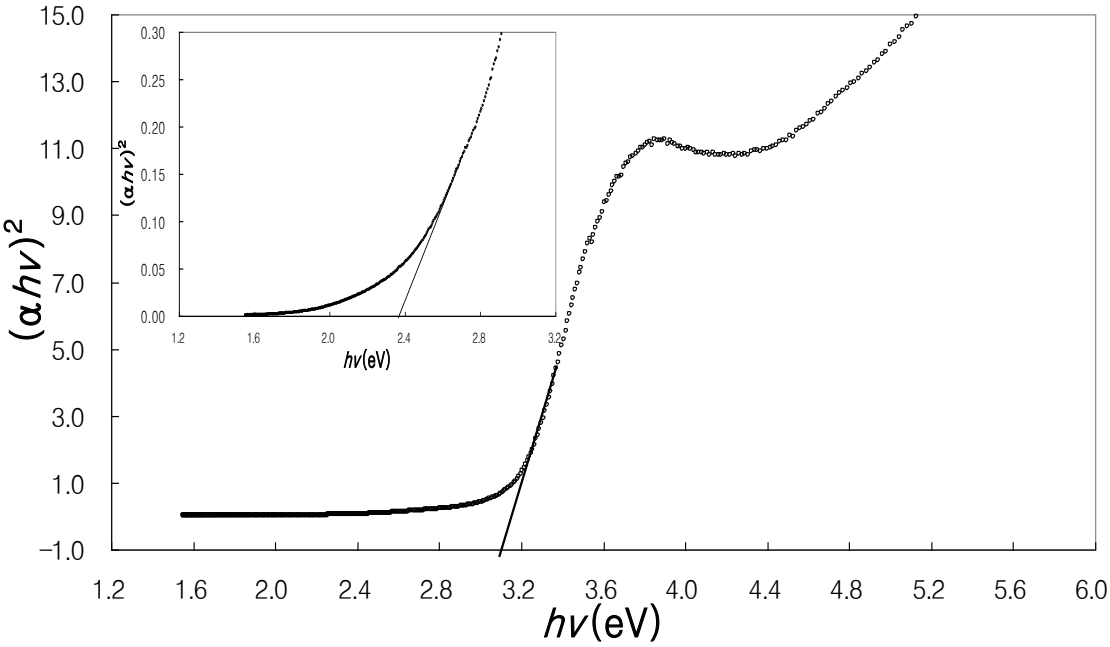


Figure 6.19. Direct optical band gap energy evaluation of 5% Sn-doped $CuCrO_2$ ($h\nu$ = 3.1 eV) thin film by $h\nu$ vs. $(\alpha h\nu)^2$ approximation. Insets show the indirect gap of $h\nu$ = 2.35 eV.

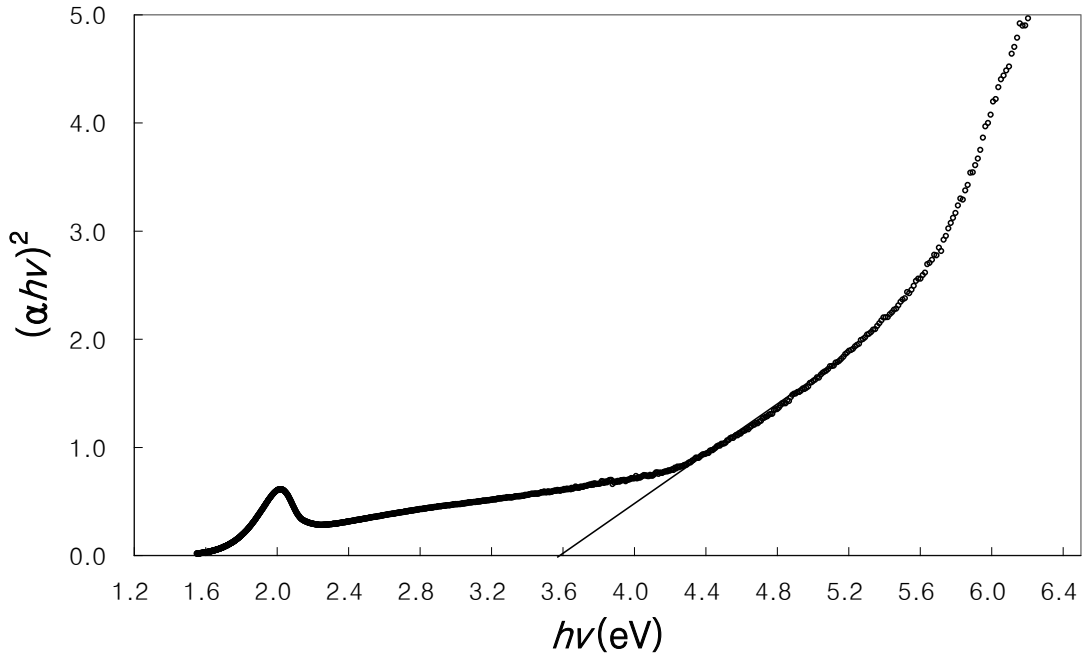


Figure 6.20. Direct optical band gap energy evaluation of undoped $CuGaO_2$ ($h\nu$ = 3.6 eV) thin film by $h\nu$ vs. $(\alpha h\nu)^2$ approximation. The indirect gap of $h\nu$ = 1.7 eV is also shown.

In conclusion, the direct optical band gaps of these undoped and Sn-doped films of $CuMO_2$ (M= Cr or Ga) generally have been obtained to the range 3.1~3.2 eV for $CuCrO_2$ films and 3.45~3.6 eV for $CuGaO_2$, respectively, with variable indirect transitions in the range 1.7~2.4 eV.

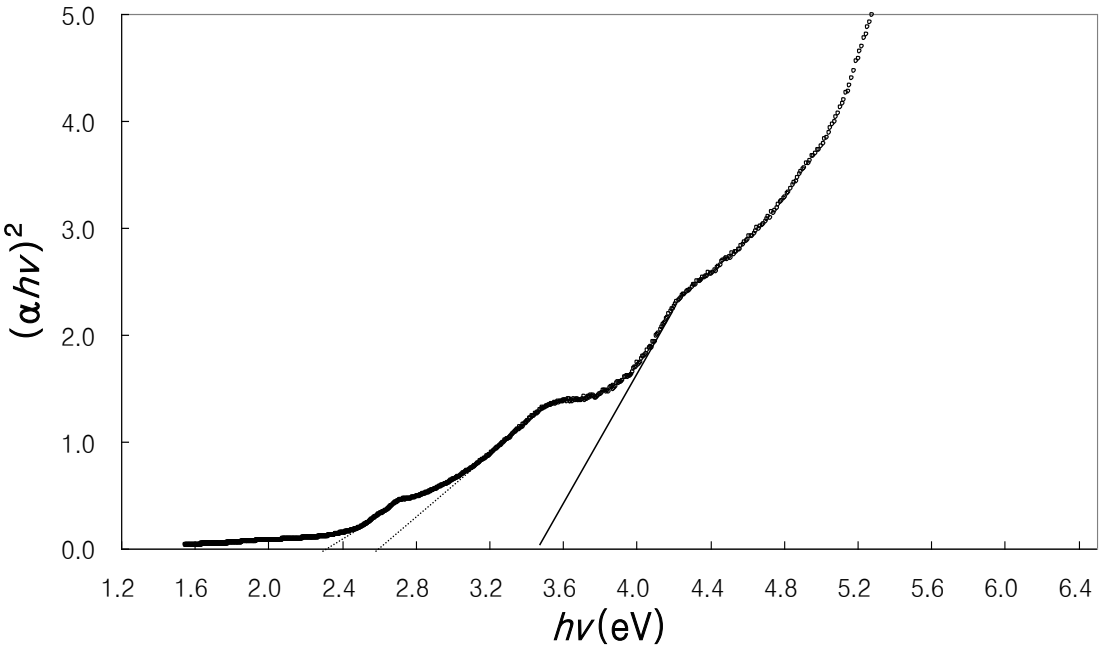


Figure 6.21. Direct optical band gap energy evaluation of 10% Sn-doped $CuGaO_2$ (hv = 3.45 eV) thin film by hv vs. $(\alpha hv)^2$ approximation. Indirect band gap energies of 2.3 eV and 2.6 eV are extrapolated as dot line.

6.3.6 Surface Morphology of $CuCrO_2$ and $CuGaO_2$ Thin Films by AFM

Figure 6.22 shows atomic force microscope surface morphology (scan size of 1.0 x 1.0 μm^2) of $CuCrO_2$ films which were grown for the bilayer using a 1:6 $Cu/CuCrO_2$ deposition time ($CuCrO_2$ top layer on Cu bottom layer) with growth temperature of 800 ^oC (figure 6.22 (a)) and 750 ^oC (figure 6.22 (b)), respectively. These undoped and Sn-doped films (figure 6.23) were then treated by post thermal annealing at 800 ^oC/10 min and 750 ^oC/10 min, respectively. The real thickness of the layers is probably around 400 nm and they exhibit significant surface roughness on the several

tens of nanometre scale, which tends to decrease as the growth temperature rises. The texture observed is suggestive of a film consisting of agglomerates of well-developed crystals, suggestive of island growth from initial nuclei with a number density of around 10^9 cm^{-2}**.** (Island area of $(0.2 \times 10^{-6}\ m)^2 = 4 \times 10^{-10}$ cm^2, number of island per $cm^2 = 1/(4x10^{-10}) = 2.5 \times 10^9$, i.e. calculation shows island of density of $2 \times 10^9/cm^2$)

This type of microstructure is more clearly reflected in the corresponding data for undoped and 10% Sn-doped $CuGaO_2$ thin films (nominal F/T = 1200 Å, G.T. = 800 ^oC) seen in figure 6.24. At small scan area of 200 x 200 nm^2, the surface roughness, RMS value was around 19.9 ±0.5 nm and 24.3 ±0.5 nm for undoped and 10% Sn-doped $CuGaO_2$ thin films, respectively, and the number of nuclei is about 10x to 20x greater than for the $CuCrO_2$ case. Images of the initial nuclei before coalescence can be seen better if the film thickness is reduced to of the order of 100 nm as seen in figure 6.25, which exhibits roughness of the order of the film thickness, suggesting it arises directly from the presence of nucleated islands on the surface. This suggests the growth of multiple single crystal phases which gradually merge together as the film evolves.

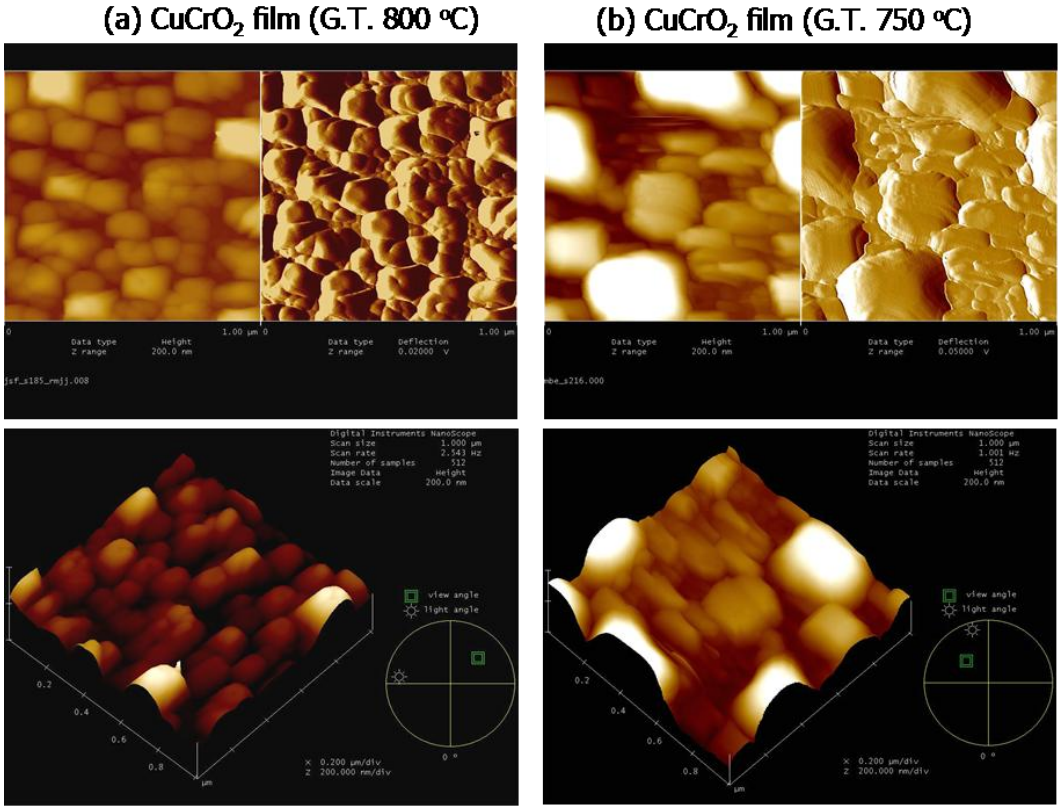


Figure 6.22. AFM images of undoped $CuCrO_2$ thin films (scan size of 1.0 x 1.0 μm^2). (a) undoped $CuCrO_2$ film with F/T = 1000 Å , RMS = 29.9 ±0.5 nm (b) 5% Sn-doped $CuCrO_2$ with F/T = 1000 Å , RMS = 53.9 ±0.5 nm. (Z-range: 200 nm).

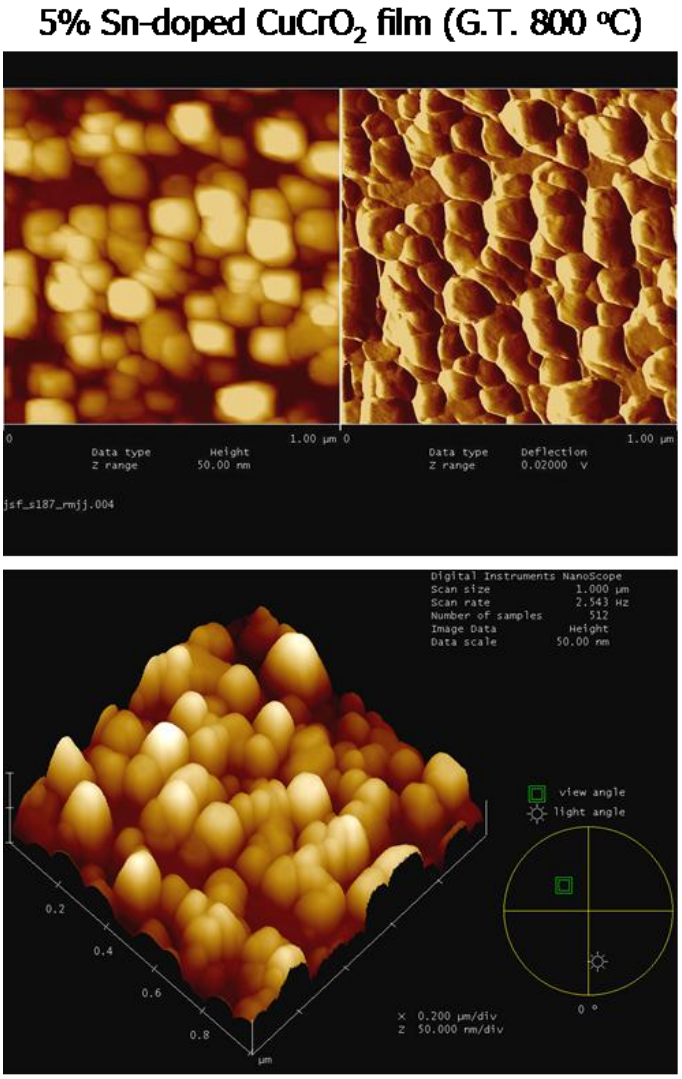


Figure 6.23. AFM images of 5% Sn-doped $CuCrO_2$ thin films (scan size of 1.0 x 1.0 μm^2). The film was grown at 800 ^oC for F/T = 1000 Å . RMS = 15.8 ±0.5 nm (Z- range: 50 nm).

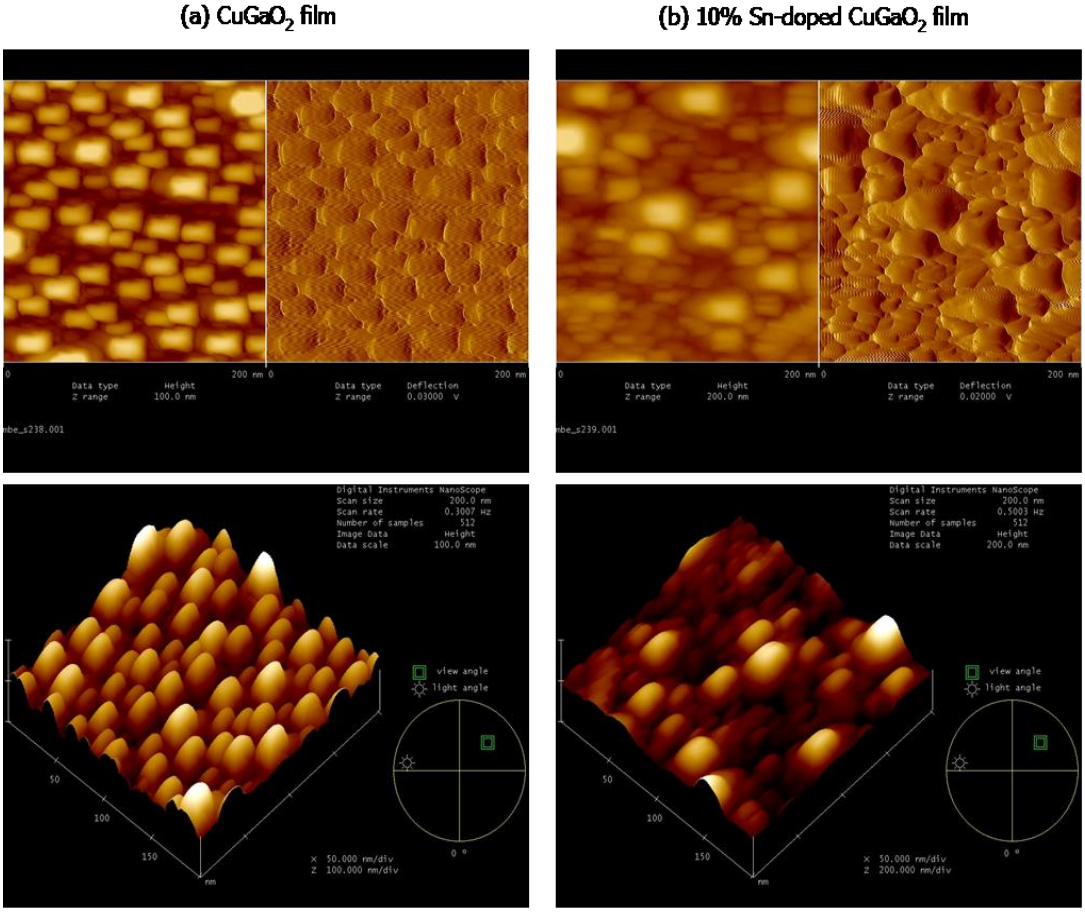


Figure 6.24. AFM images of undoped and 10% Sn-doped $CuGaO_2$ thin films (scan size = 200 x 200 nm^2). (a) undoped $CuGaO_2$ film with F/T = 1200 Å , RMS = 19.9 ±0.5 nm, (b) 10% Sn-doped $CuGaO_2$ with F/T = 1200 Å , RMS = 24.3 ±0.5 nm. Z-range is 100 nm for (a) and 200 nm for (b).

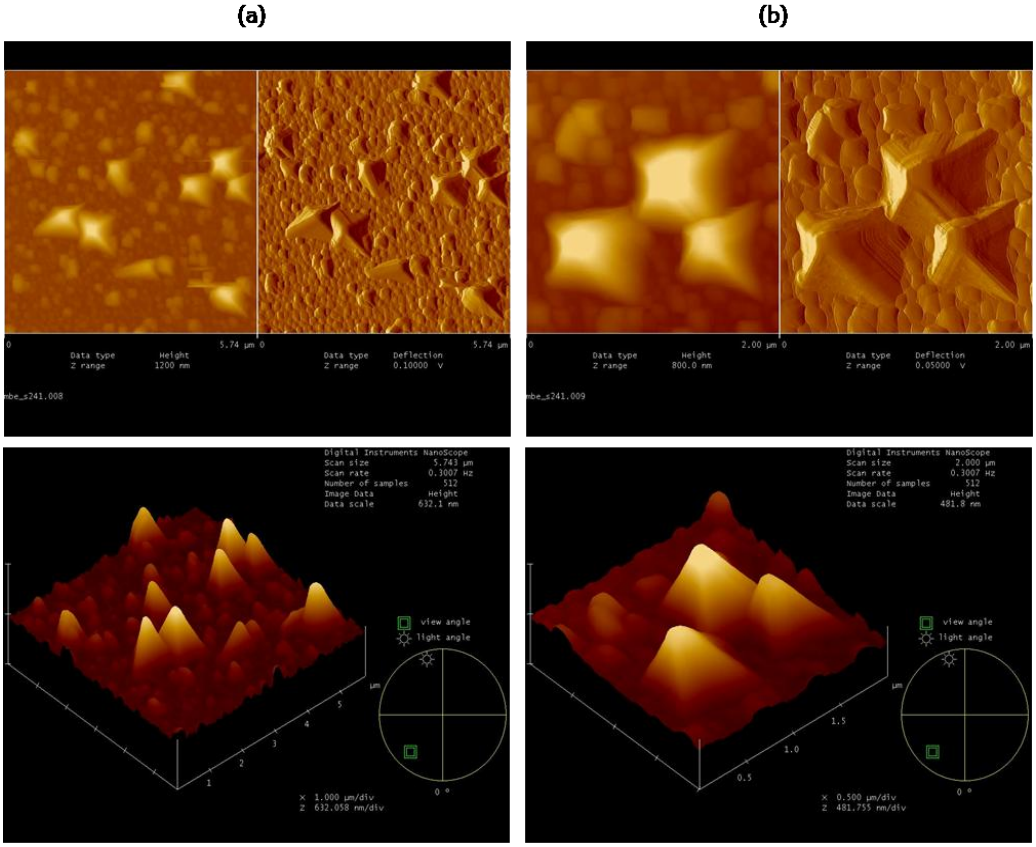


Figure 6.25. AFM images of 5% Sn-doped $CuGaO_2$ thin films. The film was grown at 600 ^oC for F/T = 400 Å . (a) scan size = 5.74 x 5.74 μm^2, Z-range = 1200 nm, RMS = 99.5 ±0.5 nm (b) scan size = 2 x 2 μm^2, Z-range = 800 nm, RMS = 136.0 ±0.5 nm

6.4 Concluding Remarks

- It has been shown that epitaxially oriented $CuCrO_2$ and $CuGaO_2$ thin films can be grown successfully by OPABE. XRD analysis indicates that the $CuCrO_2$ thin film had an (001) orientation on basal plane sapphire at 800°C, switching over to a preferential (015) orientation at lower growth temperatures. In contrast, $CuGaO_2$ showed the (015) preferred orientation throughout the temperature range.
- XPS studies indicate metal stoichiometries approximately close to the nominal subject stoichiometry, although some deviations occur, either from surface segregation, or from the presence of phases with variable stoichiometry not highlighted in the XRD studies. Cu(I) is again shown to be the dominant oxidation state using the bilayer approach adopted.
- Electronic characterisation of the deposited layers shows valence band structure typical to that expected of delafossite material, with direct band gaps in excess of 3 eV. XPS data are also suggestive that n-type doping can be achieved by incorporating Sn in the materials.
- AFM measurements show the films are rather rough. The data suggests that film growth follows an island growth mechanism, in which oriented single crystal material at a nucleation density of around $10^9 \sim 10^{10}$ cm^{-2} develop on the surface initially. Crystallite aggregation then occurs as the film thickness rises above 100 nm.

References

1. A. Walsh, J. L. F. Da Silva, S. H. Wei, C. Korber, A. Klein, L. F. J. Piper, A. DeMasi, K. E. Smith, G. Panaccione, P. Torelli, D. J. Payne, A. Bourlange and R. G. Egdell, Physical Review Letters **100** (16), 167402 (2008).

2. G. W. Watson, K. G. Godinho and A. Walsh, Journal of Physical Chemistry C **113** (1), 439-448 (2009).

3. A. F. Kohan, G. Ceder, D. Morgan and C. G. Van de Walle, Physical Review B **61** (22), 15019-15027 (2000).

4. G. Thomas, Nature **389** (6654), 907-908 (1997).

5. D. O. Scanlon and G. W. Watson, Journal of Materials Chemistry **21** (11), 3655-3663 (2011).

6. H. Yanagi, T. Hase, S. Ibuki, K. Ueda and H. Hosono, Applied Physics Letters **78** (11), 1583-1585 (2001).

7. N. Duan, A. W. Sleight, M. K. Jayaraj and J. Tate, Applied Physics Letters **77** (9), 1325-1326 (2000).

8. K. Ueda, T. Hase, H. Yanagi, H. Kawazoe, H. Hosono, H. Ohta, M. Orita and M. Hirano, Journal of Applied Physics **89** (3), 1790-1793 (2001).

9. R. Nagarajan, N. Duan, M. K. Jayaraj, J. Li, K. A. Vanaja, A. Yokochi, A. Draeseke, J. Tate and A. W. Sleight, International Journal of Inorganic Materials **3** (3), 265-270 (2001).

10. A. Tiwari and M. Snure, Applied Physics Letters **91** (9), 092123 (2007).

11. D. O. Scanlon, A. Walsh and G. W. Watson, Chemistry of Materials **21** (19), 4568-4576 (2009).

12. R. Nagarajan, A. D. Draeseke, A. W. Sleight and J. Tate, Journal of Applied Physics **89** (12), 8022-8025 (2001).

13. K. Kimura, H. Nakamura, S. Kimura, M. Hagiwara and T. Kimura, Physical Review Letters **103** (10), 107201 (2009).

14. H. Yamaguchi, S. Ohtomo, S. Kimura, M. Hagiwara, K. Kimura, T. Kimura, T. Okuda and K. Kindo, Physical Review B **81** (3), 033104 (2010).

15. R. Rao, A. Dandekar, R. T. K. Baker and M. A. Vannice, Journal of Catalysis **171** (2), 406-419 (1997).

16. K. Hayashi, K. Sato, T. Nozaki and T. Kajitani, Jpn J Appl Phys **47** (1), 59-63 (2008).

17. X. D. Fang, D. Li, Z. H. Deng, S. Zhou, R. H. Tao, W. W. Dong, T. Wang, Y. P. Zhao, G. Meng and X. B. Zhu, Journal of Physics D-Applied Physics **40** (16), 4910-4915 (2007).

18. S. Kim, J. Lee, J. Kim and Y. Heo, Current Applied Physics **12**, S123-S126 (2012).

19. T. W. Chiu, K. Tonooka and N. Kikuchi, Thin Solid Films **516** (18), 5941-5947 (2008).

20. A. C. Rastogi, S. H. Lim and S. B. Desu, Journal of Applied Physics **104** (2), 023712 (2008).

21. B. U. Kohler and M. Jansen, Zeitschrift Fur Anorganische Und Allgemeine Chemie **543** (12), 73-80 (1986).

22. X. L. Nie, S. H. Wei and S. B. Zhang, Physical Review Letters **88** (6), 066405 (2002).

23. H. Hosono, T. Mine, H. Yanagi, K. Nomura, T. Kamiya and M. Hirano, Thin Solid Films **516** (17), 5790-5794 (2008).

24. S. Mahapatra and S. A. Shivashankar, Chemical Vapor Deposition **9** (5), 238-240 (2003).

25. F. A. Benko and F. P. Koffyberg, Materials Research Bulletin **21** (6), 753-757 (1986).

26. R. Bywalez, S. Gotzendorfer and P. Lobmann, Journal of Materials Chemistry **20** (31), 6562-6570 (2010).

27. T. Okuda, T. Onoe, Y. Beppu, N. Terada, T. Doi, S. Miyasaka and Y. Tokura, Journal of Magnetism and Magnetic Materials **310** (2), 890-892 (2007).

28. K. Hayashi, K. Sato, T. Nozaki and T. Kajitani, Japanese Journal of Applied Physics **47** (1), 59-63 (2008).

29. S. Y. Zheng, G. S. Jiang, J. R. Su and C. F. Zhu, Materials Letters **60** (29-30), 3871-3873 (2006).

30. A. N. Banerjee and K. K. Chattopadhyay, Progress in Crystal Growth and Characterization of Materials **50** (1-3), 52-105 (2005).

31. M. A. Marquardt, N. A. Ashmore and D. P. Cann, Thin Solid Films **496** (1), 146-156 (2006).

32. D. O. Scanlon, K. G. Godinho, B. J. Morgan and G. W. Watson, Journal of Chemical Physics **132** (2), 024707 (2010).

33. F. A. Benko and F. P. Koffyberg, Journal of Physics and Chemistry of Solids **48** (5), 431-434 (1987).

34. F. A. Benko and F. P. Koffyberg, Journal of Physics and Chemistry of Solids **45** (1), 57-59 (1984).

35. B. J. Ingram, T. O. Mason, R. Asahi, K. T. Park and A. J. Freeman, Physical Review B **6415** (15), 5114 (2001).

36. B. J. Ingram, B. J. Harder, N. W. Hrabe and T. O. Mason, Chemistry of Materials **16** (26), 5623-5629 (2004).

37. B. J. Ingram, G. B. Gonzalez, T. O. Mason, D. Y. Shahriari, A. Barnabe, D. G. Ko and K. R. Poeppelmeier, Chemistry of Materials **16** (26), 5616-5622 (2004).

38. B. J. Ingram, M. I. Bertoni, K. R. Poeppelmeier and T. O. Mason, Thin Solid Films **486** (1-2), 86-93 (2005).

39. C. D. Wagner, L. E. Davis, M. V. Zeller, J. A. Taylor, R. H. Raymond and L. H. Gale, Surface and Interface Analysis **3** (5), 211-225 (1981).

40. T. Arnold, D. J. Payne, A. Bourlange, J. P. Hu, R. G. Egdell, L. F. J. Piper, L. Colakerol, A. Masi, P. A. Glans, T. Learmonth, K. E. Smith, J. Guo, D. O. Scanlon, A. Walsh, B. J. Morgan and G. W. Watson, Physical Review B **79** (7), 075102 (2009).

41. D. O. Scanlon, A. Walsh, B. J. Morgan, G. W. Watson, D. J. Payne and R. G. Egdell, Physical Review B **79** (3), 035101 (2009).

42. D. J. Aston, D. J. Payne, A. J. H. Green, R. G. Egdell, D. S. L. Law, J. Guo, P. A. Glans, T. Learmonth and K. E. Smith, Physical Review B **72** (19), 195115 (2005).

43. D. Shin, J. S. Foord, D. J. Payne, T. Arnold, D. J. Aston, R. G. Egdell, K. G. Godinho, D. O. Scanlon, B. J. Morgan, G. W. Watson, E. Mugnier, C. Yaicle, A. Rougier, L. Colakerol, P. A. Glans, L. F. J. Piper and K. E. Smith, Physical Review B **80** (23), 233105 (2009).

44. T. Takeuchi, H. Ishikawa, N. Takeuchi and Y. Horikoshi, Thin Solid Films **516** (14), 4593-4597 (2008).

45. J. Tauc, Grigorov.R and A. Vancu, Physica Status Solidi **15** (2), 627-637 (1966).

46. K. Santra, C. K. Sarkar, M. K. Mukherjee and B. Ghosh, Thin Solid Films **213** (2), 226-229 (1992).

47. P. D. C. King, T. D. Veal, F. Fuchs, C. Y. Wang, D. J. Payne, A. Bourlange, H. Zhang, G. R. Bell, V. Cimalla, O. Ambacher, R. G. Egdell, F. Bechstedt and C. F. McConville, Physical Review B **79** (20), 205211 (2009).

7 Concluding Remarks

The main overall conclusion of the thesis is that Cu_2O and the related delafossite compounds $CuInO_2$, $CuCrO_2$ and $CuGaO_2$ can be grown successfully using the OPABE approach, and the data also suggest that *in situ* electrical doping during growth can also be achieved.

In chapter 3, the first studies of the growth of Cu_2O by OPABE were implemented. This system posed new problems in OPABE, where the normal approach is to choose an excess oxygen atom flux to minimise oxygen vacancies in the grown structure in systems where there is little chemical ambiguity in the oxidation state of the incorporated metal atoms. For the Cu system, the problem of forming the CuO phase in competition with Cu_2O was highlighted. Whilst thermodynamic predictions that Cu_2O would be more favoured at high temperatures offered a partial solution, it was not possible to further tune the oxidation state by controlling the oxygen atom flux since the oxygen atom source only operated stably over a narrow range of conditions. Since the tendency to form Cu (II) exists in this system, an alternative approach was instead realised involving the growth and interdiffusion of oxide : Cu bilayers with Cu layer deposited capable of reducing Cu (II) to Cu(I).

The studies reported in chapter 4 were the first to use this bilayer approach to show that $CuInO_2$ could be grown using OPABE. Careful control of the Cu:In ratio was required to achieve this since : (i) the stoichiometry in the film obviously reflects in part the relative beam fluxes of the two metals. (ii) a secondary feature found was that the incorporation efficiency of Cu in the growing layers was influenced by the presence of In. Although $CuInO_2$ was the dominant phase, it was noted that small amounts of other phases such as $Cu_2In_2O_5$ and Cu_2O also were formed. Limited

surface diffusion resulted in very rough films at low temperature, whereas 3D island formation took place above 800 ^{o}C. It was also shown that Cr and Sn could be doped into the films, leading to p-type and n-type character. In chapter 5, comparisons were made with the growth of $CuInO_2$ by pulsed laser deposition. Interestingly, perhaps one of the major advantages of PLD over OPABE – stoichiometric transfer from target to sample – was not observed by XPS analysis, either suggesting significant surface segregation effects, fluence dependent ablation fluxes or target inhomogeneities. The occurrence of alternative phases was similar in PLD and OPABE, but differing film textures were observed in the two methods. Given the apparent difficulty in controlling film stoichiometry in PLD of these materials, an overall conclusion might be that OPABE offers the best prospects for this materials system since the ability to control beam fluxes enables the needed conditions to be "dialled in". However a counter to this is the greater experimental simplicity associated with PLD. In chapter 6, the general capabilities of OPABE in this area were further exemplified with the growth of $CuCrO_2$ and $CuGaO_2$. Although excellent phase purity was seen in XRD, again stoichiometric deficiencies were suggested in XPS due to inaccurate control of the beam fluxes.

Perhaps the most fascinating aspect of the whole work was the unexpected film textures observed compared to that seen with other growth methods. For Cu_2O, whilst it would have been expected that the (100) plane of Cu_2O would form parallel to the (100) MgO substrate to which it is lattice matched, in actual fact the main tendency was to observe the (110) film texture. This possibly has some origin from the fact that the MgO plane is non-polar so it is reasonable to suggest that it might help to stabilise a non-polar orientation such as (110). Indeed calculations show that this orientation is favoured [1].

A most unusual observation can be noted in the film textures of the $CuGaO_2$, $CuCrO_2$, and $CuInO_2$ compounds which showed for the former a preferred (015) texture, while for the latter two compounds the amount of (015) texture increased at lower temperatures. Thus the expected growth mode with the c-axis normal to the surface of the underlying alumina substrate is not fully observed, and a seemingly obscure crystal orientation at the interface occurs. Consider the case of $CuCrO_2$ in detail. The rhombohedral (space group $R\bar{3}m$) delafossite structure of 3*R*-$CuCrO_2$ is based on trilayer sheets comprised of Cr ions occupying the octahedral holes between two close packed layers of O ions (figure 7.1) [2]. The O ions in the sheets are linked via linear O-Cu-O dumbbells [3, 4]. Why should the (015) plane orientation have a tendency to occur with OPABE? In actual fact the stability of the (015) plane can be explained on the basis of simple structural and energetic considerations.

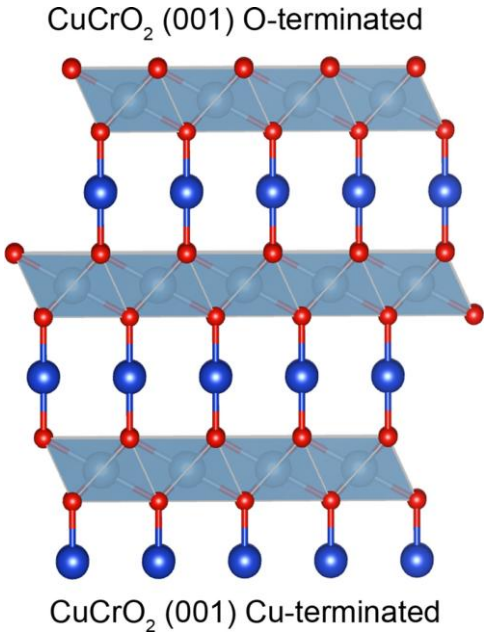


Figure 7.1. Crystal structure of the 3*R*- polymorph of $CuCrO_2$. Oxygen ions are red, copper ions dark blue and chromium light blue. The CrO_6 octahedra are shaded. (adapted from ref. 2)

Sideviews of the (015) oriented delafossite structure are shown in figure 7.2 along with a similar view of the O-terminated surface of Al_2O_3. Top views are also shown [2].

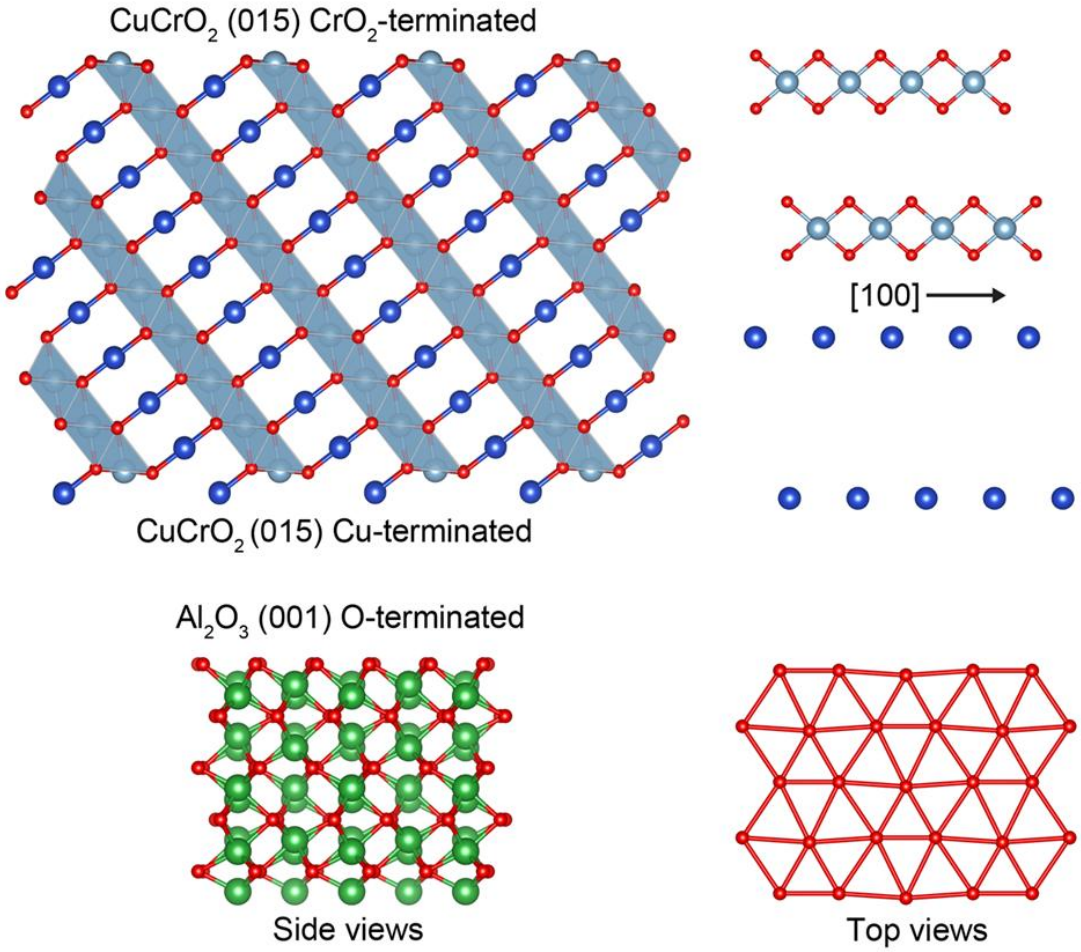


Figure 7.2. Upper panels. Left: side views of the CrO_2 and Cu (015) terminations of $CuCrO_2$. Right: top views of the two terminations showing only the ions in the outermost ionic plane. Colour coding is as in Figure 1. Lower panels. Left: side view of the O-terminated surface of Al_2O_3(001). Oxygen ions are red, aluminium ions are green. Right: top view of the (001) termination of Al_2O_3. (adapted from ref. 2)

The (001) termination shown in figure 1 involves cutting one Cu-O bond per rhombic surface unit cell ($a = b = 2.973$ Å, $\gamma = 60°$, area 7.656 Å^2) to give either a Cu or O terminated polar surface. As will emerge below alternative terminations involving cutting 3 Cr-O bonds per cell are unlikely on the basis of simple energetic considerations. The (015) surface involves cutting two Cr-O bonds and one Cu-O bond in a larger rhomboidal surface unit cell whose sides are defined by edges of length *a* and *e* ($a = 2.973$ Å, $e = 7.431$ Å, $\gamma = 78.46°$, area 21.65 Å^2). Two complementary polar terminations are then possible. The first involves stripes of edge sharing CrO_4 plaquettes running along a [100] direction with single dangling bonds on one Cr and one O per cell pointing roughly normal to the surface, together with a single dangling bond on O pointing obliquely to the surface. The complementary termination involves an outer layer of Cu atoms each with a single dangling bond oblique to the surface normal, together with normally oriented dangling bonds on one Cr and one O per cell. Using bulk thermochemical data[5] for Cu_2O and Cr_2O_3 it can be estimated that the energy associated with cutting a single Cu-O bond for two coordinate Cu(I) is 274 kJ/mole, as compared to 223 kJ/mole for a single Cr-O bond for 6-coordinate Cr(III). In this way it is possible to make rough estimates of the unrelaxed surface energies for the (001) and (015) terminations. These turn out to be respectively 2.97 Jm^{-2} for the (001) surface and 2.76 Jm^{-2} for the (015) surface. Bearing in mind that there must be very pronounced surface relaxation, it can be seen that the two surfaces have finely balanced surface energies. Moreover the separation *d* between rows of Cu or Cr ions on the (015) surfaces is equal to $b \times \sin(78.46°)$ which is 7.280 Å. It emerges that *d* is roughly equal to $3 \times a_s/2 = 7.138$ Å i.e. three times the distance between adjacent rows of O ions on the O-terminated (001) surface of Al_2O_3. The cation periodicity along <100> directions in the epilayer has a mismatch of 8.2 % with

the periodicity in oxygen positions on the Al_2O_3(001) surface, but in the orthogonal direction the mismatch in inter-row separations is only 1.99%. This allows construction of schematic interface structures with reasonable matching of atomic positions at the interface as shown in figure 7.3 [2]. For the (001) termination of $CuCrO_2$ the 11.2 % mismatch pertains in two high symmetry in-plane directions. These considerations help to explain the unexpected appearance of an (015) oriented epilayer during growth at 700 °C.

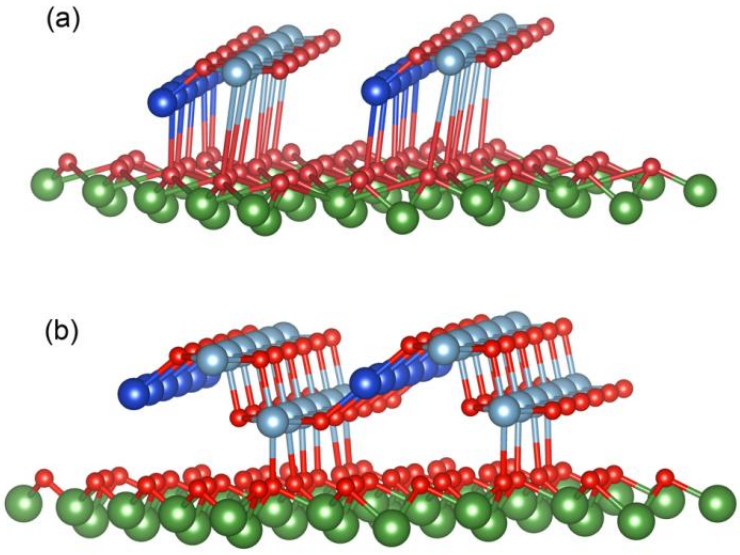


Figure 7.3. Two possible interface structures for $CuCrO_2$(015) on Al_2O_3(001). (a) For Cu terminated $CuCrO_2$(015) surface (b) for CrO_2 terminated $CuCrO_2$(015) surface. (adapted from ref. 2)

One of the interesting questions concerns the extent to which the results of OPABE can be predicted using thermodynamics, as opposed to kinetic effects which in principle must arise in what is a dynamic process. It is somewhat difficult to predict what the thermodynamic predictions are since: (i) the oxygen chemical potential is not easily evaluated in view of the fact that a significant concentration of oxygen

radicals and electronically excite species exist in the low pressure "atom" beam. (ii) there is significant uncertainty concerning the thermodynamic stability of delafossites [6]. Nonetheless for the delafossites and cuprous oxide itself, the general consensus is that oxidation of Cu+ is expected at low temperatures in the presence of oxygen, with Cu+ being stabilised at high temperatures. To a reasonable extent, these are features which were observed in the present work with cuprous oxide being favoured at high temperatures and oxidation of Cu representing a decomposition pathway. The overall conclusion is that a knowledge of the thermochemistry of a particular set of related compounds under conventional conditions seems to prove a useful outline as to the characteritics observed in OPABE. Where kinetic effects were observed seemed to relate to film morphology rather than chemical composition. For all systems studied, rather rough films were observed often transforming to islands at high temperature. This is suggestive of the fact that very limited surface diffusion occurs in many OPABE systems unless very high temperatures are involved. The experiments have somewhat highlighted difficulties associated with the growth of these materials using the fairly standard commercial MBE system design which was available to the project [7, 8]. As noted above it was found difficult to control the Cu (I) oxidation state [9], this being only achieved at high growth temperatures [10, 11] or using a "bilayer" growth approach. Ideally it should be possible to obtain additional control by varying the oxygen atom flux, but the commercial beam source provided did not seem amenable to this approach, since the flux could only be varied by a relatively small amount otherwise the plasma extinguished [12]. An improved design in this area would be welcome. Secondly it was difficult to accurately control the relative metal fluxes in the instrument available, since these had to be set prior to growth using the single thin film monitor to estimate the K-cell temperatures needed.

Some real-time direct closed-loop control of the K-cell operating conditions using *in situ* beam flux monitors for the individual K-cells should improve this aspect [13]. These are mainly simply engineering issues, but would probably significantly improve the quality of the grown layers.

One chemical issue associated with OPABE is the fact the results showed that growth seems to be nucleated by the formation of a relatively small number of three dimensional growth islands, which results in the formation of rough polycrystalline coatings, albeit crystallographically oriented, instead of the smooth single crystal layers which would be ideal [14-16]. Conventional MBE has developed various strategies to modify surface diffusion behaviour to control morphology, so it would be an interesting next step to investigate how this knowledge could be exploited in OPABE. A second chemical problem is that XPS seemed to indicate that the incorporation of Cu in the growing layer seemed to be inhibited when metal species for much more exothermic oxides such as In or Cr was simultaneously present. The origin of this effect is not clear, but flux dependent incorporation efficiencies are known to be quite problematic in conventional MBE, so this is clearly a second key issue to be addressed.

In terms of taking further the present research, the above developments should enable films with improved morphology and chemical composition to be grown. This would then merit more detailed structural studies to determine chemical properties. In terms of ultimate applications, detailed electrical characterisation of these improved layers would be a crucial step to ascertain carrier number density and transport properties, the effectiveness and degree of electrical activation of the

various possible chemical dopants, and obtain an understanding of the role of defects in controlling electronic properties.

For the future plan, we consider that as below:

- Investigation of electrical properties: Hall mobility (μ_{Hall}) and carrier concentration (*N*e) for delafossite grown film by OPABE system
- Research and development involving display application of delafossite-TFT, proposed p-channel TFT using $CuMO_2$ or the active layer (e.g. doped $CuCrO_2$)
- Temperature-dependent conductivity of delafossite showing a good fit to variable-range hopping.
- Sheet resistance on various film thicknesses

References

1. A. Soon, M. Todorova, B. Delley and C. Stampfl, Physical Review B **76** (12), 045210 (2007).

2. D. Shin, J. S. Foord, R. G. Egdell and A. Walsh, Journal of Applied Physics **112** (11), 113718 (2012).

3. T. Arnold, D. J. Payne, A. Bourlange, J. P. Hu, R. G. Egdell, L. F. J. Piper, L. Colakerol, A. Masi, P. A. Glans, T. Learmonth, K. E. Smith, J. Guo, D. O. Scanlon, A. Walsh, B. J. Morgan and G. W. Watson, Physical Review B **79** (7), 075102 (2009).

4. D. Shin, J. S. Foord, D. J. Payne, T. Arnold, D. J. Aston, R. G. Egdell, K. G. Godinho, D. O. Scanlon, B. J. Morgan, G. W. Watson, E. Mugnier, C. Yaicle, A. Rougier, L. Colakerol, P. A. Glans, L. F. J. Piper and K. E. Smith, Physical Review B **80** (23), 233105 (2009).

5. M. Binnewies and E. Milke, *Thermochemical Data of Elements and Compounds*, 2nd Edition ed. (Wiley-VCH Verlag GmBH, Weinheim, 2002).

6. Y. Kumekawa, M. Hirai, Y. Kobayashi, S. Endoh, E. Oikawa and T. Hashimoto, J Therm Anal Calorim **99** (1), 57-63 (2010).

7. A. Bourlange, D. J. Payne, R. G. Egdell, J. S. Foord, P. P. Edwards, M. O. Jones, A. Schertel, P. J. Dobson and J. L. Hutchison, Applied Physics Letters **92** (9), 092117 (2008).

8. A. Y. Cho and J. R. Arthur, Prog. Solid-State Chem. **10,** 157 (1975).

9. K. Maki and T. Itoh, Vacuum **81** (7), 904-910 (2007).

10. A. E. Rakhshani, Solid-State Electronics **29** (1), 7-17 (1986).

11. M. R. Wright, Thesis, Wayne State University, Dept. of Chemistry., 1962.

12. K. P. Muthe, J. C. Vyas, S. N. Narang, D. K. Aswal, S. K. Gupta, D. Bhattacharya, R. Pinto, G. P. Kothiyal and S. C. Sabharwal, Thin Solid Films **324** (1-2), 37-43 (1998).

13. R. G. Egdell, A. Bourlange, D. J. Payne, R. G. Palgrave, J. S. Foord, R. M. J. Jacobs, A. Schertel, J. L. Hutchison and P. J. Dobson, Thin Solid Films **517** (15), 4286-4294 (2009).

14. W. K. Burton, N. Cabrera and F. C. Frank, Philosophical Transactions of the Royal Society of London Series a-Mathematical and Physical Sciences **243** (866), 299-358 (1951).

15. I. N. Stranski, Z. Phys. Chem **136**, 259 (1928).

16. W. Kossel, Nach. Ges. Wiss. Göttingen, 135 (1927).